

## PUBLISHER :



### Address of Publisher & Editor's Office :

GDAŃSK UNIVERSITY  
OF TECHNOLOGY  
Faculty  
of Ocean Engineering  
& Ship Technology

ul. Narutowicza 11/12  
80-952 Gdańsk, POLAND  
tel.: +48 58 347 13 66  
fax : +48 58 341 13 66  
e-mail : office.pmr@pg.gda.pl

Account number :  
**BANK ZACHODNI WBK S.A.**  
I Oddział w Gdańsku  
41 1090 1098 0000 0000 0901 5569

### Editorial Staff :

**Tadeusz Borzęcki** Editor in Chief  
e-mail : tadbzor@pg.gda.pl

**Przemysław Wierzchowski** Scientific Editor  
e-mail : e.wierzchowski@chello.pl

**Jan Michalski** Editor for review matters  
e-mail : janmi@pg.gda.pl

**Aleksander Kniat** Editor for international relations  
e-mail : olek@pg.gda.pl

**Kazimierz Kempa** Technical Editor  
e-mail : kkempa@pg.gda.pl

**Piotr Bzura** Managing Editor  
e-mail : pbzura@pg.gda.pl

**Cezary Spigarski** Computer Design  
e-mail : biuro@oficynamorska.pl

Domestic price :  
single issue : 20 zł

Prices for abroad :  
single issue :  
- in Europe EURO 15  
- overseas US\$ 20

ISSN 1233-2585



## POLISH MARITIME RESEARCH

*in internet*

[www.bg.pg.gda.pl/pmr/pmr.php](http://www.bg.pg.gda.pl/pmr/pmr.php)



## POLISH MARITIME RESEARCH

No 1(63) 2010 Vol 17

## CONTENTS

- 3 **TADEUSZ SZELANGIEWICZ, TOMASZ ABRAMOWSKI**  
*Numerical analysis of influence of ship hull form modification on ship resistance and propulsion characteristics (Part II)*
- 10 **TADEUSZ SZELANGIEWICZ, TOMASZ ABRAMOWSKI, KATARZYNA ŻELAZNY**  
*Numerical analysis of influence of ship hull form modification on ship resistance and propulsion characteristics (Part III)*
- 14 **TADEUSZ KORONOWICZ, ZBIGNIEW KRZEMIANOWSKI, TERESA TUSZKOWSKA, JAN A. SZANTYR**  
*A complete design of contra-rotating propellers using the new computer system*
- 25 **TOMASZ CEPOWSKI**  
*Influence analysis of changes of design parameters of passenger-car ferries on their selected sea-keeping qualities*
- 33 **AGNIESZKA KRÓLICKA**  
*State equations in the mathematical model of dynamic behaviour of multihull floating unit*
- 39 **BOGDAN LIGAJ, GRZEGORZ SZALA**  
*Experimental verification of two-parametric models of fatigue characteristics by using the tests of S55J0 steel as an example*
- 51 **BIERNACKI RAFAŁ, PIOTR KRZYŚLAK**  
*Comparing N3-60 cascade exit angles obtained from tunnel measurements and numerical simulations*
- 57 **ZBIGNIEW KORCZEWSKI**  
*Operational causes of fatigue failures within passages of gas turbine engines*
- 62 **WOJCIECH HOMIK**  
*Diagnostics, maintenance and regeneration of torsional vibration dampers for crankshafts of ship diesel engines*
- 69 **ANTONI ISKRA**  
*Correction of the combustion engine run irregularity in hybrid systems*
- 75 **EUGENIUSZ RANATOWSKI**  
*Problems of welding in shipbuilding - an analytic-numerical assessment of the thermal cycle in haz with three dimensional heat source models in agreement with modelling rules (Part I)*
- 80 **RADOSŁAW RUTKOWSKI**  
*Dynamical control of dimensional quality of large steel structures in production enterprises of low - level technological support*

# Editorial

---

POLISH MARITIME RESEARCH is a scientific journal of worldwide circulation. The journal appears as a quarterly four times a year. The first issue of it was published in September 1994. Its main aim is to present original, innovative scientific ideas and Research & Development achievements in the field of :

**Engineering, Computing & Technology, Mechanical Engineering,**

which could find applications in the broad domain of maritime economy. Hence there are published papers which concern methods of the designing, manufacturing and operating processes of such technical objects and devices as : ships, port equipment, ocean engineering units, underwater vehicles and equipment as well as harbour facilities, with accounting for marine environment protection.

The Editors of POLISH MARITIME RESEARCH make also efforts to present problems dealing with education of engineers and scientific and teaching personnel. As a rule, the basic papers are supplemented by information on conferences , important scientific events as well as cooperation in carrying out international scientific research projects.

## Scientific Board

---

Chairman : Prof. **JERZY GIRTLEK** - Gdańsk University of Technology, Poland

Vice-chairman : Prof. **ANTONI JANKOWSKI** - Institute of Aeronautics, Poland

Vice-chairman : Prof. **MIROSLAW L. WYSZYŃSKI** - University of Birmingham, United Kingdom

---

Dr **POUL ANDERSEN**  
Technical University  
of Denmark  
Denmark

Prof. **STANISŁAW GUCMA**  
Maritime University of Szczecin  
Poland

Dr **YOSHIO SATO**  
National Traffic Safety  
and Environment Laboratory  
Japan

Dr **MEHMET ATLAR**  
University of Newcastle  
United Kingdom

Prof. **ANTONI ISKRA**  
Poznań University  
of Technology  
Poland

Prof. **KLAUS SCHIER**  
University of Applied Sciences  
Germany

Prof. **GÖRAN BARK**  
Chalmers University  
of Technology  
Sweden

Prof. **JAN KICIŃSKI**  
Institute of Fluid-Flow Machinery  
of PASci  
Poland

Prof. **FREDERICK STERN**  
University of Iowa,  
IA, USA

Prof. **SERGEY BARSUKOV**  
Army Institute of Odessa  
Ukraine

Prof. **ZYGMUNT KITOWSKI**  
Naval University  
Poland

Prof. **JÓZEF SZALA**  
Bydgoszcz University  
of Technology and Agriculture  
Poland

Prof. **MUSTAFA BAYHAN**  
Süleyman Demirel University  
Turkey

Prof. **JAN KULCZYK**  
Wrocław University of Technology  
Poland

Prof. **TADEUSZ SZELANGIEWICZ**  
Technical University  
of Szczecin  
Poland

Prof. **MAREK DZIDA**  
Gdańsk University  
of Technology  
Poland

Prof. **NICOS LADOMMATOS**  
University College London  
United Kingdom

Prof. **WITALIJ SZCZAGIN**  
State Technical University  
of Kaliningrad  
Russia

Prof. **ODD M. FALTINSEN**  
Norwegian University  
of Science and Technology  
Norway

Prof. **JÓZEF LISOWSKI**  
Gdynia Maritime University  
Poland

Prof. **BORIS TIKHOMIROV**  
State Marine University  
of St. Petersburg  
Russia

Prof. **PATRICK V. FARRELL**  
University of Wisconsin  
Madison, WI  
USA

Prof. **JERZY MATUSIAK**  
Helsinki University  
of Technology  
Finland

Prof. **DRACOS VASSALOS**  
University of Glasgow  
and Strathclyde  
United Kingdom

Prof. **WOLFGANG FRICKE**  
Technical University  
Hamburg-Harburg  
Germany

Prof. **EUGEN NEGRUS**  
University of Bucharest  
Romania

Prof. **YASUHIKO OHTA**  
Nagoya Institute of Technology  
Japan

# Numerical analysis of influence of ship hull form modification on ship resistance and propulsion characteristics

## Part II Influence of hull form modification on wake current behind the ship

Tomasz Abramowski, Ph. D.  
Tadeusz Szelangiewicz, Prof.  
West Pomeranian University of Technology, Szczecin

### ABSTRACT

*After signing ship building contract shipyard's design office orders performance of ship resistance and propulsion model tests aimed at, apart from resistance measurements, also determination of ship speed, propeller rotational speed and propulsion engine power for the designed ship, as well as improvement of its hull form, if necessary. Range of ship hull modifications is practically very limited due to cost and time reasons. Hence numerical methods, mainly CFD ones are more and more often used for such tests. In this paper consisted of three parts, are presented results of numerical calculations of hull resistance, wake and efficiency of propeller operating in non-homogenous velocity field, performed for research on 18 hull versions of B573 ship designed and built by Szczecin Nowa Shipyard.*

**Keywords:** ship hull geometry, numerical (computational) fluid dynamics, resistance, wake, propeller efficiency

### NUMERICAL COMPUTATIONS OF WAKE CURRENT

The second effect of ship hull form modification, apart from change of resistance, is change of wake current which to a large extent influences performance of screw propeller (its thrust, torque and efficiency) as well as overall propulsive efficiency of ship.

Before commencing actual numerical computations a comparative test has been performed, namely, for the initial hull form of B 573 ship wake current has been numerically calculated and obtained results compared with its model tests.

#### Comparative test for wake current computations

Ship draught  $T = 11.3$  [m]  
Water density  $\rho = 999.0$  [ $\text{kg} \cdot \text{m}^{-3}$ ]  
Kinematic viscosity  $\nu = 1.13896$  [ $\text{m}^2 \cdot \text{s}^{-1}$ ]

Wake fractions were determined in compliance with the axial component velocity  $V_x$ , according to the relation:

$$W_X = 1 - \frac{V_X}{V_M} \quad (2)$$

The computation results are presented graphically in Fig. 13 ÷ 16, and numerically - in Tab. 5. In Tab. 6 the results

of model tests [1] are given for comparison. The average value of wake fraction determined numerically within the range of values of the relative propeller radius  $r/R$  reaching from 0.25 to 1.21 is equal to 0.48, while that obtained from the model tests amounts to 0.52.

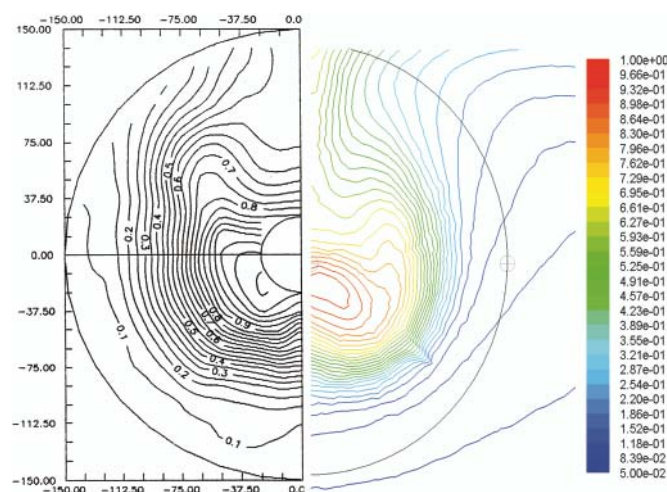


**Fig. 13.** Axial wake fraction distribution on the propeller disk plane: on the right side – results of the numerical test, on the left side – results of the model test [1]

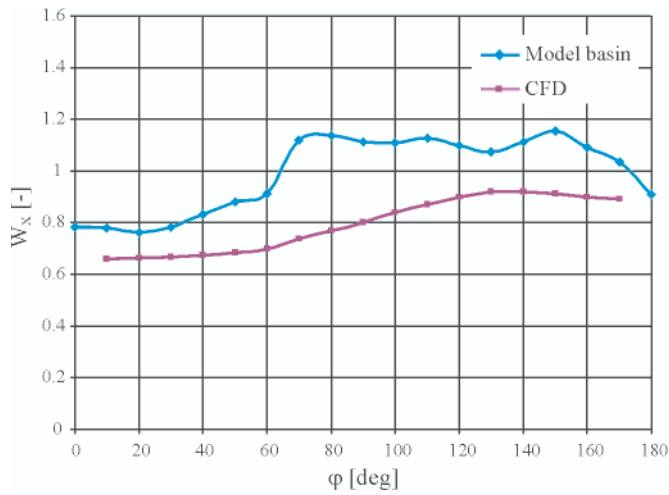


Fig. 14. Circumferential distribution of axial wake fraction component for  $r/R = 0.202$

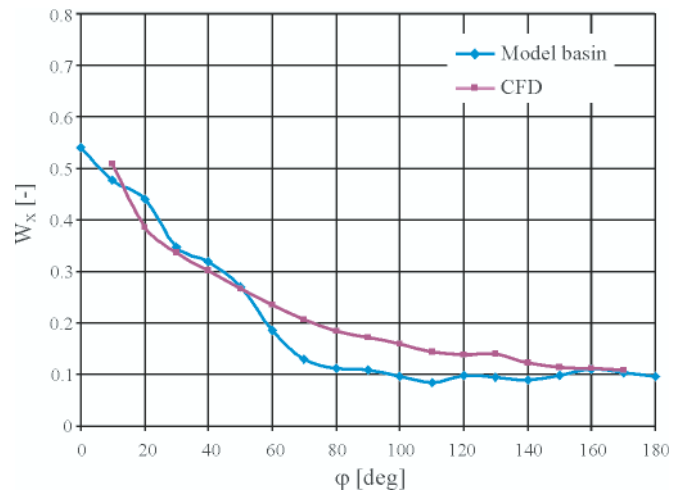


Fig. 16. Circumferential distribution of axial wake fraction component for  $r/R = 1.0$

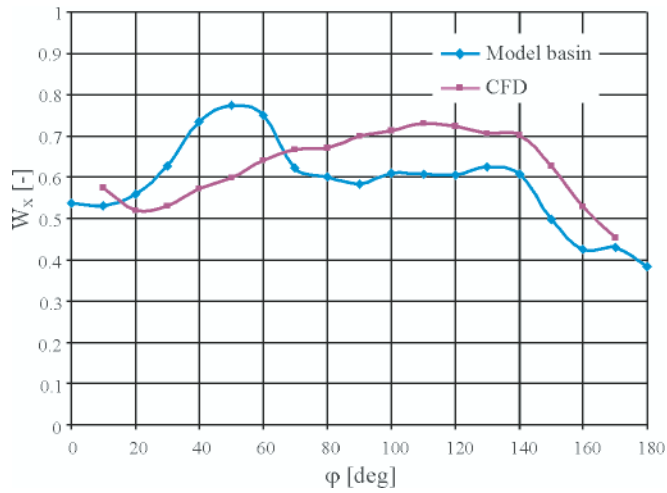


Fig. 15. Circumferential distribution of axial wake fraction component for  $r/R = 0.60$

In Fig. 17 stream lines for the initial ship hull form are also shown.

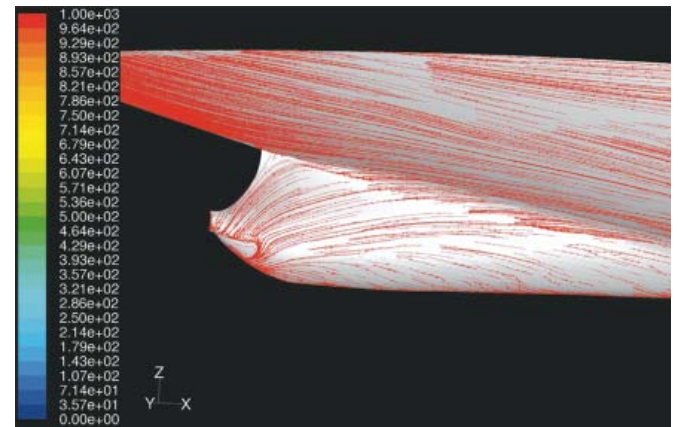


Fig. 17. Distribution of stream lines on ship hull model

Tab. 5. Results of numerical calculations of the axial wake fraction component  $W_x [-]$

r [mm]	25	37.5	50	62.5	75	87.5	100	112.5	125	137.5	150
$\phi$ [deg]											
10	0.6595	0.6383	0.6212	0.5977	0.5746	0.5451	0.521	0.5108	0.5094	0.5092	0.5389
20	0.6627	0.6353	0.5994	0.5658	0.52	0.4793	0.4383	0.4079	0.3853	0.3747	0.3787
30	0.6663	0.6316	0.6004	0.5676	0.5306	0.4839	0.4268	0.3783	0.337	0.3139	0.3028
40	0.6738	0.6365	0.615	0.5968	0.572	0.507	0.427	0.3485	0.3015	0.2709	0.2562
50	0.6843	0.6476	0.6449	0.6427	0.5997	0.5153	0.4162	0.3163	0.266	0.2385	0.2195
60	0.6998	0.674	0.6692	0.6786	0.6395	0.5285	0.3882	0.2989	0.2355	0.2072	0.1906
70	0.7364	0.6949	0.702	0.7093	0.6676	0.5308	0.3962	0.262	0.2073	0.1817	0.1677
80	0.7674	0.7267	0.7221	0.7351	0.6703	0.5154	0.3919	0.2507	0.1838	0.1636	0.1488
90	0.8005	0.7552	0.7469	0.7587	0.7001	0.5467	0.3797	0.2505	0.1715	0.1467	0.1347
100	0.8391	0.804	0.7794	0.781	0.7121	0.566	0.3707	0.2258	0.1601	0.1344	0.1225
110	0.871	0.8441	0.8131	0.7976	0.7299	0.5715	0.3586	0.2128	0.1436	0.1236	0.113
120	0.8992	0.8773	0.8404	0.8161	0.7236	0.5745	0.3484	0.1958	0.1391	0.1158	0.1053
130	0.9197	0.9042	0.8653	0.8176	0.7064	0.5448	0.3567	0.2119	0.1397	0.1101	0.0992
140	0.9204	0.9083	0.8645	0.8055	0.7012	0.4911	0.2737	0.1681	0.1227	0.1033	0.0943
150	0.9114	0.8791	0.8406	0.7467	0.6279	0.4252	0.254	0.1511	0.1143	0.1001	0.0909
160	0.8998	0.8588	0.8035	0.7018	0.5283	0.3518	0.2067	0.1414	0.1122	0.0989	0.0897
170	0.8927	0.8361	0.7455	0.6106	0.4542	0.2885	0.18	0.129	0.1088	0.0969	0.088

Tab.6. Results of model tests of the axial wake fraction component  $W_x$  [-]

r/R	0.202	0.25	0.3	0.35	0.4	0.5	0.6	0.7	0.8	0.9	0.95	1	1.21
r [mm]	25	31	37.2	43.4	49.6	62	74.4	86.8	99.2	111.6	117.8	124	150
$\varphi$ [deg]													
0	0.783	0.736	0.692	0.652	0.617	0.566	0.537	0.531	0.535	0.537	0.538	0.540	0.570
10	0.778	0.731	0.686	0.646	0.612	0.562	0.531	0.516	0.506	0.492	0.484	0.478	0.466
20	0.763	0.715	0.671	0.633	0.604	0.570	0.559	0.551	0.526	0.485	0.463	0.440	0.359
30	0.784	0.741	0.702	0.670	0.646	0.626	0.628	0.611	0.537	0.433	0.387	0.348	0.250
40	0.830	0.797	0.767	0.744	0.727	0.718	0.734	0.702	0.583	0.432	0.369	0.319	0.197
50	0.881	0.857	0.835	0.816	0.801	0.785	0.774	0.701	0.552	0.389	0.323	0.270	0.152
60	0.913	0.893	0.874	0.856	0.840	0.807	0.750	0.630	0.458	0.294	0.232	0.186	0.116
70	1.119	1.121	1.105	1.068	1.005	0.814	0.623	0.458	0.312	0.198	0.157	0.130	0.111
80	1.138	1.141	1.122	1.079	1.006	0.789	0.600	0.438	0.291	0.177	0.138	0.112	0.104
90	1.111	1.113	1.098	1.063	1.005	0.817	0.584	0.391	0.253	0.157	0.126	0.108	0.111
100	1.108	1.109	1.095	1.061	1.005	0.824	0.610	0.423	0.271	0.157	0.119	0.097	0.112
110	1.127	1.130	1.113	1.073	1.005	0.802	0.608	0.438	0.281	0.155	0.112	0.084	0.087
120	1.099	1.101	1.088	1.057	1.004	0.832	0.605	0.408	0.263	0.157	0.121	0.098	0.089
130	1.073	1.074	1.065	1.042	1.003	0.865	0.626	0.415	0.266	0.153	0.116	0.094	0.104
140	1.112	1.114	1.099	1.064	1.005	0.819	0.607	0.422	0.271	0.155	0.115	0.089	0.083
150	1.156	1.159	1.138	1.089	1.007	0.754	0.498	0.302	0.182	0.124	0.109	0.099	0.088
160	1.090	1.080	1.049	0.991	0.902	0.650	0.426	0.263	0.167	0.128	0.118	0.110	0.091
170	1.034	1.018	0.985	0.932	0.856	0.643	0.429	0.261	0.161	0.121	0.111	0.103	0.079
180	0.909	0.876	0.834	0.783	0.721	0.565	0.383	0.226	0.134	0.103	0.098	0.096	0.079

### RESULTS OF ANALYSIS OF WAKE CURRENT FOR MODIFIED VERSIONS OF SHIP HULL

Numerical calculations of wake current were performed for the same modified ship hull versions as in the case of the resistance investigations (Tab. 2).

The ship hull model speed  $V = 1.492$  [m/s].

The collected results of numerical calculations in the form of the average wake fraction according to Eq. (2), are given in Tab. 7.

The influence of particular modified geometrical parameters of ship hull model on the average value of wake fraction is presented in Figs. 18 ÷ 20, and, in Fig. 21 and 22 are given circumferential distributions of axial and tangential wake fraction components for  $r/R = 0,6$ .

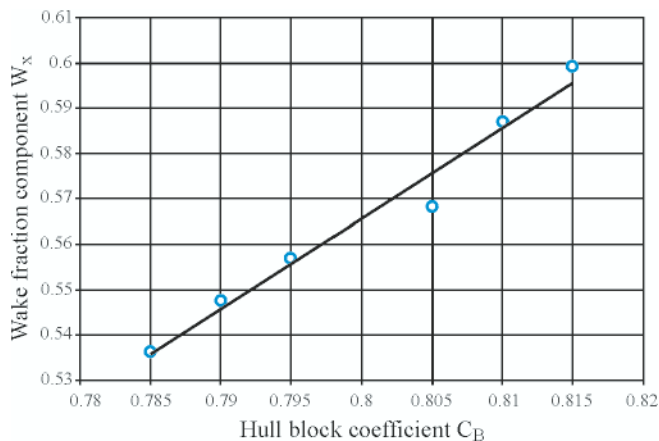


Fig. 18. Wake fraction component  $W_x$  calculated in function of  $C_B$

Tab. 7. Average values of axial wake fraction for modified hull versions of B 573 ship

Number of variant	Modified parameter	Average value of axial wake fraction
	$C_B$	$W_x$
1	0.79	0.547
2	0.795	0.556
3	0.785	0.536
4	0.81	0.586
5	0.805	0.568
6	0.815	0.599
	$C_p$	
7	0.78	0.539
8	0.77	0.523
9	0.76	0.507
10	0.8	0.578
11	0.81	0.602
	LCB	
12	47%	0.517
13	46%	0.491
14	45%	0.468
15	49%	0.593
16	50%	0.620
17	51%	0.681
18	Manual modification	0.471

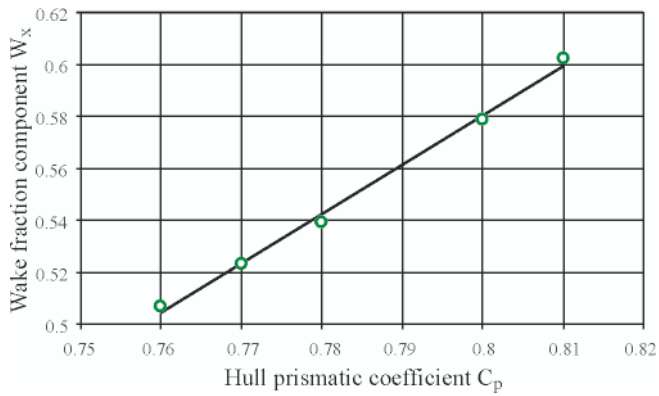


Fig. 19. Wake fraction component  $W_x$  calculated in function of  $C_p$

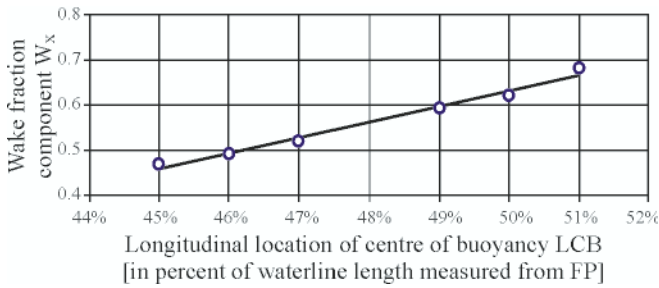


Fig. 20. Wake fraction component  $W_x$  calculated in function of LCB

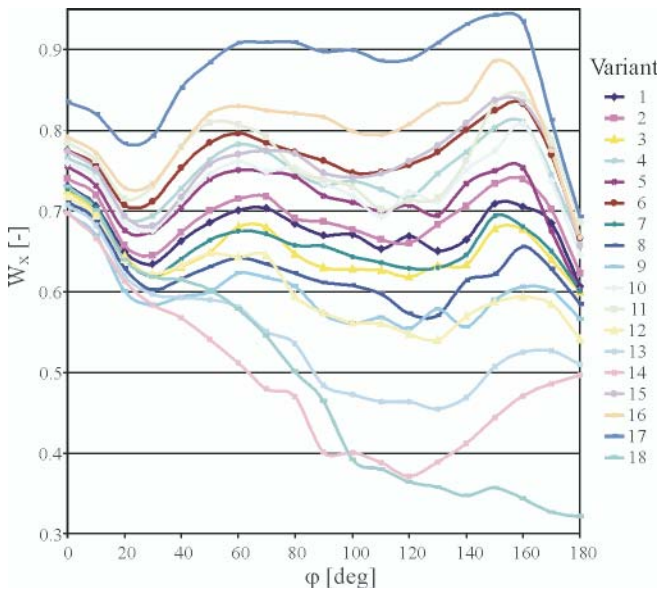


Fig. 21. Circumferential distribution of field of the axial wake fraction component for  $r/R = 0.6$ , calculated for all the analyzed variants (18 in number)

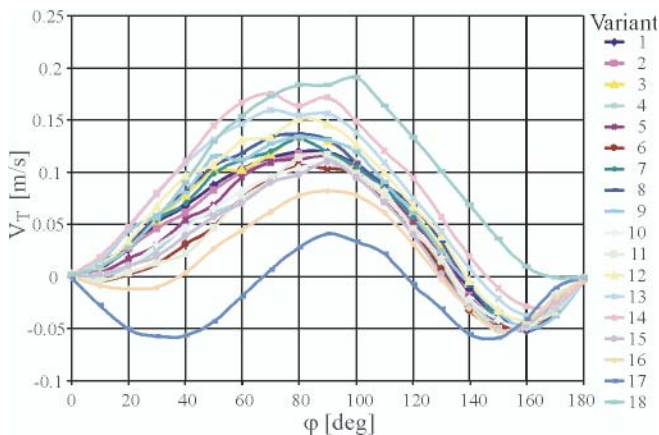
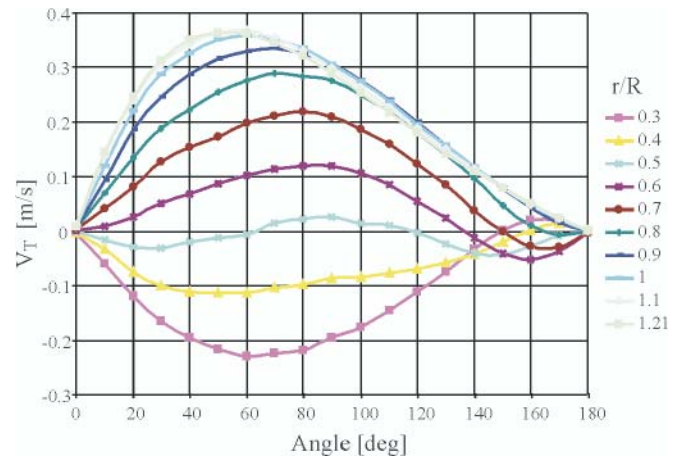
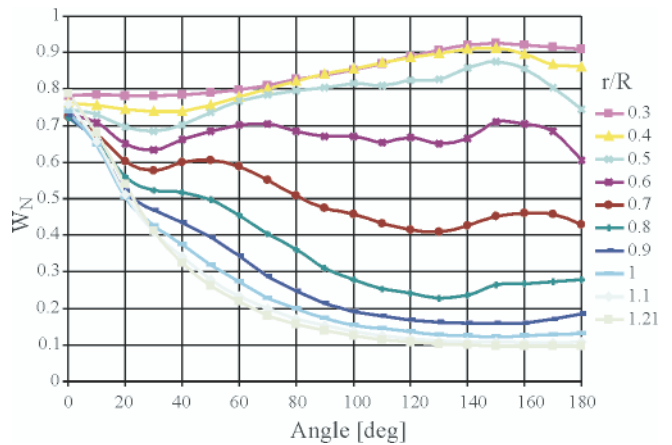


Fig. 22. Circumferential distribution of field of the tangential velocity component for  $r/R = 0.6$ , calculated for all the analyzed variants (18 in number)

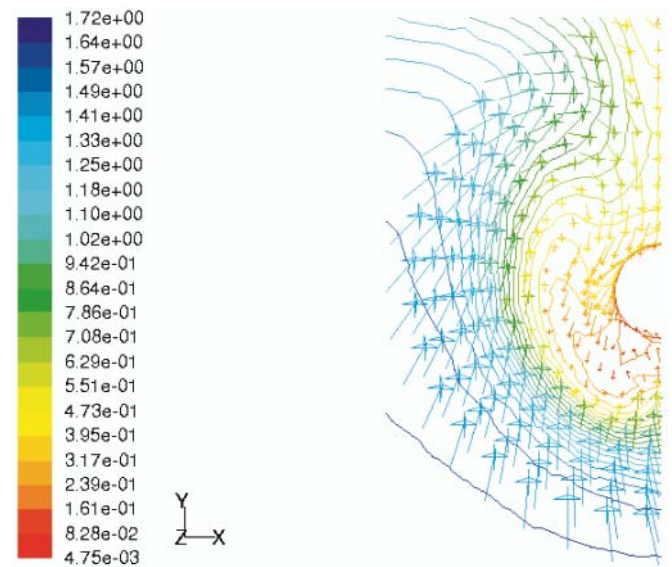
In Figs. 23 ÷ 29 are exemplified distributions of tangential and axial wake fractions as well as velocity vectors on the propeller disk plane for selected variants of B 573 ship hull modification. The complete set of numerical calculation results is contained in the report on the research project [2].



Distribution of the tangential velocity  $V_T$

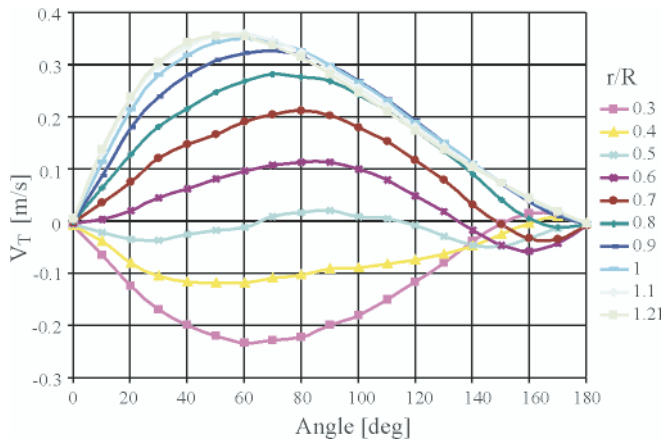


Distribution of the axial wake fraction component  $W_N$

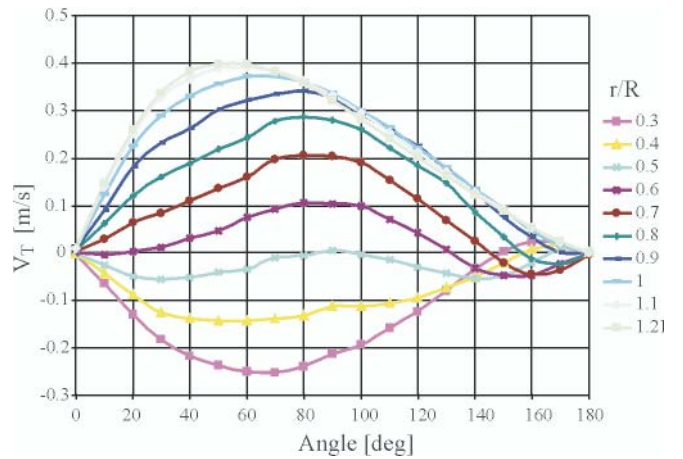


Wake current velocity vectors

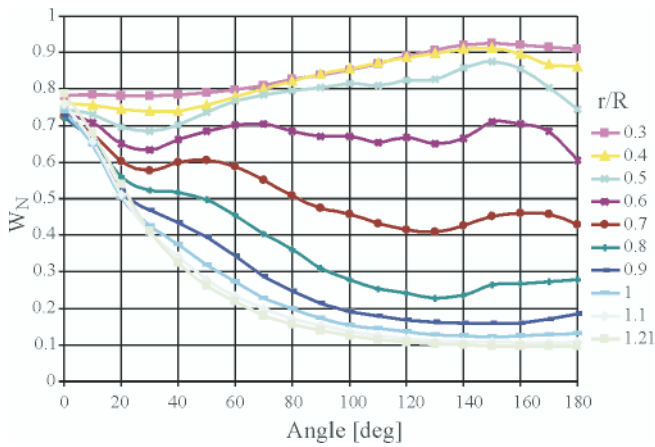
Fig. 23. Distributions of tangential velocities and axial wake fraction as well as velocity vectors in propeller disk plane for variant 1 of B 573 ship hull modification



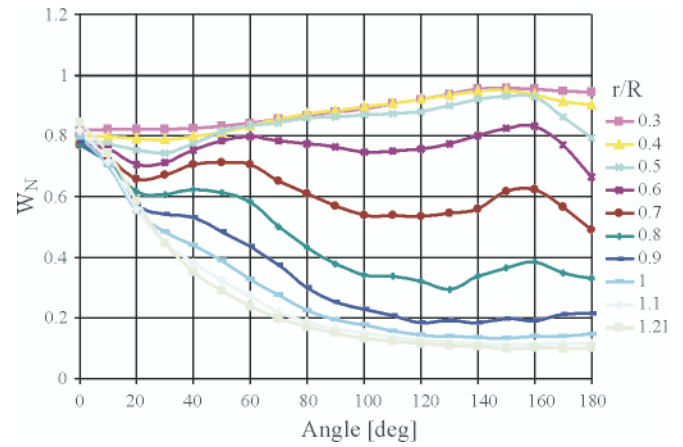
Distribution of the tangential velocity  $V_T$



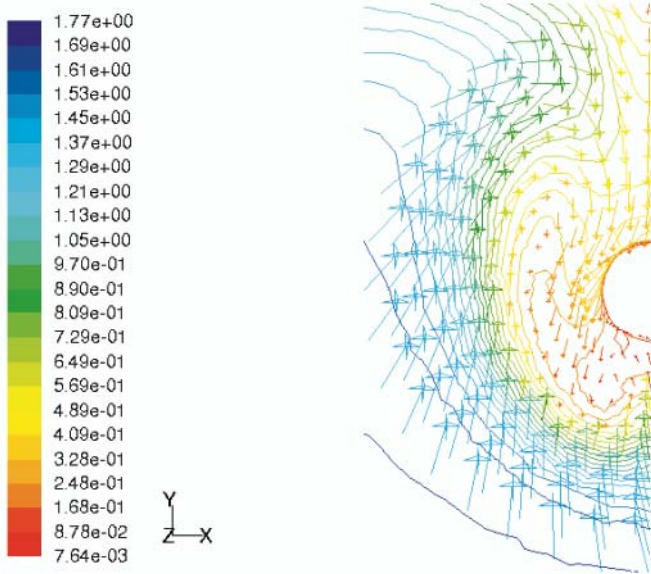
Distribution of the tangential velocity  $V_T$



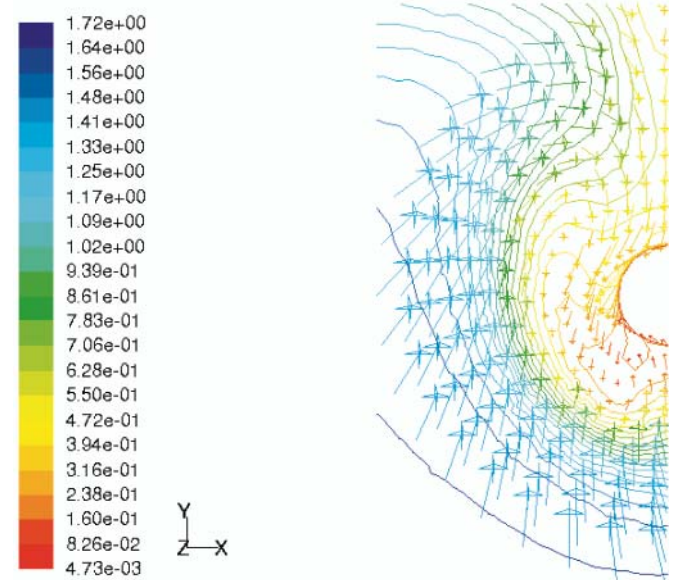
Distribution of the axial wake fraction component  $W_N$



Distribution of the axial wake fraction component  $W_N$



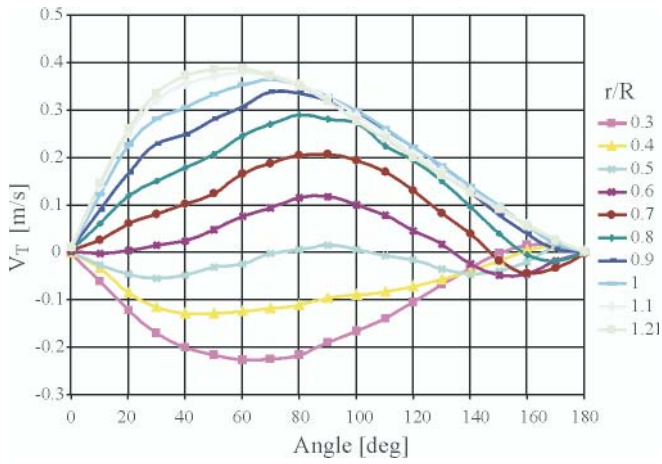
Wake current velocity vectors



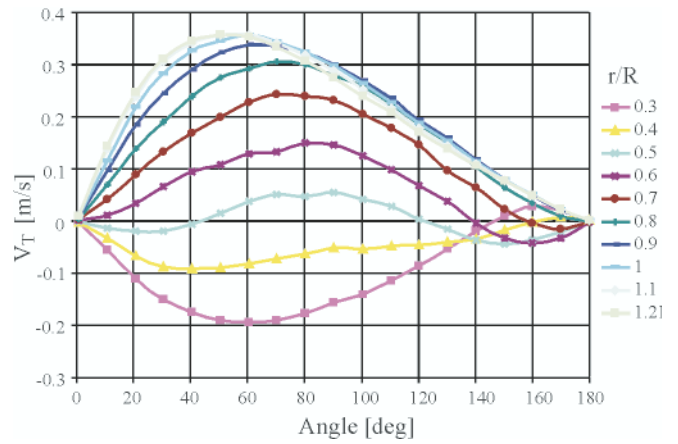
Wake current velocity vectors

Fig. 24. Distributions of tangential velocities and axial wake fraction as well as velocity vectors on propeller disk plane for variant 6 of B 573 ship hull modification

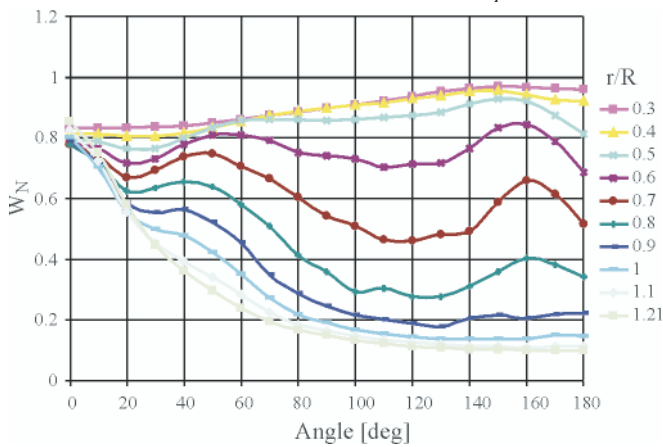
Fig. 25. Distributions of tangential velocities and axial wake fraction as well as velocity vectors on propeller disk plane for variant 7 of B 573 ship hull modification



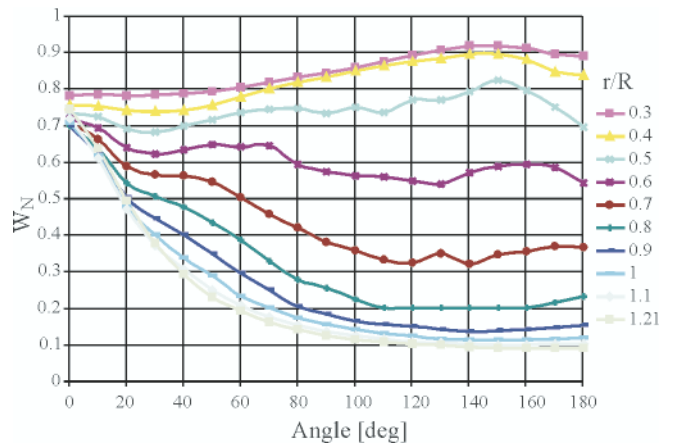
Distribution of the tangential velocity  $V_T$



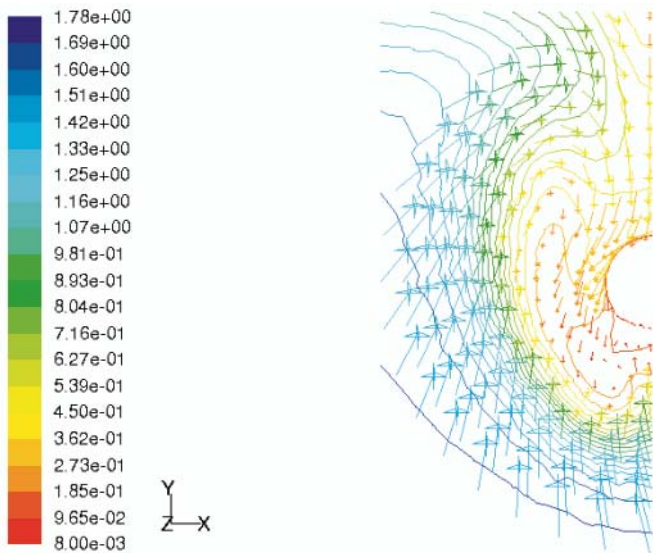
Distribution of the tangential velocity  $V_T$



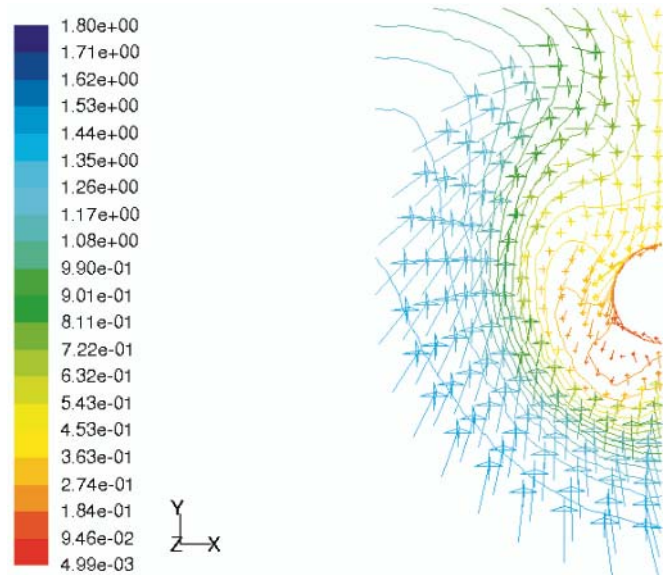
Distribution of the axial wake fraction component  $W_N$



Distribution of the axial wake fraction component  $W_N$



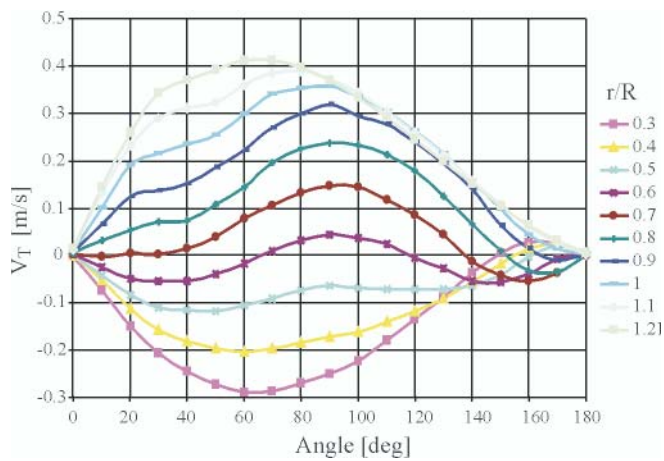
Wake current velocity vectors



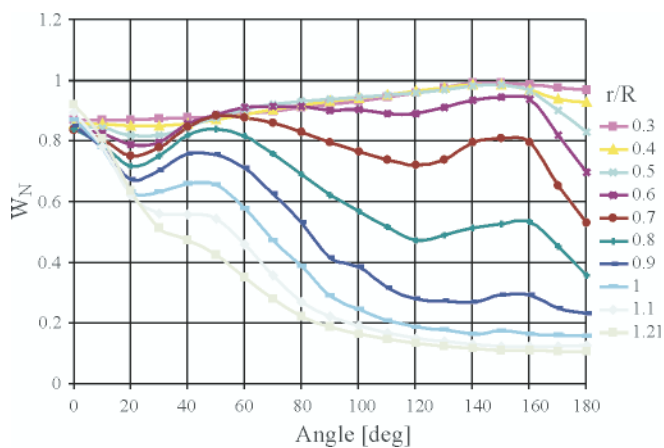
Wake current velocity vectors

Fig. 26. Distributions of tangential velocities and axial wake fraction as well as velocity vectors on propeller disk plane for variant 11 of B 573 ship hull modification

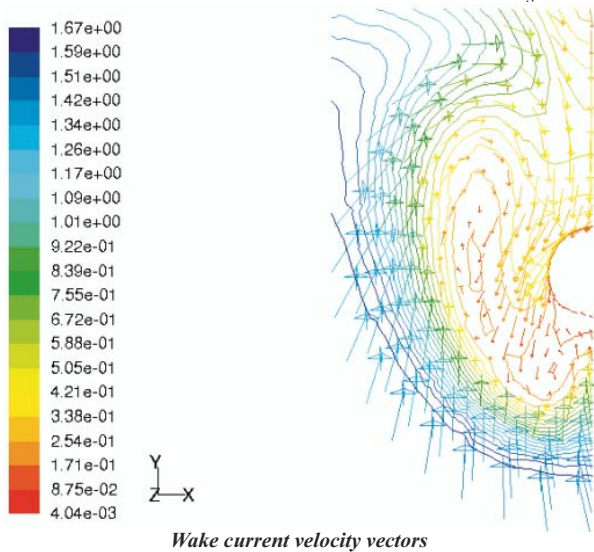
Fig. 27. Distributions of tangential velocities and axial wake fraction as well as velocity vectors on propeller disk plane for variant 12 of B 573 ship hull modification



Distribution of the tangential velocity  $V_T$

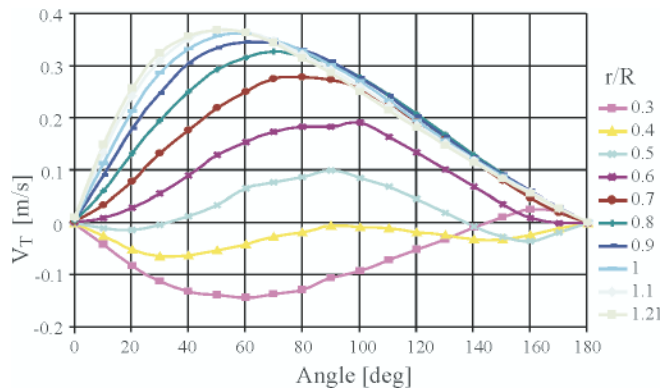


Distribution of the axial wake fraction component  $W_N$

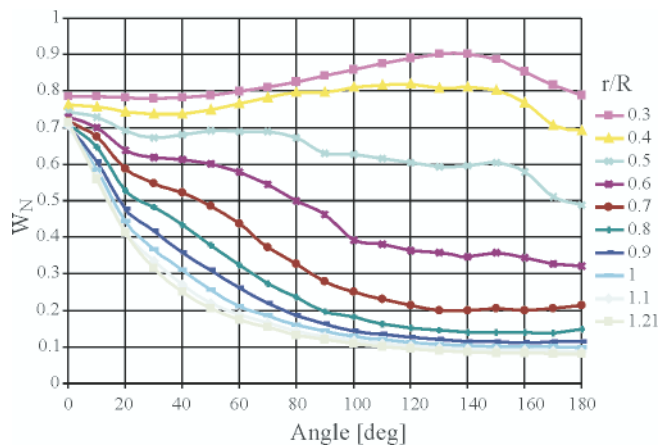


Wake current velocity vectors

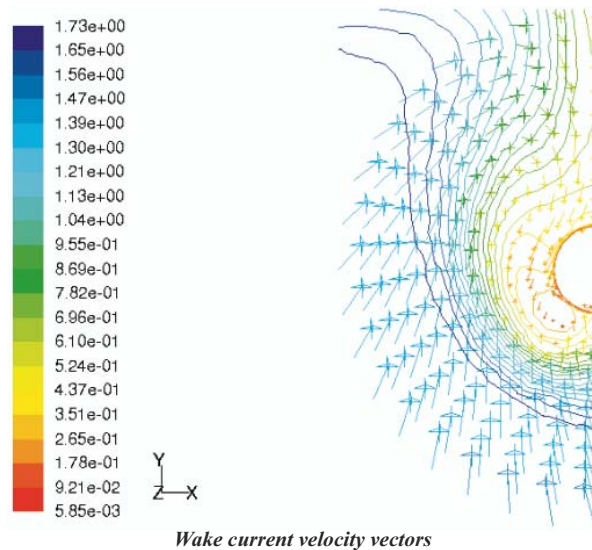
Fig. 28. Distributions of tangential velocities and axial wake fraction as well as velocity vectors on propeller disk plane for variant 17 of B 573 ship hull modification



Distribution of the tangential velocity  $V_T$



Distribution of the axial wake fraction component  $W_N$



Wake current velocity vectors

Fig. 29. Distributions of tangential velocities and axial wake fraction as well as velocity vectors on propeller disk plane for variant 18 of B 573 ship hull modification

## Acknowledgements

Results of the investigations presented in this paper have been financed by Ministry of Science and Higher Education in the frame of the research project no. R10 008 01.

## BIBLIOGRAPHY

1. Jaworski S., Syrocki W.: *Ship B 573: Results of Model Tests - Resistance, Wake Measurements*, Technical Report No. RH-95/T-041A, Ship Design and Research Centre, Gdańsk, 1995
2. Szelangiewicz T.: *Numerical investigations on ship rudder-propeller-stern co-operation aimed at the improving of*

transport ship propulsion and manoeuvrability properties (in Polish). Appendix to the final report on realization of the development project No. R 10 008 01, Szczecin 2009.

## CONTACT WITH THE AUTHORS

Tomasz Abramowski, Ph. D.  
Tadeusz Szelangiewicz, Prof.  
West Pomeranian University of Technology, Szczecin  
Faculty of Marine Technology  
Al. Piastów 41  
71-065 Szczecin, POLAND  
e-mail: tadeusz.szelangiewicz@ps.pl

# Numerical analysis of influence of ship hull form modification on ship resistance and propulsion characteristics

## Part III Influence of hull form modification on screw propeller efficiency

Tomasz Abramowski, Ph. D.  
Katarzyna Żelazny, D.Sc., Eng.  
Tadeusz Szelangiewicz, Prof.  
West Pomeranian University of Technology, Szczecin

### ABSTRACT

*After signing ship building contract shipyard's design office orders performance of ship resistance and propulsion model tests aimed at, apart from resistance measurements, also determination of ship speed, propeller rotational speed and propulsion engine power for the designed ship, as well as improvement of its hull form, if necessary. Range of ship hull modifications is practically very limited due to cost and time reasons. Hence numerical methods, mainly CFD ones are more and more often used for such tests. In this paper consisted of three parts, are presented results of numerical calculations of hull resistance, wake and efficiency of propeller operating in non-homogenous velocity field, performed for research on 18 hull versions of B573 ship designed and built by Szczecin Nowa Shipyard.*

**Keywords:** ship hull geometry, numerical (computational) fluid dynamics (CFD), resistance, wake current, propeller efficiency

### SHIP PROPULSION EFFICIENCY

In design practice the overall propulsive efficiency is presented in the form of the product of efficiency components [1]:

$$\eta = \eta_{HT} \eta_0 \eta_{RT} \eta_S \eta_G \quad (3a)$$

or:

$$\eta = \eta_{HQ} \eta_0 \eta_{RQ} \eta_S \eta_G \quad (3b)$$

where:

- $\eta_{HT}$  – ship hull „efficiency” determined under the assumption that the open-water -propeller thrust  $T$  is equal to the behind-the-hull propeller thrust  $\bar{T}$
- $\eta_{HQ}$  – ship hull „efficiency” determined under the assumption that the torque  $Q_D$  delivered to the open-water propeller is equal to the torque  $\bar{Q}_D$  delivered to the behind-the-hull propeller
- $\eta_0$  – open-water propeller efficiency
- $\eta_{RT}, \eta_{RQ}$  – rotative „efficiency” determined under the same assumption as for hull „efficiency”
- $\eta_S$  – shaftline efficiency
- $\eta_G$  – reduction gear efficiency.

The two components:  $\eta_S$  and  $\eta_G$  are mechanical efficiencies, not associated with water flow around ship's hull, propeller

and rudder. Therefore they do not affect ship's hull-propeller - rudder collaboration.

The first three components, being of hydrodynamic character, are decisive of overall propulsive efficiency, and basin model tests to be performed have to provide ship designer with information necessary a.o. to determine their values.

- However worth paying attention is that :
- for determining  $\eta_H$  and  $\eta_R$  are used averaged values obtained from measurements taken during model basin tests (the wake current velocity field measured during model tests is easily converted to ship scale, that not always brings good results)
  - the presented efficiency components do not contain other factors affecting the overall propulsive efficiency (influence of some of them can be determined by conducting multiple model basin tests e.g. for various versions of ship hull stern part)
  - in the above presented formulas is contained the open-water-propeller efficiency  $\eta_0$  determined for the screw propeller operating in homogenous water velocity field without presence of ship hull, whereas the behind-the-hull screw propeller operates in a very non-homogenous velocity field, and the coefficients  $\eta_H, \eta_R$  do not reflect essence of the problem,

- also, in the above presented formulas effects of rudder, especially streamline one, which may increase efficiency of screw propeller, are lacking
- the above presented formulas do not contain information on mutual location of screw propeller and blade rudder relative to ship stern, and on its impact on propulsive efficiency.

The above described way of the determining of propulsive efficiency contains certain ambiguities (e.g. those associated with wake-fraction determining) hence in the publications [2, 3] it is postulated to introduce the coefficients connected with the behind-the-hull propeller efficiency:

$$\xi_Q = \frac{Q_D}{Q_D} \quad (4a)$$

$$\xi_T = \frac{T}{T} \quad (4b)$$

called the torque modifier and thrust modifier, respectively.

Regardless of that which approach would be applied to determining the ship propulsive efficiency, it is rational to determine thrust and torque of the behind-the-hull screw propeller as well as its efficiency in non-homogenous water velocity field for mean working point equivalent to mean service speed of ship (the mean statistical ship speed was discussed in [4]).

To determine real propulsive efficiency of ship or also efficiency of propeller operating behind the hull in non-homogenous velocity field, is possible by using CFD techniques. Hence in this part of the paper are presented results of numerical computation of efficiency of screw propeller operating in non-homogenous water velocity field, performed for 18 modified hull versions of B 573 ship. For the computations use is made of the results of numerical calculation of wake currents, presented in the part II of the paper.

## NUMERICAL CALCULATION OF HYDRODYNAMIC CHARACTERISTICS OF SCREW PROPELLER

Before the calculations of efficiency of a screw propeller operating in non-homogenous velocity field, hydrodynamic characteristics of a store screw propeller used to propulsion model tests of B 573 ship [5], were calculated (the screw geometry is presented in Fig. 30).

The calculations of the store screw propeller were performed in the scale 1:1 by modelling the flow with the use of RANS equations and RNG k-epsilon model was applied to turbulence phenomena. Boundary layer was modeled by means of standard flow approximating functions, where the parameter  $y^+ = 50$ .

To discretize domains a numerical non-structural network of prismatic elements within boundary layer (Fig. 31), which was further adjusted to polyhedral elements (Fig. 32). was applied. The non-structural network was elaborated by using Gambit system; and the conversion was performed by using Fluent system. All screw propeller blades were modeled, that demands on one hand a greater computer capacity, but on the other hand makes non-stationary calculations of screw propeller with taking into account non-design conditions, possible.

Calculation time step was equal to 0.00012 s, that was equivalent to about 1° of one screw-propeller revolution at its rotational speed of 17 rps. Two complete screw-propeller revolutions were covered by the calculations, hence the total time of the calculated flow was equal to 0.0864 s.

### Results of numerical calculations:

- pressure distribution on screw propeller blades is presented in Fig. 33 and 34
- streamlines – in Fig. 35
- total velocity profiles – in Fig. 36
- hydrodynamic characteristics – in Fig. 37 ÷ 39

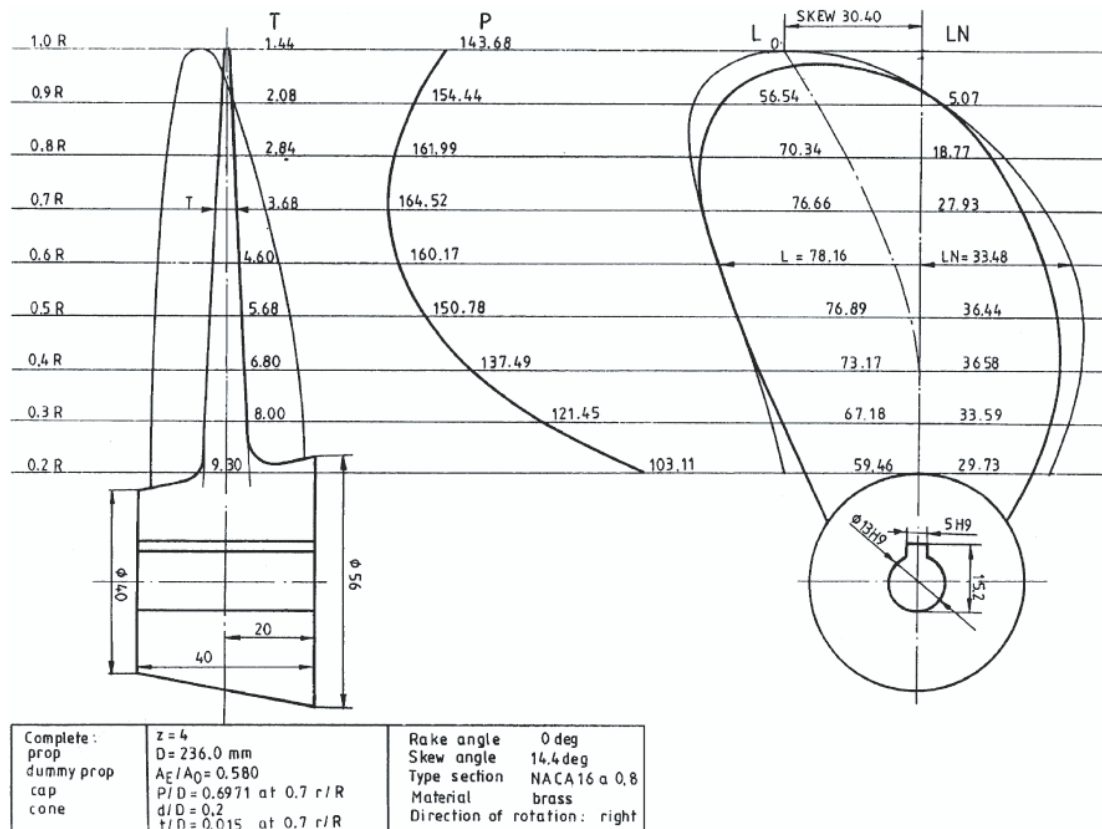


Fig. 30. Geometry of the store screw propeller No. P 355 [5]

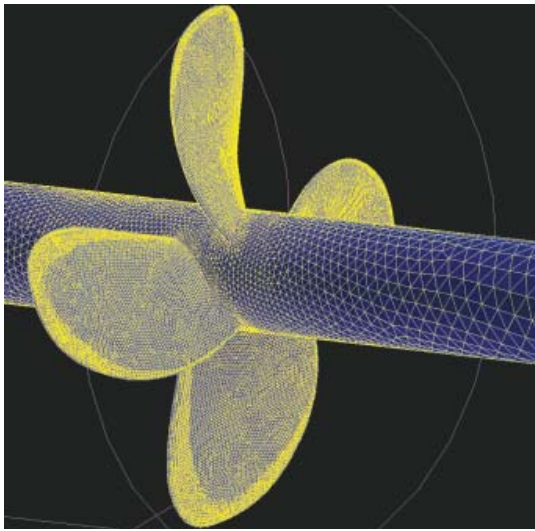


Fig. 31. Non-structural network of elements before conversion

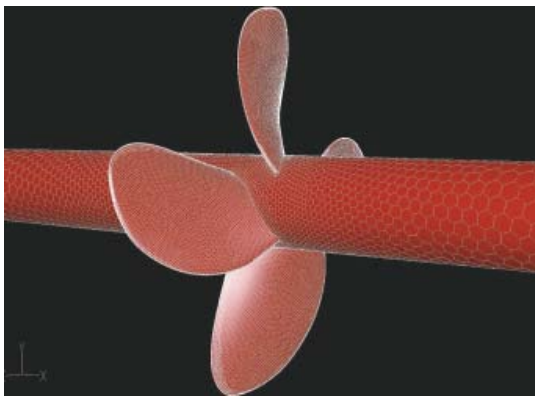


Fig. 32. Polyhedral network of elements converted from non-structural one

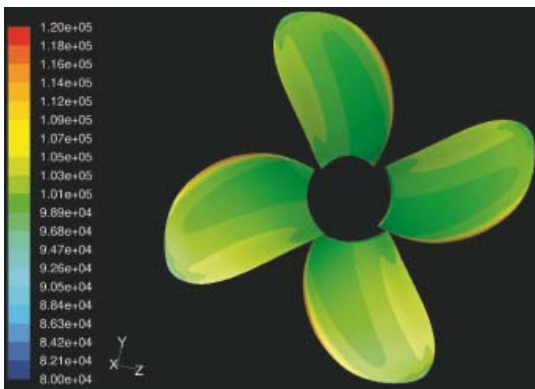


Fig. 33. Pressure distribution on driving face of screw propeller blades, the advance ratio  $J = 0.4$

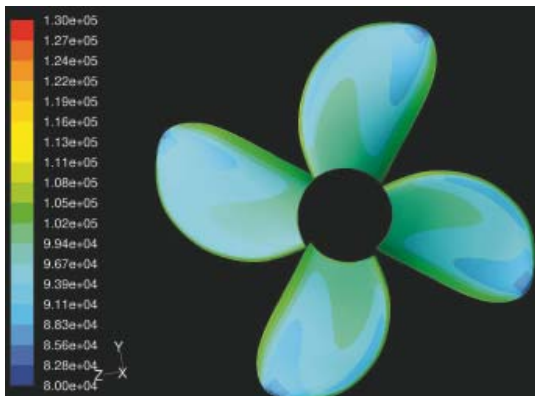


Fig. 34. Pressure distribution on drag surface of screw propeller blades, the advance ratio  $J = 0.4$

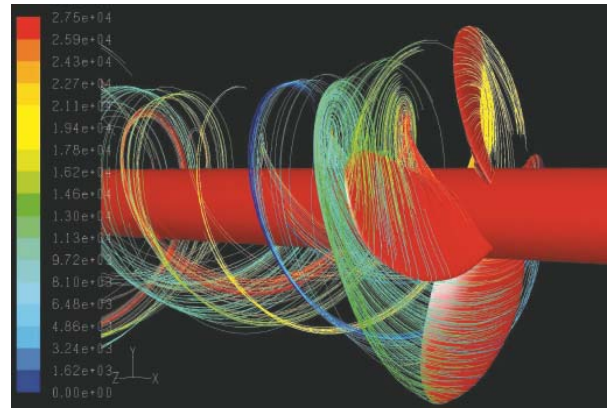


Fig. 35. Streamlines behind the screw propeller

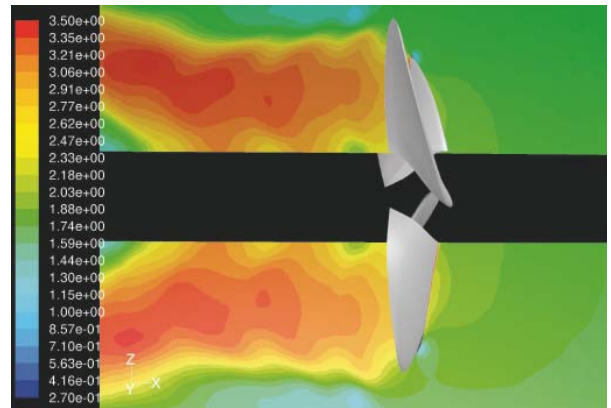


Fig. 36. Total velocity profiles

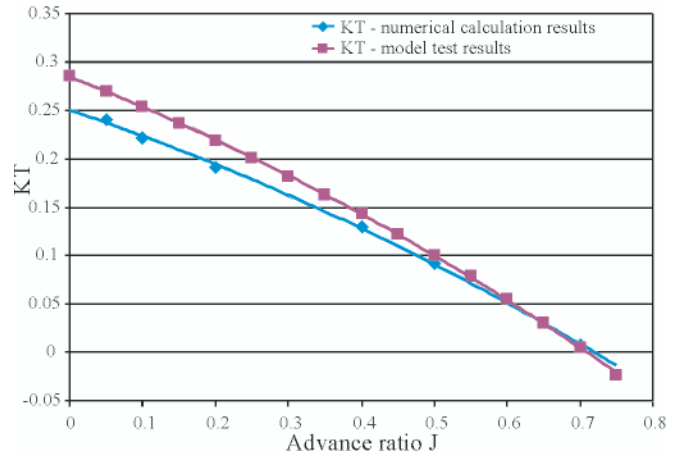


Fig. 37. Calculation results of the thrust coefficient  $K_T$  compared with model test results [5]

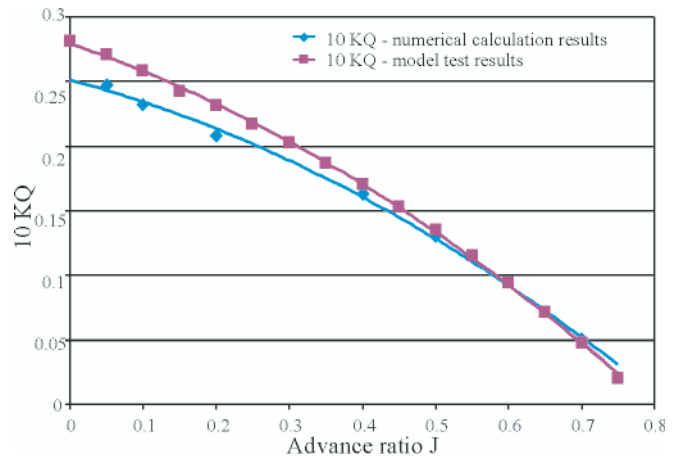


Fig. 38. Calculation results of the torque coefficient  $K_Q$  compared with model test results [5]

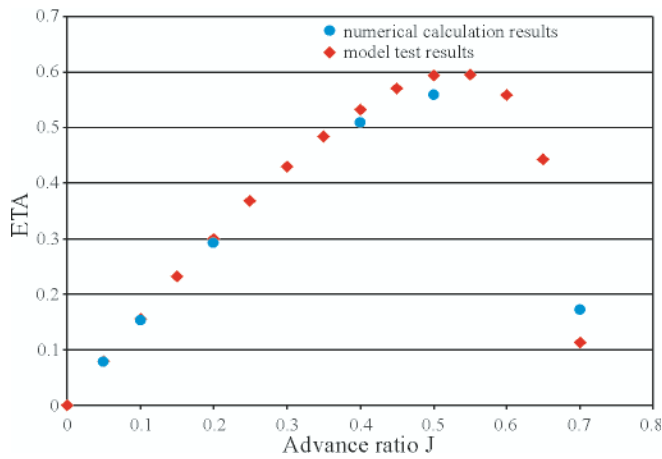


Fig. 39. Calculation results of the screw propeller efficiency  $\eta_a$  compared with model test results [5]

### MEAN EFFICIENCY OF FINAL SCREW PROPELLER IN NON-HOMOGENOUS WAKE CURRENT VELOCITY FIELD

The modification of B 573 ship's hull form was aimed at investigations of influence of the introduced hull form changes on the ship's resistance, wake current and screw propeller efficiency. The obtained distributions of wake current were used for determining the mean efficiency of the final screw propeller for B 573 ship.

The numerical calculations were performed for the final screw propeller of B 573 ship [6] in the same way as for the store screw propeller, however in the case of the final screw propeller, the water velocity field (in which axial and circumferential components were taken into account), calculated for each of the modified version of the ship's hull form, was introduced. The final results of the analyses are presented in Fig. 40 in the form of the mean efficiency of screw propeller operating in non-homogenous wake current field. In the figure the mean efficiency values are shown for particular versions (variants) of the modified ship hull forms in compliance with Tab. 1. The case 0 is calculated for the screw propeller operating in the non-homogenous flow velocity field measured during model tests of the B 573 ship hull (of non-modified form). The continuous line (marked red) stands for the maximum efficiency of the final open-water screw propeller operating in homogenous flow velocity field.

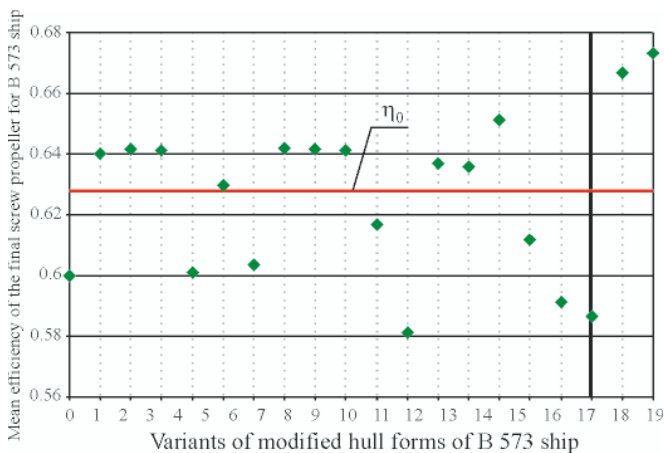


Fig. 40. Mean efficiency of B 573 ship's screw propeller operating in non-homogenous wake current field, where:  $\eta_0$  – maximum efficiency of the final screw propeller in homogenous flow velocity field, variant 0 – original hull form (without modification) in wake current velocity field measured during model tests, variant 18 – symmetrical hull form with manually modified stern part

### FINAL CONCLUSIONS

- The tests performed in advance each of the main calculations demonstrated a good conformity of CFD calculations to model tests. Certain observed differences may result from various causes (some of them were discussed in the Part I of this work). The differences in hydrodynamic characteristics of the store screw propeller could also result from some, out of all necessary to elaborate a 3D model and numerical network, geometrical quantities lacking in [5]. Therefore it is not certain whether the computational model of the store screw propeller has represented exactly its real features. In the case of the final screw propeller there was no available results of model tests or other calculations to make verification of the CFD computation results possible.
- Numerical calculations of the mean efficiency of screw propeller for 18<sup>th</sup> hull version of B 573 ship (Fig. 40) demonstrated that small modifications can have either favourable or unfavourable effect onto efficiency. Especially favourable effect in the form of elevated efficiency was obtained by using manual modification of only stern part of the ship's hull (18<sup>th</sup> variant, Fig. 40). It means that by suitable modelling hull form in its stern part only it is possible to make flow velocity field before the propeller more favourable from the point of view of efficiency.
- Mean values of screw propeller efficiency for wake currents corresponding to particular versions of ship hull were calculated for the same final screw propeller. Investigations on searching for optimum screw propeller geometry for each of the ship's hull versions, are under way.
- Numerical methods based on the CFD provide even greater possibilities, e.g. investigations on propulsive efficiency of the whole system composed of ship hull, screw propeller and streamline rudder, that would make performing a more advanced optimization of ship propulsion system, possible.

### BIBLIOGRAPHY

1. Dudziak J.: *Ship theory* (in Polish). 2nd Edition, Fundacja Promocji Przemysłu Okrętowego i Gospodarki Morskiej (Fundation for Promotion of Ship Industry and Maritime Economy), Gdańsk 2008
2. Jarzyna H.: *Some Consequences of the Analytical Design of the Ship Propellers*. Proceedings of the Conference on Advances in Propeller Research and Design, PAN, IMP (Institute of Fluid Flow Machinery, Polish Academy of Sciences), Gdańsk 1981
3. Jarzyna H., Koronowicz T., Szantyr J.: *Design of Marine Propellers. Selected Problems*. Zakład Narodowy im. Ossolińskich, Wydawnictwo PAN (Publishing House of Polish Academy of Sciences), Wrocław 1996
4. Szelangiewicz T., Żelazny K.: *Calculation of the mean long-term service speed of transport ship. Part I - Polish Maritime Research (PMR), No. 4/2006, Part II - PMR No. 1/2007, Part III - PMR No. 2/2007*
5. Syrocki W.: *Ship B 573 – Results of Model Tests*. Ship Design and Research Centre, Technical Report No. RH-96/T-023A, Gdańsk 1995
6. Syrocki W.: *Ship B 573 – Final Design of Propeller*. Ship Design and Research Centre, Technical Report No. RH-95/T-115 A, Gdańsk 1995.

### CONTACT WITH THE AUTHORS

Tomasz Abramowski, Ph. D.  
 Katarzyna Żelazny, D. Sc.  
 Tadeusz Szelangiewicz, Prof.  
 West Pomeranian University of Technology, Szczecin  
 Faculty of Marine Technology  
 Al. Piastów 41  
 71-065 Szczecin, POLAND  
 e-mail: tadeusz.szelangiewicz@ps.pl

# A complete design of contra-rotating propellers using the new computer system

Tadeusz Koronowicz, Prof.  
Zbigniew Krzemianowski, Ph. D.  
Teresa Tuskowska, Ph. D.  
The Szewalski Institute of Fluid Flow Machinery  
of the Polish Academy of Sciences in Gdansk  
Jan A. Szantyr, Prof.  
Gdansk University of Technology

## ABSTRACT

*The computer system for the complete design of the contra-rotating propellers presented in this article has several common blocks and procedures with the systems for design of single propellers and tandem co-rotating propellers, presented in detail in the Polish Maritime Research No.1 and No.4 of the Volume 16, 2009. In this article only the blocks and procedures developed specially for the contra-rotating propellers are described. The system is based on the lifting line and lifting surface models and on the Computational Fluid Mechanics methods. The comparative analysis of the contra-rotating propellers and the tandem co-rotating propellers is included.*

**Keywords:** ship propellers, contra-rotating propellers, design methods, computational fluid dynamics

## INTRODUCTION

Many years of experience and practice have shown that the classical single propellers in most cases fulfil the highest requirements regarding efficiency, cavitation characteristics, level of unsteady hydrodynamic shaft forces, pressure pulsations generated on the hull and noise/vibration. However, in realistic applications certain areas may be found in which other types of screw propellers are better. Consequently, the contra-rotating propellers (CRP) may be advantageous in some specific conditions. For example, the requirement of minimum slipstream rotation is achievable for single shaft installations only with contra-rotating propellers (a very important requirement for underwater vehicles).

The design of contra-rotating propellers is based on the same requirements and assumptions which are employed in the design of single propellers and tandem co-rotating propellers [4, 6]. In general, the design requirements of contra-rotating are similar to those of tandem propellers, but they differ in the following characteristic features:

- a) in the design program for contra-rotating propellers the determination of the aft propeller diameter is required
- b) detailed information about the velocity field induced by both propellers of the set is required not only in the design program, but also in the program for analysis of the contra-rotating propellers operation in the non-uniform wake.

The long-term practical experience and the analysis of the propeller-induced velocity fields shows that:

- the diameter of the aft propeller must be correlated with the diameter of the slipstream behind the forward propeller in such a way that the tip vortices shed from the forward propeller pass outside the tips of the aft propeller blades

- the number of blades of the forward and aft propellers of the contra-rotating set should be different
- the rate of rotation of both propellers of the contra-rotating set is recommended to be different.

Similarly as in the case of design of other propeller types the computer design system for contra-rotating propellers includes three interacting programs (blocks of procedures):

- 1) program for determination of the design velocity field for both propellers of the contra-rotating set
- 2) program for propeller design
- 3) program for analysis of the contra-rotating propellers operation in the design velocity field, including the effects of mutual interaction between both propellers.

In comparison to the system for design of single propellers the system for design of contra-rotating includes the following special elements (similarly as the system for tandem propellers):

- a) procedures for the independent graphical presentation of both propellers of the set
- b) procedures for determination of the design velocity field for both propellers, taking into account their mutual interaction
- c) procedures for modification of the velocity field for the analysis of the contra-rotating propeller operation in the non-uniform inflow velocity field
- d) procedures for determination of the induced pressure pulsations for each propeller separately and for the entire set of contra-rotating propellers
- e) procedures for determination of the unsteady hydrodynamic forces and moments for each propeller separately and for the entire set of contra-rotating propellers.

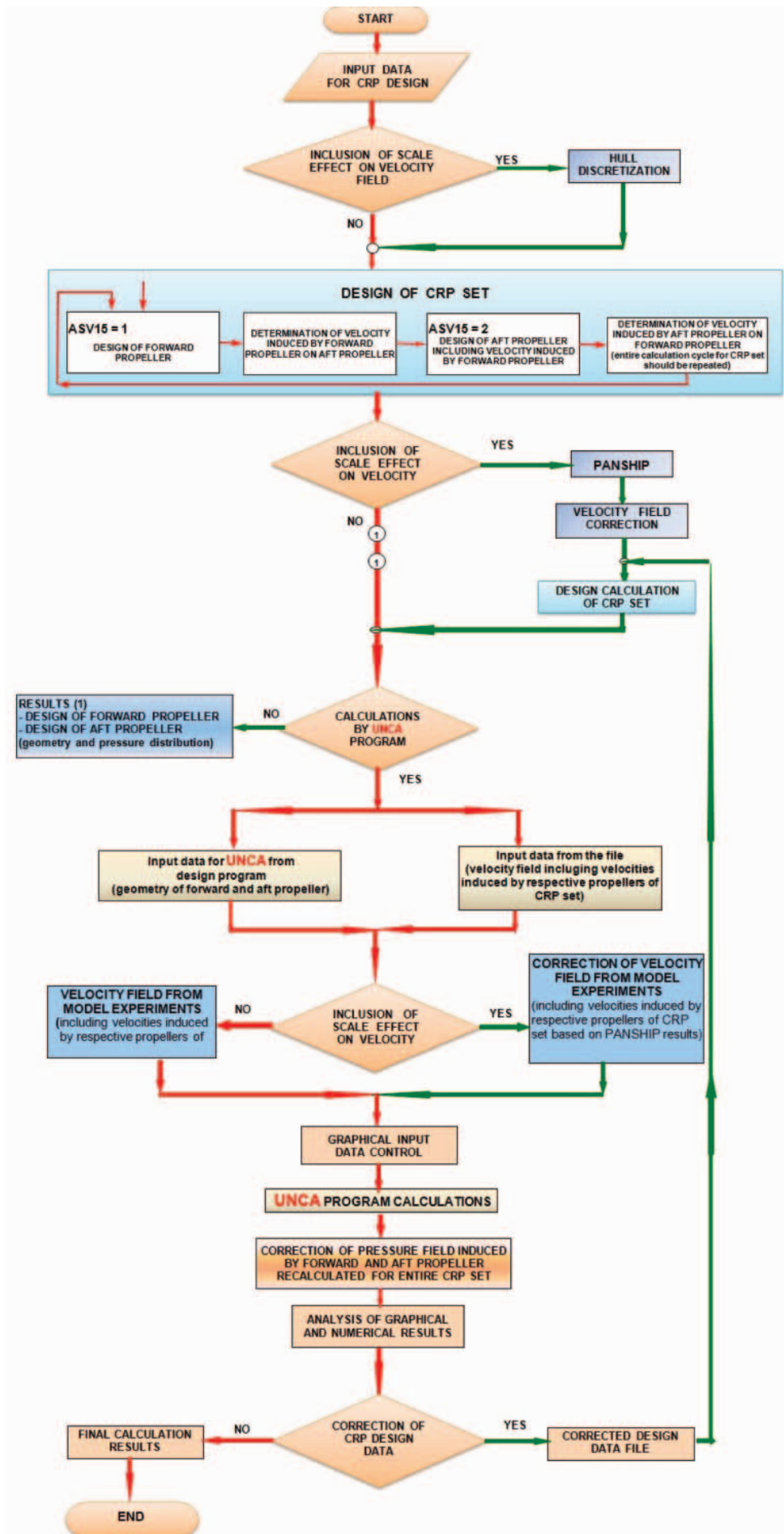


Fig. 1. The block diagram of the computer system for the complete design of the contra-rotating propellers

The appropriate co-operation between all programs and procedures, supplemented with the above listed elements, ensures effective and complete design of the contra-rotating propellers. The system is organized in such a way that the designer controls the entire design process from the computer screen and the data transfer between the respective elements of the system is fully automatic.

Similarly as in the case of the previously presented systems [4, 5, 6] an extensive use has been made of computer graphics for control and correction of the input data, for control of the

intermediate results, for modification of the geometry of both propellers at consecutive stages of design and for presentation of the final results.

The block diagram of the system for design of the contra-rotating propellers, shown in Fig. 1, is similar to that for design of tandem propellers [6]. The basic block diagram of the propeller design process is extensively supplemented with blocks for the design of contra-rotating propellers (cf. Fig. 2) and for the analysis of contra-rotating propellers operation in the non-uniform inflow velocity field (cf. Fig. 3).

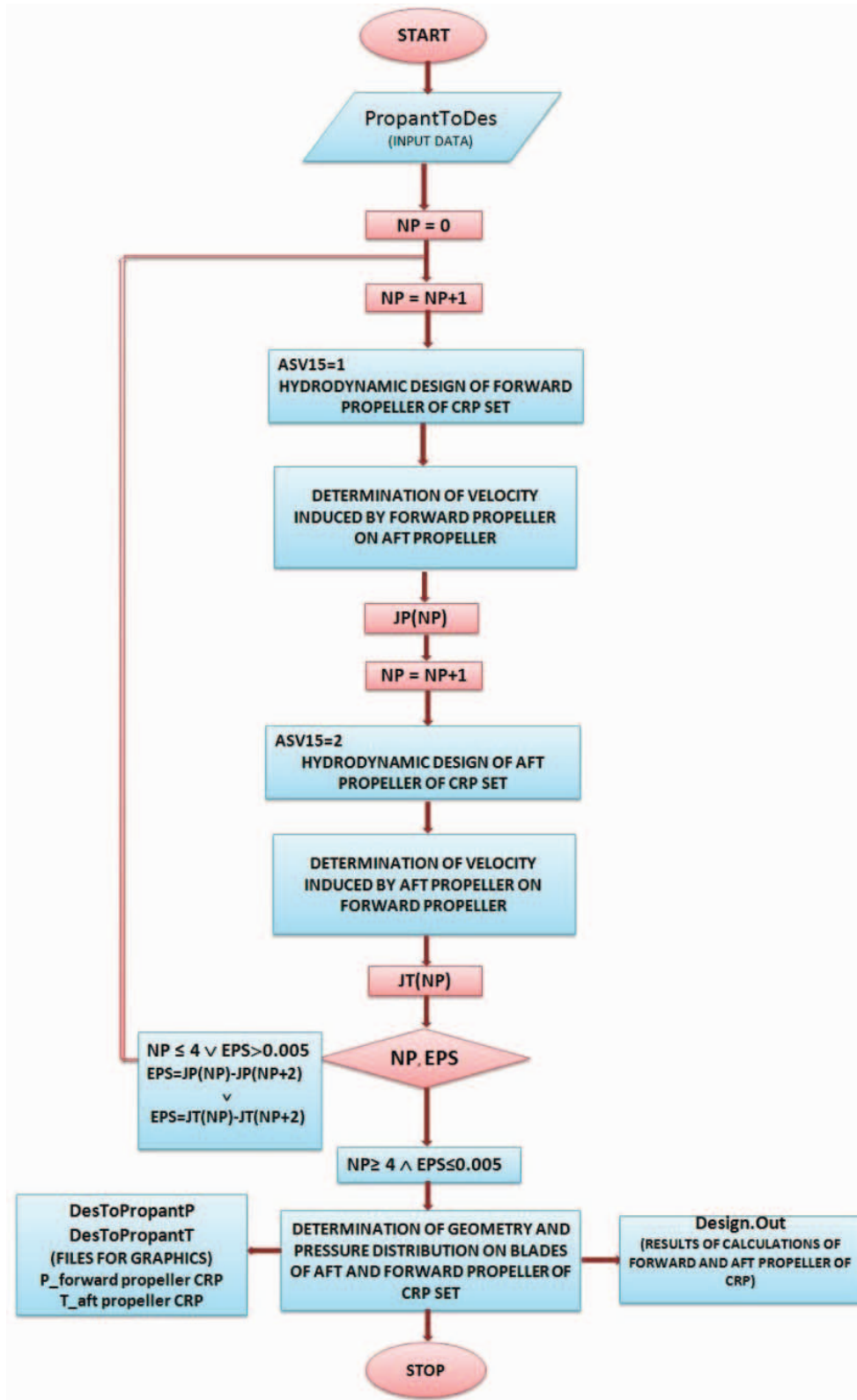


Fig. 2. The block diagram of the design procedure of the contra-rotating propellers

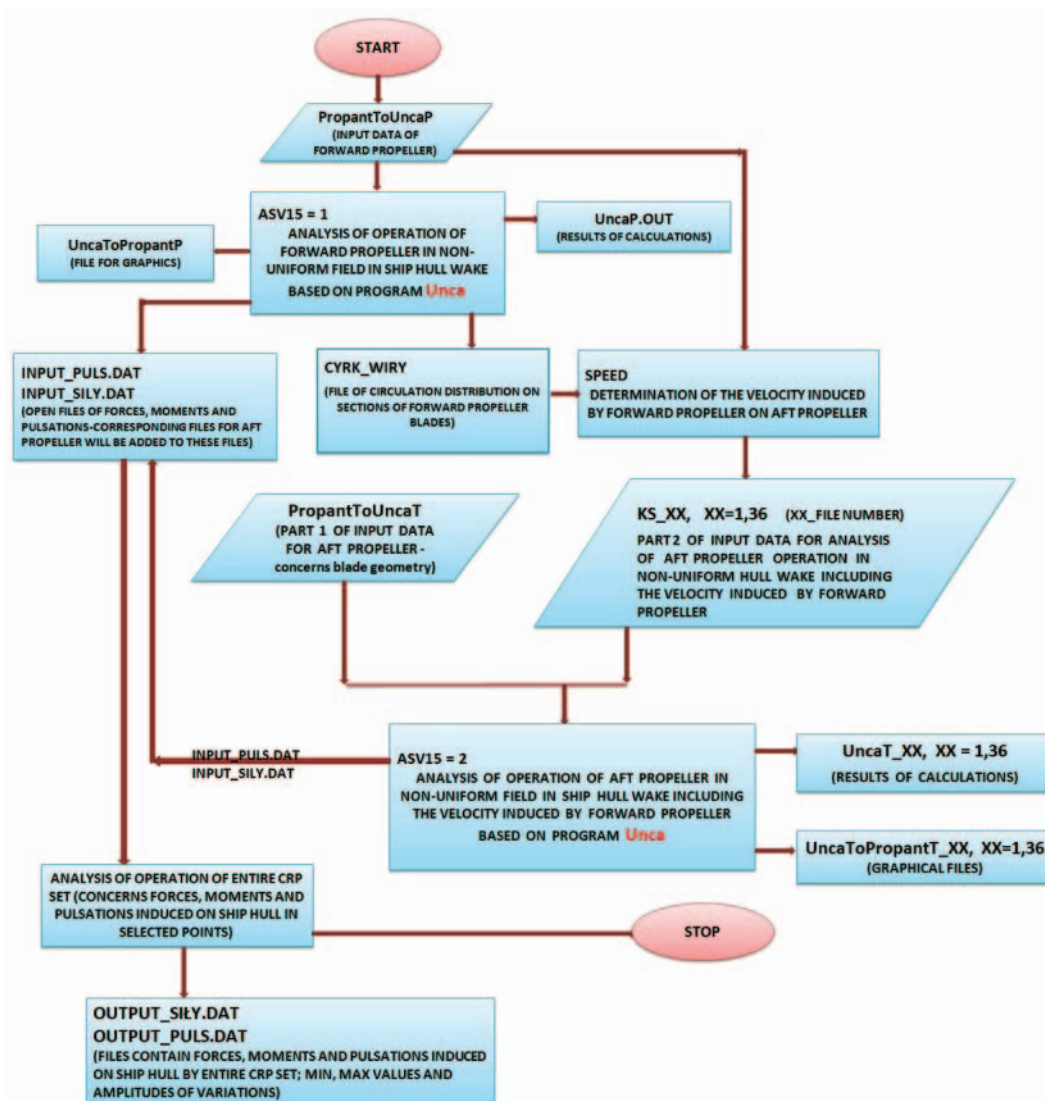


Fig. 3. The block diagram of the analysis procedure of the contra-rotating propellers

## PRESENTATION OF THE SELECTED BLOCKS OF THE NEW COMPUTER SYSTEM

The computer system for design of the contra-rotating propellers has several blocks identical to those incorporated in the systems for design of single or tandem co-rotating propellers. Only the blocks concerning the specific problems of contra-rotating propellers are described in detail below.

### *The input data*

The input data include all information required for initiation of the variant of design calculation selected out of four available options, similarly as for other types of propellers described in earlier publications [4, 5, 6]. The input data may be introduced either in the form of the previously prepared input data file or directly from the computer terminal in an interactive mode.

The input magnitude which is typical both for the tandem co-rotating and contra-rotating propellers is the axial distance between the generator lines of the forward and aft propeller. The features distinguishing the contra-rotating propellers from the tandem co-rotating propellers is the difference in diameters of the forward and aft propellers and the recommended difference in number of blades and rate of rotation. The diameter of the

aft propeller must be smaller than the local diameter of the slipstream shed from the forward propeller. This requirement is based on two reasons: firstly, there is a marked jump in velocity at the slipstream boundary (see Figs 9 and 10), which cannot be accommodated by the blade geometry (it would require a corresponding jump in the blade pitch) and secondly, there is danger of cavitation erosion caused by the tip vortices shed from the forward propeller.

The program enables graphical control and correction of the input data, especially the radial distributions of geometrical parameters such as blade outline, maximum thickness of the blade section profiles, blade skewback, inflow velocity in the ship wake etc. Fig. 4 shows an example of correction of the radial distribution of the circumferentially averaged inflow velocity in the ship wake.

### *The design program*

The algorithm of the design program for contra-rotating propellers differs in the following details from the analogical programs for single or tandem co-rotating propellers [4, 6]:

- the calculations are performed only for the given value of the total thrust of the CRP set
- the division of the total thrust between the forward and aft propeller may be given in the input data or may be determined in the design program

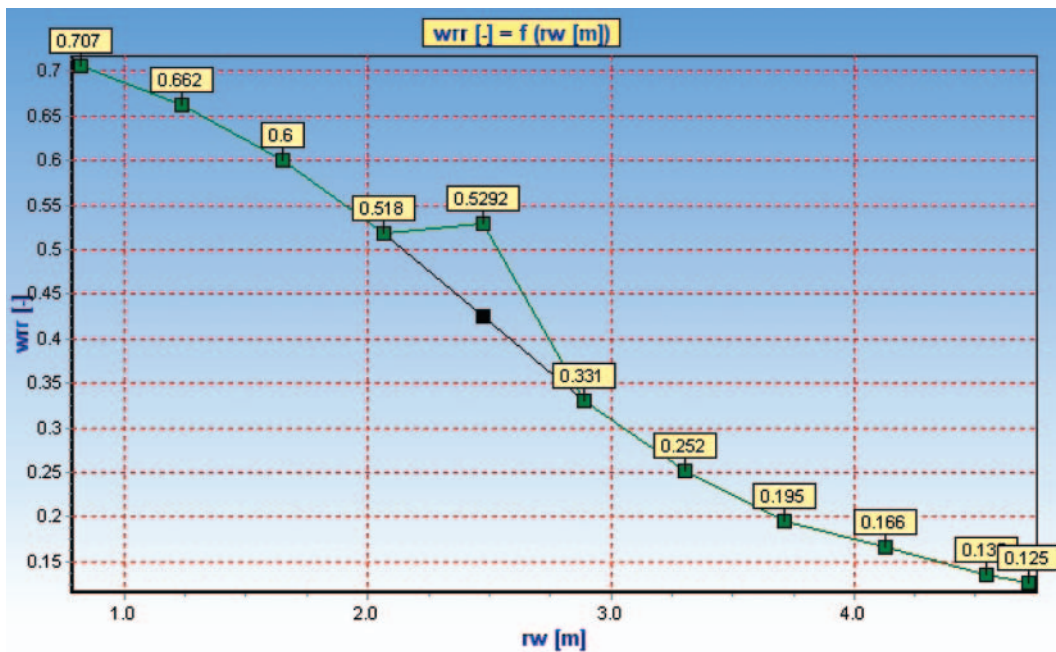


Fig. 4. The control display of the given radial distribution of the circumferentially averaged velocity in the ship wake, showing the correction of the erroneously set value

- c) the diameter of the aft propeller may be given in the input data or may be determined in the design program (the determined value may still be corrected by the designer during calculations)
- d) the determination of the velocity field induced by both propellers of the CRP set is necessary (this is done automatically in the design program).

The design calculations are performed in the same way for every selected version of the design task (similarly as in the case of classical single propellers). The results of design calculations are available in the form of the appropriate numerical files and drawings on the computer screen, which may be saved and, or printed. An example of such a drawing is shown in Fig. 5. This drawing may be viewed on the screen from different angles and then printed in the most suitable configuration.

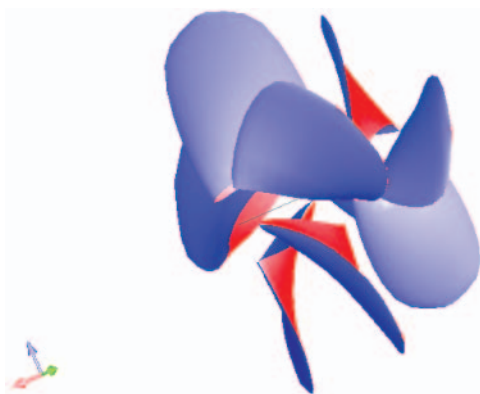


Fig. 5. The contra-rotating propellers as represented in the design program

As it has been mentioned above, the determination of the velocity fields induced by the bound and trailing vortex systems representing both propellers of the CRP set is an indispensable element of the design program. It may be seen in the block diagram shown in Fig. 2 that the design of CRP is an iterative process based on the mutual hydrodynamic interaction between the both propellers of the CRP set. The results of these calculations are presented in the format similar to that of the tandem co-rotating propellers [6].

### The induced velocity field

In the propeller design program based on the vortex theory the systems of bound and trailing vortices are determined in a simplified form, which is sufficient for calculation of the velocities induced on the blades of the propellers, but it may be insufficient for calculation of the velocities induced at certain distance in front and behind the propeller blades (i.e. at locations of the respective propellers of the CRP or tandem co-rotating set of propellers).

The trailing vortex system of any propeller undergoes contraction, deformation and concentration (rolling-up of vortices with simultaneous viscous dissipation of vorticity) [7, 8, 9, 10]. As a result, tip vortices are formed behind every blade and a strong hub vortex is formed behind the propeller hub. The velocity field induced by such a system of concentrated vortices is strongly three-dimensional, being a function of all three co-ordinates (for example  $x$ ,  $\Phi$ ,  $r$  in the cylindrical system). In the design task of CRP set we are interested in the circumferentially averaged values of the induced velocities, while in the case of tandem co-rotating propellers the fully local induced velocity field must be known. The examples of the induced velocity field behind a propeller in the selected cross-section  $x = \text{const}$  of the slipstream are shown in Figs 6, 7 and 8. The velocities induced by the aft propeller at the location of the forward propeller have much smaller values and more uniform spatial distribution.

In case of the CRP set the velocity field induced by the forward propeller, combined with the inflow velocity field of the hull wake is an important design parameter. All three velocity components of that induced velocity field are averaged circumferentially (on the basis of the flow volumetric intensity) for a required number of radii. The radial distribution of these averaged velocity components shows a marked discontinuity at the local tip vortex radius. At the distances behind the propeller larger than the propeller radius both velocity components (axial and tangential) are equal zero outside the slipstream and they reach quite high values inside the slipstream. Such a sudden jump of the velocity cannot be accommodated by the appropriate geometry of the aft propeller blades. Hence the requirement to reduce the aft propeller diameter to the value

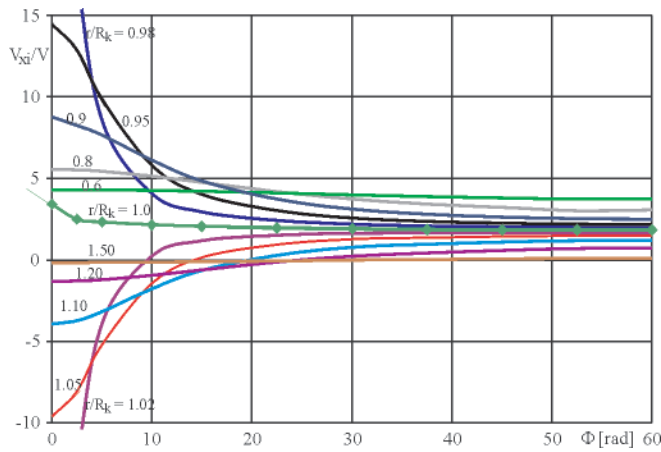


Fig. 6. The axial component of the velocity induced behind a three-bladed propeller

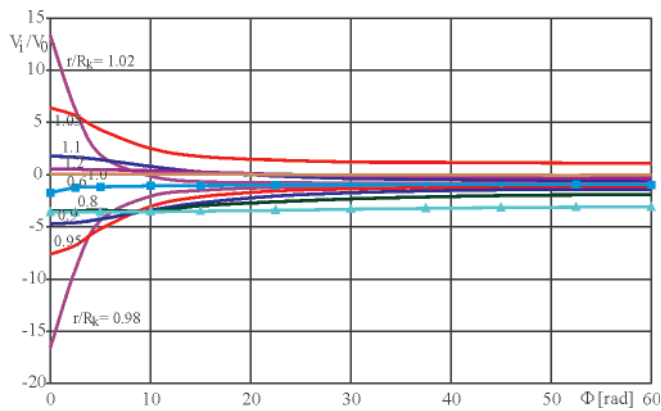


Fig. 7. The tangential component of the velocity induced behind a three-bladed propeller

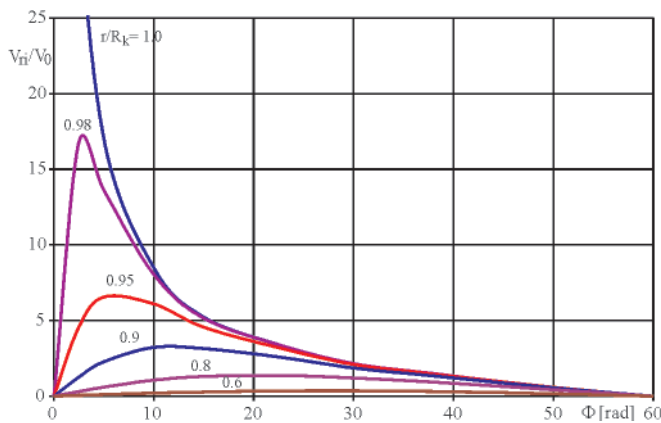


Fig. 8. The radial component of the velocity induced behind a three-bladed propeller

which ensures that the tips of the blades are already inside the slipstream shed from the forward propeller.

The volumetric averages of the velocities induced in front of the aft propeller are much smaller, their radial distribution is smooth and it does not exhibit any discontinuities (the volumetric average of the tangential induced velocity in front of the propeller is theoretically equal zero).

### The program for analysis of the contra-rotating propellers operation in the non-uniform velocity field

The computer program UNCA for the analysis of the ship propeller operation in the non-uniform velocity field is a very

important element of the design process of all propeller types. The central part of the algorithm of this program is the determination of the size and extent of various forms of cavitation on the blades of the propeller operating in the circumferentially non-uniform velocity field. The original theoretical model combines the unsteady vortex lifting surface model with the model of unsteady sheet cavitation bubble. The detailed description of the algorithm of UNCA may be found in [18, 19].

In the case of a CRP set the modification of the non-uniform velocity field of the ship hull wake due to the velocity field induced by the propeller other than this currently analyzed is a very important part of the computation algorithm. In order to fulfil this task an additional procedure has been incorporated in the program. This procedure calculates the induced velocity field both in front and behind the propeller.

The appropriately modified velocity field enables the detailed analysis of the operation of both forward and aft propeller by means of the program UNCA. In comparison with other propeller types the analysis of the CRP operation in the non-uniform inflow is particularly complicated and time-consuming. The aft propeller of the set operates in the non-uniform velocity field being the result of superposition of the hull wake and the velocity field induced by the forward propeller (see Figs. 9, 10 and 11). This analysis is additionally complicated by the fact that for each angular position of the forward propeller all selected angular positions of the aft propeller must be analyzed. The total number of the analyzed angular blade positions depends also on the number of blades of both propellers of the CRP set, but as a rule this number exceeds one thousand (for example for  $Z_f = 5$  and  $Z_a = 4$  the total number of the analyzed angular blade positions is  $n = 35 \cdot 36 = 1260$ ). For each of these blade positions the appropriate numerical files containing results are generated, which undergo further re-calculations, but they also may be presented on the computer screen in the numerical or graphical form or directly printed. These results include, among other data, the calculated cavitation phenomena on the aft propeller, shown in Fig. 12.

The results of calculations of the unsteady hydrodynamic forces and moments on the aft propeller for the angular position of the forward propeller equal to  $AF = 0$  are presented below (Figs. 13, 14 and 15). Similar diagrams may be presented for every mutual position of the forward and aft propeller. Independently, analogical results are available for the forward propeller.

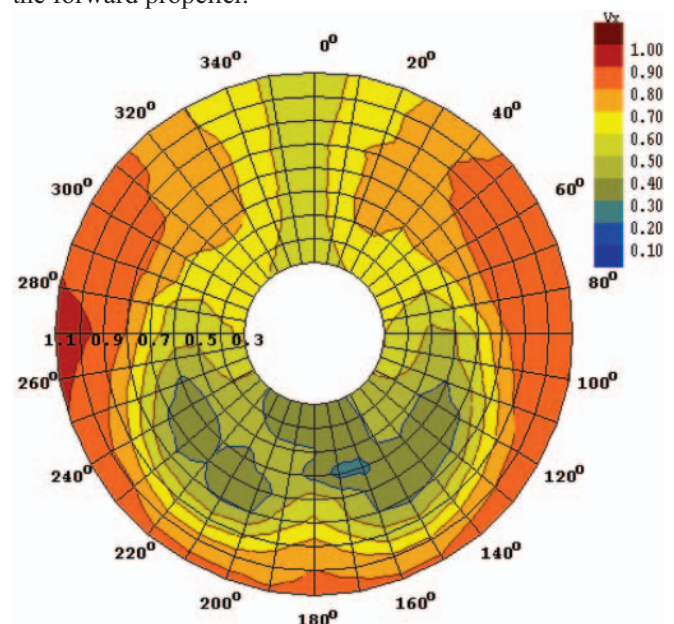


Fig. 9. The velocity field behind the ship hull

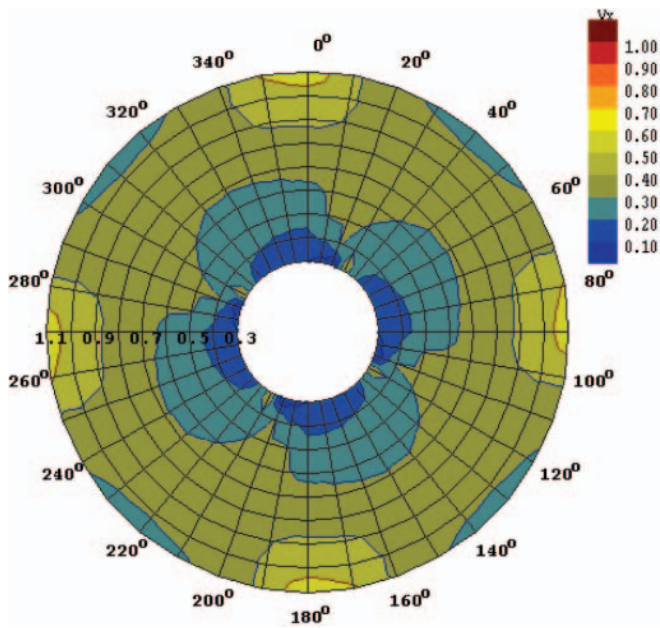


Fig. 10. The velocity induced by the forward propeller at the location of the aft propeller at the angular position of the forward propeller  $AF = 0$

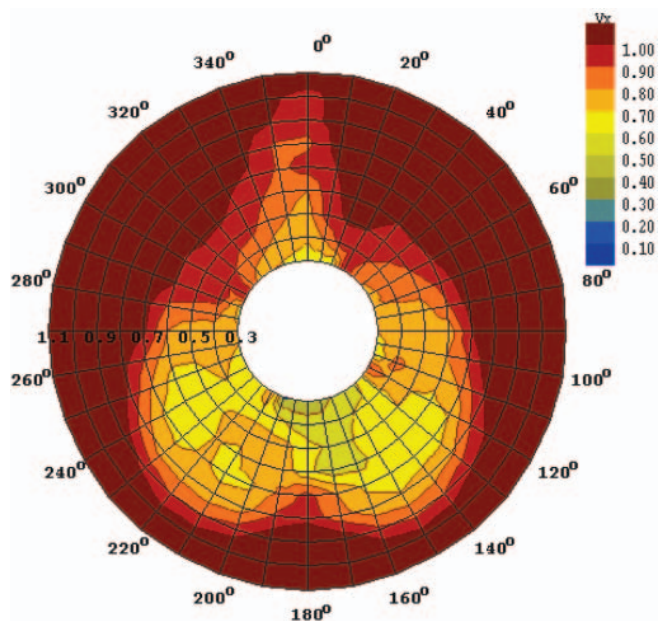


Fig. 11. The resultant velocity field at the location of the aft propeller for the angular position of the forward propeller  $AF = 0$

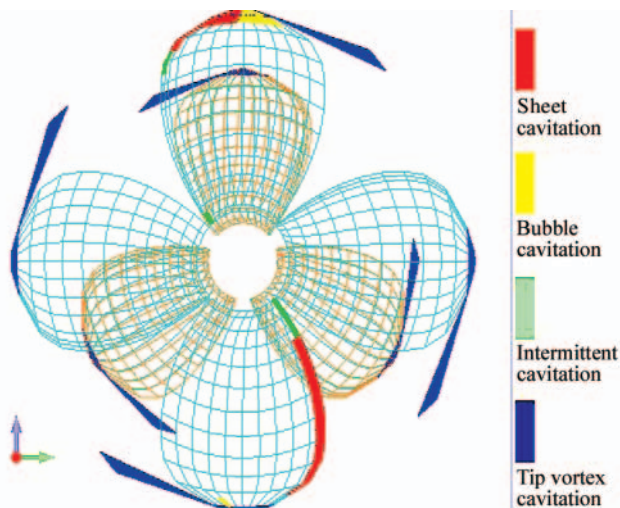


Fig. 12. The example of computed cavitation phenomena on the contra-rotating propellers

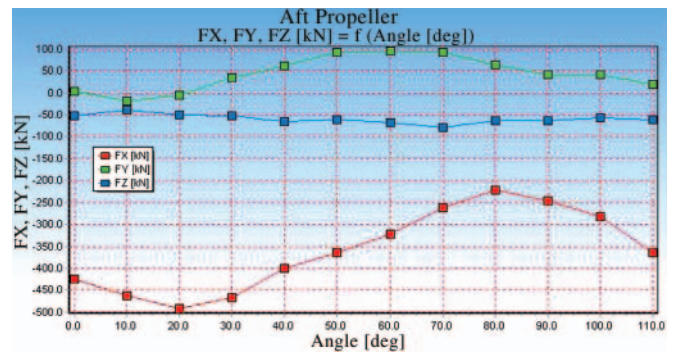


Fig. 13. The computed hydrodynamic force components  $FX, FY, FZ$  on the aft propeller for the angular position of the forward propeller  $AF = 0$

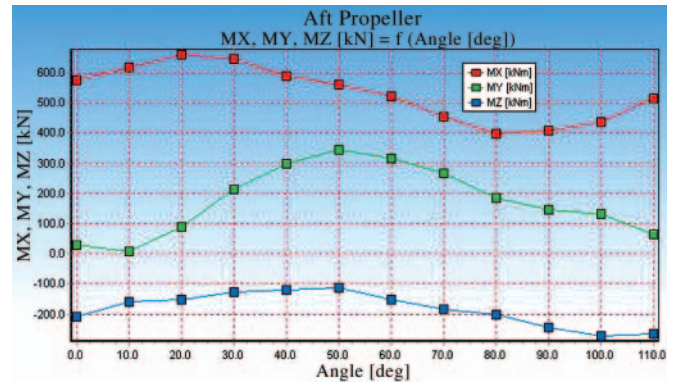


Fig. 14. The computed hydrodynamic moment components  $MX, MY, MZ$  on the aft propeller for the angular position of the forward propeller  $AF = 0$

For every angular blade position of the forward propeller of CRP the maximum and minimum values of the calculated pressure pulsations generated on the hull by the aft propeller and of the unsteady shaft forces are extracted. These data are presented in the numerical and graphical form (see Figs. 17 and 21).

Both propellers of the CRP set are analyzed by means of the program UNCA from the following points of view:

- the intensity and extent of the different forms of cavitation in different angular positions of both propellers in the combined non-uniform velocity field including the hull wake and the propeller-induced velocities,
- the level of pressure pulsations generated by the CRP set and by the forward and aft propeller separately on the hull surface or in the surrounding space,
- the level of the fluctuating hydrodynamic shaft forces and moments for the forward and aft propeller separately.

After such an analysis the designer may return to the CRP design calculation, modifying the selected details of the geometry and hydrodynamic parameters of both propellers of the set:

- the radial distribution of blade skewback
- the radial distribution of the blade section chord lengths
- the radial distribution of the maximum blade section thickness
- the type of blade section thickness distribution
- the type of blade section mean line
- the radial distribution of hydrodynamic loading of the blades
- the number of blades of both propellers
- the division of CRP total thrust between the forward and aft propeller
- the diameter of one or both propellers of CRP.

The above described analysis of CRP is performed only for the design condition, because any change of the ship speed or the propellers rates of rotation changes the operating conditions of both propellers – consequently the fields of induced velocities of both propellers change in the qualitative and quantitative sense.

The numerical results of the above analysis are stored in three separate files, referring respectively to the forward propeller, aft propeller and to the entire CRP set.

The method of graphical presentation of the results is similar to that applied to the classical single propellers [4], with the modification that in case of CRP it may refer separately to the forward or aft propeller or to the entire CRP set. The examples of such presentation are shown in the next section.

## COMPARATIVE ANALYSIS OF CRP AND TANDEM CO-ROTATING PROPELLERS

In the preceding publications [4,6] the results of design calculations of the single propeller and of the tandem co-rotating propellers. The case of the same large fast cargo vessel has been used in the design of the CRP set described below. The design ship speed is  $V = 25.3$  [knots] and the required thrust of the propulsor is  $T = 3250$  [kN]. The design rate of rotation of the engine and of the forward propeller is 100 [rpm]. In the case of CRP set the rate of rotation of the aft propeller may be different and it may be optimized from the point of view of propulsive efficiency, cavitation, pressure pulsations on the hull and unsteady hydrodynamic shaft forces. In the process of such an optimization the best performance of CRP was achieved for the number of blades of the forward propeller  $Z_f = 5$ , number of blades of the aft propeller  $Z_a = 3$  and for the rate of rotation of the aft propeller equal to 115 [rpm]. The optimum diameter of the aft propeller was determined on the basis of the appropriate semi-empirical formulae concerning the slipstream behind the forward propeller. The calculated main characteristics of the forward and aft propellers of the CRP set are given in Tab. 1 below.

Tab. 1. Main parameters of the designed CRP set

Characteristic	Forward propeller	Aft propeller
Propeller diameter [m]	7.80	5.83
Expanded blade area ratio [-]	0.59	0.42
Shaft power [kW]	30060	11800
Mass of the blades [kg]	23343	7300
Static moment of inertia [kgm**2]	511944	76419

The comparison of the above results for CRP with those obtained for other propeller types [4, 6] shows that the propulsive efficiency of the CRP set is about 5 percentage points higher than that of a single propeller and about 2.5 percentage points higher than the tandem co-rotating propellers. However, the CRP set is worse than the other analyzed propellers as far as the pressure pulsations on the hull (probably also acoustic pressures) and the unsteady hydrodynamic shaft forces are concerned.

Figs. 15 and 16 below present the calculation results for the CRP set, concerning the harmonic amplitudes of the unsteady hydrodynamic shaft forces and moments, shown separately for the forward and aft propeller. Presentation of the results is done separately for each of the propellers of the CRP set because their different numbers of blades and different rates of rotation prohibit presentation of the results on one common diagram of harmonic amplitudes.

Moreover, the calculations of the harmonic amplitudes of the unsteady hydrodynamic shaft forces are performed separately for each angular position of the forward and aft propellers. The numerical files containing the results or their graphical representations may be inspected. However, the analysis of about 1000 diagrams or files is not easy. In order to facilitate this analysis, for each angular position of one of the propellers only the maximum and minimum values of the respective components of the unsteady shaft forces and moments are extracted. These values are appropriately added together and presented in the form of a relatively short numerical file or as one diagram. Example of such a diagram is presented in Fig. 17. This diagram includes also the differences between the maximum and minimum values because these differences are decisive parameters in some Classification Society Rules.

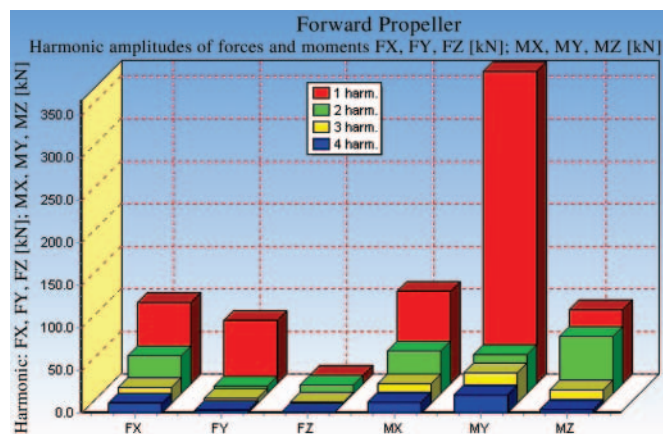


Fig. 15. The computed harmonic amplitudes of the hydrodynamic force and moment components for the forward propeller of the CRP set

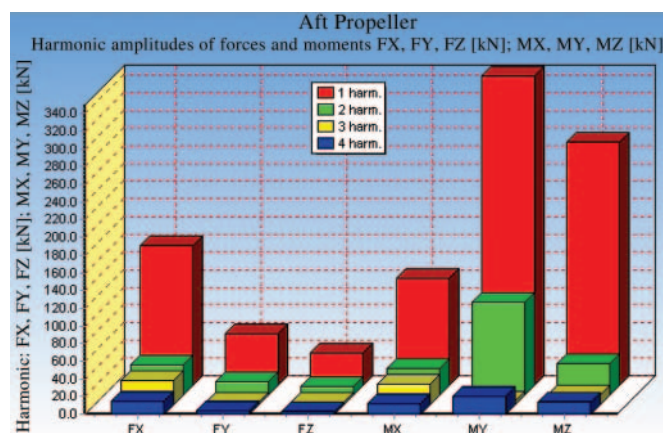


Fig. 16. The computed harmonic amplitudes of the hydrodynamic force and moment components for the aft propeller of the CRP set for the angular position  $AF = 0$  of the forward propeller

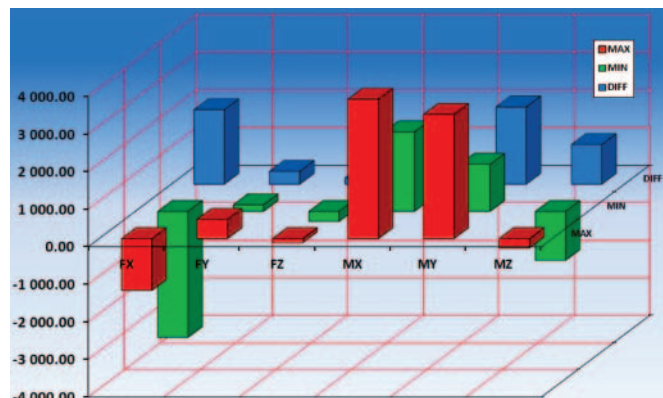


Fig. 17. Maximum and minimum values, together with their differences, for the hydrodynamic shaft forces [kN] and moments [kNm] on the entire CRP set

For the sake of comparison the corresponding results of calculations for the tandem co-rotating set, designed for the same ship and operating in the same non-uniform velocity field [6], are presented in the analogical format in Fig. 18.

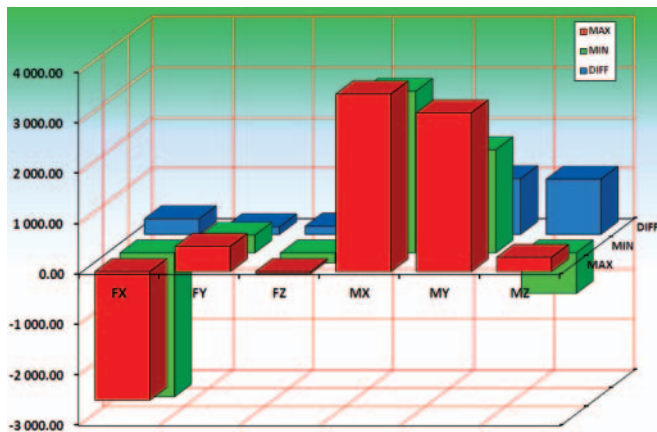


Fig. 18. Maximum and minimum values, together with their differences, for the hydrodynamic shaft forces [kN] and moments [kNm] on the set of tandem co-rotating propellers

A similar presentation of the calculation results may be done for the pressure pulsations generated on the hull (or acoustic pressures in the surrounding space). In Figs. 19 and 20 the harmonic amplitudes of the pressure pulsations generated in the selected points on the hull by each propeller of the CRP set separately are presented. Fig. 21 shows the maximum and minimum values of these pressure pulsations, together with their differences. For the sake of comparison, the corresponding values calculated for the tandem co-rotating propellers, designed for the same ship and operating in the same non-uniform velocity field are shown in Fig. 22.

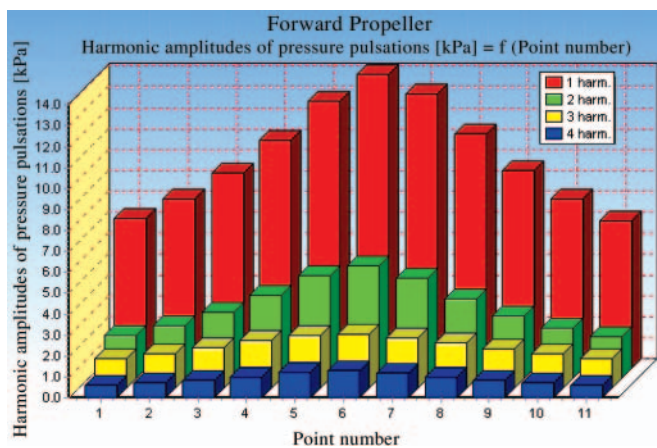


Fig. 19. Harmonic amplitudes of the pressure pulsations generated on the hull by the forward propeller of the CRP set

Similarly as in the case of other propeller types, the program determines the presence and extent of the various cavitation forms, which are described as numerical files or corresponding illustrations. In Figs. 23, 24 and 25 the examples of graphical presentation of the computed cavitation phenomena are shown.

The cavitation pictures may be viewed independently for each of the propellers (Figs. 23 and 24) or in combination (Fig. 25). Apart from the static pictures the program enables viewing the CRP set in motion, exhibiting the calculated unsteady cavitation phenomena. The complete revolution of both propellers of the CRP set may be presented, showing the time-dependent variation of the cavitation phenomena on the propeller blades in the non-uniform velocity field (in this presentation the forward or aft propeller is alternatively

immobilized and the other performs one full revolution). This presentation may be also recorded in the format of a film.

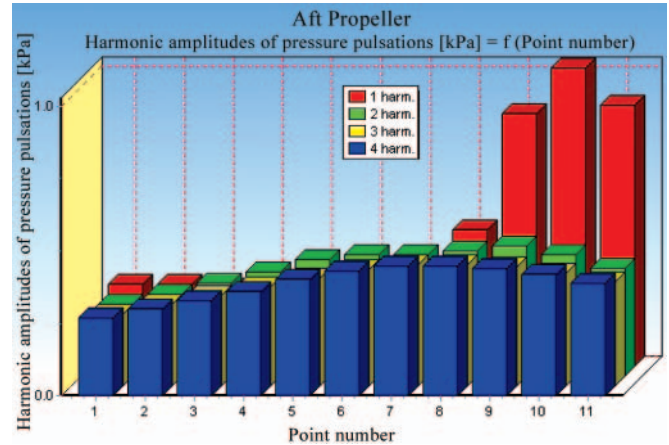


Fig. 20. Harmonic amplitudes of the pressure pulsations generated on the hull by the aft propeller of the CRP set

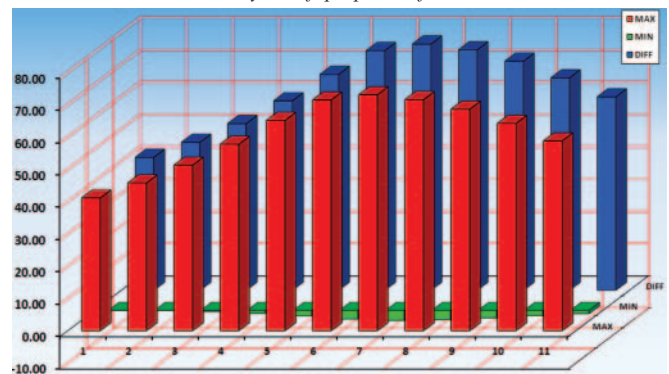


Fig. 21. Maximum and minimum values, together with their differences, of the pressure pulsations [kPa] induced on the hull by the entire CRP set

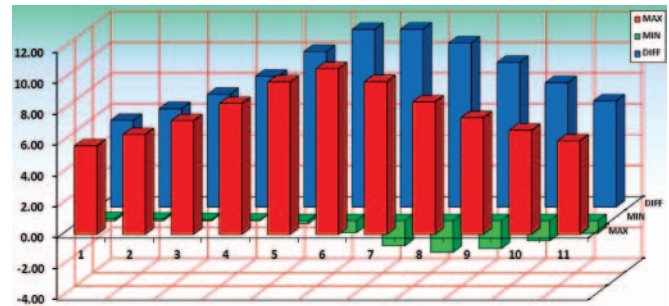


Fig. 22. Maximum and minimum values, together with their differences, of the pressure pulsations [kPa] induced on the hull by the entire set of tandem co-rotating propellers

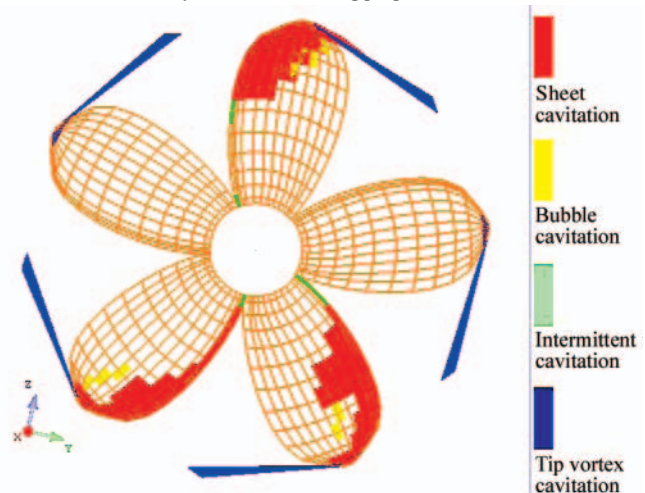


Fig. 23. Example of the computed cavitation phenomena on the forward propeller of the CRP set

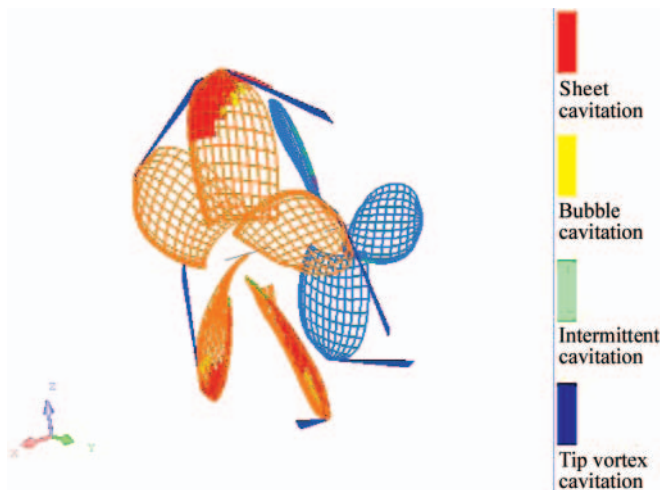


Fig. 24. Example of the computed cavitation phenomena on the aft propeller of the CRP set

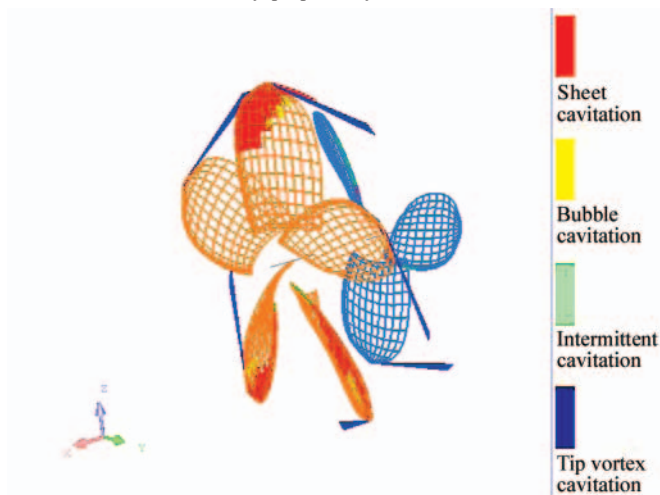


Fig. 25. Example of the computed cavitation phenomena on both propellers of the CRP set for their selected position in the non-uniform inflow

It may be concluded from the analysis of the above examples, that from the point of view of propulsive efficiency the CRP set is better than the tandem co-rotating propellers and than the classical single propeller. This is not a general rule, the design example presented in [4,5,6] is selected in such a way, that it may be demonstrated that in certain areas of propeller operation the CRP or tandem co-rotating propellers may be more efficient than the classical single propeller.

The problem of cavitation performance, unsteady hydrodynamic shaft forces and pressure pulsations is much more involved and it requires a thorough analysis of the results of comparative calculations. The computer systems presented in the current line of publications [4, 5, 6] facilitate the optimum selection of the appropriate propeller type for every application.

## CONCLUSIONS

- The computer system presented above fully facilitates the process of design of the contra-rotating propellers. This system incorporates all elements necessary in the correct design process of CRP. The computational process itself is relatively fast (although much slower than in the case of other, simpler propellers), and the graphical subroutines enable efficient analysis of the consecutively designed CRP sets, directing the whole process towards an optimum solution of the design task.

- The relatively short computation time allows for calculation of a large number of variants of the designed CRP set. For example the following parameters may be modified in the course of design without leaving the system:
  - number and geometry of the blades of both propellers of the CRP set (including the geometry of the blade sections)
  - diameters of both propellers of the CRP set
  - ship speed and rates of rotation of both propellers of the CRP set (equal or different)
  - division of the total thrust between the forward and aft propeller of the CRP set
  - radial distribution of the hydrodynamic loading of the blades
  - axial distance between both propellers of the CRP set.
- The above listed modifications enable the optimization of the CRP set from the point of view of efficiency, cavitation performance, induced pressure pulsations and unsteady hydrodynamic shaft forces and moments. The widely employed graphical presentation of the results greatly facilitates such an optimization analysis.
- The above presented design example, together with the results of calculations of the ducted propeller included in [5] and tandem co-rotating propellers included in [6], lead to the conclusion that **it is worthwhile to include in the design analysis different propeller types**. The four propeller design systems presented in the current line of publications [4, 5, 6], which accept very similar input data files (relatively the most onerous part of the design process), enable very fast and efficient comparative analysis, leading to the selection and consecutive design of the optimum propeller type in every practical application.

## BIBLIOGRAPHY

1. Bjaerne E.: *Systematic Studies of Contra-rotating Propellers for Merchant Ships*, Transactions RINA 1973
2. Glover E.J.: *Contra-rotating Propellers for High Speed Cargo Vessels*, Transactions NECIES, February 1967
3. van Gunsteren L.A.: *Application of Momentum Theory in Contra-rotating Propellers*, International Shipbuilding Progress, No. 206, 1971
4. Koronowicz T., Krzemianowski Z., Tuskowska T., Szantyr J.A.: *A Complete Design of Ship Propellers Using the New Computer System*, Polish Maritime Research No. 1, vol. 16, 2009
5. Koronowicz T., Krzemianowski Z., Tuskowska T., Szantyr J.A.: *A Complete Design of Ducted Propellers Using the New Computer System*, Polish Maritime Research No. 2, vol. 16, 2009
6. Koronowicz T., Krzemianowski Z., Tuskowska T., Szantyr J.A.: *A Complete Design of Tandem Co-rotating Propellers Using the New Computer System*, Polish Maritime Research No. 4, vol.16, 2009
7. Koronowicz T.: *Algorithm of the Design Program Based on the Single Layer Lifting Surface Model Applied to the Arbitrarily Skewed Propellers* (in Polish), IFFM Report No. 295/1986
8. Koronowicz T.: *Analysis of the Velocity Field of the Helical Vortices* (in Polish), IFFM Report No. 643/1969
9. Koronowicz T.: *Determination of the Velocity Field in the Close Vicinity of the Screw Propeller* (in Polish), IFFM Report No. 58/729/1973
10. Koronowicz T.: *Determination of the Variation of Induced Velocities in the Propeller Wake* (in Polish), IFFM Report No. 83/745/1974
11. Lerbs H.W.: *Contra-rotating Optimum Propellers Operating in Radially Non-uniform Wake*, DTMB Report 941-1955

12. Lindgren H.: *Hydrodynamic Aspects of Contra-rotating Propellers*, Shipping World and Shipbuilder, November 1967
13. van Manen J.D., Sentic A.: *Contra-rotating Propellers*, NSMB Publication No. 126/1956
14. Minsaas K.: *A Method for the Design of Contra-rotating Propellers*, Publication NSET No. 112, 1971
15. Młynarczyk J.: *Design of the Contra-rotating Propellers on the Basis of Lerbs Theory* (in Polish) IFFM Report No. 37/898/1978
16. Morgan W.B.: *The Design of Contra-rotating Propellers Using Lerbs Theory*, Transactions SNAME, 1960
17. Szantyr J.A.: *A Computer Program for Calculation of Cavitation Extent and Excitation Forces for a Propeller Operating in the Non-uniform Velocity Field*, International Shipbuilding Progress No. 296, vol. 26, 1979
18. Szantyr J.A.: *The Method of Deformable Lifting Surface Theory for Determination of the Unsteady Cavitation and its Hydrodynamic Consequences*, Doctor of Science Thesis, IFFM Report No. 183/1110/1984
19. Szantyr J.A.: *A Method for Analysis of Cavitating Marine Propellers in Non-uniform Flow*, International Shipbuilding Progress No. 427, vol.41, 1994

#### CONTACT WITH THE AUTHORS

Tadeusz Koronowicz, Prof.  
 Zbigniew Krzemianowski, Ph. D.  
 Teresa Tuskowska, Ph. D.  
 Institute of Fluid-Flow Machinery,  
 Polish Academy of Sciences  
 Fiszerza 14  
 80-952 Gdansk, POLAND  
 e-mail: ttk@interecho.com

Jan A. Szantyr, Prof.  
 Department of Turbomachinery  
 and Fluid Mechanics,  
 Gdańsk University of Technology  
 Narutowicza 11/12  
 80-233 Gdansk, POLAND  
 e-mail: jas@pg.gda.pl

# Influence analysis of changes of design parameters of passenger-car ferries on their selected sea-keeping qualities

**Tomasz Cepowski**, Assoc. Prof.  
Szczecin Maritime University

## ABSTRACT



*The main scientific aim of this research was to elaborate design guidelines which could make it possible to improve sea-keeping qualities of passenger-car ferries. The searched-for design guidelines were prepared in the form of regression functions as well as artificial neural networks on the basis of the results obtained from calculations with the use of numerical methods based on the theory of planar flow around a body. The guidelines make it possible to predict ship roll, sea-sickness index, lateral and vertical accelerations on the basis of quantities available in the preliminary stage of ship design.*

**Keywords:** passenger-car ferry, design guidelines, preliminary design stage, sea-keeping qualities, rolling, sea-sickness (motion-sickness) index, vertical accelerations, lateral accelerations, ship main dimensions

## INTRODUCTION

Many dividing criteria of sea-going ships can be found because of variety of floating units, e.g. according to their functions, size, propulsion, architectural form, design problems, spatial subdivision etc. For most types of ships sea-keeping qualities are not an important design limitation. Exceptions from the rule are certain types of ships which can be divided into the following groups:

1. group of ships which have to fulfil their mission independent of weather conditions
2. group of ships characterized by design features which increase their susceptibility to weather conditions
3. group of ships intended for the carrying of passengers
4. group of transport ships for which sea-keeping qualities are only one of the limitations imposed on them.

The ships belonging to the groups have to be characterized by various sea-keeping qualities which can be modeled on different design levels (preliminary design – technical design). For each of the above mentioned ship groups important sea-keeping qualities resulting from the functions to be fulfilled by them, can be formulated.

In this work only the group of passenger ships has been selected out of all the groups. The group can be further divided into:

1. ships intended for the carrying of passengers only:
  - excursion ships (cruisers)
  - passenger ships
  - sanatorium and hospital ships
  - yachts

2. ships intended for the carrying of passengers and general cargo:

- passenger-cargo ships
- passenger-cargo ferries:
  - passenger-car ferries
  - passenger-train ferries
- ropax ships
- passenger-container carriers.

The main design problems of ships of the group are first of all: their internal capacity, speed, and necessity of providing safety and comfort for passengers.

Among the first subgroup of the ships a. o. excursion ships (cruisers) are numbered. And, with a view of their large dimensions, to provide them with good sea-keeping qualities is not a problem. However for the remaining ships of the group, especially passenger ships intended for carrying cargo, design solutions are searched for to improve their sea-keeping qualities, such as these aimed at:

- the decreasing of roll motion which can cause cargo to shift and in consequence to impair ship stability
- the decreasing of accelerations which can cause lashing of fixed cargo to break (or cargo to shift)
- the moderating of accelerations which can generate sea-sickness
- the avoiding of parametric resonance of motion.

The passenger-car ship is a typical representative of the ships' group regarding the problems associated with the providing-for of appropriate sea-keeping qualities.

# PROBLEM OF MODELING SEA-KEEPING QUALITIES OF PASSENGER-CAR FERRIES DURING PRELIMINARY DESIGN STAGE

In ship design process design solutions which satisfy both economic criteria and technical limitations, are searched for. In the case of passenger-car ferry the economic criteria are consisted of many requirements put by shipowner, to which a.o. internal hull capacity or service speed can belong. And, the technical limitations are formed from a.o. a group of factors affecting ship safety, i.e. first of all appropriate ship stability, unsinkability and hull strength.

Ship designers are often and often required to design some of the passenger-car ferries so as to additionally provide them, apart from general design merits, with immunity to weather conditions, i.e. good sea – keeping qualities.

Hull form and dimensions of a ferry are to a great extent decisive of its sea-keeping qualities. Therefore they should be modelled already in the preliminary design stage. An important feature of preliminary ship design is that exact form of ship hull is represented by means of the so-called main dimensions and global coefficients which characterize hull form, e.g. hull block, midship-section and vertical prismatic coefficients. The scarce set of information makes using the known methods of determination ship motions in waves, based on the classical linear or non-linear ship motion theory, not possible; hence in present it is important problem how to take fully into account the entire range of sea-keeping qualities already in the preliminary ship design stage. And, another problem is that the selection of improper values of ship main dimensions and hull form coefficients irreversibly worsens sea-keeping qualities (and other design merits as well) since any change of any dimensions of a ship after its building is economically unjustified.

Therefore this work has been aimed at the elaborating of design guidelines focused on improvement of sea-keeping qualities of sea-going passenger-car ferry already in the preliminary stage of its design.

## METHOD OF INVESTIGATIONS

To reach the aim of this research the method consisted of the following phases, has been selected:

1. elaboration of a list of ferry-ships covering a broad range of their forms and dimensions
2. elaboration of operational scenarios important from the point of view of ferry operation and significantly affecting certain technical features of such ships
3. simplification of physical model by:
  - a. replacement of real weather conditions by statistical ones

- b. replacement of real waves by a standard wave energy spectral density function
- c. replacement of instantaneous ship response values by conventional statistical ones.
4. elaboration of symbolic mathematical model which describes the ferry design parameters  $X_1, X_2, \dots, X_n$ , as well as the sea-keeping qualities  $K$  important from the point of view of an assumed ferry operational scenario
5. use of the exact numerical methods to calculate values of the parameter  $K$
6. selection of approximating functions for a set of discrete values of  $K$ -parameter, and elaboration of design guidelines with taking into account the parameter in question
7. assessment of the elaborated design guidelines
8. determination of a range of application and limitation of the elaborated formulas.

The detailed research algorithm is presented in Fig. 1.

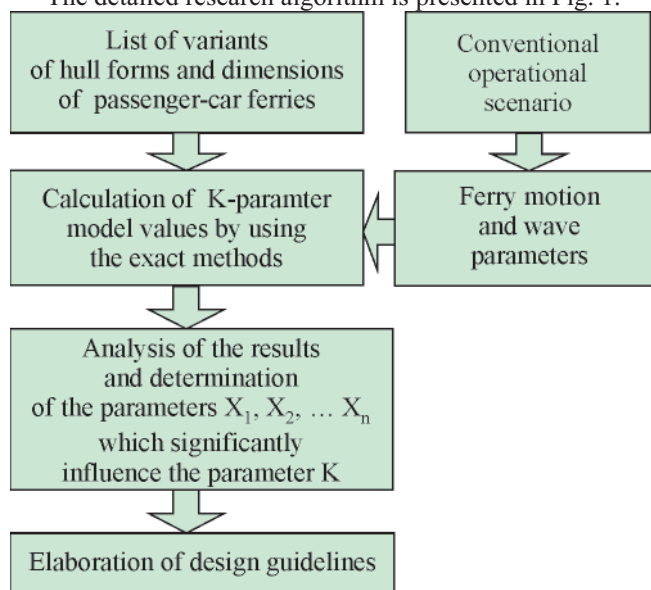


Fig. 1. Algorithm of the applied research method, where:  $X_1, X_2, \dots, X_n$  – ship design parameters,  $K$  – a parameter which describes ship sea-keeping qualities

## LIST OF VARIANTS OF HULL FORMS AND DIMENSIONS OF PASSENGER-CAR FERRIES

While elaborating the list of variants of hull forms of passenger-car ferries the recommendations contained in the report [4] were taken into account. In this research the list of 3072 variants was prepared by using a combination of the following items:

Tab. 1. Variants of passenger-car ferry hull form

Variant	CB [-]	CB(Lpp) [-]	CB(L) [-]	CB(V) [-]	CWL [-]	CWL(Lpp) [-]	CM [-]	XB/Lpp [%]	XF/Lpp [%]
1	0.557	0.597	0.618	0.740	0.752	0.807	0.965	48.60	42.83
2	0.642	0.642	0.657	0.777	0.826	0.826	0.977	48.79	44.44
3	0.614	0.635	0.645	0.786	0.781	0.808	0.984	48.11	45.44
4	0.614	0.614	0.638	0.743	0.826	0.826	0.963	48.00	45.34
5	0.618	0.618	0.647	0.762	0.811	0.811	0.955	47.24	45.64
6	0.629	0.629	0.657	0.743	0.847	0.847	0.958	46.62	45.04
7	0.585	0.623	0.642	0.734	0.797	0.849	0.971	47.16	43.59
8	0.609	0.609	0.639	0.759	0.803	0.803	0.954	47.61	46.00

CB – block coefficient of underwater ship hull part, CB(Lpp) – block coefficient of underwater ship hull part related to ship length between perpendiculars, CM – midship section coefficient, CB(L) – cylindrical coefficient of underwater ship hull part, CB(V) – vertical prismatic coefficient of underwater ship hull part, CWL – waterplane coefficient, CWL(Lpp) – waterplane coefficient related to ship length between perpendiculars, XF – distance between geometrical centre of waterplane and aft perpendicular, XB – distance between centre of buoyancy and aft perpendicular, Lpp – ship length between perpendiculars

a) the ranges of ferry dimensions:

- $Lb d = 19\ 000, 28\ 000, 37\ 000, 46\ 000\ m^3$  (where: L – waterline length, B – waterline breadth, d – ship draught)
- $L/B = 5.8, 6.6, 7.4, 8.2$

- $B/d = 3, 3.5, 4, 4.5$

b) the set of eight hull form variants (Fig. 2), represented by the global hull form coefficients contained in Tab. 1

c) the values of the initial transverse metacentric height GM, ranging from 0.4 m to 1.4 m every 0.2 m.

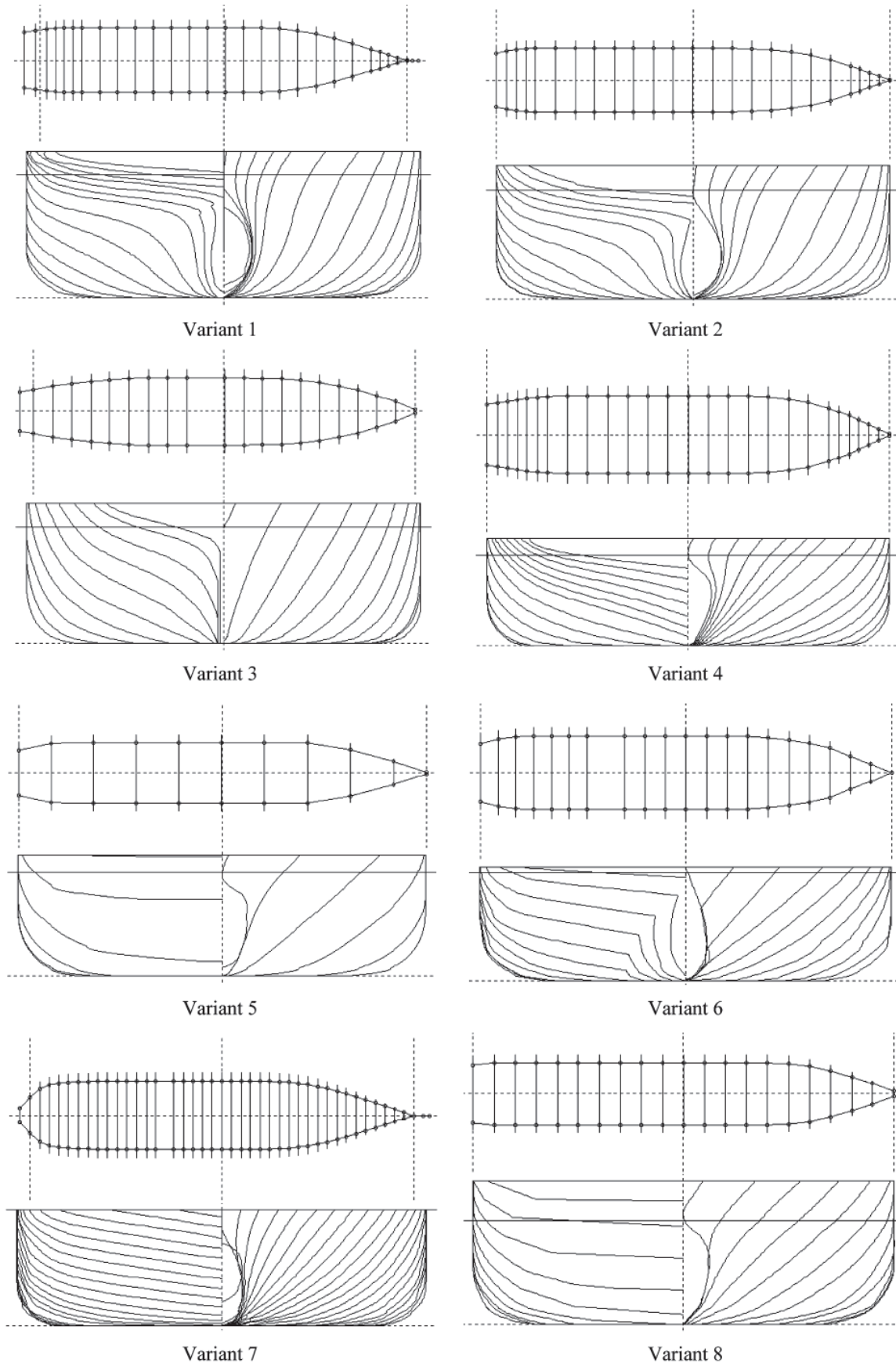


Fig. 2. Hull forms of passenger-car ferries, used in the research in question

## OPERATIONAL SCENARIOS

In the research it was assumed that the design guidelines will be elaborated for ferries operating in conventional service conditions. It was the conditions important from the point of view of its operational merits, in which a ferry could operate. Such approach has been based on the target assignment concept recommended by IMO Maritime Safety Committee for the elaborating of new assessment standards of ship stability [5].

Ship sea-keeping qualities are significantly influenced by a.o. wave parameters, ship motion parameters (ship speed and wave encounter angle) as well as hydrodynamic ship hull parameters dependent on a form of its underwater part and weight distribution. For instance in Fig. 3 is presented impact of the characteristic wave frequency on statistically significant roll amplitudes of a ship, depending on varying values of initial transverse metacentric height of the ship moving with steady parameters of its motion.

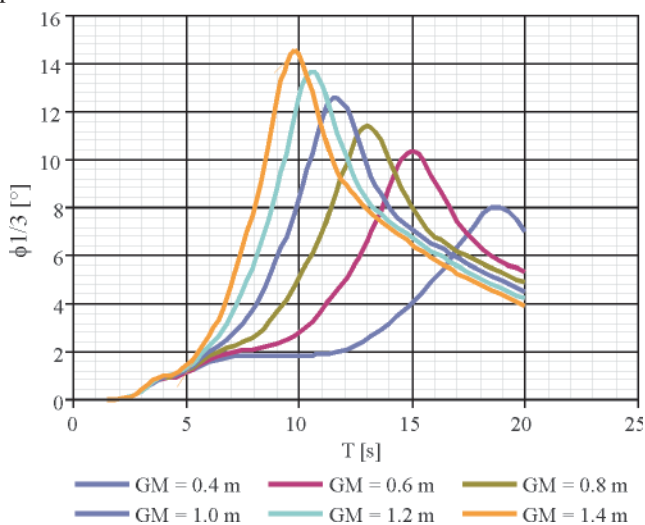


Fig. 3. Significant ship roll amplitudes in function of the characteristic wave frequency  $T$ , and:  $GM = \text{var}$ ,  $H_s = 3 \text{ m}$ ,  $\beta = 60^\circ$  (where:  $0^\circ$  – head wave,  $180^\circ$  – aft wave),  $v = 0 \text{ m/s}$

As results from Fig. 3, the characteristic wave frequency together with the initial transverse metacentric height greatly influence ship rolling motion. From the point of view of design problems it is difficult to determine waving conditions in which a given ship operates, and especially troublesome to determine the characteristic wave frequency.

Therefore only such values of the characteristic wave frequency which generate maximum values of the considered sea-keeping qualities, were taken into account in order to eliminate influence of their impact on ship's behaviour.

In Fig. 4 for instance, is presented the relation between the initial transverse metacentric height and significant ship roll amplitudes for:

- a given value of the characteristic wave frequency (series 1)
- varying values of the characteristic wave frequency, in which significant ship roll amplitudes reach their maxima (series 2).

As results from Fig. 4, the series 2 show another trend and higher values of statistical ship rolling than the series 1. Hence it results that the series 2 show influence of the initial transverse metacentric height on rolling motion of ship sailing in waves of the most unfavourable characteristic frequency.

With a view of the above mentioned aspects the following conventional operational scenarios were taken into account:

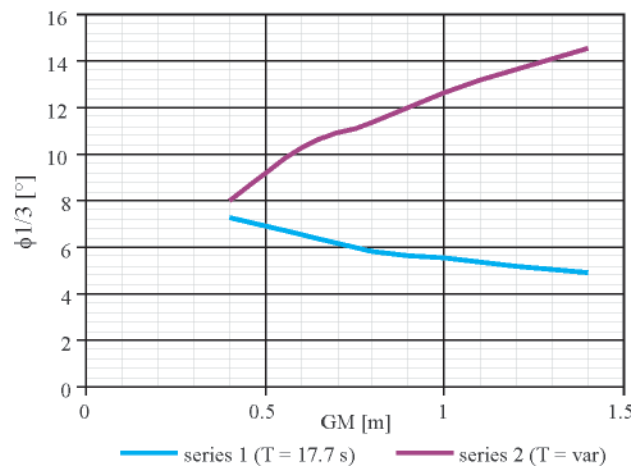


Fig. 4. Significant ship roll amplitudes in function of the initial transverse metacentric height  $GM$ : series 1 – for the characteristic wave frequency  $T = 17 \text{ s}$ , series 2 – for the characteristic wave frequency  $T$  for which maximum ship roll values occur;  $H_s = 3 \text{ m}$ ,  $\beta = 60^\circ$ ,  $v = 0 \text{ m/s}$

1. the ferry has lost its propulsion (ship speed  $v=0 \text{ m/s}$ ) and found itself in waving conditions in which dangerous values of its rolling motion occur:
  - a. the ferry is obliquely situated relative to the incoming wave, that results in occurrence of maximum values of its rolling motion
  - b. the wave is of the characteristic frequency which produces maximum values of ship rolling motion
  - c. the significant wave height  $H_s$  is contained within the range of  $1 \div 3 \text{ m}$ .
2. the ferry sails with the service speed  $V = 12.5 \text{ m/s}$  in waving conditions which intensify occurrence of sea-sickness among crew members and passengers:
  - a. the ferry is obliquely situated respective to the incoming wave, that results in occurrence of maximum values of the sea-sickness index
  - b. the wave is of the characteristic frequency which produces maximum values of the sea-sickness index
  - c. the significant wave height  $H_s$  is contained within the range of  $1 \div 3 \text{ m}$ .
3. the ferry sails with the service speed  $V = 12.5 \text{ m/s}$  in waving conditions which generate large vertical and lateral accelerations in the point P (Fig. 5), which could cause trailers placed on car deck to shift [8]:
  - a. the ferry is situated at the angle against incoming wave, most unfavourable from the point of view of vertical and lateral accelerations
  - b. the wave is of the characteristic frequency which produces maximum values of vertical and lateral accelerations
  - c. the significant wave height  $H_s$  is contained within the range of  $1 \div 3 \text{ m}$ .

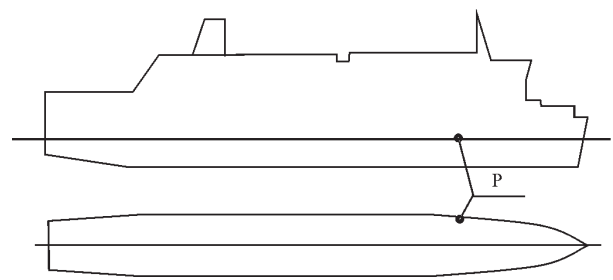


Fig. 5. The coordinates of the point P located on the car deck,  $(0.75L_{pp}, 0.45B, d)$ , for which vertical and lateral accelerations were calculated, where:  $L_{pp}$  – ship length between perpendiculars,  $B$  – ship breadth,  $d$  – ship draught

## NUMERICAL CALCULATIONS

For every variant of the passenger-car ferry sailing in the assumed operational conditions the following sea-keeping qualities (the parameter K, acc. Fig. 1), were calculated;

1. the maximum values of the significant statistical ship roll amplitudes,  $\phi_{1/3\max}$
2. the maximum significant values of the sea (motion) - sickness index,  $MSI_{\max}$  (acc. [6])
3. the maximum values of the significant amplitudes of vertical accelerations,  $a_{v\max}$ , and lateral ones,  $a_{t\max}$ , in the point P, acc. Fig. 3.

For calculations of ship motion in statistical waves the JONSWAP wave spectrum was assumed to be a wave energy spectral density function. The calculations were performed by using the numerical methods of the SEAWAY software, based on the theory of planar flow around a body. The method given in [3] was used for calculations of hydrodynamic coefficients. The accuracy tests of the SEAWAY software presented in [2], show a high accuracy of calculations carried out with the use of the program in question.

## SELECTION OF APPROXIMATING FUNCTIONS

This research phase was aimed at elaboration of simplified analytical relations suitable for predicting selected sea-keeping qualities on the basis of ship design parameters.

To preliminarily identify the parameters which significantly impact the assumed sea-keeping qualities, the subject-matter literature, analysis of parameter influence on particular sea-keeping qualities, as well as sensitiveness analysis was used by applying artificial neural networks. Next, the parameters characterized by the following features, were selected:

1. suitably high variability
2. strong correlation relative to dependent variable
3. weak correlation relative to the remaining independent variables of considered model
4. availability in preliminary ship design stage.

The selection of the approximating function was performed by verifying first the simplest linear functions. In the case when the verifying hypothesis was erroneous, non-linear functions (power, exponential, rational ones, etc), as well as functions represented by artificial neural networks which reveal the highest accuracy of approximation and the lowest dispersion, were searched for.

The approximation accuracy was assessed by using Pearson correlation coefficient, and the dispersion – by means of standard deviation of error.

## DESIGN GUIDELINES

The performed research resulted in the elaboration of the design guidelines presented in the form of the following relations (1), (2), (3), (4) and (5):

$$\phi_{1/3\max} = H_s \cdot \frac{\left( \frac{1}{1 + e^{-([0.072 \cdot B - 1.378, 11.373 \cdot CB - 6.532, GM - 0.4] \times A_1 - A_2)}} \times A_3 - 3.3488 \right) + 0.059}{0.0218} \quad (1)$$

$$\phi_{1/3\max} = H_s \cdot \left( 1.6221 + \frac{2.5695}{CB} - 0.0997 \cdot \frac{B}{\sqrt{GM}} \right) \quad (2)$$

$$MSI_{\max} = 97287997 \cdot \left( \frac{\exp(H_s)}{Fw} \right)^3 \quad (3)$$

$$av_{1/3\max} = 36.57 \cdot \frac{H_s}{\sqrt{Fw}} \quad (4)$$

$$at_{1/3\max} = H_s \cdot \frac{\left( \frac{1}{1 + e^{-([0.007 \cdot LWL - 929, 0.072 \cdot B - 1.378, 0.017 \cdot XF - 0.926, 32.787 \cdot CM - 31.269, GM - 0.4] \times A_4 - A_5)}} \times A_6 - 1.107 \right) + 0.066}{0.059} \quad (5)$$

where:

- $\phi_{1/3\max}$  – significant roll amplitude (maximum value) [°]
- $MSI_{\max}$  – Motion Sickness (sea-sickness) Index (maximum value) [%]
- $av_{1/3\max}$  – significant amplitude of vertical accelerations (its maximum value) [°]
- $at_{1/3\max}$  – significant amplitude of lateral accelerations (its maximum value) [°]
- B – ship breadth [m]
- CB – block coefficient of underwater part of ship hull [-]
- CM – midship section coefficient [-]
- GM – initial transverse metacentric height [m]
- Fw – waterplane surface area [m<sup>2</sup>]
- LWL – waterline length [m]

XF – distance between geometric centre of waterplane and its aft end [m]

$H_s$  – significant wave height [m]

$A_i$  – matrix of weight values:

$$\begin{bmatrix} -8.2648 & -4.4049 & 2.6160 & 0.9067 \\ 0.7385 & 0.6195 & 1.2891 & -0.4663 \\ -13.5773 & -7.7457 & -0.0425 & 1.7976 \end{bmatrix}$$

$A_2$  – vector of threshold values:

$$[-8.2648 \ -4.4049 \ 2.6160 \ 0.9067]$$

$A_3$  – column vector of weight values:

$$[-3.2109 \ 5.8162 \ -1.7407 \ 5.4637]$$

$A_4$  – matrix of weight values:

$$\begin{bmatrix} 1.244 & 0.400 & 1.205 & -0.763 & -1.714 \\ -3.021 & -0.137 & 3.079 & -4.673 & -0.040 \\ -2.501 & -0.516 & 0.898 & -2.687 & 1.653 \\ -0.416 & 7.030 & -0.718 & 0.707 & 5.162 \\ -3.699 & -0.436 & -3.545 & 4.176 & -0.364 \end{bmatrix}$$

$A_5$  – vector of threshold values:

$$[1.610 \ 4.976 \ 0.700 \ -2.982 \ 4.313]$$

$A_6$  – column vector of weight values:

$$[2.141 \ 2.494 \ 1.493 \ 1.221 \ -3.467]$$

The relations (1) and (5) are in the form of MLP artificial neural networks whose structures are shown in Fig. 6.

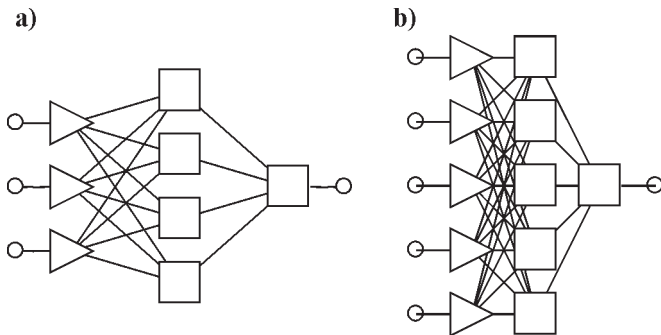


**Fig. 6.** Structures of MLP artificial neural networks used to approximate:  
**a)** significant roll amplitudes (maximum values), by inputs: CB, GM, B;  
**b)** significant amplitudes of lateral accelerations (maximum values), by inputs: LWL, B, XF, CM, GM

## ASSESSMENT OF THE ELABORATED DESIGN GUIDELINES

As results from Tab. 2, the relations (1), (2), (3), (4) and (5) are characterized by relatively high accuracy of approximation and low dispersion. The diagrams of Fig. 7 through 20 show comparison of accuracy of the formulas relative to their model values, as well as influence of the independent variables on approximation of the dependent variables. As results from Tab. 2 and the above mentioned diagrams all the relations are characterized by high correlation and low dispersion. Especially the relations (1) and (4) are characterized by high accuracy of approximation.

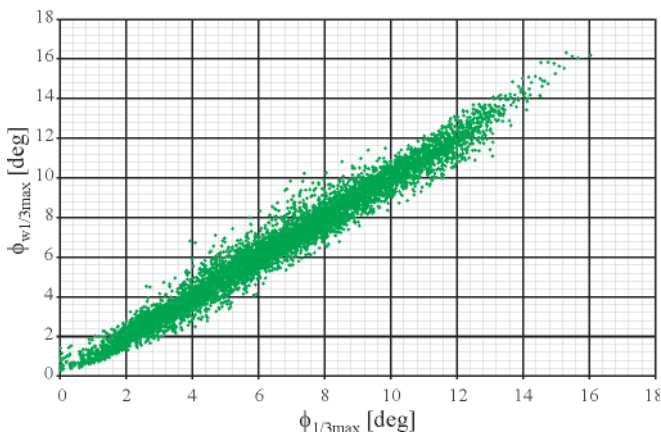


**Fig. 7.** Comparison of approximation accuracy relative to model values:  
 $\phi_{wl/3max}$  - model value of roll motion;  $\phi_{l/3max}$  - roll motion value approximated by using Eq. (1)

**Tab.2.** Selected regression statistics

	Eq.(1)	Eq. (2)	Eq. (3)	Eq.(4)	Eq.(5)
<b>Pearson regression coefficient R</b>	0.976	0.891	0.93	0.98	0.91
<b>Standard deviation of error</b>	0.48°	1.03°	4.25 [%]	0.06 m/s <sup>2</sup>	0.3 m/s <sup>2</sup>

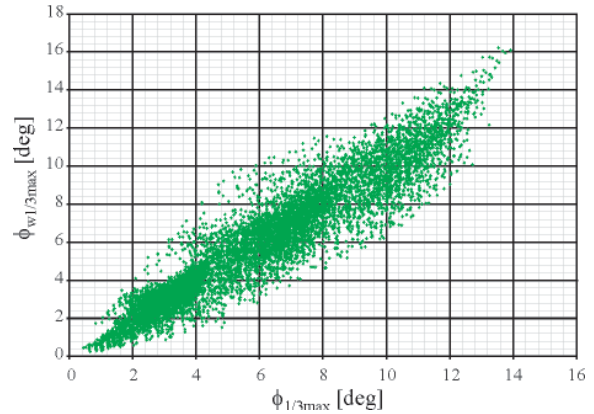


**Fig. 8.** Comparison of approximation accuracy relative to model values:  
 $\phi_{wl/3max}$  - model value of roll motion;  $\phi_{l/3max}$  - roll motion value approximated by using Eq. (2)

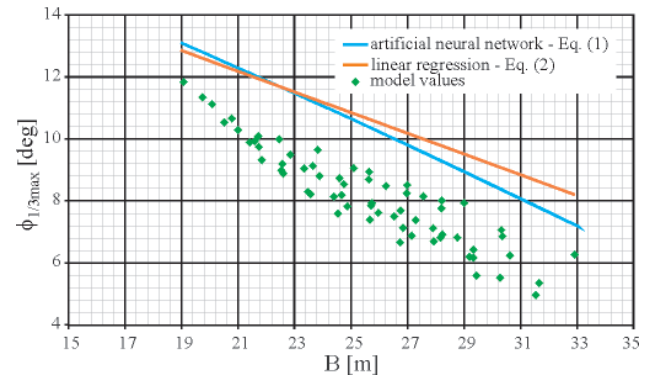


**Fig. 9.** Comparison of approximation accuracy relative to model values:  
 $B = \text{var}$ ;  $CB = 0.61$ ,  $GM = 0.8 \text{ m}$ ,  $H_s = 3 \text{ m}$

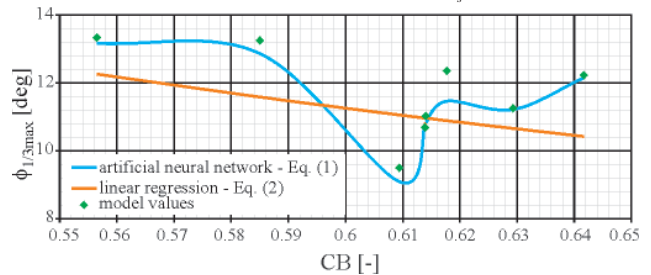


**Fig. 10.** Comparison of approximation accuracy relative to model values:  
 $CB = \text{var}$ ;  $B = 21.6 \text{ m}$ ,  $GM = 1.0 \text{ m}$ ,  $H_s = 3 \text{ m}$

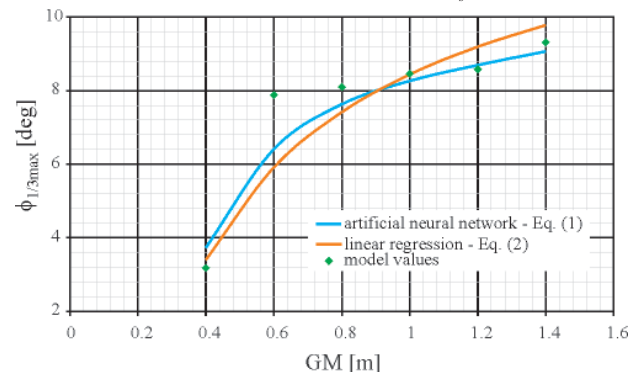


**Fig. 11.** Comparison of approximation accuracy relative to model values:  
 $GM = \text{var}$ ;  $B = 29.0 \text{ m}$ ,  $CB = 0.63$ ,  $H_s = 3 \text{ m}$

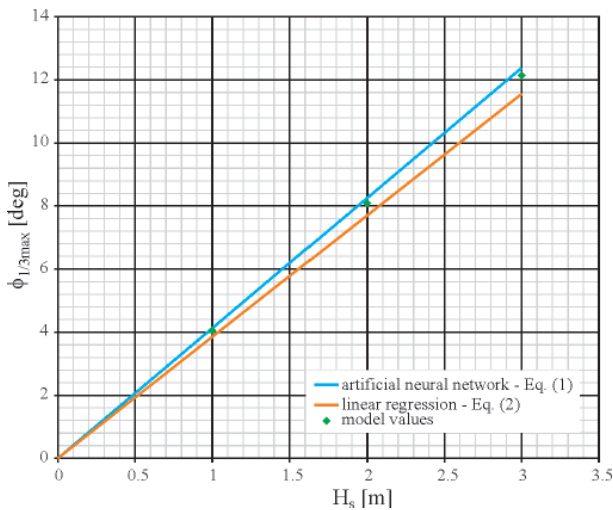


Fig. 12. Comparison of approximation accuracy relative to model values:  $H_s = \text{var}$ ,  $B = 21.42 \text{ m}$ ,  $CB = 0.56$ ,  $GM = 0.8 \text{ m}$

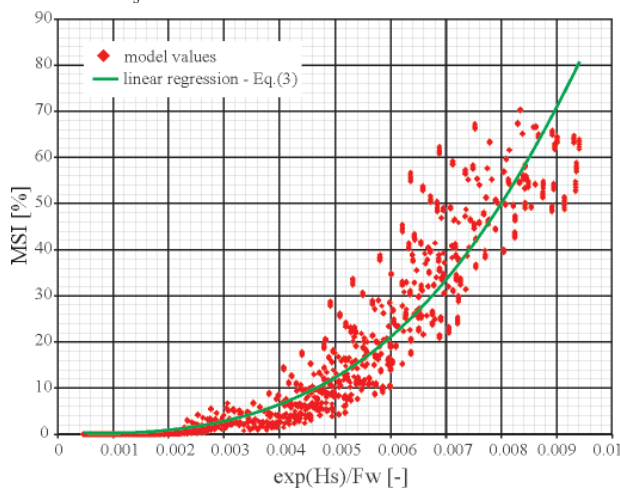


Fig. 13. Comparison of approximation accuracy of the MSI relative to model values

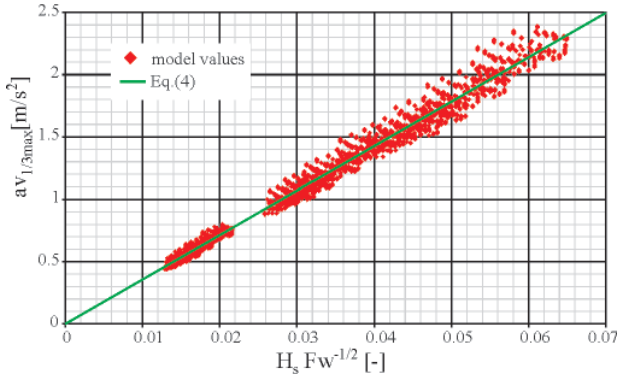


Fig. 14. Comparison of approximation accuracy of vertical accelerations relative to model values

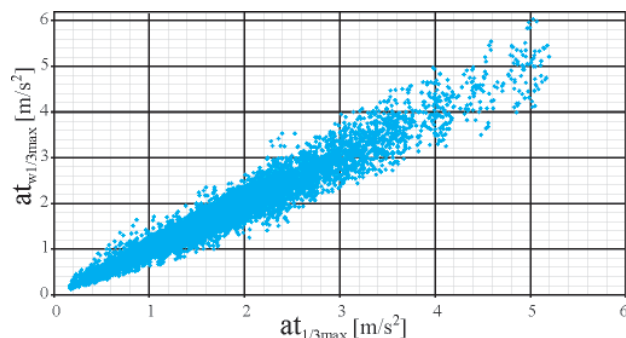


Fig. 15. Comparison of approximation accuracy of lateral accelerations relative to model values:  $at_{wl/3max}$  - model value of significant amplitudes of lateral accelerations,  $at_{1/3max}$  - value of significant amplitudes of lateral accelerations, approximated by means of Eq. (5)

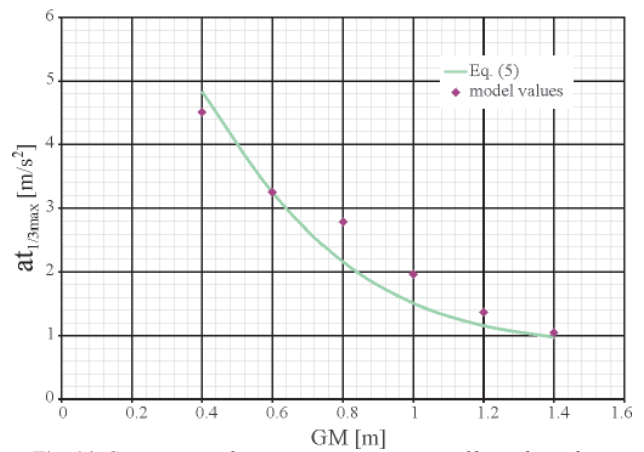


Fig. 16. Comparison of approximation accuracy of lateral accelerations relative to model values:  $GM = \text{var}$ ,  $Lwl/B = 6.22$ ,  $CM = 0.97$ ,  $H_s = 3 \text{ m}$

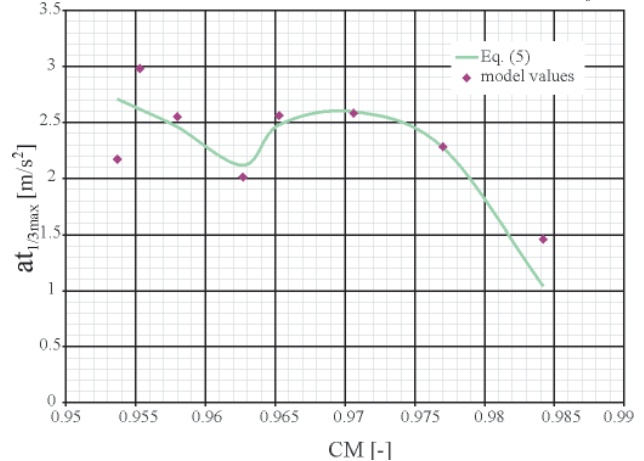


Fig. 17. Comparison of approximation accuracy of lateral accelerations relative to model values:  $CM = \text{var}$ ,  $Lwl/B = 7.4$ ,  $GM = 0.8 \text{ m}$ ,  $H_s = 3 \text{ m}$

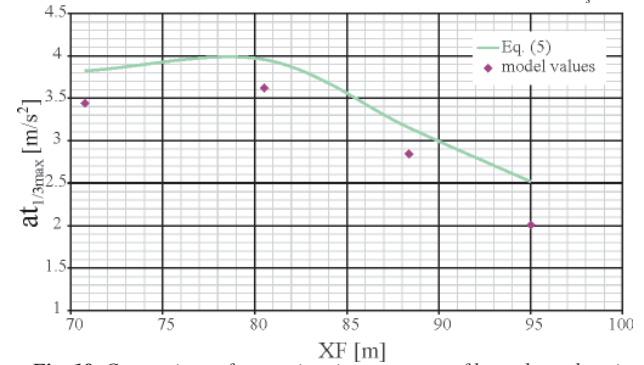


Fig. 18. Comparison of approximation accuracy of lateral accelerations relative to model values:  $XF = \text{var}$ ,  $Lwl/B = 7.4$ ,  $CM = 0.95$ ,  $GM = 0.6 \text{ m}$ ,  $H_s = 3 \text{ m}$

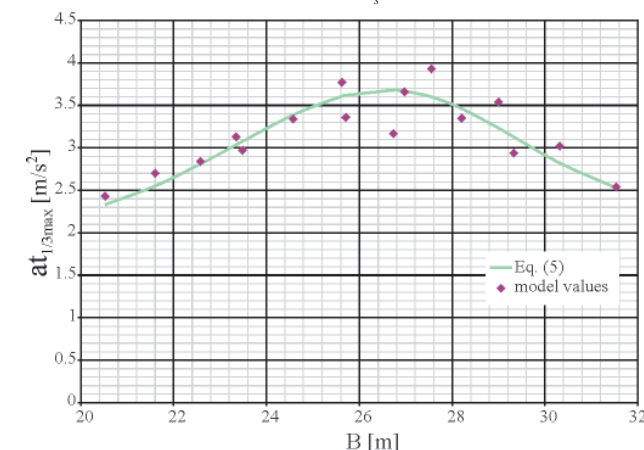
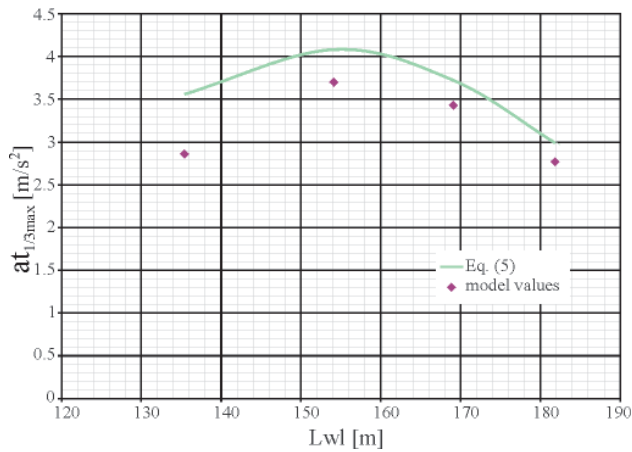


Fig. 19. Comparison of approximation accuracy of lateral accelerations relative to model values:  $B = \text{var}$ ,  $Lwl/B = 7.0$ ,  $CM = 0.97$ ,  $GM = 0.8 \text{ m}$ ,  $H_s = 3 \text{ m}$



**Fig. 20.** Comparison of approximation accuracy of lateral accelerations relative to model values:  $Lwl = var$ ;  $Lwl/B = 6.6$ ,  $CM = 0.95$ ,  $GM = 0.6 m$ ,  $H_s = 3 m$

## RANGE OF APPLICATIONS AND LIMITATIONS OF THE ELABORATED RELATIONS

The elaborated design guidelines may find application to design calculations of the passenger-car ferries:

- of parameters and hull forms consistent with the ranges used for the model variants,
- intended to operate in the assumed service conditions.

With taking into account the first group of the above mentioned limitations, the relations (1), (2), (3), (4) and (5) can be especially used for design calculations of passenger-car ferries of the following dimensions and parameters:

1.  $LBd = 19\ 000 \div 46\ 000\ m^3$
2.  $L/B = 5.8 \div 8.2$
3.  $B/d = 3 \div 4.5$
4.  $CB = 0.56 \div 0.64$
5.  $CWL = 0.75 \div 0.85$
6.  $LWL = 124 \div 258\ m$
7.  $B = 19 \div 33\ m$
8.  $CM = 0.95 \div 0.98$
9.  $XF = 55.2 \div 117.6\ m$
10.  $Fw = 2\ 100 \div 6\ 000\ m^2$ .

## CONCLUSIONS

- The elaborated design guidelines can be applied to preliminary ship design as target functions or technical limitations.

- If recommended limit values of the presented sea-keeping qualities are known limit values of ship design parameters can be determined. For instance, to keep MSI value below 20% is recommended according to [6]. And, by making use of Eq. (3) the limit area of waterplane can be calculated depending on the significant wave height  $H_s$ .
- The elaborated relations are characterized by different levels of complexity and approximation accuracy. Eqs. (1) and (5) are of the most complex structure (they were elaborated with the use of artificial neural networks), but simultaneously they show the highest approximation accuracy.
- All the relations are based on the data available in the preliminary stage of ship design process.

## BIBLIOGRAPHY

1. Dudziak J.: *Ship theory* (in Polish). Fundacja Promocji POiGM (Ship Industry & Maritime Economy Promotion Foundation), Gdańsk 2008
2. Journée J.M.J.: *Verification and Validation of Ship Motions Program SEAWAY*. Report1213a, Delft University of Technology, The Netherlands, 2001
3. Frank W.: *Oscillation of Cylinders in or below the Free Surface of Deep Fluids*. Technical Report 2375, Naval Ship Research and Development Centre, Washington DC, U.S.A., 1967
4. BALTIC GATEWAY Report: *Future trends in the design of ro-ro and ro-pax vessels operating in the southern Baltic.*, Sea Highways Ltd, 2005
5. Kobyliński L.: *Goal-based stability standards*. Proceedings of the 9th International Ship Stability Workshop, Germanischer Lloyd Operating 24/7, Hamburg 2007
6. Riola J.M., M.Garcia de Arboleya: *Habitability and personal space in sea-keeping behaviour*. Journal of Maritime Research, Vol III, No 1, 2006
7. Schneekluth H., Bertram V.: *Ship Design for Efficiency and Economy*. Butterworth-Heinemann, 1998
8. Szozda Z.: *A concept of Ship Stability Criteria Based on Cargo Shift Caused by Rolling due to Gust*. Zeszyty Naukowe (Scientific Bulletin) No. 2(74), Szczecin Maritime University, Szczecin 2004.

## CONTACT WITH THE AUTHOR

Tomasz Cepowski, Assoc. Prof.  
Institute of Marine Navigation,  
Maritime University of Szczecin  
Wały Chrobrego 1/2  
70-500 Szczecin, POLAND  
e-mail: cepowski@am.szczecin.pl

# State equations in the mathematical model of dynamic behaviour of multihull floating unit

Agnieszka Królicka, M. Sc.  
Gdansk University of Technology

## ABSTRACT



*This paper concerns dynamic behaviour of multihull floating unit of catamaran type exposed to excitations due to irregular sea waves. Dynamic analysis of multihull floating unit necessitates, in its initial stage, to determine physical model of the unit and next to assume an identified mathematical model. Correctly elaborated physical models should contain information on the basis of which a mathematical model could be built. Mathematical models describe mutual relations between crucial quantities which characterize a given system in time domain. The dynamic analysis of multihull unit was performed under assumption that the unit's model has been linear and exposed to action of irregular sea waves. Mathematical model of such dynamic system is represented by state equations. The formulated equations take into account encounter of head wave which generates symmetrical motions of the unit, i.e. surge, heave and pitch. For solving the equations the following three wave spectra were taken into consideration:*

- ISSC (International Ship Structures Congress) spectrum
- Pierson-Moskowitz spectrum
- Paszkiewicz spectrum.

**Keywords:** dynamics of multihull floating unit, sea waves, stochastic processes, wave spectra

## INTRODUCTION

Motion of a dynamic system can be generated by different external or internal factors. At mathematical modelling external excitation factors of the most significant effect on the system, are selected. Such external factors are usually called excitations. Response of the system to given excitations is mathematically characterized by a definite transformation called operator of a system. For a broad class of dynamic systems the relation between excitations and response is characterized by differential equations of motion. The equations can be linear or non-linear, of constant or varying coefficients, ordinary or differential, deterministic or stochastic ones. The mathematical models used for practical applications almost always necessitate to simplify the equations which form a given model. It amounts mainly to lowering their order by forming partial models and time – local ones with an assumed practical accuracy. Dynamic mechanical systems which represent floating objects are tightly associated with stochastic processes. State variables and input parameters of the models are of probabilistic character. Mathematical models of such systems are represented by sets of stochastic differential equations, and form sets of Itô It equations. Multihull units such as catamarans and trimarans belong to complex, highly non-linear dynamic systems. If dynamic system model is of floating unit's linear system then the equations:

$$\sum_{i,j=1}^6 I_{ij} \ddot{\eta}_i + B_{ij} \dot{\eta}_i + C_{ij} \eta_i = F_i(t) \quad (1)$$

where:

- I = M + A – inertia matrix
- M – elements of matrix of generalized masses of structures
- A – elements of matrix of generalized hydrodynamic added masses
- B – hydrodynamic damping matrix
- C – hydrostatic stiffness matrix
- $\eta$  – generalized displacement vector
- F(t) – vector of exciting forces and moments

can be analyzed as a set of two mutually non-coupled groups of mutually coupled equations. It is assumed that the coupling takes place by linear and non-linear damping coefficients and hydrostatic stiffness coefficients.

In these considerations the examined object is taken as a linear dynamic system of six degrees of freedom.

Among them are the following:

- translational oscillations:

- a) surging –  $\eta_1$
- b) swaying –  $\eta_2$
- c) heaving –  $\eta_3$

- angular oscillations:

- d) rolling –  $\eta_4$
- e) pitching –  $\eta_5$
- f) yawing –  $\eta_6$

The catamaran-fixed coordinate frame is shown in Fig. 1.

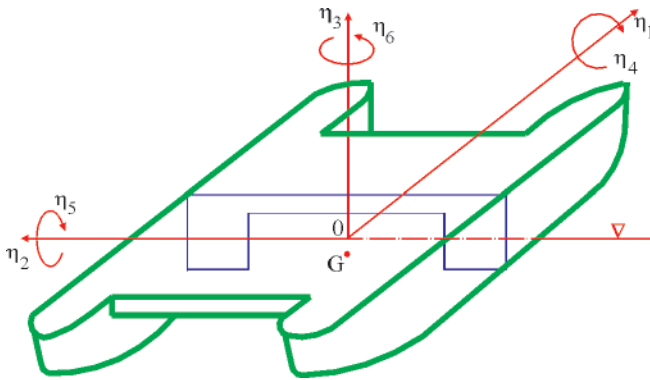


Fig. 1. Schematic diagram of physical model of catamaran

Local motions of the unit constitute its response to sea-wave-induced excitations. To the first group belong the equations which describe the symmetrical motions:  $\eta_1, \eta_3, \eta_5$ . The second group is formed by the equations which describe the anti-symmetrical motions:  $\eta_2, \eta_4, \eta_6$ . Constructional reasons (symmetry) of multihull floating units make it possible to analyze group-coupled motions of the object and in consequence to limit number of state variables which appear in the equations.

### SET OF STATE EQUATIONS

State equations are one of the possible ways for representing mathematical model of a dynamic system. An alternative way to describe a dynamic system is transmittance in which the initial state is assumed equal to zero.

The operator transmittance, otherwise called the transfer function  $G(s)$ , is ratio of output signal Laplace transform and input signal Laplace transform of the system in zero initial conditions. The transmittance describes general features of a stationary linear system of one input and one output, depending on a kind of excitation. For the systems described by linear differential equations of constant coefficients the transmittance is rational function of the complex variable  $s$ , which can be represented by the quotient of two polynomials (2).

To determine the set of state equations the following assumptions have been applied:

- 1) resultant motion of the object on an irregular wave is formed by superposing its motions in regular waves
- 2) only encounter of the head wave which generates only the motions: surging  $\eta_1$ , heaving  $\eta_3$  and pitching  $\eta_5$ , is taken into consideration
- 3) it is assumed that the response of the object, in the form of the generalized wave-generated forces  $F_i$  ( $i = 1, 3, 5$ ), to excitation due to the wave of the height  $\xi(t)$ , can be approximated by means of a system whose transmittance is of the form:

$$\frac{F(s)}{\xi(s)} = \frac{b_0 s^2 + b_1 s + b_2}{s^2 + a_1 s + a_2} \quad (2)$$

where:

$$F(F_1, F_3, F_5) \\ b_0(b_{01}, b_{03}, b_{05}), b_1(b_{11}, b_{13}, b_{15}), b_2(b_{21}, b_{23}, b_{25}) \\ a_1(a_{11}, a_{13}, a_{15}), a_2(a_{21}, a_{23}, a_{25}).$$

The relation (2) can be written by using the following set of state equations:

$$\begin{aligned} \dot{f}_1 &= F - h_0 \xi \\ \dot{f}_2 &= \dot{F} - h_0 \dot{\xi} - h \xi_1 \end{aligned} \quad (3)$$

$$\left. \begin{aligned} \dot{f}_1 &= f_2 + h_1 \xi \\ \dot{f}_2 &= -a_2 f_1 - a_1 f_2 + h_2 \xi \end{aligned} \right\} \quad (4)$$

where:

$h_0, h_1, h_2$  – constants defined by the coefficients of the equation (2)

$$f_1(f_{11}, f_{13}, f_{15}), f_2(f_{21}, f_{23}, f_{25}) \\ h_0(h_{01}, h_{03}, h_{05}), h_1(h_{11}, h_{13}, h_{15}), h_2(h_{21}, h_{23}, h_{25}).$$

To obtain random process of the irregular wave height  $\xi(t)$  the well-known energy (wave) spectra of the wave which encounters the object, can be used:

$$\phi_{\xi\xi}(\omega) = \left\{ \begin{aligned} &\text{e.g. Pierson - Moskowitz spectrum} \\ &\text{or ISSC spectrum} \end{aligned} \right. \quad (5)$$

The selected spectrum is approximated by means of the spectral density function in the form:

$$g(\omega) = \frac{C\omega^2}{\omega^4 - 2V\omega_0^2\omega^2 + \omega_0^4} \quad (6)$$

Then, the shape filter is introduced by making use of the following assumptions:

1. In both the spectra, i.e.(5) and (6), their maxima appear at the same frequency and are of the same value
2.  $\int_0^{\infty} \phi_{\xi\xi}(\omega) d\omega = \int_0^{\infty} g(\omega) d\omega$
3. The wave height processes are generated by the transfer function  $G(s)$  which constitutes the so-called shape filter if „white noise” is at input.

The transfer function  $G(s)$  is given by the relation:

$$G(s) = \frac{a_0 s}{s^2 + a_1 s + a_2} \quad (7)$$

The relation (7) corresponds to the following set of state equations:

$$\left. \begin{aligned} g_1 &= \xi \\ g_2 &= \dot{\xi} - a_0 W \end{aligned} \right\} \quad (8)$$

$$\left. \begin{aligned} \dot{g}_1 &= g_2 + a_0 W \\ \dot{g}_2 &= -a_2 g_1 - a_1 g_2 - a_0 a_1 W \end{aligned} \right\} \quad (9)$$

where:

$W$  - „white noise”

$\xi(t)$  - wave height process.

The above given matrix (Tab. 1) can be written in the general form of Itô equation:

$$\dot{X} = \tilde{A}X + \tilde{B}W \quad (10)$$

From the matrix the following is obtained:

$$\left. \begin{aligned} \dot{f}_{11} &= f_{21} \\ \dot{f}_{21} &= -a_{21} f_{11} - a_{11} f_{21} \\ \dot{f}_{13} &= f_{23} \\ \dot{f}_{23} &= -a_{23} f_{13} - a_{13} f_{23} \\ \dot{f}_{15} &= f_{25} \\ \dot{f}_{25} &= -a_{25} f_{15} - a_{15} f_{25} \\ \dot{g}_1 &= g_2 + a_0 W \\ \dot{g}_2 &= -a_2 g_1 - a_1 g_2 - a_0 a_1 W \end{aligned} \right\} \quad (11)$$

Tab. 1. Matrix of state equations

$\dot{q}_1$	0	0	0	1			0	0	0	0	0	0	0	0	$q_1$	0	
$\dot{q}_3$	0	0	0		1		0	0	0	0	0	0	0	0	$q_3$	0	
$\dot{q}_5$	0	0	0			1	0	0	0	0	0	0	0	0	$q_5$	0	
$\dot{q}_1$	$[-\frac{C}{A}]$			$[-\frac{B}{A}]$			$[\frac{D}{A}]$							$[\frac{E}{A}]$		$\dot{q}_1$	0
$\ddot{q}_3$	$[-\frac{C}{A}]$			$[-\frac{B}{A}]$			$[\frac{D}{A}]$							$[\frac{E}{A}]$		$\dot{q}_3$	0
$\ddot{q}_5$	$[-\frac{C}{A}]$			$[-\frac{B}{A}]$			$[\frac{D}{A}]$							$[\frac{E}{A}]$		$\dot{q}_5$	0
$\dot{f}_{11}$	0	0	0	0	0	0	0	1	0	0	0	0	0	0	$f_{11}$	0	
$\dot{f}_{21}$	0	0	0	0	0	0	-a <sub>21</sub>	-a <sub>11</sub>		0	0	0	0	0	$f_{21}$	0	
$\dot{f}_{13}$	0	0	0	0	0	0	0	0	0	1	0	0	0	0	$f_{13}$	0	
$\dot{f}_{23}$	0	0	0	0	0	0	0	0	-a <sub>23</sub>	-a <sub>13</sub>	0	0	0	0	$f_{23}$	0	
$\dot{f}_{15}$	0	0	0	0	0	0	0	0	0	0	0	1	0	0	$f_{15}$	0	
$\dot{f}_{25}$	0	0	0	0	0	0	0	0	0	0	-a <sub>25</sub>	-a <sub>15</sub>	0	0	$f_{25}$	0	
$\dot{g}_2$	0	0	0	0	0	0	0	0	0	0	0	0	0	1	$g_1$	a <sub>0</sub>	
$\dot{g}_2$	0	0	0	0	0	0	0	0	0	0	0	0	-a <sub>2</sub>	-a <sub>1</sub>	$g_2$	-a <sub>0</sub> a <sub>1</sub>	

where:

$$I_{ij} = \begin{bmatrix} I_{11} & I_{13} & I_{15} \\ I_{31} & I_{33} & I_{35} \\ I_{51} & I_{53} & I_{55} \end{bmatrix} \quad I^{-1} = \frac{1}{|I|} I^D \quad |I| = \det I \quad E = \begin{bmatrix} h_{01} & 0 \\ h_{03} & 0 \\ h_{05} & 0 \end{bmatrix} \quad D = \begin{bmatrix} 1 & 0 & 0 & 0 & 0 \\ 0 & 0 & 0 & 0 & 0 \\ 0 & 0 & 0 & 1 & 0 \end{bmatrix} \quad B_{ij} = \begin{bmatrix} b_{11} & b_{13} & b_{15} \\ b_{31} & b_{33} & b_{35} \\ b_{51} & b_{53} & b_{55} \end{bmatrix} \quad C_{ij} = \begin{bmatrix} c_{11} & 0 & 0 \\ 0 & c_{33} & c_{35} \\ 0 & c_{53} & c_{55} \end{bmatrix}$$

The parameters  $\ddot{q}_1, \ddot{q}_2, \ddot{q}_3$  can be determined after finding and solving the particular coefficients of damping, hydrostatic stiffness as well as inertia ones.

Now  $\omega$  - value at which the extremum appears, is determined, i.e.:

$$g(\omega) = \frac{C\omega^2}{\omega^4 - D\omega^2 + E} \quad (16)$$

$$\frac{\partial}{\partial \omega} [\phi(\omega)] = \frac{\partial}{\partial \omega} [g(\omega)] \quad (17)$$

From the condition that extremum is present in the same point the following is obtained:  
i.e. the first equation:

$$\left(\frac{4B}{5}\right)^{\frac{1}{4}} = E^{\frac{1}{4}} \text{ so } E = \frac{4}{5}B \quad (18)$$

From the second assumption that:

$$\phi(\omega) = g(\omega)$$

$$\left| \omega = \left(\frac{4}{5}B\right)^{\frac{1}{4}} \right| \quad \left| \omega = E^{\frac{1}{4}} \right|$$

the following is obtained:  
i.e. the second equation:

$$\frac{5A\sqrt[4]{5}}{4B\sqrt[4]{4B}} e^{\frac{4}{5}} = \frac{C}{2\sqrt{E-D}} \quad (19)$$

### EXAMPLE SOLUTIONS FOR THE SELECTED WAVE SPECTRA

#### 1 ISSC wave spectrum

$$\phi(\omega) = \frac{A}{\omega^5} \exp\left(-\frac{B}{\omega^4}\right) \quad (12)$$

where:

$$\left. \begin{aligned} B &= 691 \left(\frac{2\pi}{\omega_1}\right)^{-4} \\ A &= 173h_{1/3}^2 \left(\frac{2\pi}{\omega_1}\right)^{-4} \end{aligned} \right\} \quad (13)$$

The wave spectrum is approximated by means of the spectral density function of the following form:

$$g(\omega) = \frac{C\omega^2}{\omega^4 - 2v\omega_0^2\omega^2 + \omega_0^4} \quad (14)$$

Let it be:

$$\left. \begin{aligned} 2v\omega_0^2 &\equiv D \\ \omega_0^4 &\equiv E \end{aligned} \right\} \quad (15)$$

and the third equation

$$\int_0^{\infty} \frac{C\omega^2}{\omega^4 - D\omega^2 + E} d\omega = \int_0^{\infty} \frac{A}{\omega^5} \exp\left(-\frac{B}{\omega^4}\right) d\omega \quad (20)$$

From the right-hand side of the Eq. (20):

$$\int_0^{\infty} \frac{A}{\omega^5} \exp\left(-\frac{B}{\omega^4}\right) d\omega = A \int_0^{\infty} \omega^{-5} \exp\left(-\frac{B}{\omega^4}\right) d\omega \quad (21)$$

by substituting:

$$\begin{aligned} \omega^{-4} &\equiv t \\ -4\omega^{-5} d\omega &\equiv dt \Rightarrow d\omega = -\frac{1}{4}\omega^5 dt \end{aligned}$$

the following is achieved:

$$\begin{aligned} &A \int_0^{\infty} \omega^{-5} \exp(-Bt) \left[-\frac{1}{4}\omega^5 dt\right] = \\ &= -\frac{A}{4} \int_0^{\infty} \exp(-Bt) dt = \frac{A}{4B} e^{-Bt} \Big|_0^{\infty} = -\frac{A}{4B} \end{aligned} \quad (22)$$

The left-hand side of Eq. (20) is of the form:

$$\int_0^{\infty} \frac{C\omega^2}{c\omega^4 - b\omega^2 + a} d\omega \quad (23)$$

in which „C” means „white noise”, and the coefficients a, b, c are equal to:

$$\left. \begin{aligned} b &= 2v\omega_0^2 \\ a &= \omega_0^4 \\ c &= 1 \end{aligned} \right\} \quad (24)$$

After solving the above given integral the final solution is achieved as follows:

$$\begin{aligned} &\int_0^{\infty} \frac{C\omega^2}{\omega^4 - D\omega^2 + E} d\omega = \\ &= \frac{-C\pi}{2\omega_0 \left[ (v - \sqrt{v^2 - 1})^{\frac{1}{2}} + (v + \sqrt{v^2 - 1})^{\frac{1}{2}} \right]} \end{aligned} \quad (25)$$

By comparison of the left hand side and right hand side (the third equation) the following is obtained:

$$-\frac{A}{4B} = \frac{-C\pi}{2\omega_0 \left[ (v - \sqrt{v^2 - 1})^{\frac{1}{2}} + (v + \sqrt{v^2 - 1})^{\frac{1}{2}} \right]} \quad (26)$$

This way the third, lacking equation for the unknowns C, v,  $\omega_0$ , has been achieved.

The first assumption (Eq. (18)) yields the following:

$$E \equiv a = \omega_0^4 = \frac{4}{5}B \Rightarrow \omega_0^2 = \pm \sqrt{\frac{4B}{5}} \quad (27)$$

The second equation (Eq. (19)) yields the relation:

$$\frac{5A}{4B} \left(\frac{5}{4B}\right)^{\frac{1}{4}} e^{\frac{4}{5}} = \frac{C}{2\sqrt{E-D}} \quad (28)$$

By introducing the following substitution:

$$\left. \begin{aligned} D &\equiv b = 2v\omega_0^2 \\ E &\equiv \omega_0^4 \end{aligned} \right\} \quad (29)$$

the relation is achieved:

$$\frac{5A}{4B} \left(\frac{5}{4B}\right)^{\frac{1}{4}} \cdot e^{\frac{4}{5}} = \frac{C}{2\omega_0^2(1-v)} \quad (30)$$

The constants A and B are equal to:

$$\left. \begin{aligned} B &\equiv 691 \left(\frac{2\pi}{\omega_1}\right)^{-4} \\ A &\equiv 173h_s^2 \left(\frac{2\pi}{\omega_1}\right)^{-4} \end{aligned} \right\} \quad (31)$$

From Eq. (30) is obtained the quantity C expressed as follows:

$$C = \frac{2A(1-v)}{\omega_0^3 \cdot e^{5/4}} \quad (32)$$

From Eq. (26) is determined the quantity C equal to:

$$C = \frac{2A\omega_0}{4\pi B} \left[ (v - \sqrt{v^2 - 1})^{\frac{1}{2}} + (v + \sqrt{v^2 - 1})^{\frac{1}{2}} \right] \quad (33)$$

Next the right hand sides of the above given equations are compared to each other to get the equation for determining the unknown „v”.

$$\left. \begin{aligned} v_1 &= 1 + \frac{1}{L^2} + \frac{\sqrt{4L^2 + 1}}{L^2} \\ v_2 &= 1 + \frac{1}{L^2} - \frac{\sqrt{4L^2 + 1}}{L^2} \end{aligned} \right\} \quad (34)$$

Now the quantity L = 4.500406826 and its square  $L^2 = 20.2536616$  is determined.

Hence:

$$\left. \begin{aligned} v_1 &= 1.496512384 \\ v_2 &= 0.602235192 \end{aligned} \right\} \quad (35)$$

By substituting  $v_1$  the following is obtained:

$$a_2 = 0.596\omega_1^2 \quad (36)$$

$$C \cong -0.068635565h_s^2 \cdot \omega_1 \quad (37)$$

$$\left. \begin{aligned} a_0 &= \sqrt{C} \cong 0.261983903h_s \sqrt{\omega_1} \\ a_1 &= \omega_0 \sqrt{2(1-v)} = \\ &= 0.772010362\omega_1 \cdot 0.996506281 \cong \\ &\cong 0.769313175\omega_1 \end{aligned} \right\} \quad (38)$$

By substituting  $v_2$  the following is obtained:

$$C = \frac{137.6266236}{2502.977614} = 0.054985159h_s^2 \cdot \omega_1 \quad (39)$$

$$\left. \begin{aligned} a_0 &= \sqrt{C} \cong 0.234489144h_s \sqrt{\omega_1} \\ a_1 &= 0.772010362\omega_1 \cdot 0.891924669 \cong \\ &\cong 0.688575087\omega_1 \end{aligned} \right\} \quad (40)$$

## 2. Pierson-Moskowitz wave spectrum

$$\phi = \frac{A}{\omega^5} e\left(-\frac{B}{\omega^4}\right) \quad (41)$$

$$\left. \begin{aligned} T_1 &= 0.771T_0 \\ T_2 &= 0.92T_1 \end{aligned} \right\} \quad (42)$$

$$A = \frac{1}{8\pi^2} \left(\frac{2\pi}{T_2}\right)^5 = \frac{1}{8\pi^2} \left(\frac{2\pi}{0.92T_1}\right)^5 = \frac{1}{8\pi^2 (0.92)^5} \left(\frac{2\pi}{T_1}\right)^5 = 188.17 \quad (43)$$

$$B = \frac{1}{\pi} \left(\frac{2\pi}{T_1}\right)^4 = 496.1$$

On the assumption that:  $L = 4.500406826$  and  $v_1 = 1.496512384$ ,  $v_2 = 0.602235192$ , value of the constant  $C$  is calculated:

$$C = \frac{188.1787h_s^2 \cdot 0.71037\omega_1 \cdot 2.234507723}{2\pi \cdot 496.1} = h_s^2 \cdot \omega_1 \cdot 0.095826987 \quad (44)$$

$$a_0 = \sqrt{C} = 0.309559344 \cdot h_s \cdot \sqrt{\omega_1} \quad (45)$$

$$\omega_0 = \sqrt[4]{\frac{4B}{5}} = 0.710370681\omega_1 \quad (46)$$

$$a_2 = \omega_0^2 = 0.504626504\omega_1^2 \quad (47)$$

$$a_1 = \omega_0 \sqrt{2(1-v)} = 0.996506281\omega_0 = 0.707888844\omega_1 \quad (48)$$

## 3. Paszkiewicz wave spectrum

$$A = 0.812 \cdot 10^{-3} \left(\frac{2\pi}{T_1}\right)^5 = 7.95 \quad (49)$$

$$B = 0.723 \left(\frac{2\pi}{T_1}\right)^4 = 1126.8$$

$$\omega_0 = \sqrt[4]{\frac{4B}{5}} = 0.760526133\omega_1 \quad (50)$$

$$a_2 = \omega_0^2 = 0.5784\omega_1^2 \quad (51)$$

$$a_1 = \omega_0 \sqrt{2(1-v)} = 0.99650628\omega_0 = 0.757869067\omega_1 \quad (52)$$

$$C = h_s^2 \cdot \omega_1 \cdot 1.9082547 \cdot 10^{-3} \quad (53)$$

$$a_0 = \sqrt{C} = 0.043683574 \cdot h_s \cdot \sqrt{\omega_1} \quad (54)$$

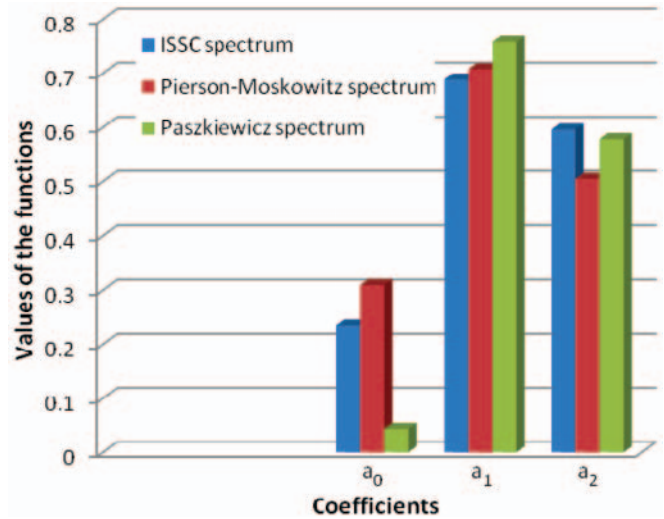


Fig. 2. Distribution of values of the coefficients for the selected wave spectra

Values of the functions for  $\omega_1 = 1$  and  $h_s = 1$ .

## CONCLUSIONS

- The coefficients  $a_0$ ,  $a_1$ ,  $a_2$  which appear in the shape filter (7) were determined. They were determined with taking into consideration the three wave spectra:
  - ISSC (International Ship Structures Congress) spectrum
  - Pierson-Moscowitz spectrum
  - Paszkiewicz spectrum
- The set of state equations which takes into account symmetrical motions of catamaran, was presented in the form of the matrix equation (given in Tab.2). They constitute the equations of dynamic behaviour of catamaran on irregular wave, called also Itô equations. The quantities  $\omega_0$ ,  $v$ ,  $C$  obtained from Eqs. (18 ÷ 20) made it possible to determine the coefficients  $a_0$ ,  $a_1$ ,  $a_2$ .
- Further continuation of the subject matter in question is aimed at achieving a solution of the elaborated matrix equation.

Tab. 2. Functional expressions for the coefficients of the selected wave spectra

Spectrum of	ISSC	Pierson-Moskowitz	Paszkiewicz
$C$	$h_s^2 \cdot \omega_1 \cdot 0.054985159$	$h_s^2 \cdot \omega_1 \cdot 0.095826987$	$h_s^2 \cdot \omega_1 \cdot 1.9082547 \cdot 10^{-3}$
$a_0$	$0.234489144h_s \sqrt{\omega_1}$	$0.309559344 \cdot h_s \cdot \sqrt{\omega_1}$	$0.043683574 \cdot h_s \cdot \sqrt{\omega_1}$
$a_1$	$0.688575087\omega_1$	$0.707888844\omega_1$	$0.757869067\omega_1$
$a_2$	$0.596\omega_1^2$	$0.504626504\omega_1^2$	$0.5784\omega_1^2$

## BIBLIOGRAPHY

1. Druet Cz.: *Sea dynamics* (in Polish). Wyd. Uniwersytetu Gdańskiego (Publ. of Gdańsk University), Gdańsk, 2000
2. Kang D., Hasegawa K.: *Prediction method of hydrodynamic forces acting on the hull of a blunt-body ship in the even keel condition*. Journal of Marine Science and Technology, vol. 12, no. 1, pp.1÷14, 2007
3. Królicka A.: *Multihull vessel excitations in stochastic formulation*, Polish Maritime Research, Gdańsk University of Technology, Faculty of Ocean Engineering & Ship Technology, no. 4, vol. 15, Gdańsk, 2008
4. Królicka A.: *Stochastic approach to movements of a multihull on waves*. Vibrations in physical systems, Vol.XXIII, pp. 217÷222, Poznań, 2008
5. Plucińska A., Pluciński E.: *Probabilistics, Probability calculus, Mathematical statistics, Stochastic processes* (in Polish). Wyd. Naukowo-Techniczne (Scientific Technical Publishing House), Warszawa, 2006
6. Rumianowski A.: *Research on dynamic behaviour of selected sea floating objects* (in Polish), Wyd. PG (Publishing House of Gdańsk University of Technology), Gdańsk, 2003
7. Sobczyk K.: *Stochastic differential equations* (in Polish), Warszawa, 1996
8. Sobczyk K., Spencer Jr.,B.F.: *Stochastic models of fatigue of materials* (in Polish). Wyd.Naukowo-Techniczne (Scientific Technical Publishing House), Warszawa, 1996.

---

### CONTACT WITH THE AUTHOR

Agnieszka Królicka, Ms. C.  
Faculty of Ocean Engineering  
and Ship Technology,  
Gdańsk University of Technology  
Narutowicza 11/12  
80-952 Gdańsk, POLAND  
e-mail: krag@pg.gda.pl  
phone: (58) 347-11-46

# Experimental verification of two-parametric models of fatigue characteristics by using the tests of S55J0 steel as an example

Bogdan Ligaj, Ph. D.  
Grzegorz Szala, Ph. D.  
University of Technology and Life Science, Bydgoszcz

## ABSTRACT

*This paper presents experimental verification of models of two-parametric fatigue characteristics  $N(\sigma_a, \sigma_m)$  on the basis of results of fatigue tests of specimens made of S355J0 steel. On the basis of comparative analysis of results of computations and fatigue life tests of the specimens, performed under constant amplitude sinusoidal loads of different cycle asymmetry ratios, the most versatile models were distinguished. The tests in question were carried out in the high-cycle fatigue range.*

**Keywords:** two-parametric models, fatigue characteristics, tests of S55J0 steel, computations, fatigue life tests, high-cycle fatigue range

## INTRODUCTION

Random loads commonly occur in service conditions of machines and devices including sea-going ships, ocean engineering objects, land road vehicles, aircrafts, heavy machines etc. From the point of view of mathematical theory of stochastic processes operational loads are non-stationary stochastic processes [1, 2], that makes direct application of the theory in question to calculating fatigue life of structural elements, difficult.

In practice fatigue life of structural elements is calculated in accordance with the schematic diagram shown in Fig. 1. As results from it, the following should be known to carry out fatigue calculations: service load spectrum and fatigue characteristics, as well as to assume an appropriate hypothesis of cumulating fatigue damage [3].

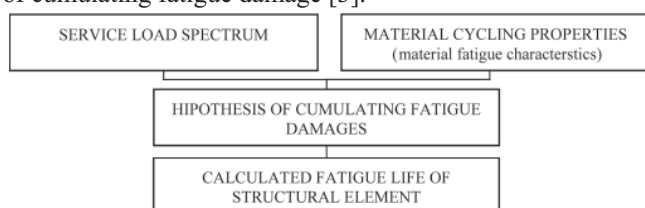


Fig. 1. Schematic diagram of calculation process of structural element fatigue life

In fatigue life calculations random run of service loads is usually substituted by a set of sinusoidal cycles determined in accordance with appropriate methods [4]. Their spectra can be described by means of distribution of load amplitude substitute values as in the case of broad-band random loads

—by distribution of  $S_a$  - amplitude values and  $S_m$  - mean values of cycles or  $S_{\min}$  - minimum values and  $S_{\max}$  - maximum values. Fig. 2 shows a scheme of possible cases of sinusoidal cycles having different parameters. The sinusoidal cycle is unambiguously described by the following parameters:  $S_{\min}$ ,  $S_{\max}$ ,  $f = 1/T$ , or  $S_a$ ,  $S_m$ ,  $f$ .

Influence of the load frequency  $f$  on fatigue life of structural elements is usually low and neglected in calculations of many elements. Location of a load cycle within the reference system ( $S_{\min}$ ,  $S_{\max}$ ) or ( $S_a$ ,  $S_m$ ) is determined by the cycle asymmetry ratio  $R = S_{\min}/S_{\max}$ , or sometimes – the load steadiness ratio  $\chi = S_m/S_a$ .

Load spectra are then elaborated in one of the two reference systems: ( $S_{\min}$ ,  $S_{\max}$ ) [5] or ( $S_a$ ,  $S_m$ ) [4, 6]. In such cases appropriate fatigue characteristics is that characterized by two parameters:  $N(S_a, S_m)$  or  $N(S_{\min}, S_{\max})$ .

In this paper the problem is discussed of experimental verification of selected two-parametric fatigue characteristics, performed on the basis of test results of specimens made of S355J0 steel.

## DESCRIPTION OF SELECTED TWO-PARAMETRIC FATIGUE CHARACTERISTICS

Concept of description of limit stress diagrams (fatigue limit range) with taking into account mean value of cycle amplitude was presented in [7]. The descriptions of range of limited fatigue life were presented in [8, 9, 10, 11, 12, 13].

In Tab. 1 are collected the formulae describing the above mentioned characteristics together with references to their

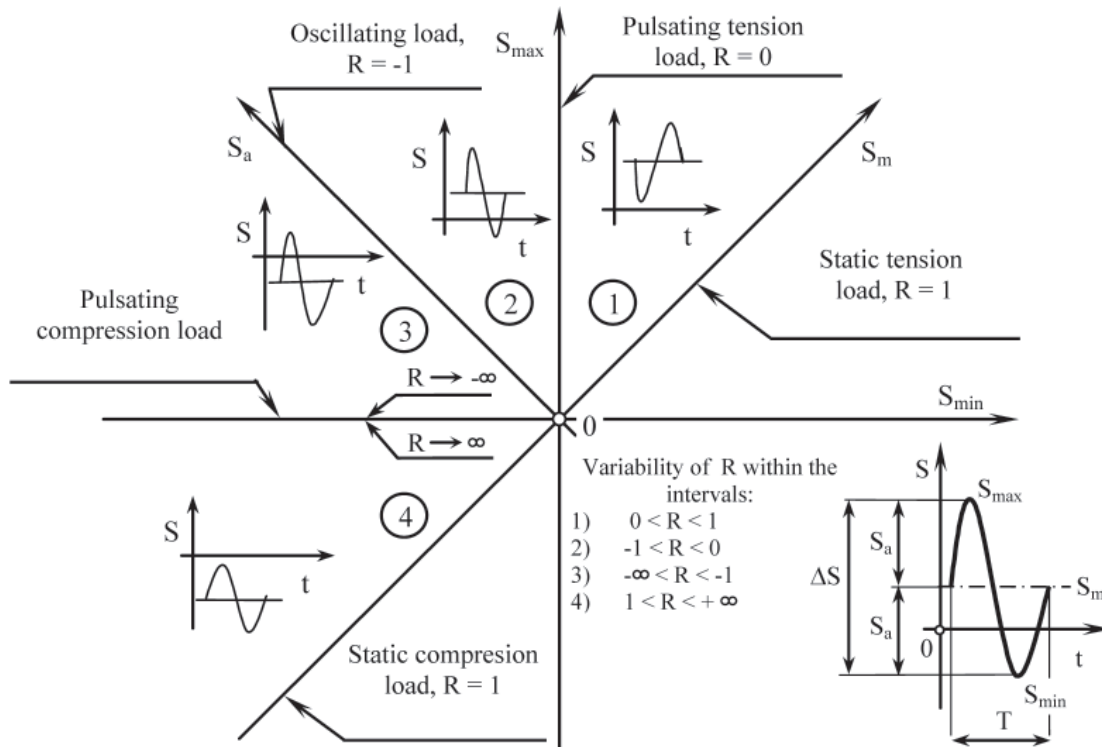


Fig. 2. Plane of variability of sinusoidal load parameters

literature sources. The formulae (4), (5) and (10) concern description of limit stresses within the range of fatigue limit called also the unlimited fatigue life (FL) ( $N \rightarrow \infty$ ) for steel. In practice it is assumed that it concerns the cycle number  $N > N_0$ , and  $N_0$  is the cycle number corresponding with the slope change point on Wöhler fatigue diagram. The remaining formulae: (1), (2), (6), (7), (8), (9), (11) and (12) deal with description within the high-cycle fatigue range (HCF), called also the limited fatigue life. The range is described by the conditions:

$$S_{\max} = S_a + S_m < R_m \quad \text{- for elastic-brittle materials}$$

$$S_{\max} = S_a + S_m \leq R_e \quad \text{- for elastic-plastic materials.}$$

In the first three positions of Tab 1. are given the relations corresponding with limit stress diagrams in the reference system ( $S_m, S_a$ ) for unlimited fatigue life ( $N \rightarrow \infty$ ). The simplest form of Goodman's relation, i.e. the formula (1), corresponds with straight line in the above mentioned reference system. Gerber's limit stress diagram, i.e. the formula (2), is of parabolic form. Haigh's diagram, i.e. the formula (3), is based on elliptic relationship.

The two-parametric fatigue characteristics analyzed in this paper constitute a generalized form of the above mentioned relations used for description of limit stress diagrams in the range of high-cycle fatigue (HCF), i.e. the limited fatigue life range. The relations are here shortly called models. The oldest is Heywood's model (H) described in the subject-matter literature [4, 8], which is used, in this paper, for comparison with the remaining models. The model I, an expanded form of Haigh's relation, consists of two straight line sections; the first of them corresponds with the variability range of the cycle asymmetry ratio  $R$  between 0 and 1, the second – between 0 and  $-\infty$ .

The diagram in the broken-line form crosses the three points: ( $S_a = 0; R_m$  or  $R_e$ ), ( $1/2 R_0^N; 1/2 R_0^N$ ) and ( $S_m = 0; R_{-1}^N$ ). The model II, a generalized form of Goodman's relation, covers, by single relation, the variability range of  $R$  from 1 to  $-\infty$ . The diagram lines of the model cross the two points: ( $S_a = 0; R_m$  or  $R_e$ ) and ( $S_m = 0; R_{-1}^N$ ).

The model III is an expansion of Gerber's relation [the formula (2)], and the model IV is an expansion of Haigh's relation [the formula (3)]. In both the above mentioned models the diagram lines cross the points: ( $S_a = 0; R_m$  or  $R_e$ ) and ( $S_m = 0; R_{-1}^N$ ).

The model V which connects features of the models: H, I and III, is based on parabolic relation where the parable crosses the three characteristic points as in the model I.

The last model, acc. Bołotin, is a transformation of the model I into the reference system ( $S_{\min}, S_{\max}$ ) and hence it has been not subjected to any detail analysis.

## EXAMPLE TWO-PARAMETRIC FATIGUE CHARACTERISTICS FOR S355J0 STEEL

Strength properties of S355J0 steel under monotonic loads is given in Tab. 2, and its cyclic properties – in Tab. 3.

Tab. 2. Static strength properties of S355J0 steel

	Static properties of S355J0 steel				
	$R_e$ [MPa]	$R_m$ [MPa]	E [MPa]	$A_5$ [%]	Z [%]
Mean value	499.9	678.0	208159	17.2	59.8
Standard deviation	8.4	7.1	1306	0.99	0.9

Tab. 3. Cyclic mechanical strength properties of S355J0 steel

Type of load	Equation form	Exponent	Free term	Fatigue limit	
				$R_f$	$N_0$
Oscillating load ( $R=-1$ )	$S_a^{m_0} \cdot N = C_0$	$m_0 = 12.33$	$C_0 = 1.156 \cdot 10^{36}$	$R_{-1} = 274$	$10^6$
Pulsating load ( $R=0$ )	$S_{\max}^m \cdot N = C$	$m = 15.92$	$C = 6.163 \cdot 10^{48}$	$R_0 = 480$	$10^6$

Tab. 1. Collection of the formulae which describe fatigue characteristics

No.	Name and form of formula	Application range Variability range R	Literat. source
1	2	3	4
1.	Fatigue diagram acc. Goodman $\frac{S_a}{R_{-1}} + \frac{S_m}{R_m} = 1 \quad (1)$	Range of fatigue limit (FL) $S_{az} \leq R_{-1}$	[14]
2.	Fatigue diagram acc. Gerber $\frac{S_a}{R_{-1}} + \left(\frac{S_m}{R_m}\right)^2 = 1 \quad (2)$	Range of fatigue limit FL $S_{az} \leq R_{-1}$	[7]
3.	Fatigue diagram acc. Haigh $\left(\frac{S_a}{R_{-1}}\right)^2 + \left(\frac{S_m}{R_m}\right)^2 = 1 \quad (3)$	Range of fatigue limit FL $-\infty < R \leq 1.0$	[14]
4.	Fatigue diagram acc. Heywood $\frac{S_a}{R_m} = \left(1 - \frac{S_m}{R_m}\right) [A_0 + \gamma(1 - A_0)] \quad (4)$ where: $A_0$ and $\gamma$ - constants determined with the use of smooth specimens: - for steel: $\gamma = \frac{S_m}{3R_m} \left(2 + \frac{S_m}{R_m}\right), A_0 = \frac{1 + 0.0038(\log N)^4}{1 + 0.008(\log N)^4}$ - for Al alloys: $\gamma = \frac{S_m}{R_m \left[1 + \frac{R_m(\log N)^4}{225}\right]}, A_0 = \frac{1 + 0.0031(\log N)^4}{1 + 0.0031(\log N)^4}$	Range of HCF for: - brittle materials $S_{max} = S_a + S_m \leq R_m$ - elastic-plastic materials $S_{max} = S_a + S_m \leq R_e$ $-\infty < R < 1.0$	[4] [8]
5.	Fatigue diagram acc. Szala (the model I) $N = \frac{N_0 R_{-1}^{m_0}}{(S_a + \psi_N S_m)^{m_0}} \quad (5)$ $N = N_0 \left[ \frac{R_{-1}(R_m + S_a - S_m)}{S_a R_m (1 + \psi_N)} \right]^{m_0} \quad (6)$ where: $\psi_N = 2C_0^{m_0} C^{-\frac{1}{m}} N^{\left(\frac{1}{m} - \frac{1}{m_0}\right)} - 1 \quad (7)$ Formulae (6) and (7) presented in another form: $\frac{S_a}{R_m} = -\psi_N \frac{S_m}{R_m} + \frac{R_{-1}}{R_m} \left(\frac{N_0}{N}\right)^{\frac{1}{m_0}} \quad (5a)$ $\frac{S_a}{R_m} = \frac{R_{-1}}{R_m \left(\frac{N}{N_0}\right)^{\frac{1}{m_0}} (1 + \psi_N) - R_{-1}} \left(1 - \frac{S_m}{R_m}\right) \quad (6a)$	Range of HCF: $-\infty < R \leq 0$ $0 < R \leq 1.0$ $-\infty < R \leq 0$ $0 < R \leq 1.0$	[9] [12]

Tab. 1. Collection of the formulae which describe fatigue characteristics

No.	Name and form of formula	Application range Variability range R	Literat. source
1	2	3	4
7.	<p>Fatigue diagram acc. Lipski (the model III)</p> $N = N_0 \left[ \frac{R_{-1}}{S_a} \left( 1 - \left( \frac{S_m}{R_m} \right)^2 \right) \right]^{m_0} \quad (9)$ <p style="text-align: center;">or</p> $\frac{S_a}{R_m} = \frac{R_{-1}}{R_m} \left( \frac{N_0}{N} \right)^{\frac{1}{m_0}} \left[ 1 - \left( \frac{S_m}{R_m} \right)^2 \right] \quad (9a)$	<p>Range of HCF:</p> $-\infty < R \leq 1.0$	[12]
8.	<p>Fatigue diagram acc. Lipski (the model IV)</p> $N = N_0 \left[ \frac{R_{-1}}{S_a} \sqrt{1 - \left( \frac{S_m}{R_m} \right)^2} \right]^{m_0} \quad (10)$ <p style="text-align: center;">or</p> $\frac{S_a}{R_m} = \frac{R_{-1}}{R_m} \left( \frac{N_0}{N} \right)^{\frac{1}{m_0}} \sqrt{1 - \left( \frac{S_m}{R_m} \right)^2} \quad (10a)$	<p>Range of HCF:</p> $-\infty < R \leq 1.0$	[12]
9.	<p>Fatigue diagram acc. Lipski (the model V)</p> $\frac{S_a}{R_m} = a_1 \left( \frac{S_m}{R_m} \right)^2 + a_2 \frac{S_m}{R_m} + \left( \frac{C_0}{N} \right)^{\frac{1}{m_0}} R_m^{-1} \quad (11)$ <p style="text-align: center;">where:</p> $a_1 = 2R_m \left[ \left( \frac{C}{N} \right)^{\frac{1}{m}} (1 - a_2) - 2 \left( \frac{C_0}{N} \right)^{\frac{1}{m_0}} \left( \frac{C_0}{N} \right)^{\frac{2}{m_0}} \right] \quad (12)$ $a_2 = \frac{4R_m^2 \left( \frac{C_0}{N} \right)^{\frac{1}{m_0}} - \left( \frac{C}{N} \right)^{\frac{1}{m}} \left[ 2R_m^2 + \left( \frac{C_0}{N} \right)^{\frac{1}{m_0}} \left( \frac{C}{N} \right)^{\frac{1}{m}} \right]}{R_m \left[ \left( \frac{C}{N} \right)^{\frac{1}{m}} - 2R_m \right] \left( \frac{C}{N} \right)^{\frac{1}{m}}} \quad (13)$	<p>Range of HCF:</p> $-\infty < R \leq 1.0$	[12]
10.	<p>Fatigue diagram acc. Bołotin</p> $N = \frac{2^{m_0} N_0 R_{-1}^{m_0}}{[(1 + \psi)S_{\max} - (1 - \psi)S_{\min}]^{m_0}} \quad (14)$ $N = \frac{2^{m_0} N_0 R_{-1}^{m_0}}{[(1 - \psi')S_{\max} - (1 + \psi')S_{\min}]^{m_0}} \quad (15)$ <p style="text-align: center;">where: <math>\psi</math> and <math>\psi'</math> - material constants (factors of material sensitivity to cycle asymmetry)</p>	<p>Range of HCF:</p> <p>for <math>S_{\max} + S_{\min} \geq 0</math></p> <p>for <math>S_{\max} + S_{\min} &lt; 0</math></p>	[13]
<p>Comments and basic formulae:                      Wöhler diagram for <math>R = -1</math>:                      - general form: <math>S_a^{m_0} \cdot N = C_0</math>                      - logarithmic form: <math>\log S_a = -\frac{1}{m_0} \log N + \log C_0</math>                      Wöhler diagram for <math>R = 0</math>:                      - general form: <math>S_{\max}^{m_0} \cdot N = C</math>                      - logarithmic form: <math>\log S_{\max} = -\frac{1}{m} \log N + \log C</math>                      cycle asymmetry ratio: <math>R = \frac{S_{\min}}{S_{\max}} = \frac{(S_m - S_a)}{(S_m + S_a)}</math></p>			

Knowledge of mechanical properties of S355J0 steel makes it possible to determine two-parametric fatigue characteristics complying with the models presented in Tab. 1. The models specified in items: 1, 5, 6, 7, 9 and 10 have been taken into consideration for further analyses.

### Heywood's model

The Heywood's model (item. 4, Tab. 1) was selected to exemplify a way of determining two-parametric fatigue characteristics, their graphical form and characteristic features of diagrams. Such diagrams are elaborated in the reference system ( $S_m, S_a$ ), in the form of contour line diagrams. Particular contour lines are of constant fatigue life  $N$ . Hence when an appropriate value  $N$  is assumed a corresponding contour line can be determined on the basis of the formulae (4) by calculating  $S_a$  - value for varying values of  $R$ . For subsequent values of  $N$  subsequent contour lines are determined the same way.

The contour line diagram for S355J0 steel, according to Heywood's formulae, is shown in Fig. 3 for  $N = 10^3, 10^4, 10^5, 10^6$  and  $10^7$ .

As results from Fig. 3 varying values of  $S_m$  - stresses take place within the range ( $-R_m; +R_m$ ), and those of  $S_a$  - amplitudes within the range ( $0; R_m$ ). To the diagram are also introduced example lines corresponding with the directions of constant values of:

- cycle asymmetry ratio ( $R = \text{const}$ )
- cycle maximum stresses ( $S_{\text{max}} = \text{const}$ )
- cycle minimum stresses ( $S_{\text{min}} = \text{const}$ )
- amplitude of stresses ( $S_a = \text{const}$ )
- cycle mean stresses ( $S_m = \text{const}$ ).

Similar diagrams were elaborated on the basis of calculation results according to the models: I - (see Fig. 4), II - (Fig. 5), III - (Fig. 6), IV - (Fig. 7) and V - (Fig. 8).

From a general assessment of runs of diagram's constant -value lines for the assumed values of  $N$ , significant differences in the runs for the particular models can be observed.

For practical applications of the discussed models of two-parametric fatigue characteristics conformity of results of calculations and verifying tests is of fundamental importance.

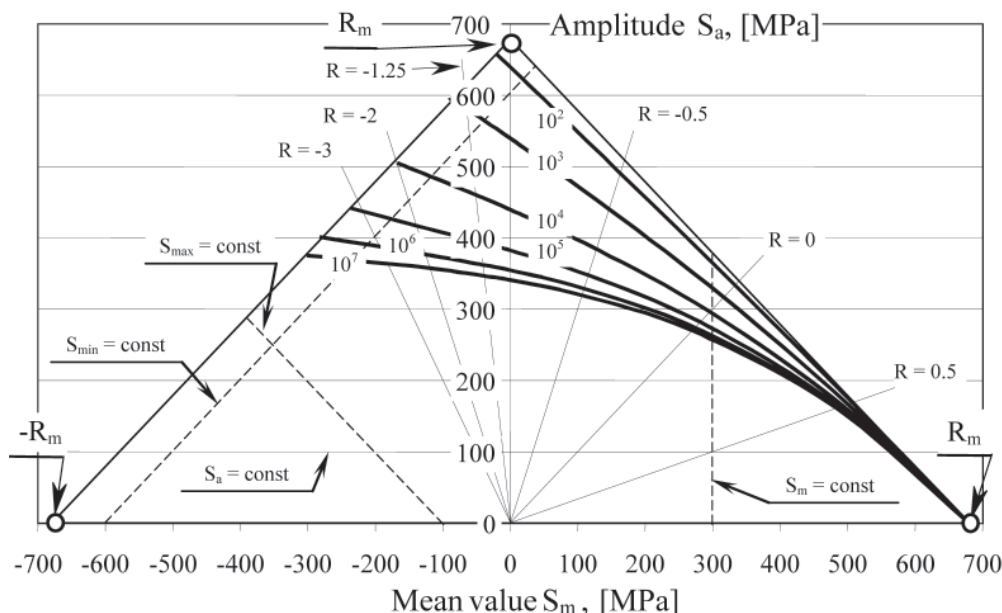


Fig. 3. Two-parametric fatigue diagram acc. Heywood's model (formula 4) for S355J0 steel

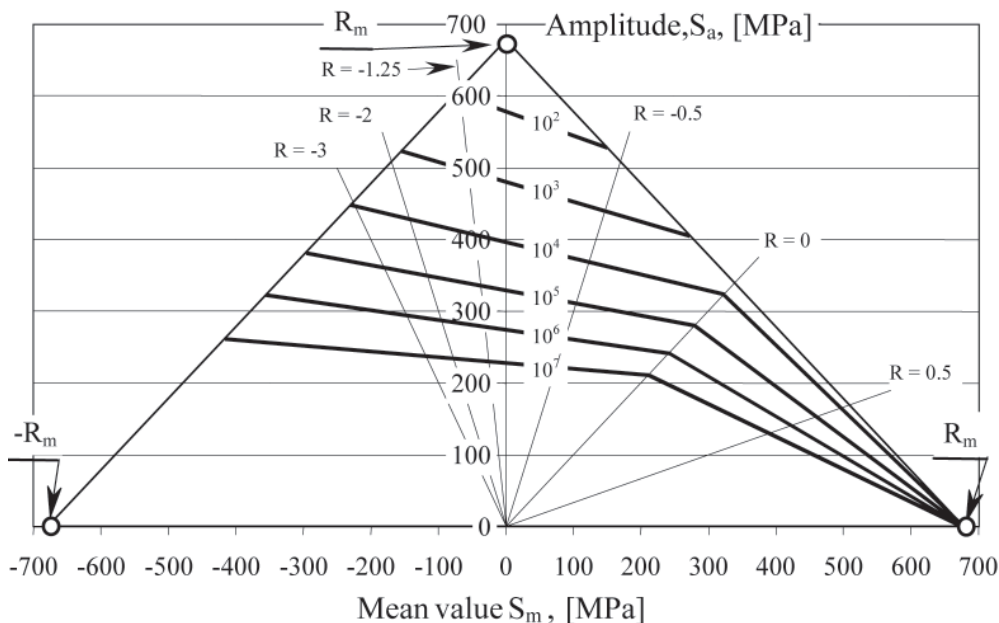


Fig. 4. Two-parametric fatigue diagram acc. Szala's model (formula 5 and 6) for S355J0 steel

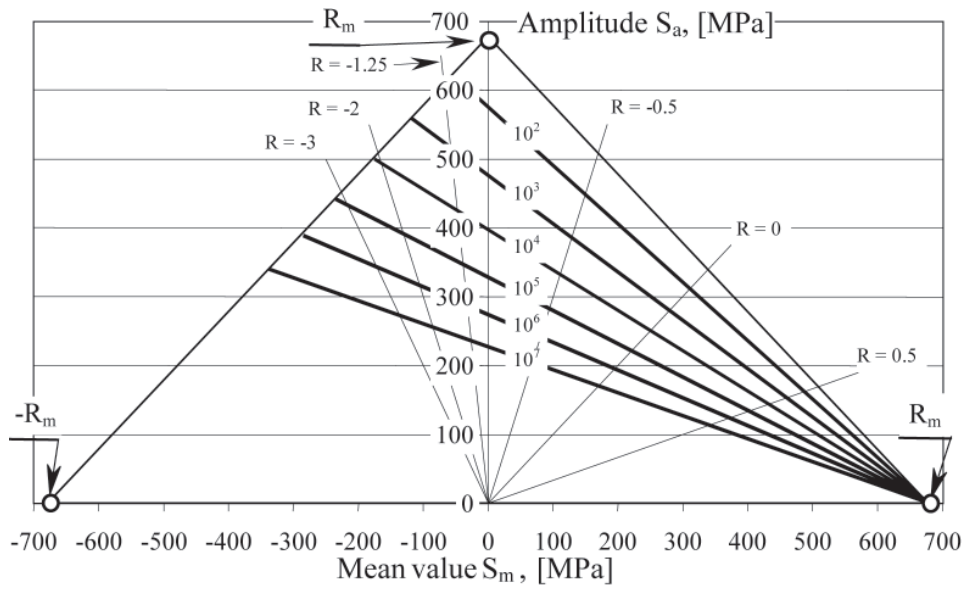


Fig. 5. Two-parametric fatigue diagram acc. Szala's model (formula 8) for S355J0 steel

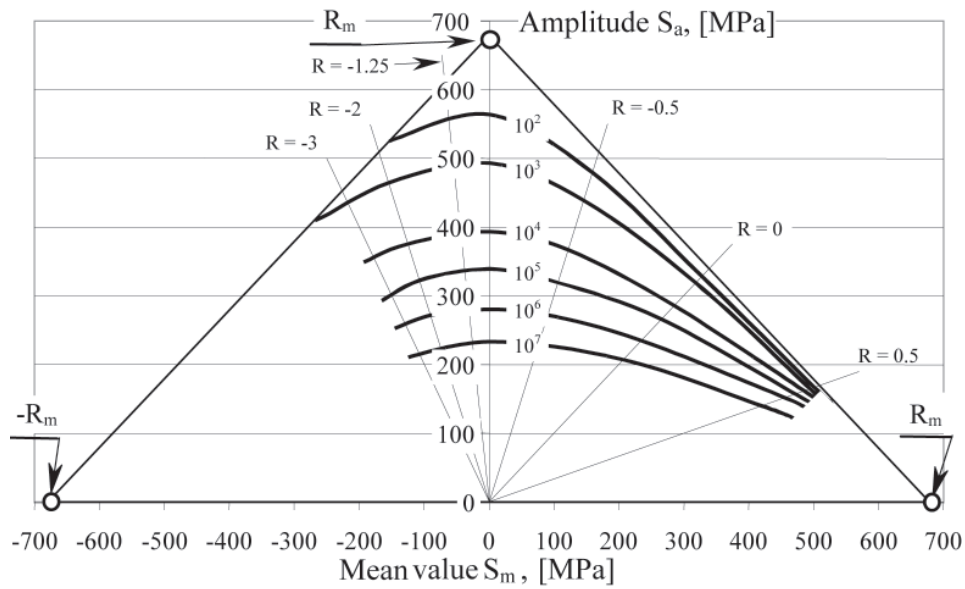


Fig. 6. Two-parametric fatigue diagram acc. Lipski's model (formula 9) for S355J0 steel

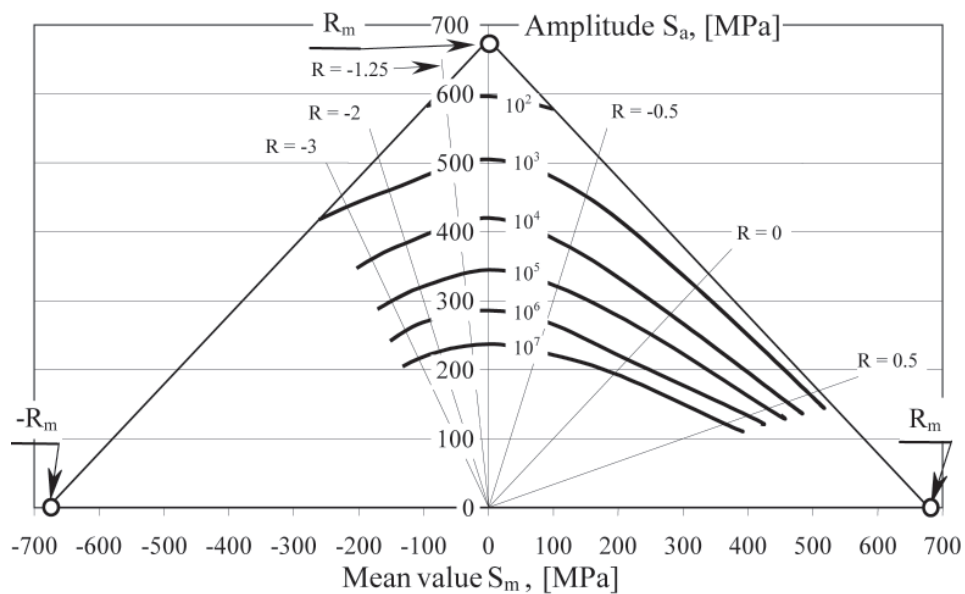


Fig. 7. Two-parametric fatigue diagram acc. Lipski's model IV (formula 10) for S355J0 steel

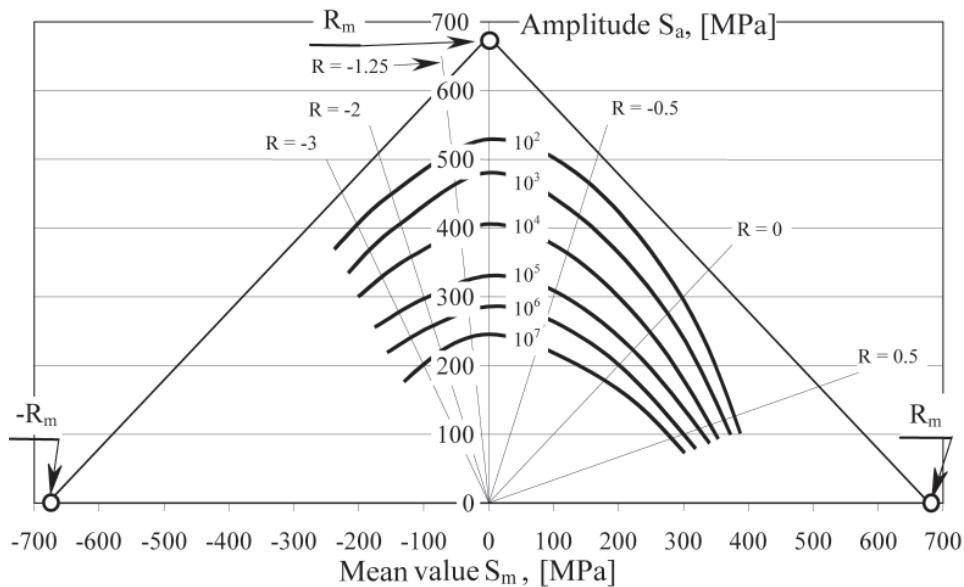


Fig. 8. Two-parametric fatigue diagram acc. Lipski's model V(formula 11) for S355J0 steel

## VERIFYING TESTS

Quantitative analysis of conformity of results of calculations and verifying tests can be performed on the basis of comparison of Wöhler fatigue diagrams for definite values of the cycle asymmetry ratio  $R$ . In this research the following values of  $R$  were assumed:  $R = 0,5; 0; -0,5; -1,0; -1,25; -2,0$  and  $-3,0$ . The values cover to a large extent the parameter variability area of sinusoidal cycles, shown in Fig. 2.

Results of the experimental tests and Wöhler fatigue diagrams in the reference system  $S_{ac}(N)$ , determined on their basis for the above mentioned values of the cycle asymmetry ratio  $R$ , are given in Fig. 9. The diagrams in the bi-logarithmic form are described by the equations (16):

$$\log S_a = a \log N + b \quad (16)$$

Values of the parameter  $a$  and  $b$  are given in Tab. 4.

Data contained in Tab. 4 make it possible to present results of the tests in the form of a contour - line diagram of two-parameter fatigue characteristics (Fig. 10) similar to the diagrams based on results of calculations carried out in compliance with the analysed models (Fig. 3 through 8).

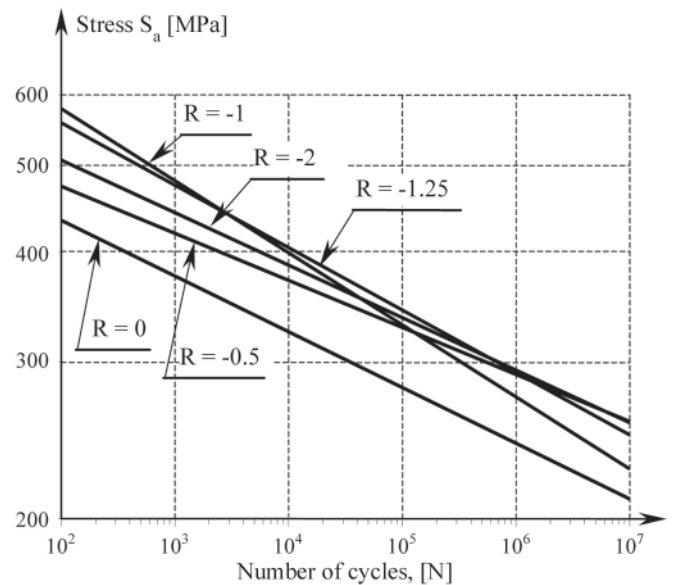


Fig. 9. Results of the fatigue tests and Wöhler fatigue diagrams determined on their basis, for the selected values of the cycle asymmetry ratio  $R$

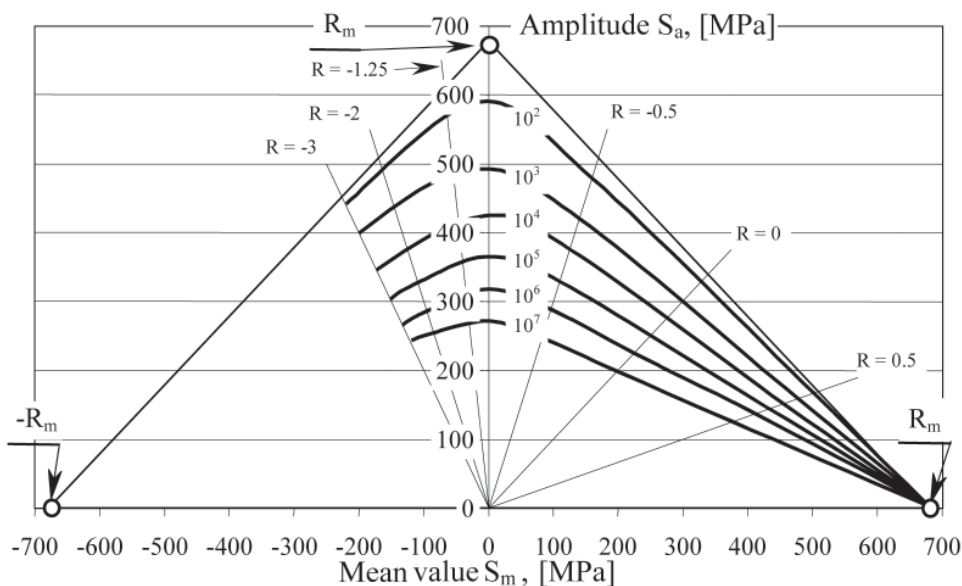


Fig. 10. Two-parametric fatigue diagram elaborated on the basis of experimental data for S355J0 steel

Tab. 4. Values of the directional coefficient  $a$  and the free term  $b$  in the equations describing Wöhler fatigue diagram, for the assumed values of the cycle asymmetry ratio  $R$

	Cycle asymmetry ratio $R$				
	0	-0.5	-1.0	-1.25	-2.0
	1	2	3	4	5
<b>a</b>	-0.0628	-0.0528	-0.0811	-0.0709	-0.0592
<b>b</b>	2.7630	2.7810	2.9247	2.8894	2.8233

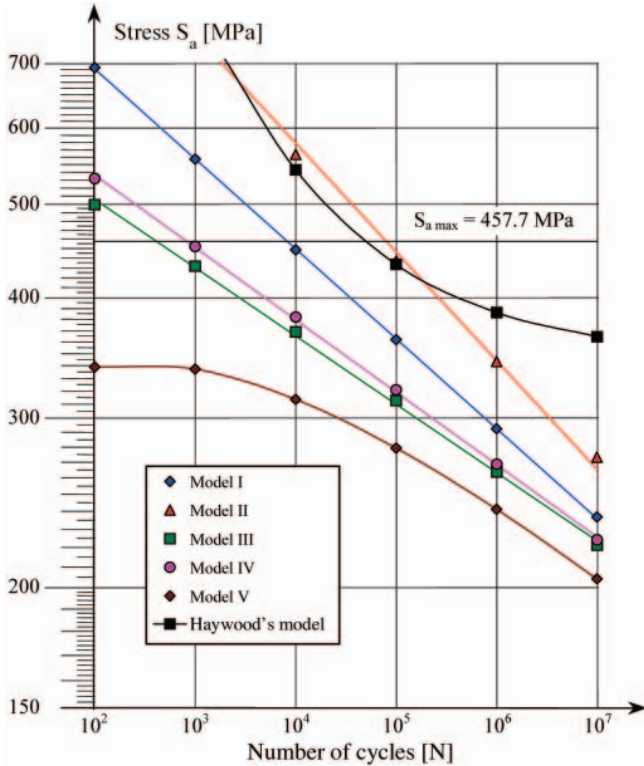


Fig. 11. Results of fatigue calculations according to the assumed models of two-parametric fatigue characteristics for  $R = -3$

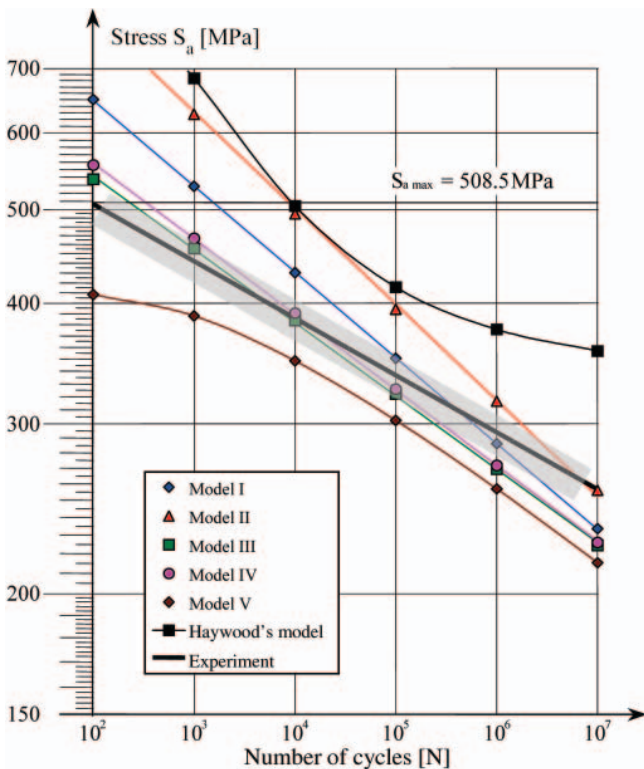


Fig. 12. Results of fatigue calculations according to the assumed models of two-parametric fatigue characteristics for  $R = -2$

In the subsequent figures, Fig. 11 through 17, comparison is presented of calculation results obtained by using the selected models of two-parametric fatigue characteristics for the particular values of the cycle asymmetry ratio  $R$ , with experimental test results. In Fig. 12 through 16 the calculation results are presented on the background of experimental diagrams. The shadowed zones indicate breadth of experimental data scatter bands. Moreover, in the diagrams a maximum value of  $S_{a \max}$  complying with the condition  $S_{a \max} < R_m$ , is given.

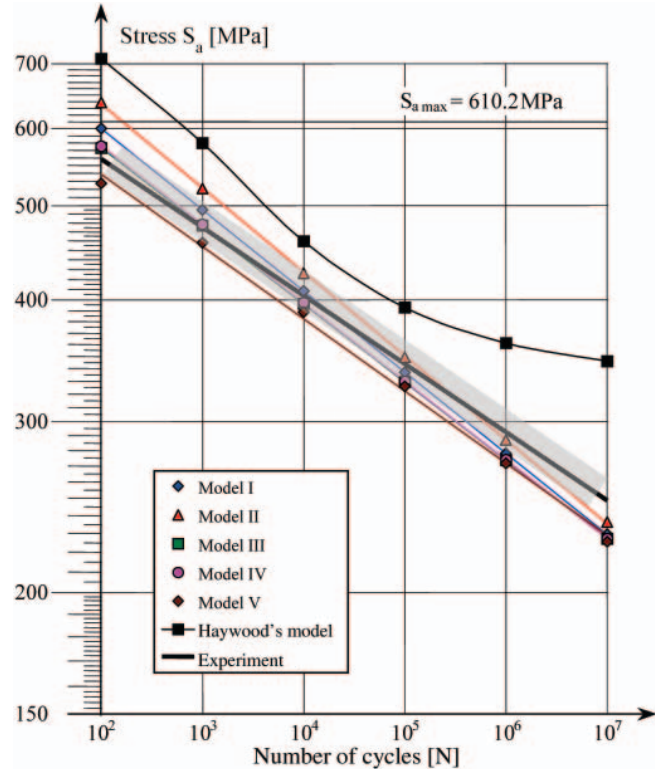


Fig. 13. Results of fatigue calculations according to the assumed models of two-parametric fatigue characteristics for  $R = -1.25$

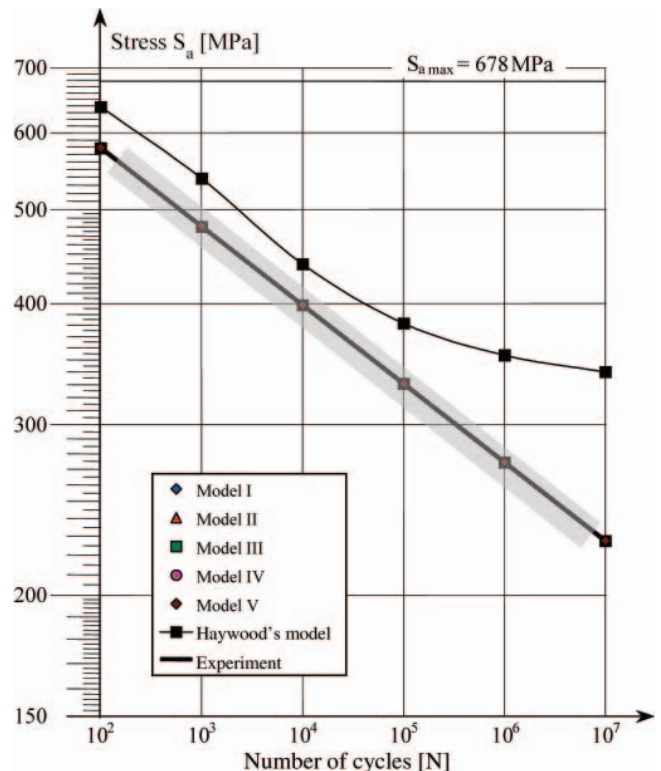


Fig. 14. Results of fatigue calculations according to the assumed models of two-parametric fatigue characteristics for  $R = -1.0$

In Fig. 11 (for  $R = -3$ ) and in Fig. 17 (for  $R = 0.5$ ) the experimental fatigue diagrams were determined by extrapolating the test results for the range of  $R$  (-2,0; 0).

From overall assessment of the data shown in Fig. 1 through 17 result differences between values of the calculated stress amplitudes  $S_{ac}$  and those obtained from tests,  $S_{ex a}$ , depending on an assumed calculation model, assumed value of fatigue life  $N$  and values of the cycle asymmetry ratio  $R$ .

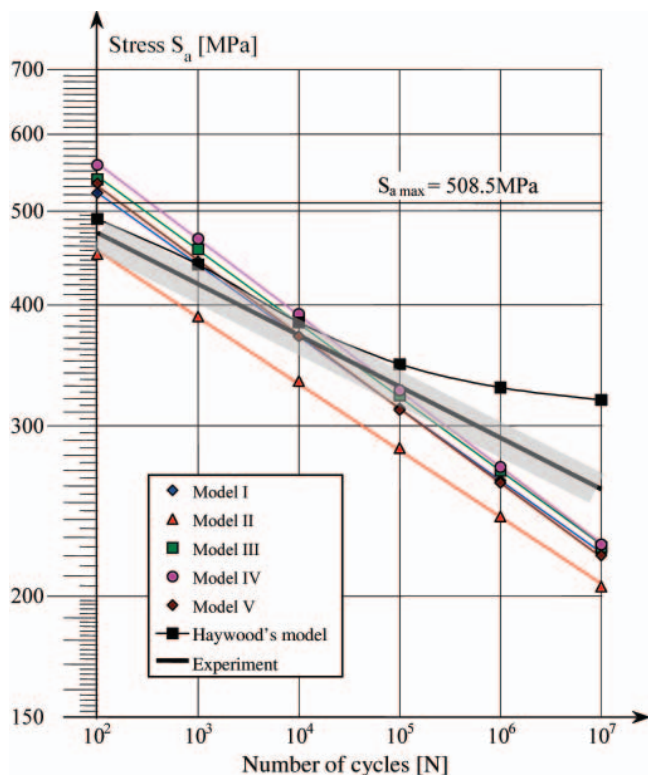


Fig. 15. Results of fatigue calculations according to the assumed models of two-parametric fatigue characteristics for  $R = -0.5$

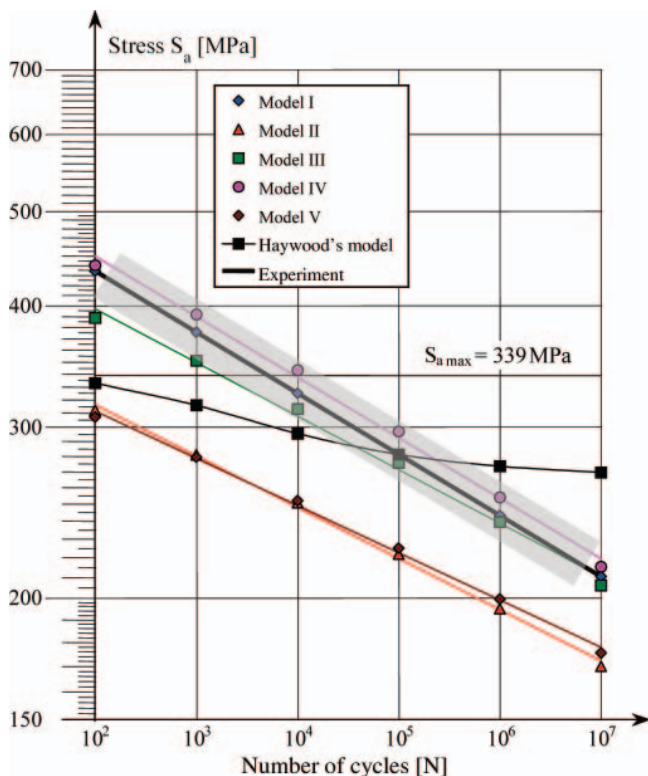


Fig. 16. Results of fatigue calculations according to the assumed models of two-parametric fatigue characteristics for  $R = 0$

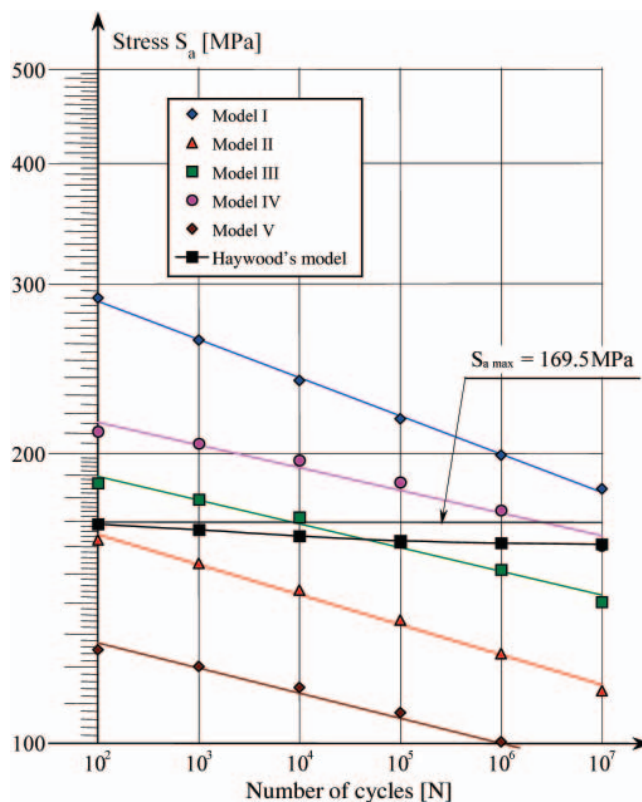


Fig. 17. Results of fatigue calculations according to the assumed models of two-parametric fatigue characteristics for  $R = 0.5$

## ANALYSIS OF THE CALCULATION AND TEST RESULTS

Differences between results of calculations of  $S_{ac}$  and results of tests of  $S_{ex a}$  related to amplitude values depend on a model of assumed values of the fatigue life  $N$  and cycle asymmetry ratio  $R$ , taken for calculations.

The relative differences,  $\delta$ , between results of calculations and tests, determined according to the formula (17):

$$\delta = \frac{S_{ac} - S_{a ex}}{S_{a ex}} \cdot 100\% \quad (17)$$

are presented in the form of bar diagrams in the successive figures as follows: for the Heywood's model – in Fig.18, model I - Fig.19, model II - Fig. 20, model III - Fig. 21, model IV- Fig. 22 and model V - Fig. 23. Within the entire variability range of the fatigue life  $N$  and cycle asymmetry ratio  $R$  the largest differences appear in the Heywood's model (H), and in the extreme cases they reach values from +49.32% to -23.21%. The largest differences occur for high values of fatigue life ( $N = 10^5 \div 10^7$ ). The interval corresponds with stress values observed in the cycles of a significant share in service load spectra of structural elements. The fact greatly affects fatigue calculations whose aim is to assess serviceability of structural elements.

The above mentioned differences result from that the Heywood's model was based on the data of material strength properties obtained from monotonic tension tests.

In the remaining models material properties are represented by the fatigue life determined either from the test under oscillating load ( $R = -1$ ) – in the case of the models: II, III, IV and V, or the test under oscillating load ( $R = -1$ ) and pulsating load ( $R = 0$ ) – in the case of the model I. Therefore the calculation results according to the above mentioned models for values of  $R = -1$ , and additionally to the model I for  $R = 0$ , are in full conformity with the test results, that is obvious and in particular diagrams marked:  $\delta = 0$ .

Out of all the analyzed models for the entire range of fatigue life  $N$  and cycle asymmetry ratio  $R$  the calculations according to the models: I, III and IV showed the greatest conformity with the experiment.

In the case of the model I the calculations for  $R = 0.5$  constitutes an exception, whose discrepancies from test results reached about 65% for  $N = 10^2$ .

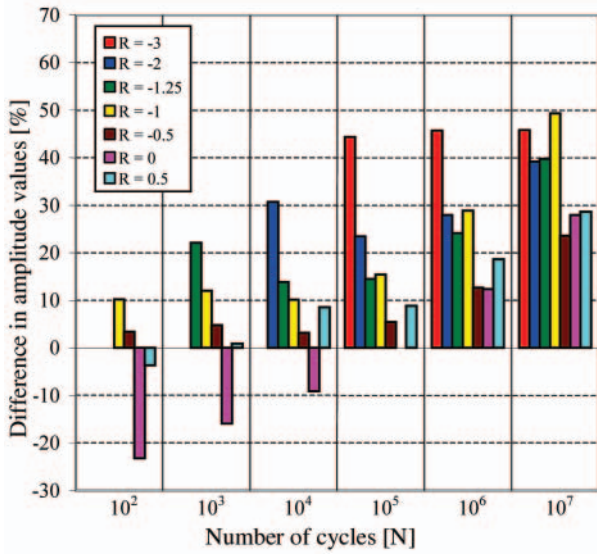


Fig. 18. Diagram showing difference in amplitude values determined with the use of Heywood's model

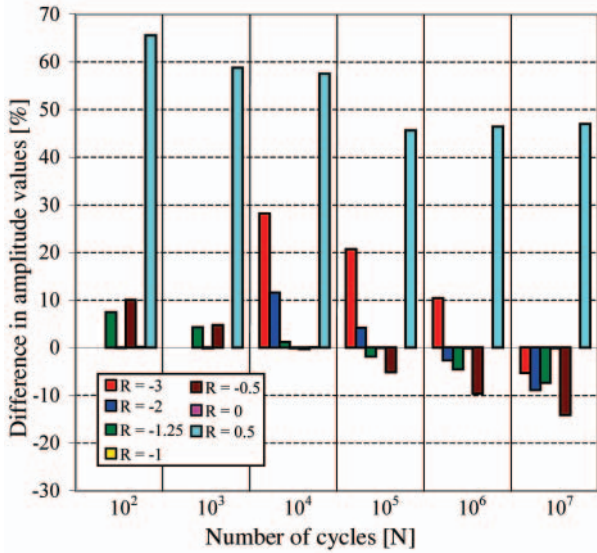


Fig. 19. Diagram showing difference in amplitude values determined for the model I

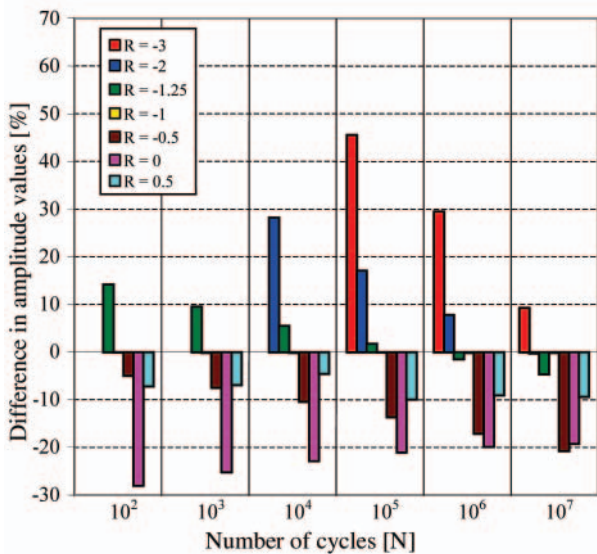


Fig. 20. Diagram showing difference in amplitude values determined for the model II

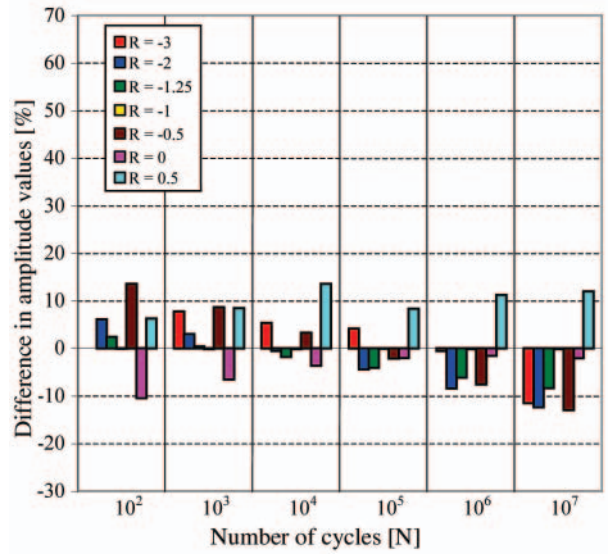


Fig. 21. Diagram showing difference in amplitude values determined for the model III

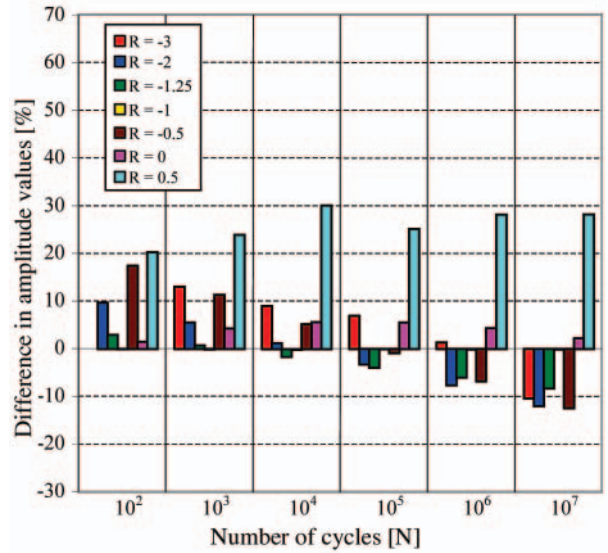


Fig. 22. Diagram showing difference in amplitude values determined for the model IV

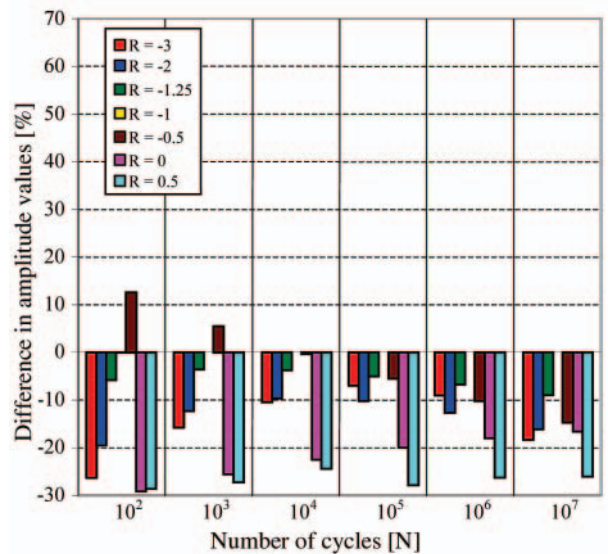


Fig. 23. Diagram showing difference in amplitude values determined for the model V

The model I is sensitive to magnitude of the factor of material sensitivity to cycle asymmetry,  $\psi_N$ . In the case of the results shown in Fig. 19 the calculations were carried out with the use of  $\psi_N$  - value determined from Eq. (7), Tab. 1. Data for the calculations were taken from Wöhler diagrams for the load variability ratios:  $R = -1$  and  $R = 0$ . The large scatter of fatigue test results on the basis of which the diagrams were determined, makes accuracy of determination of the factor  $\psi_N$  from Eq. (7), low.

By modifying the model I with regard to magnitude of the factor  $\psi_N$ , conformity between calculations performed for the model and appropriate experimental data can be greatly improved.

## CONCLUSIONS

From the above presented analysis the following results:

- conformity between calculation results and fatigue test results greatly depends on assumed two-parametric fatigue characteristics
- within the entire range of the analysis the highest conformity was obtained for the models: I, III, IV, and the lowest - for Heywood's model
- the low conformity of calculations according to Heywood's model results from the assumption of the tensile strength  $R_m$  as a quantity characterizing properties of material subjected to cyclic loads
- the higher conformity of calculation results according to the remaining models: I through V, results from the assumption of Wöhler fatigue diagram parameters as characteristics of material mechanical properties; such data for a variety of materials can be obtained from tests or literature sources of different kind, e.g. [16, 17]
- for preliminary calculations, e.g. structural design process in which precise data on material cyclic properties and service loads are not yet known, the simple models I and II are recommended
- for further considerations an analysis of influence of the differences in two-parametric fatigue characteristics described in this paper, on calculation results of fatigue life in conditions of service load spectra, is of a great importance
- as results from literature data, especially those contained in [7], the above described models can yield different conformity with results of tests of other materials, the opinion is confirmed by the paper [12] devoted to tests of aircraft Al-alloys
- another important problem is determining range of application of the described models to high-cycle fatigue (HCF), which requires determining an area of two-parametric fatigue characteristics in compliance with the assumed criterion [17]; as the criterion  $S_{max} \leq R_e$ , commonly met in the subject-matter literature, is considered approximate and ineffective in some cases
- a separate problem important from the point of view of practical applications is description of two-parametric fatigue characteristics for notched elements.

The problems specified in the points: f), g), h), i) will be discussed in next papers.

## NOMENCLATURE

A	– elongation [% ]
C	– constant in the formula describing Wöhler fatigue diagram for off-zero pulsating load ( $R = 0$ )
$C_0$	– constant in the formula describing Wöhler fatigue diagram for oscillating load ( $R = -1$ )
N	– cycle number - general notation (fatigue life)
$N_0$	– cycle number – fatigue life corresponding with fatigue limit
$R = S_{min} / S_{max}$	– cycle asymmetry ratio
$R_e$	– material yield point [MPa]
$R_f$	– fatigue limit - general notation [MPa]
$R_m$	– material tensile strength [MPa]
$R_0$	– fatigue limit under pulsating load ( $R = 0$ ) for $N_0$ cycle number, [MPa]
$R_0^N$	– fatigue strength under sinusoidal pulsating load ( $R = 0$ ) for N cycle number, [MPa]
$R_{-1}$	– fatigue limit under oscillating load ( $R = -1$ ) for $N_0$ cycle number, [MPa]
$R_{-1}^N$	– fatigue strength under sinusoidal oscillating load ( $R = -1$ ) for N cycle number, [MPa]
S	– specimen stress – general notation, [MPa]
$S_a = 0,5(S_{max} - S_{min})$	– sinusoidal cycle stress amplitude [MPa ]
$S_m = 0,5(S_{max} + S_{min})$	– mean sinusoidal cycle stress [MPa ]
$S_{max}$	– maximum sinusoidal cycle stress [MPa ]
$S_{min}$	– minimum sinusoidal cycle stress [MPa ]
Z	– contraction [%]
m	– exponent in formula describing Wöhler fatigue diagram for pulsating load ( $R = 0$ )
$m_0$	– exponent in formula describing Wöhler fatigue diagram for oscillating load ( $R = -1$ )
$\psi$	– factor of material sensitivity to cycle asymmetry, for $N = N_0$
$\psi_N$	– factor of material sensitivity to cycle asymmetry, for $N \neq N_0$ .

## BIBLIOGRAPHY

- Bendat J.S., Pierdol A.G.: Methods of analysis and measurement of random signals (in Polish), PWN, Warszawa, 1976
- Szala J., Boroński D.: Assessment of material fatigue state in diagnostics of machines and devices, Chapter 9 (in Polish). Wydawnictwo Instytutu Technologii Eksploatacji – Państwowego Instytutu Badawczego (Publishing House of Operation Technology Institute - State Research Institute), Bydgoszcz, 2008
- Kocak M. (Editor), Webster S., Janosch J.J., Ainsworth R.A., Koers R.: FITNET - Fitness – for - Service Procedure, Final Draft MK7, 2006
- Kocańda S., Szala J.: Background for fatigue calculations (in Polish). PWN, Warszawa, 1997
- Fricke W., Petershagen H., Paetzold H.: Fatigue Strength of Ship Structures - Part I: Basic Principle. Information from Germanischer Lloyd Group, 1, Hamburg, 1997
- Fricke W., Petershagen H., Paetzold H.: Fatigue Strength of Ship Structures – Part II: Examples. Information from Germanischer Lloyd Group, 1, Hamburg, 1998
- Figge I.E.: An Empirical Equation Relating Fatigue Limit and Mean Stress. NASA Technical Note D-3883, Washington, 1967
- Heywood R.B.: Designing Against Fatigue. Chapman Hall, London, 1962
- Szala J.: Tests and calculations of machine elements under random and programmed loads (in Polish). Instytut Podstawowych Problemów Techniki, PAN (Institute of Fundamental Engineering Problems, Polish Academy of Sciences), Warszawa, 1979
- Szala J., Szala G.: Two-parametric fatigue characteristic – formulating problem. Problemy Eksploatacji 3/2001(42), Wydawnictwo Instytutu Technologii Eksploatacji (Publishing House of Operation Technology Institute), Radom, 2001.

11. Szala J., Szala G.: Comparative analyses of two-parametric fatigue characteristic and their experimental verification. *Problemy Eksploatacji* 3/2001(42), Wydawnictwo Instytutu Technologii Eksploatacji (Publishing House of Operation Technology Institute), Radom, 2001
  12. Szala J., Lipski A.: A concept of description of material fatigue properties for fatigue life calculations of structural elements (in Polish). *Zagadnienia Eksploatacji Maszyn (Problems of Operation of Machines)*, Quarterly of KBM PAN, Bulletin 2 (142), 2005
  13. Bołotin W.W.: Statistical methods applied to mechanics of structures (in Polish). Wydawnictwo Arkady (Arkady Publishing House), Warszawa, 1968
  14. Collins J.A.: Failure of Materials in Mechanical Design, Analysis, Prediction, Prevention. John Wiley & Sons Inc., 1993
  15. Howard E. Boyer (Editor): Atlas of Fatigue Curves. ASM International, The Materials Information Society, Fifth printing, August, 2003
  16. Трощенко В.Т., Сосновский Л.А.: Сопротивление усталости металлов и сплавов. Киев, Наукова Думка, 1987
  17. Szala G., Ligaj B.: Evaluation criteria of low- and high-cycle fatigue in fatigue life calculations of constructional elements. *Logistyka*, No. 6, 2009
- Note:* This work has been elaborated in the frame of the project No. 0715/B/T02/2008/35 financed by Polish Ministry of Sciences and Higher Education.

---

#### CONTACT WITH THE AUTHORS

Bogdan Ligaj, Ph. D.,  
Grzegorz Szala, Ph. D.  
Faculty of Mechanical Engineering,  
University of Technology and Life Science,  
Prof. S. Kaliskiego 7  
85-763 Bydgoszcz, POLAND  
e-mail: bogdanj@utp.edu.pl

# Comparing N3-60 cascade exit angles obtained from tunnel measurements and numerical simulations

**Biernacki Rafał**, Ph. D.  
 Gdansk University of Technology  
**Piotr Krzyślak**, Assoc. Prof.  
 Poznan University of Technology

## ABSTRACT

*The article compares the results of the measurements performed in the aerodynamic tunnel owned by the Czestochowa University of Technology and the numerical simulation done using the code FLUENT for a plane cascade of N3-60 profiles. The comparison study aims at assessing differences between the exit angles measured experimentally and those obtained from numerical calculations. Variable parameters in the measurements and the calculations were the relative pitch and the profile stagger angle. The measurements were performed in the flow of air. The same medium and having the same inlet parameters was assumed in the calculations. The calculations were performed in two dimensions for the compressible flow. The k-ε RNG turbulence model was used to complete the equation system. Comparing the measured and calculated results provides opportunities for assessing the range of differences between the experiment and the simulation. The obtained results and formulated conclusions will find the application not only in the power industry, but also in the shipbuilding industry for analysing the operation of steam and gas turbines used as main and auxiliary propulsion systems on both merchant vessels and battle ships.*

**Keywords:** numerical calculations, profile characteristics, gas turbines, steam turbines

## GEOMETRY OF N3 PROFILE

The N3-60 profile is a basic profile used in impulse turbines produced in Poland. In the eighties, a series of tests of those profiles were performed in the aerodynamic tunnel owned by the Czestochowa University of Technology. Variable parameters in these tests were the profile stagger angle  $\alpha_u$  and the relative pitch  $t/b$ . The tests aimed at preparing basic flow characteristics of the profiles and cascades to use them in the turbine design process. An isolated profile N3 is shown in Fig. 1.

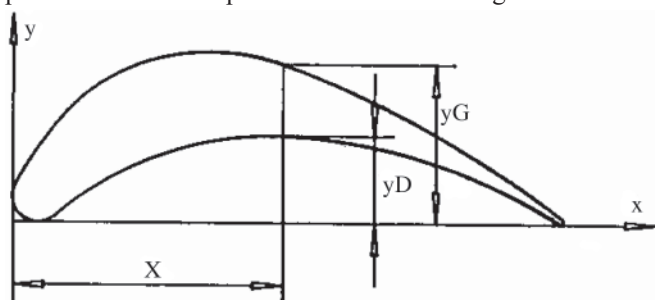


Fig. 1. N3 profile contour lines [1]

Basic geometrical parameters which define the N3-60 profile are given in Fig. 2. For the changing stagger angle  $\alpha_u$

and the relative pitch  $t/b$  we can calculate the effective cascade exit angle, see the diagram in Fig. 3.

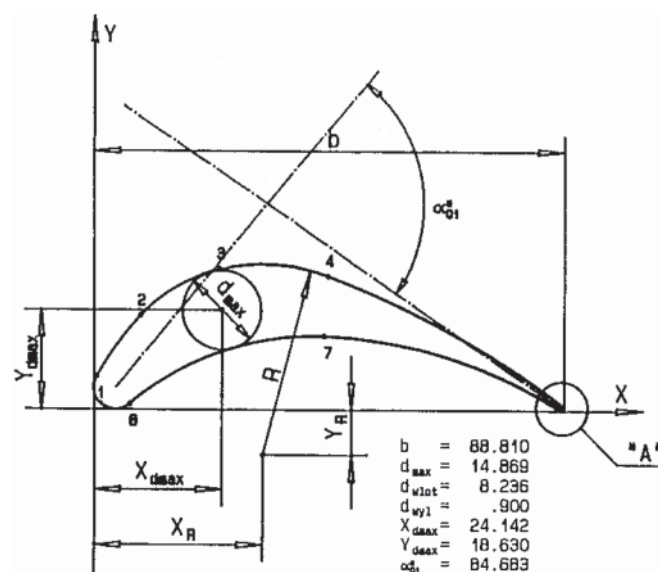


Fig. 2. Geometrical parameters of N3-60 profile. [1]

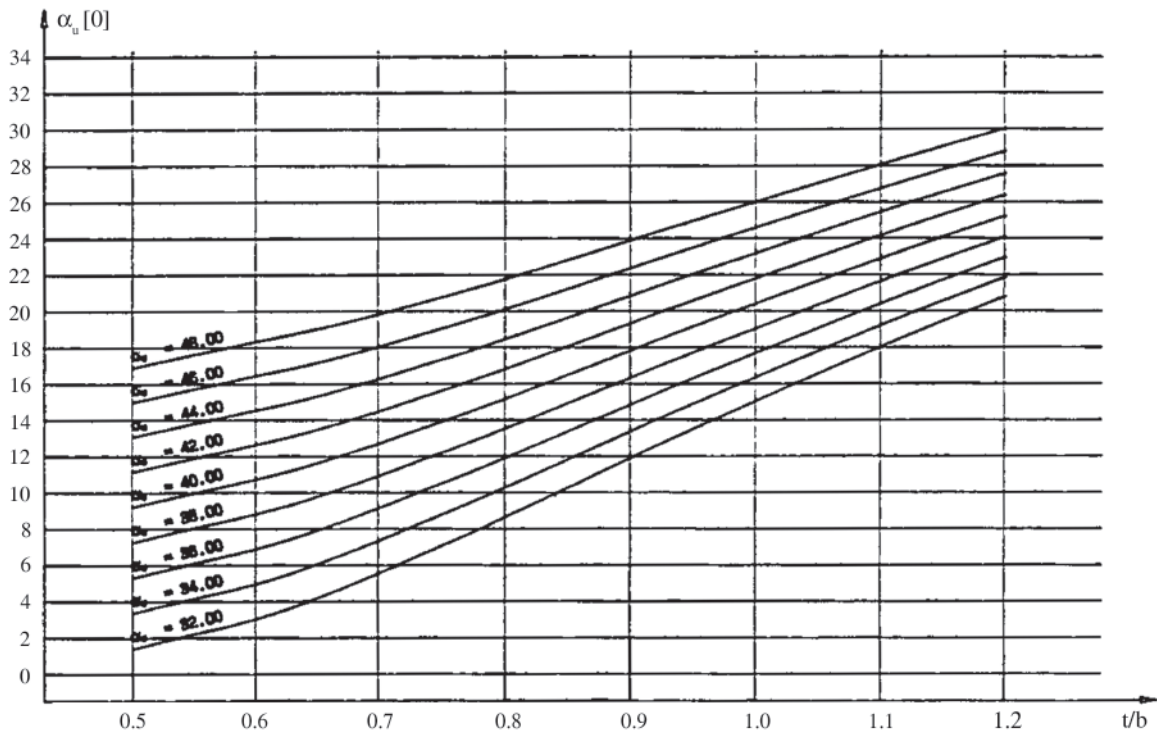


Fig. 3. Effective N3-60 cascade exit angle [1]

## DISCUSSION OF THE EXISTING RESULTS OF N3 PROFILE MEASUREMENTS

The existing results of N3 profile measurements are published in [1]. The ranges of parameters changing in the profile tests were the following:

- relative pitch  $t/b$  - 0.5 to 1.2
- inlet flow angle -  $45^\circ, 75^\circ, 90^\circ, 120^\circ$
- cascade stagger angle -  $34.6^\circ$  to  $48.6^\circ$
- inlet flow velocity -  $Ma = 0.2$
- resultant Reynolds number -  $0.38 \times 10^6$

The measured results, having the form of velocity distributions, were integrated and averaged to obtain one-dimensional characteristics of the cascade for the assumed profile stagger angle and pitch. The quantities determined in those measurements included the profile loss, the trailing edge loss, and the exit flow angle  $\alpha_u$ . Fig. 3 shows the flow exit angle as a function of the relative pitch for the inlet flow angle  $\alpha_0$  equal to  $90^\circ$ . The basic goal of this study was to verify the differences between the real results obtained from the measurements and those calculated using the numerical model of the cascade.

## AUTOMATION OF THE GEOMETRY GENERATION PROCESS

The profile co-ordinates were entered to the Excel calculation sheet. The entered data included fifty pairs of points in the Cartesian coordinate system which defined the upper and lower profile curve. The next step was to calculate the camber line, defined as:

$$x_s = x_g = x_d$$

$$y_s = 1/2(y_g + y_d)$$

For an arbitrary N3 profile stagger angle, the algorithm rotated the profile and its camber line using the following scheme:

$$x' = x \cos(\alpha) - y \sin(\alpha)$$

$$y' = x \sin(\alpha) + y \cos(\alpha)$$

After the rotation  $x_g \neq x_d \neq x_s$ . The passage axis was generated by shifting parallelly the camber line up and down by half of the assumed cascade pitch, and then extrapolated beyond the profile as the straight lines extending from  $x = -25$  to  $x = 100$ . The input data for the geometry generation algorithm comprised a list of points which defined the profile in standard position, complemented by the rotation angle and the cascade pitch. Based on these data, the algorithm generated a script which introduced to the code Rhino a sequence of points describing the passage geometry after rotation and transformation. This method was used for creating a series of passage geometries taking into account different profile stagger angles and cascade pitches. Fig. 4 shows a sample geometry before and after the transformation for the stagger angle  $\alpha = 44.58^\circ$  and the relative pitch  $t/b = 0.6$ .

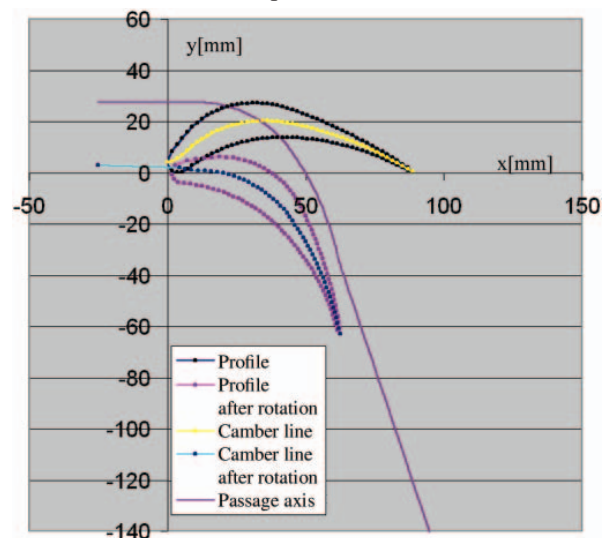


Fig. 4. Profile transformation and creation of the passage axis

The oriented N3 profile, mapped using the code Rhinoceros, was used as a basis for generating the calculation grid. The 2D calculation domain was bordered in front by a vertical inlet section, and at rear by a vertical exit section. From the top and the bottom the calculation domain was bordered by the axis of the blade-to-blade passage, treated as the border of periodical type.

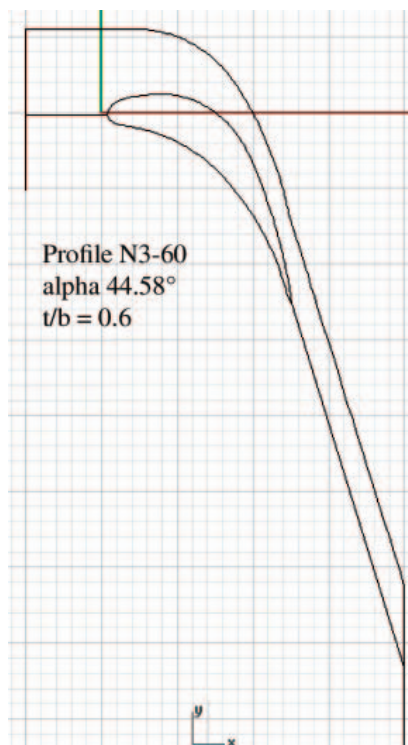


Fig. 5. Geometry prepared for grid generation

### ASSUMPTIONS ADOPTED WHEN GENERATING THE CALCULATION GRID

In all cases, the geometry presented in the previous Section has made the basis for generating the calculation grid. The upper and lower boundaries of the calculation domain (see Fig. 5), which define the flow passage axis, were considered the periodic boundaries. The calculation domain was divided into two subdomains – over and below the plate, which made it possible to generate the boundary layer on the surface of the profile washed round by the flow. The calculation grids of structural type and dimensions  $160 \times 450$  elements were generated automatically by the code, which made it possible to generate an optimised structure for each examined geometry variant. The generated grid was optimised with respect to the orthogonality of the gridlines. One of basic criteria for assessing the quality of the created grid was the minimum angle between the lines which limit the grid element. Tab.1 collects the values of the minimal angles for different calculation variants.

Tab. 1. Minimal calculation grid angles

		Profile stagger angle $\alpha_u$			
		36.58	40.58	44.58	48.58
Cascade	0.6	3.06°	2.70°	3.55°	4.47°
pitch	0.8	3.64°	3.44°	5.49°	6.44°
t/b	1.0	3.91°	5.15°	6.89°	7.78°

Fig. 6 presents a sample calculation grid generated for the variant characterised by parameters:  $\alpha_u = 44.58^\circ$ ,  $t/b = 0.6$ .

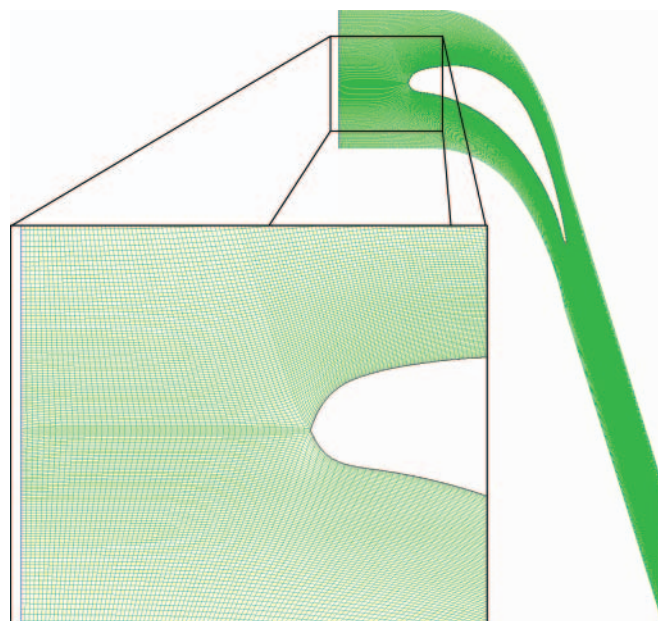


Fig. 6. Sample calculation grid for N3-60 profile

### RANGE OF CALCULATIONS

The calculation grid similar to that shown in the previous Section was generated for each individual pair of profile stagger angle  $\alpha_u$  and pitch  $t/b$ . The calculations done using these grids made use of parameters, the range of which is given in Tab. 2:

Tab. 2. Range of parameters used in calculations

		Profile stagger angle $\alpha_u$			
		36.58	40.58	44.58	48.58
Cascade	0.6	☑	☑	☑	☑
pitch	0.8	☑	☑	☑	☑
t/b	1.0	☑	☑	☑	☑

The calculations were performed using the code Fluent [2]. The boundary conditions for all variants were taken from the experimental data. The assumed quantities included:

- mass flow rate through a single passage
- pressure at flow area exit
- type of working medium (the experiment was carried out for air)
- inlet temperature of the working medium
- model of fluid (viscous, compressible)
- turbulence model (k- $\epsilon$  RNG)
- values of turbulence parameters  $k$  and  $\epsilon$  at passage inlet.

Part of the above parameters was constant for all calculated variants. This list includes: total inlet pressure assumed as equal to 100 kPa, inlet temperature of the working medium -300 K, and the model and parameters of the working medium. Boundary conditions which changed from variant to variant are given in Tab. 3.

Tab. 3. Variable boundary conditions

		$\dot{m}$ [kg/s]	$k$ [m <sup>2</sup> /s <sup>2</sup> ]	$\epsilon$ [m <sup>2</sup> /s <sup>3</sup> ]
Cascade	0.6	2.480	21.627	2112.7
pitch	0.8	3.307	21.627	1584.5
t/b	1.0	4.133	21.627	1267.6

The values assumed in the calculations imitated the flow conditions recorded in the experiment.

## SAMPLE RESULTS OF NUMERICAL CALCULATIONS

The obtained results of the calculations have made it possible to assess the effect of the distance of the test section from the trailing edge on the values of the exit angle  $\alpha_1$ . As could be expected, the calculated angle did not change much after leaving the profile cascade. Changes of this angle as a function of the distance from the blade trailing edge are shown in Fig. 7, for the selected sample pitch  $t/b = 0.6$ . When comparing with the results of the measurements, it was assumed that the distance from the trailing edge was equal to 5 mm.

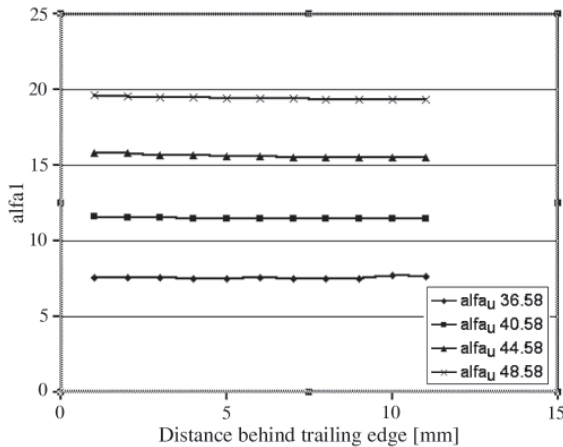


Fig. 7. The angle  $\alpha_1$  vs. the distance from the trailing edge

The next figures show the streamline and exit angle distributions in the calculation domain, as well as the exit angle distributions along the traverse line  $x = +5$  mm downstream of the trailing edge.

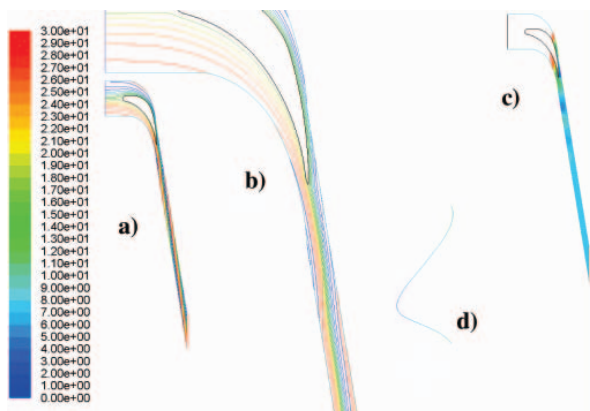


Fig. 8. Results of calculations for profile N3-60,  $\alpha_u = 36.58^\circ$ ,  $t/b = 0.6$ ; a) streamlines; b) streamlines – enlarged; c) exit angles (scale on the left); d) changes of exit angle  $\alpha_1$  along datum +5 mm

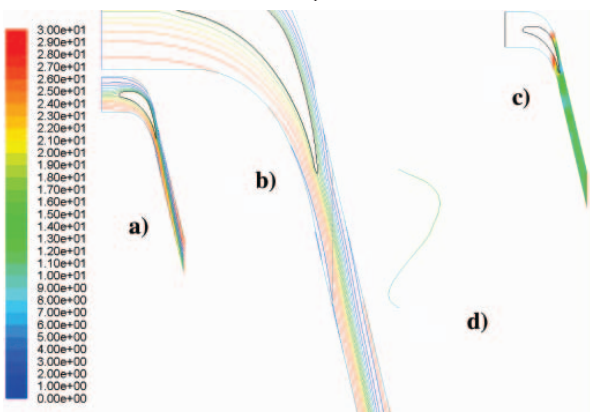


Fig. 9. Results of calculations for profile N3-60,  $\alpha_u = 40.58^\circ$ ,  $t/b = 0.6$ ; a) streamlines; b) streamlines – enlarged; c) exit angles (scale on the left); d) changes of exit angle  $\alpha_1$  along datum +5 mm

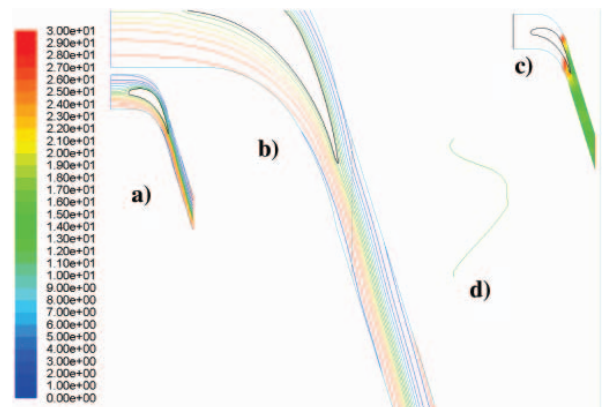


Fig. 10. Results of calculations for N3-60 profile,  $\alpha_u = 44.58^\circ$ ,  $t/b = 0.6$ ; a) streamlines; b) streamlines – enlarged; c) exit angles (scale on the left); d) changes of exit angle  $\alpha_1$  along datum +5 mm

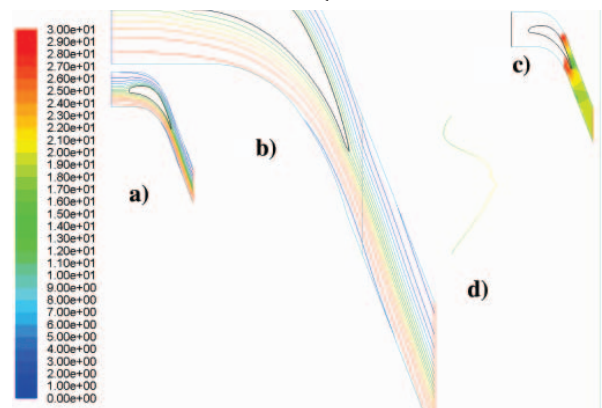


Fig. 11. Results of calculations for profile N3-60,  $\alpha_u = 48.58^\circ$ ,  $t/b = 0.6$ ; a) streamlines; b) streamlines – enlarged; c) exit angles (scale on the left); d) changes of exit angle  $\alpha_1$  along datum +5 mm

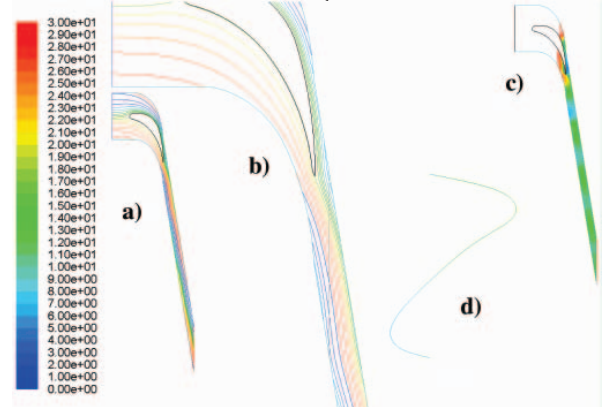


Fig. 12. Results of calculations for profile N3-60,  $\alpha_u = 36.58^\circ$ ,  $t/b = 0.8$ ; a) streamlines; b) streamlines – enlarged; c) exit angles (scale on the left); d) changes of exit angle  $\alpha_1$  along datum +5 mm

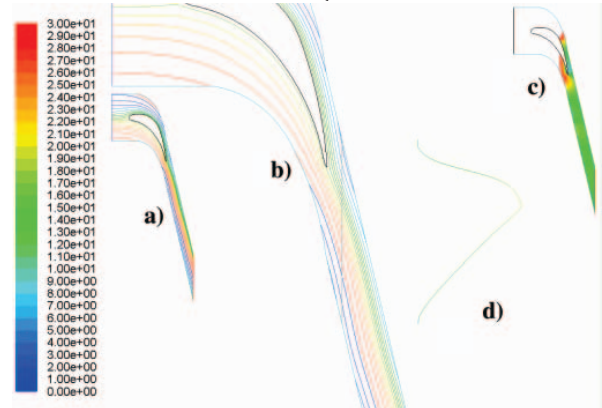


Fig. 13. Results of calculations for profile N3-60,  $\alpha_u = 40.58^\circ$ ,  $t/b = 0.8$ ; a) streamlines; b) streamlines – enlarged; c) exit angles (scale on the left); d) changes of exit angle  $\alpha_1$  along datum +5 mm

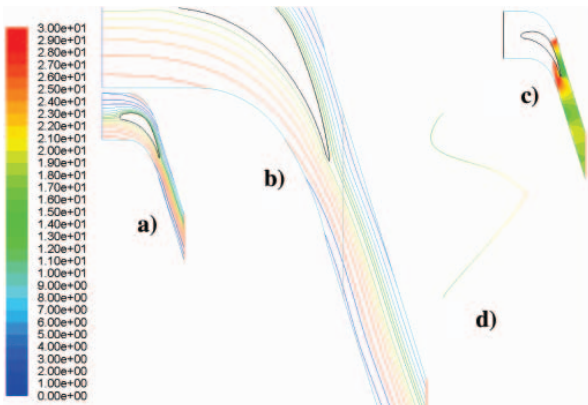


Fig. 14. Results of calculations for profile N3-60,  $\alpha_u = 44.58^\circ$ ,  $t/b = 0.8$ ; a) streamlines; b) streamlines – enlarged; c) exit angles (scale on the left); d) changes of exit angle  $\alpha_1$  along datum +5 mm

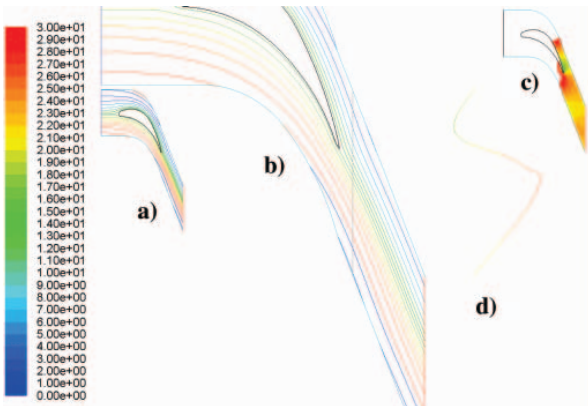


Fig. 15. Results of calculations for profile N3-60,  $\alpha_u = 48.58^\circ$ ,  $t/b = 0.8$ ; a) streamlines; b) streamlines – enlarged; c) exit angles (scale on the left); d) changes of exit angle  $\alpha_1$  along datum +5 mm

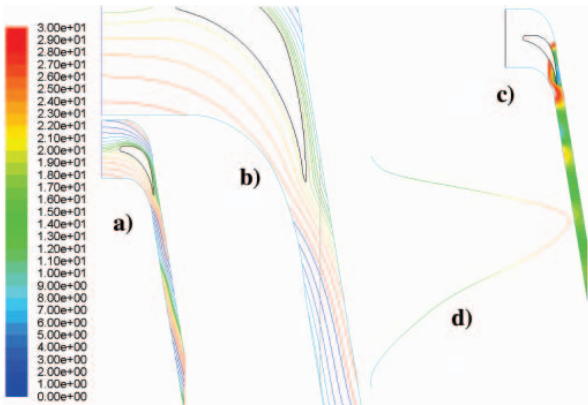


Fig. 16. Results of calculations for profile N3-60,  $\alpha_u = 36.58^\circ$ ,  $t/b = 1.0$ ; a) streamlines; b) streamlines – enlarged; c) exit angles (scale on the left); d) changes of exit angle  $\alpha_1$  along datum +5 mm

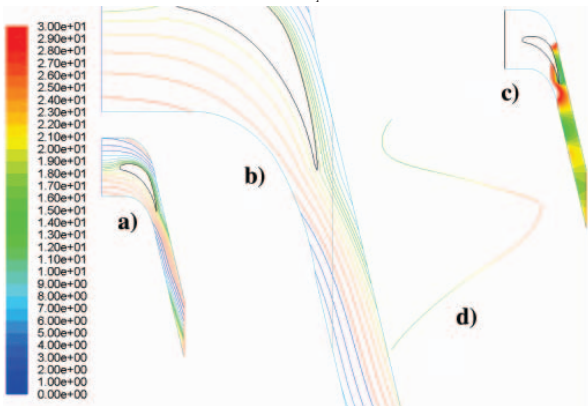


Fig. 17. Results of calculations for profile N3-60,  $\alpha_u = 40.58^\circ$ ,  $t/b = 1.0$ ; a) streamlines; b) streamlines – enlarged; c) exit angles (scale on the left); d) changes of exit angle  $\alpha_1$  along datum +5 mm

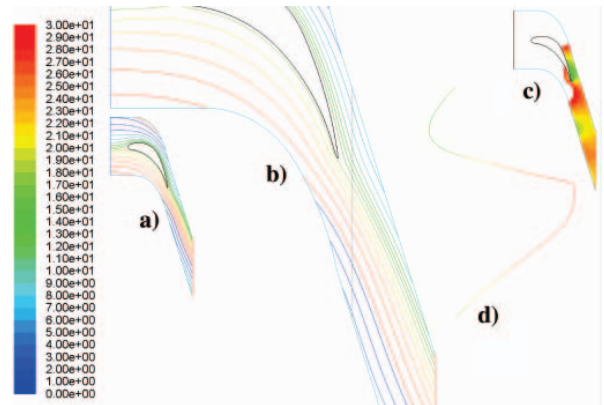


Fig. 18. Results of calculations for profile N3-60,  $\alpha_u = 44.58^\circ$ ,  $t/b = 1.0$ ; a) streamlines; b) streamlines – enlarged; c) exit angles (scale on the left); d) changes of exit angle  $\alpha_1$  along datum +5 mm

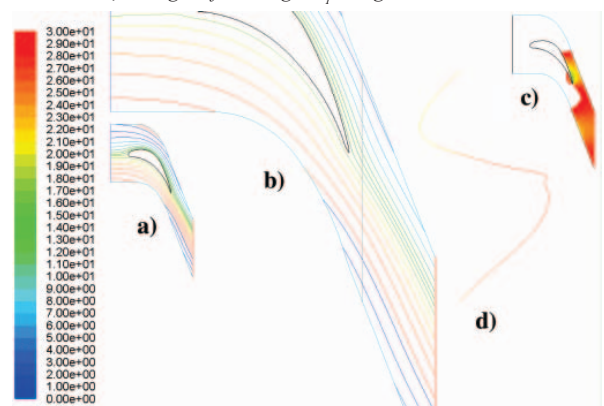


Fig. 19. Results of calculations for profile N3-60,  $\alpha_u = 48.58^\circ$ ,  $t/b = 1.0$ ; a) streamlines; b) streamlines – enlarged; c) exit angles (scale on the left); d) changes of exit angle  $\alpha_1$  along datum +5 mm

## COMPARING THE EXPERIMENTAL AND NUMERICAL RESULTS

The measured data presented in [1] include the exit angles  $\alpha_1$  in the form of the diagram shown in Fig. 20. These data were used as the reference for the calculations.

The comparison of the angles  $\alpha_1$  measured experimentally and calculated is given in Fig. 21. For small cascade profile stagger angles  $\alpha_u$ , we can observe remarkable differences between the experiment and calculation.

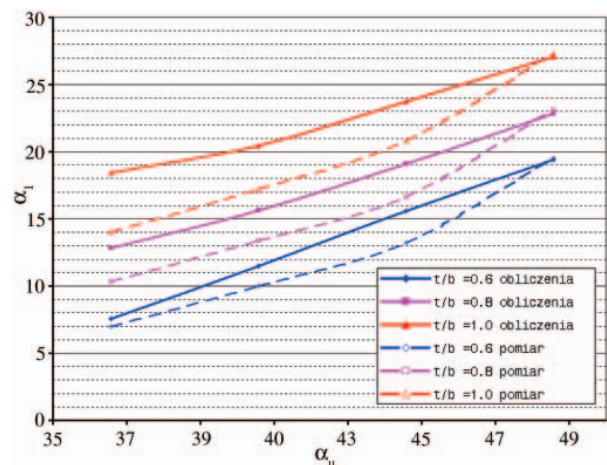


Fig. 21. Comparing exit angles  $\alpha_1$  obtained from measurement and calculations as a function of pitch  $t/b$  and stagger angle  $\alpha_u$

From the point of view of impulse turbine flow system calculations these difference are of high significance. For the

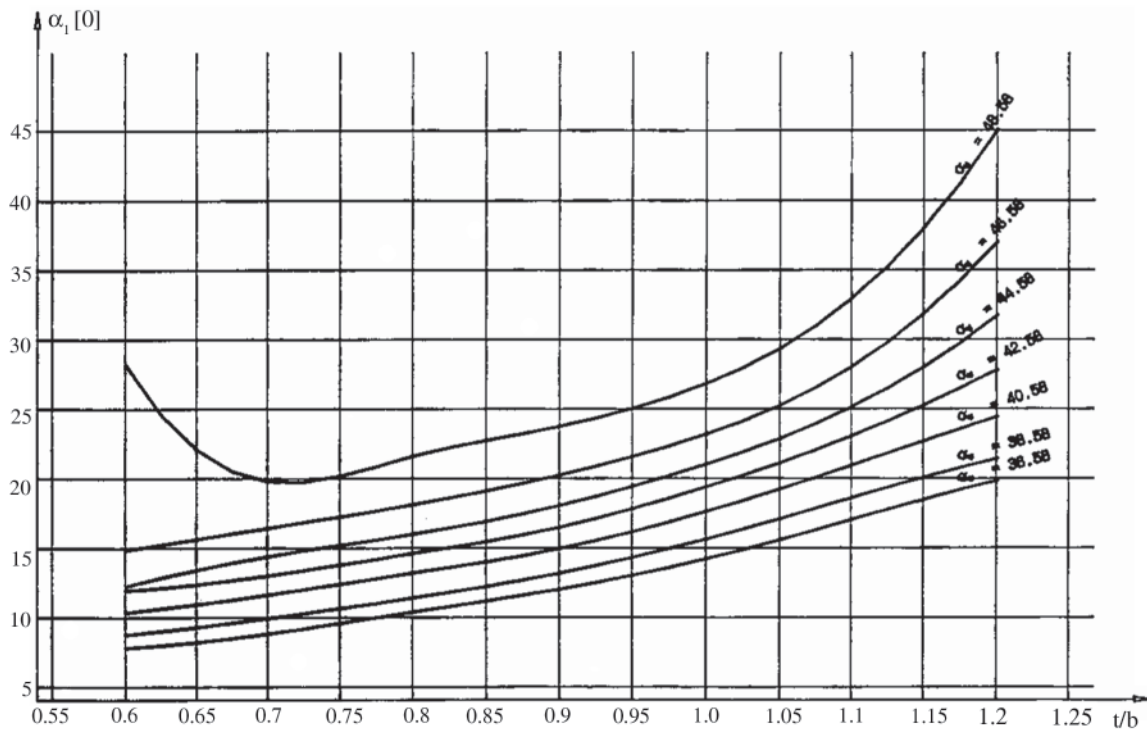


Fig. 20. Exit angles  $\alpha_1$  for profile cascade N3-60 vs. pitch  $t/b$  and stagger angle  $\alpha_u$  [1]

smallest stagger angles (about  $36^\circ$ ) this difference approximately equals to  $3^\circ$ . Taking into account that the exit angles in this area are within  $12^\circ$ - $15^\circ$ , the above difference corresponds to an error of an order of 20-30 %, which then leads to a similar error in assessing the mass flow rate through the turbine flow system. To better illustrate this problem, Fig. 22 shows the differences between the calculated and measured values:

$$\Delta\alpha = \alpha_{\text{obl}} - \alpha_{\text{pom}}$$

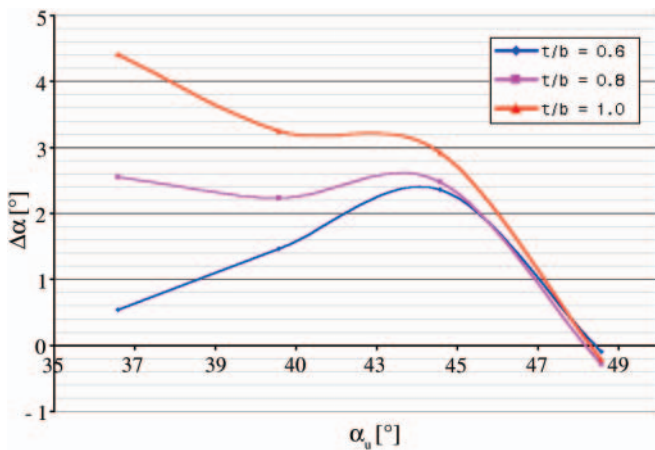


Fig. 22. Differences between measured and calculated exit angles  $\alpha_1$  vs. pitch  $t/b$  and stagger angle  $\alpha_u$

The diagram in Fig. 22 reveals that for large stagger angles in the N3 cascade, the differences between the measured and calculated angles are negligible. For smaller stagger angles, systematic increase of the difference between the calculated and real values is observed. Moreover, a remarkable effect of the cascade pitch on the range of these differences is observed.

In extreme cases, for large  $t/b$  and small stagger angles the difference between the measured and calculated exit angles can approximately reach as much as  $4.5^\circ$ .

#### BIBLIOGRAPHY

1. Thermal and flow characteristics of operation of turbine profiles and stages produced in ZAMECH. Report of the Czestochowa University of Technology (in Polish), 1988.
2. FLUENT 6.3 User's Guide, Chapter 11: Modeling Flows Using Sliding and Deforming Meshes.
3. R. Puzyrewski: Analysis of model turbine investigations of cylindrical stages. VIII Conf. on Turbines of Large Output 1984
4. R. Puzyrewski, P. Krzyślak: Parametric analysis of the efficiency function of radial impulse stages (in Polish) – IF-FM Report no. 334/94 – Gdańsk – 1994
5. Dobes, Fort, Halama, Kozel: Numerical simulation of a flow for turbomachinery applications – Con. INTERNAL FLOW – 2001.

#### CONTACT WITH AUTHORS

Biernacki Rafał, Ph. D.  
Faculty of Mechanical Engineering  
Gdansk University of Technology  
Narutowicza 11/12  
80-952 Gdansk, POLAND  
e-mail: rbiernac@pg.gda.pl

Piotr Krzyślak, Assoc. Prof.  
Faculty of Mechanical Engineering and Management  
Poznan University of Technology  
Piotrowo 3  
60-965 Poznan, POLAND  
e-mail: piotr.krzyślak@put.poznan.pl

# Operational causes of fatigue failures within passages of gas turbine engines

Zbigniew Korczewski, Assoc. Prof.  
Gdansk University of Technology

## ABSTRACT



*In this paper a short presentation of fatigue wear process of structural elements of gas turbine engines has been given. The primary causes of fatigue crack formation within engine mechanical system and flow passages have been highlighted. Special attention was paid to low-cycle fatigue associated with unsteady heat-and-gas-flow processes developed in the passages. The selected damages have been demonstrated of gas flow paths of the engines operating in aviation, navy and power industry, along with origins of their formation and growth.*

**Keywords:** gas turbine engines, passages, fatigue wear, operational failures

## INTRODUCTION

In the period of intensive investigations to improve operational reliability, durability and economic merits of gas turbine engines, a problem of effective methods of their technical state assessment becomes more and more important especially that in recent years a trend is observed of passing from the operation-based, planned maintenance to that based on current technical state, [1, 6, 7]. This is specially recommended when an unforeseen failure of engine is associated with a great hazard to traffic safety at sea, air and land [9, 14].

It is especially complicated to evaluate unserviceability states of turbine engine flow passages irrespective of an area of engine application. Technical state assessment traditionally performed on the basis of service measurements of gas-dynamic parameters does not bring satisfactory results in the case of fast developing surface defects of flow passages, which do not generate usually observable diagnostic symptoms. Service experience justifies that just most troublesome are flow passages of engine high-temperature part which is most exposed to thermal low-cycle fatigue whose consequences bring many hazards to engine safe operation. It is influenced by many factors, and the most important of them is associated with destructive and unavoidable effects of varying mechanical and thermal loads applied to elements of engines during their work in unsteady states [2, 3, 14].

## LOW-CYCLE FATIGUE

One of the parameters which impact turbine engine durability the most is fatigue strength of material of which

its structure is built. During engine operation on a ship cyclic elastic and plastic deformations of structural elements take place, which result from multifold changes of mechanical loads (caused by gas forces generated by thermal dynamic cycle of engine as well as by rotary motion inertia forces of rotor units) and thermal loads (resulting from temperature gradients within structural elements). They cause variable internal stresses developing finally resulting in fatigue cracks. With a view of initial causes of fatigue failure development the following can be distinguished:

- high-cycle fatigue (mechanical), which is characteristic for engine rotating units (engine rotor units) and occurs below yield point of structural material. Fatigue failures appear after a cycle number of load changes over  $10^4$  (usually over  $10^7$ ) [3,4,5,9];
- low-cycle fatigue (thermal) which concerns the engine elements exposed to high-temperature effects due to exhaust gas flow (combustion chamber, stationary load-carrying elements of turbine part) which occurs over yield point of material. Fatigue cracks appear already below the cycle number of load changes equal to  $10^4$  [3, 4, 5, 10].

Relation between stress amplitude and cycle number of load changes, at which structural elements become failed due to material fatigue, is represented by the so - called Wöhler curve [5,10].

High-cycle fatigue of rotating elements of turbine engine rotor units is caused by vibrations, that means resonance phenomenon to appear:

- *in global sense* when the entire engine suffers vibrations and then it constitutes a problem for designers,

- *in local sense* when one of the natural vibration frequencies of a given engine element,  $f_0$ , appears close to the frequencies of periodically changeable vibration exciting forces,  $f_{exc}$ . In this case the increasing of deformations and stress amplitudes takes place and after a longer period of engine's operation in such conditions a crack may appear in the element and its failure may happen due to material fatigue.

Maximum amplitude of resonance vibrations depends on stiffness and damping properties of supports of engine rotor units. The higher values of stiffness coefficients the smaller amplitude of resonance vibrations [1, 3].

Loss of stability of engine mechanical system under operation results from occurrence and development of the following detrimental phenomena:

- slowly worsening unbalance state of rotor units resulting from sediments, erosion, corrosion and bent shafts;
- sudden increase of unbalance state of rotor units resulting from broken-off fragments of a rotating element, e.g. a blade;
- exceedance of allowable load of bearings;
- rotors seizing in engine body elements in labyrinth sealings,
- appearance of self-exciting vibrations of rotor blades, mainly in compressors, (so-called flutter), during steady flow of working medium [11],
- air and exhaust gas pressure pulsations within flow passages, as well as due to non-uniform distribution of temperature and flow velocity around flow passage circumference.

Mechanical resonance phenomenon is of a very great influence on engine's serviceability and durability. However especially dangerous to its reliability is thermal fatigue of structural elements of combustion chamber and turbines, as a result of occurring unsteady processes such as start-ups, load changes (accelerations and decelerations), as well as engine turn-offs from operation.

For instance, during engine's starting-up, within a few seconds structural elements of combustion chamber are exposed to dynamic thermal loads characterized by instantaneous exhaust gas temperature increments reaching about  $80 \div 90$  K/s [16]. In the case of exceeding the allowable temperature gradients, pumping phenomenon and even that of structural material creeping and deformation of turbine blades can occur, Fig. 1.

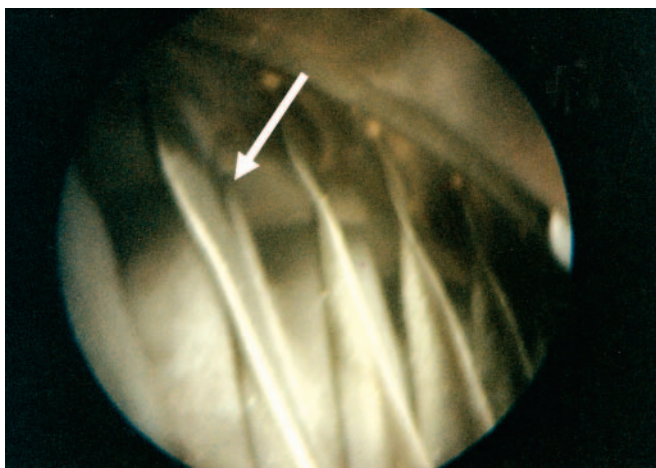


**Fig. 1.** Deformations of LP turbine rotor blades, resulting from structural material creeping (acc. endoscopic examination)

In extreme cases, local burning-off edges and tips of HP turbine blades can happen, Fig. 2 and 3. Such failures of ship engine flow part usually result from sudden and unforeseeable operational events such as:

- choking the exhaust gas outflow due to fire in outlet channel,
- choking the engine air inlet (frozen air inflow shutters, sucking-in random things such as protective covers of shipboard devices etc).

And, in the case of immediate stopping the engine during its operation in nominal (or near nominal) conditions, associated with eliminating idle running cooling phase, rotor seizure in turbine body may happen, Fig. 4 and 5.

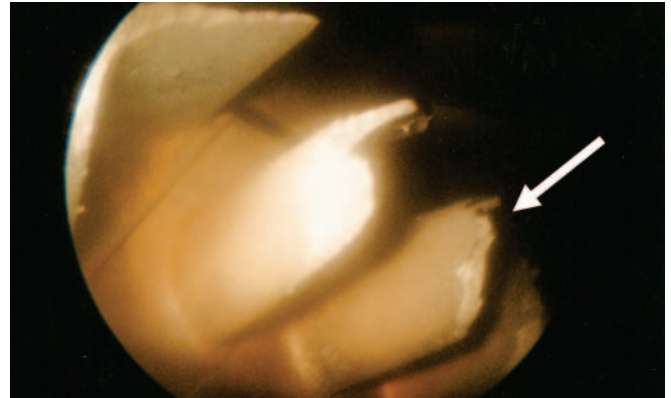


**Fig. 2.** Burnt-off tips of HP turbine rotor blades (acc. endoscopic examination)

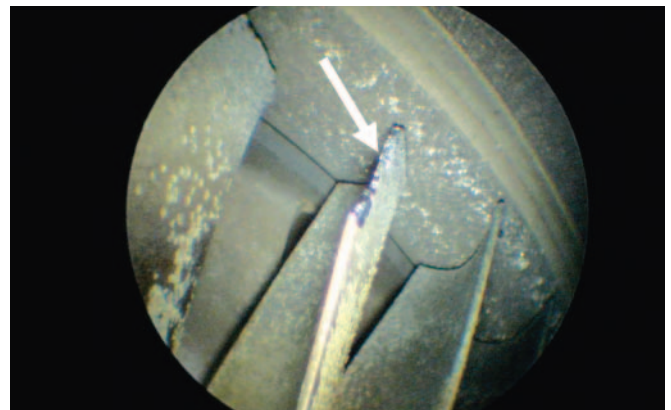


**Fig. 3.** Burnt-off tips of HP turbine rotor blades (acc. endoscopic examination)

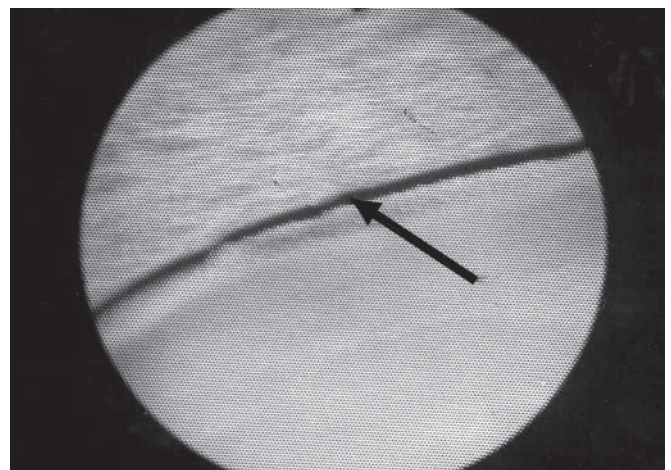


**Fig. 4.** Increased tip clearance of HP turbine blade with visible traces of seizing in engine body (acc. endoscopic examination)

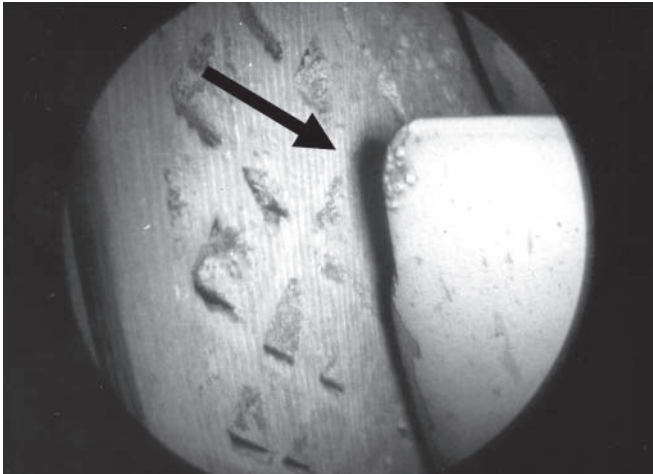
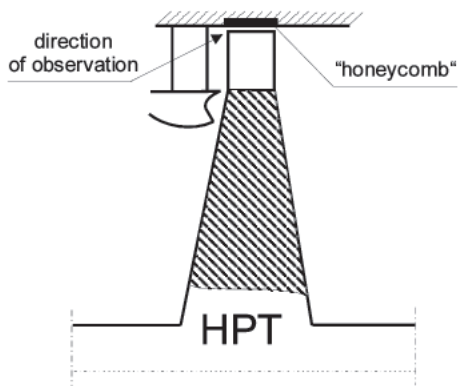


**Fig. 5.** Wear of sealing of HP turbine (HPT) rotor blades due to their seizing in engine body (acc. endoscopic examination)

It usually results in an intensive wear of body sealing of „honeycomb” type (Fig. 5), that in consequence leads to significant increasing the clearance of rotor blades of turbine and dropping its efficiency even by 10% [13]. It impairs efficient performance of entire engine because, as a result of increased radial clearance of HP turbine, character of distribution, to successive turbine stages, of disposed enthalpy drop becomes changed. The largest power drop occurs at the last turbine stages, i.e. engine propulsion turbine [12,13].

Another hazard to engine reliability, which results from rotor seizing in engine body, consists in possible cracking the compressor body, Fig. 6. The presented failure has been identified during endoscopic examination of a GTU6a single-shaft engine (of block structure) driving ship electric generating set. Compressor’s body was made of 40HNMA Cr-Ni low-alloy steel of a higher metallurgical purity. The situation occurred as a result of immediate switching-off the engine from operation under nominal load and passing over the cooling phase under idle running. Such decision of operators resulted from a fire observed in exhaust gas channel and entering the engine into unsteady operation range. After that the engine was dismantled and sent to its producer. Repair of the body consisted in vacuum electron-beam welding the crack.

On the basis of the character of the appeared failure of the compressor body it can be concluded that the initial cause of the crack was a material defect, e.g. presence of sulfides at place of fracture. In effect of action of dynamic loads the fatigue fracture propagating just from the edge of the material defect, was initiated. As a result of rotor seizing in the compressor body in the temperature of about 700-800 K, further propagation of the gap took place in the form of cleavage fracture. As the body was cooled more fast than the rotor the gap became separated mainly due to tensile forces (axial ones) with an influence of shear forces.

Designers of gas turbine engines take into account possible stopping the engine working under high load with passing over the cooling phase under idle-running. It is covered by manufacturer’s testing program. Therefore the seizing of rotor units in engine body should not happen at all. However in the described case the engine immediate stopping was preceded by its unsteady work when a flash-back towards engine intake took place causing an inadmissible, very intensive rise of compressor material temperature much over its permissible value of 520 K, determined by the manufacturer [15].

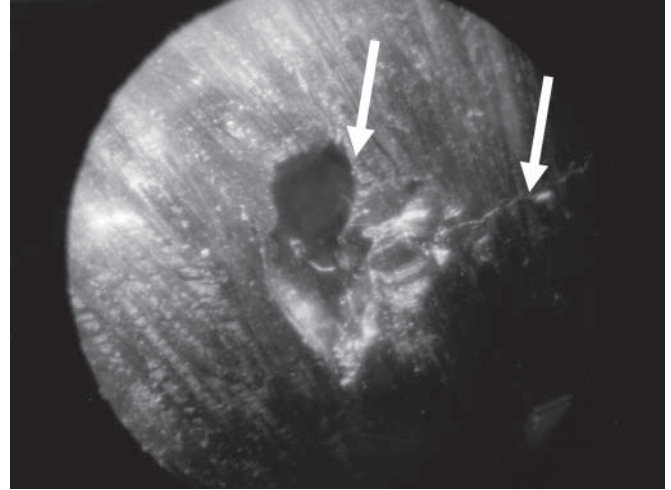


**Fig. 6.** Internal surface of GTU6a turbine engine compressor body, showing a fatigue fracture (acc. endoscopic examination)

The presented examples, despite their immediate destructive consequences to the engine’s reliability, had also secondary consequences to its durability. During every load change, deformations and thermal stress changes of engine structural elements took place. In elevated temperatures they exceed material yield point and cause plastic compression-tension deformations at every heating-cooling cycle of the material. It turns out that even after a small number of such cycles the material surface cracking of deformed elements can happen, which, while propagating into their structure, can lead to dangerous breaking-off a fragment of the structure. This is an especially hazardous defect in the case of combustion chamber flame tubes, Fig. 7. There are known initial causes of an aircraft crash of tragic consequences where due to low-cycle fatigue of flame tube material of one of the engines fatigue cracks in its structure occurred. During start-up of the engine a relatively large metallic fragment was broken out of it. The fragment protruded engine casing and wing sheeting and caused fuel to leak and in consequence a violent fire to break in the rear part of the fuselage, that took the toll of 60 persons [acc. Discovery Science].

If low-cycle fatigue characteristics of a structural material are known it can be possible to easily determine a number of cycles after which surface cracking may happen, depending on a single amplitude value of the strain  $\epsilon$  which occurs during one heating-cooling cycle of the material operation, Fig. 8.

From the numerical data given by the fatigue characteristics the conclusion can be made that if the engine, for example an UGT3000 Zorya engine, has to be started 2÷3 thou times during its life-time determined to be 12 years equivalent to 4 thou working hours, then one-sided deformations of the material (short-range local strain) should not exceed 0.2÷0.3 %, at each start-up, [15].

Stress concentration occurring in places of significant curvature changes of structural element outer surfaces (i.e. at notches) is conducive to local strains and fatigue fracture generation. Hence they appear mainly in necks of load-carrying

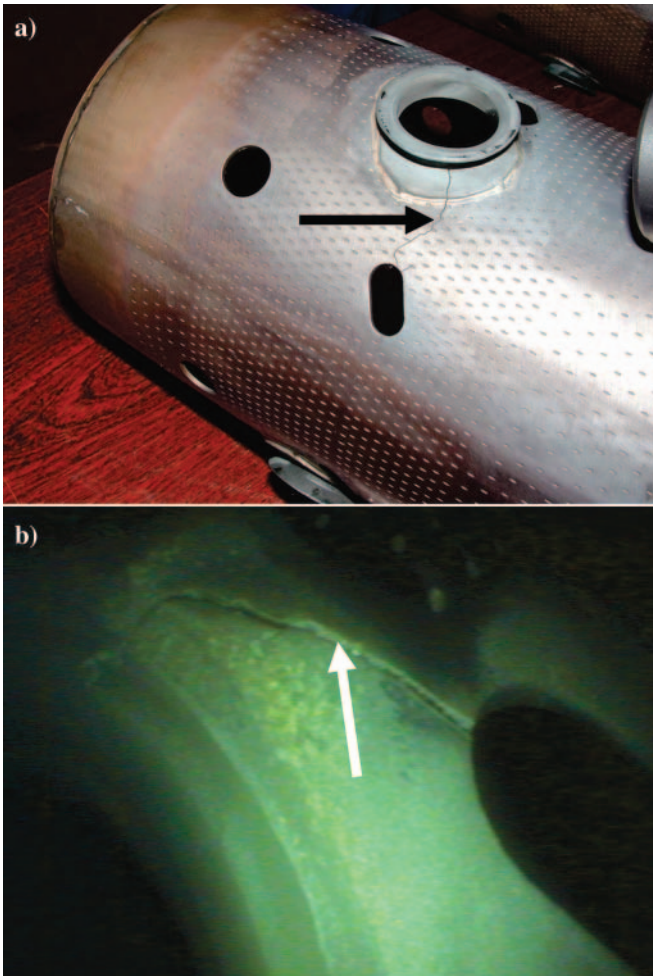


**Fig. 7.** Low-cycle fatigue fracture of flame tube of turbine engine combustion chamber: **a)** picture recorded just after the engine's dismantling; **b)** picture obtained by endoscopic examination

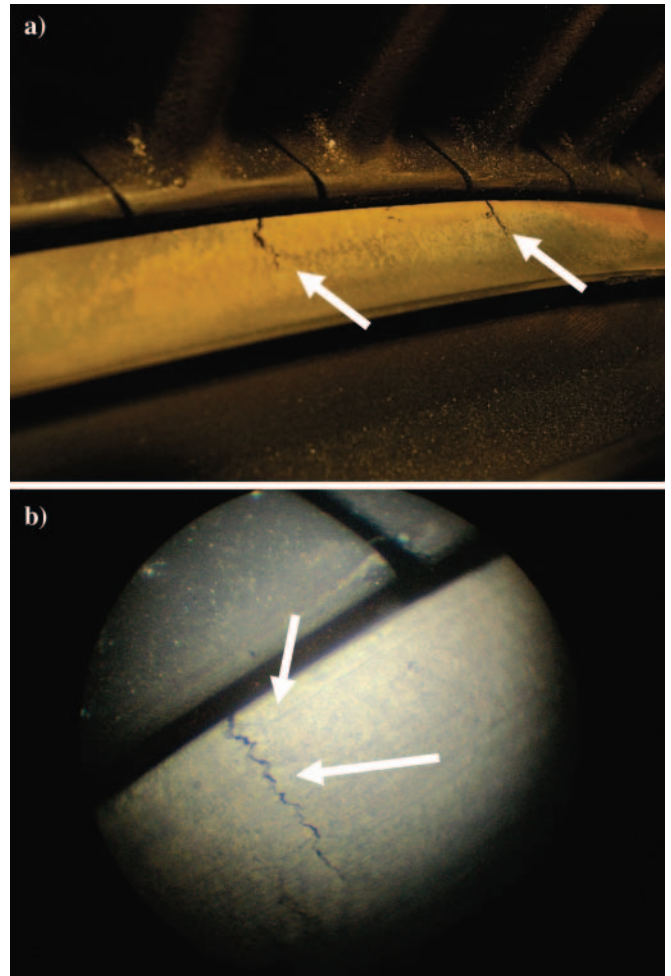


**Fig. 9.** Low-cycle fatigue fracture on internal body surface, under HP turbine guide vanes of a Zorya UGT3000 engine: **a)** picture recorded just after the engine's dismantling; **b)** picture obtained by endoscopic examination.

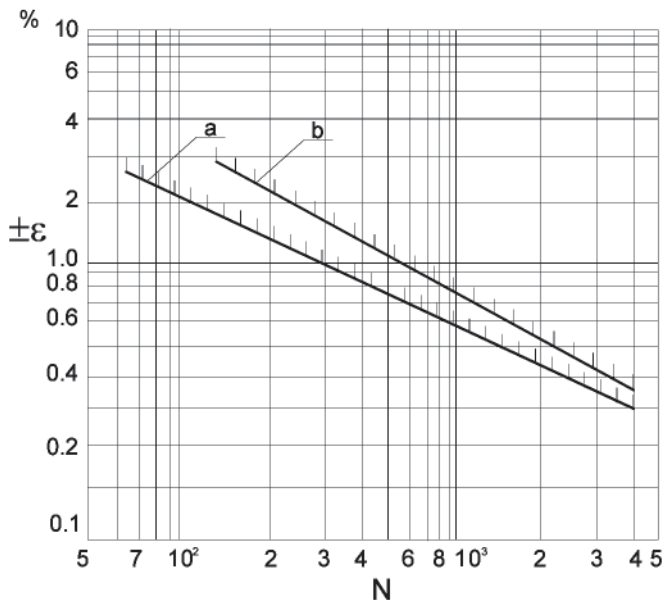


**Fig. 8.** Low-cycle fatigue characteristics:  $\epsilon$  – strain (single amplitude),  $N$  – number of cycles (heating - cooling), **a, b** – fatigue limit (shown for two different materials)

disks of rotors, in places of the greatest diameter changes, close to openings and gaps of combustion chamber flame tubes as well as in neighborhood of significant changes of profiled cross-sections of internal shell bodies, Fig. 9.

## CONCLUSIONS

- Crucial diagnostic problem of gas turbine engines is to be able to early detect and correctly identify initial failures of structural elements of engine flow part during early phase of their development.
- While analyzing the research results presented in this paper it seems impossible to overestimate importance of new possibilities introduced, to the aspect in question, by more and more dynamically developing endoscopic methods.
- On the basis of available statistical data as well as results of the author's research it can be concluded that in present about 60% of all recorded failures of flow part of turbine engines is detected by means of endoscopic methods, which are also identified by other diagnostic methods.
- However in the case of fatigue failures endoscopy effectiveness is even higher, provided the diagnosing personnel is well experienced and possesses deep knowledge on probable places of occurrence and characteristic features of surface defects which have been so far happened in engines of given type series.

## BIBLIOGRAPHY

1. Boliński B., Stelmaszczyk Z.: *Aircraft drives. Operation of turbine engines* (in Polish). WKiŁ (Traffic and Telecommunication Publishers), Warsaw 1981
2. Cohen H., Rogers G.F.C., Saravanamuttur H.I.H.: *Gas turbine theory*. Longman Scientific & Technical, New York 1987
3. Dzierżanowski P. et al.: *Aircraft drives. Turbine propeller and helicopter engines* (in Polish). WKiŁ, (Traffic and Telecommunication Publishers), Warsaw 1985
4. Kocańda S., Szala J.: *Background of fatigue calculations* (in Polish). PWN(State Scientific Publishing House), Warsaw 1985
5. Kocańda S.: *Fatigue fracture of metals* (in Polish). WNT (Scientific Engineering Publishers), Warsaw 1985
6. Korczewski Z.: *A method for diagnosing flow part of ship gas turbine engine in service* (in Polish). Doctor thesis. AMW(Polish Naval Academy), Gdynia 1992
7. Korczewski Z.: *Diagnostic-purpose identification of gas-dynamic processes in gas turbine engine compressor unit* (in Polish). AMW (Polish Naval Academy), Gdynia 1999
8. Korczewski Z.: *Endoscopy of ship engines* (in Polish). AMW (Polish Naval Academy), Gdynia 2008
9. Lewitowicz J., Wieczorek O., Żyłuk A.: *Damages of structural components and units of a gas turbine engine*. Journal of Polish CIMAC, Diagnosis, Reliability and Safety, Vol. 4, No. 2/ 2009
10. Neimitz A.: *Fracture mechanics* (in Polish). PWN(State Scientific Publishing House), Warsaw 1998
11. Rządkowski R.: *Flutter of turbine rotor blades in inviscid flow*. AMW (Polish Naval Academy), Gdynia 2004
12. Szczeciński S.: *Aircraft two-rotor and two-flow turbine engines* (in Polish). WKiŁ (Traffic and Telecommunication Publishers), Warsaw 1971
13. Szczeciński S.: *Study on tip clearance of rotor units of aircraft turbine engines, taken as a design and operation parameter* (in Polish). Appendix to Bulletin of WAT(Military Technical Academy), No.4 (248), Warsaw 1973
14. Soares C.: *Gas turbines. A handbook of air, land and sea application*. Butterworth-Heinemann, Elsevier Inc. 2008
15. *Technical and operational documentation of ship gas turbine engines of the types: GTU6a, DE59, UGT Zorya, LM2500 General Electric*.
16. *Reports on diagnostic tests of piston and turbine combustion engines used on Polish Navy ships* (in Polish). Research projects, AMW (Polish Naval Academy), Gdynia 1992 ÷ 2008.

---

### CONTACT WITH THE AUTHOR

Zbigniew Korczewski, Assoc. Prof.  
Faculty of Ocean Engineering  
and Ship Technology  
Gdansk University of Technology  
Narutowicza 11/12  
80-233 Gdansk, POLAND  
e-mail : sek4oce@pg.gda.pl

# Diagnostics, maintenance and regeneration of torsional vibration dampers for crankshafts of ship diesel engines

Wojciech Homik, Ph. D.  
Rzeszow University of Technology

## ABSTRACT



*Periodically changeable gas and inertia forces which occur during operation of engine generate transverse, axial and torsional vibrations of crankshafts of multi-cylinder combustion engines. Torsional vibrations are those which endanger crankshafts of multicylinder combustion engines the most. In order to minimize their impact a torsional vibration damper is installed at crankshaft's free end. Its technical state directly influences lifetime and reliability of engine. In this paper methods of diagnosing, maintenance and regeneration of torsional vibration dampers used in shipbuilding, are discussed. Also, are presented results of multi-year statistical investigations carried out in cooperation with a firm maintaining and regenerating ship engine torsional vibration dampers, which illustrate types of failures occurring in viscous and spring torsional vibration dampers.*

**Keywords:** crankshaft, torsional vibrations, damping of torsional vibrations, torsional vibration dampers, durability and reliability of multi-cylinder engine, diagnostics, maintenance, regeneration

## INTRODUCTION

Multi-cylinder combustion engine in operation generates vibrations which directly and detrimentally impact lifetime of engine's parts and the whole propulsion system.

Crankshaft is one of many engine's parts which is exposed to effects of forced vibrations. Periodically changeable gas and inertia forces occurring in piston combustion engines generate:

- transverse vibrations (Fig. 1a)
- axial vibrations (Fig. 1b)
- torsional vibrations (rys. 1c)

which produce, by affecting flexible engine crankshaft, its changeable deformations [1, 2].

Transverse vibrations produce bending deformations of crankshaft between its support points, i.e. main bearings. However they do not endanger the crankshaft seriously because it has a low transverse flexibility resulting from the way of its bearing in engine's body. Practically every crank of the shaft is supported by main bearings. Due to crankshaft's design solution itself also axial vibrations affect very seldom its operation especially in the case of engines used for propulsion of land vehicles. However such vibrations are able to generate failures of ship propulsion engine more often.

Resonant torsional vibrations are most dangerous for engine's crankshaft [1,2,3], as - in contrast to transverse and axial vibrations - they do not propagate to other parts of the

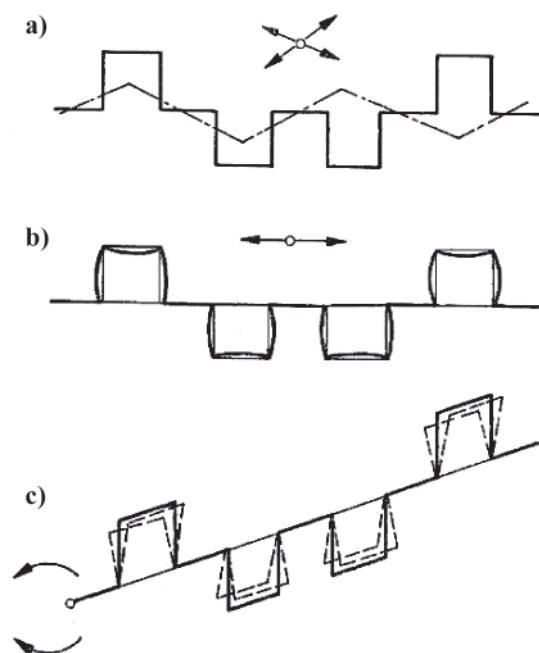


Fig. 1. Kinds of crankshaft vibrations: a) transverse, b) axial, c) torsional

engine, e.g. bearing casings, and in many cases they also do not generate noise which is a factor informing engine's operator on an incorrect work of the engine. It results from that torsional deformations of cranks of the shaft are generally not restrained

by any factor except its rigidity hence torsional vibration amplitude can exceed allowable limits leading to twist damage of the crankshaft.

Users of combustion engines expect the engines used by them to be reliable and durable. Engine designers make all efforts to place frequency of k-th harmonic of excitation force as far away as possible from natural torsional frequency of engine's crankshaft. In ship large multi-cylinder engines the problem can not be fully solved. For design and service reasons changes of engine rotational speed (service speed), run of excitation forces, or natural frequency of shaft are difficult to be made [4]. In such cases combustion engine designers decide to introduce an intermediate solution and apply vibration eliminators, i.e. torsional vibration dampers which are installed at free end of engine crankshaft (Fig. 2).



Fig. 2. a) 8S70MC-C diesel engine for ship propulsion [18], b) Crankshaft of RTA96 Wartsila-Sulzer diesel engine, the largest-in-the-world [16], 1- torsional vibration damper

Their task is to lower amplitudes of torsional vibrations of engine crankshaft. A correctly designed damper of torsional vibrations makes it possible to lower even ten times resonant amplitude of torsional vibrations [5,6,7]. However it should be remembered that every damper consumes a part of engine's effective output.

For years to minimize hazard resulting from torsional vibrations in ship diesel engines the following types of dampers have been applied:

- frictional dampers,
- rubber dampers,
- viscous dampers,
- spring dampers.

The above specified dampers are typical dynamic ones in which inertia force is used to damp torsional vibrations.

Despite their common name the dynamic dampers differ to each other not only by design solutions but also operational characteristics (Fig. 3) [8].

Irrespective of an applied design solution to dynamic damper, its technical state is decisive of its effectiveness, which greatly depends on service conditions of engine at which the damper is installed. As majority of torsional vibration dampers operate in periodically changeable conditions (e.g. changeable rotational speed) or changeable atmospheric conditions the dampers should be periodically diagnosed like other devices to ensure correct operation of engine.

Practically it is not possible to elaborate universal diagnosing methods for all kinds of dampers of ship engine torsional vibrations. This mainly results from differences in their design.

Every producer of dampers should have at his disposal effective methods for diagnosing vibration dampers to make it possible to check if a given used damper still maintains its effectiveness. One of the damper's effectiveness criteria can be magnitude of torsional vibration amplitude of the shaft at which the damper is installed:  $|\varphi_{\max}| \leq \varphi_{\text{dop}}$ . However the criterion can be insufficient for assessing damper's effectiveness. Taking the fact into consideration, the damper producers should require - from the side of operators of the engines at which torsional vibration dampers are installed - to perform periodical diagnostic tests and overhaul of the dampers with help of personnel of specialist firms or certified servicemen. Irrespective of a design solution, all torsional vibration dampers fixed on ship engine crankshafts should be subjected to periodical survey every  $18000 \div 20000$  hours of operation.

## DIAGNOSTICS OF FRICTION TORSIONAL VIBRATION DAMPERS

Friction torsional vibration dampers of Lanchester type have been the first applied to damping torsional vibrations of ship engine crankshafts (Fig. 4).

In such dampers the inertia ring's motion relative to the boss rigidly connected with the engine crankshaft is possible to be realized only when the inertia force moment  $M_p$  of the active inertia  $I_p$  is greater than the friction moment  $M_f$ . During the motion resulting from dry friction between friction linings, torsional vibration energy is transformed into heat and discharged to the environment [9].

Motion of the inertia ring relative to the fixed boss, due to high frequency of vibrations and the amplitude of crankshaft torsional vibrations  $\varphi_{\max} > \varphi_{\text{dop}}$ , results in an intensive wear of friction lining which leads to changing value of friction force and the so - called detuning of the damper.

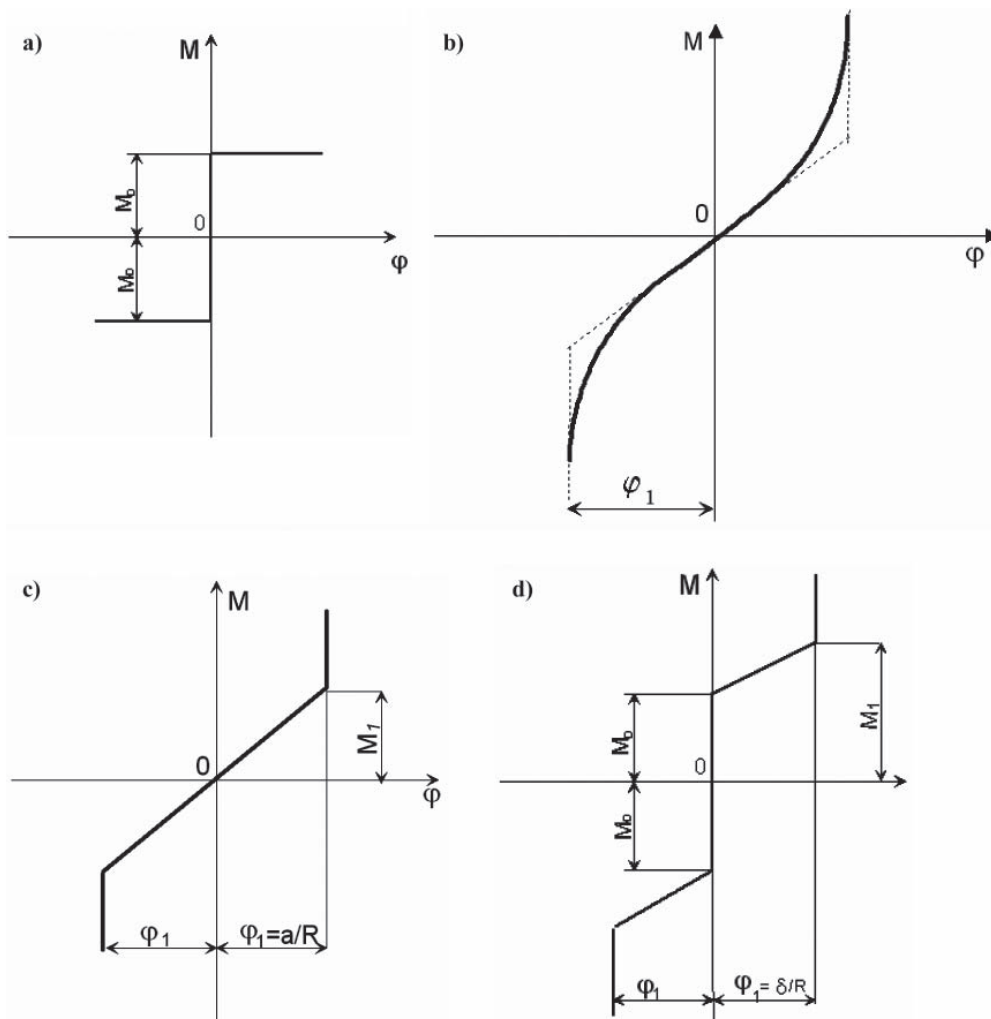


Fig. 3. Operational characteristics of dampers: a) Lanchester's frictional damper, b) a damper of non-linear characteristics, c) a spring dynamic damper of linear characteristics, d) a spring damper of prestrained springs

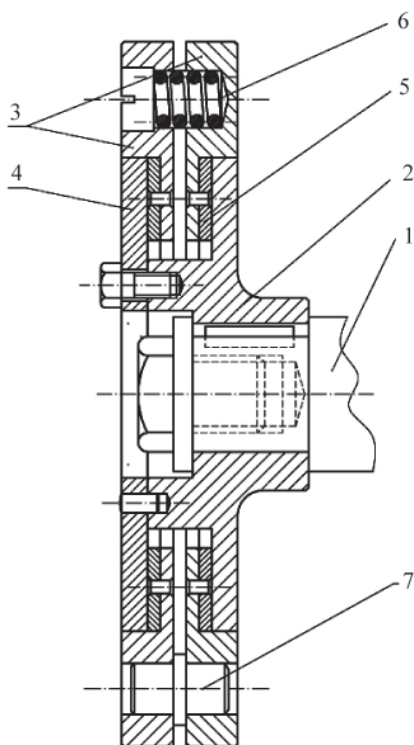


Fig. 4. Friction torsional vibration dampers of Lanchester type: 1) shaft, 2) boss, 3) inertia ring, 4) disc, 5) friction lining, 6) tension spring, 7) driving dog

The fact directly impacts effectiveness of the damper and forces the engine operator to perform its frequent monitoring and maintaining.

Control of friction torsional vibration damper is limited to checking quality state of friction surfaces and regulation of holding down force of linings with the use of the tension springs. In justified cases, i.e. when wear of friction lining exceeds a limiting value, producers of the dampers recommend definitely their replacement.

Lack of possibility to maintain value of the friction moment  $M_f$  constant during operation of the damper results from difference in rate of wear of friction linings as well as from getting water, oil or mechanical contaminations between friction surfaces. Despite their doubtless merits the friction torsional vibration dampers have fallen short of expectations put in them and have been soon replaced by other dampers.

## DIAGNOSTICS OF RUBBER TORSIONAL VIBRATION DAMPERS

In shipbuilding industry rubber torsional vibration dampers were first time used in 1915. Big hopes have been put in them but service experience has verified it within short time.

It has turned out that structure of rubber undergoes ageing, like many other organic materials, which results in increased viscosity, hardness or brittleness [10, 11]. Rubber ageing process results from action of oxygen as well as ozone contained in air and it very fast develops in high temperature. As a result of

ageing rather large decrease of rubber strength properties as well as significant drop of its resistance to periodically changing loads takes place.

Lack of stable physical properties of rubber, connected with the above described phenomena, has not provided the rubber torsional vibration dampers with a greater role in shipbuilding industry. At the end of the 1950s application of rubber dampers was practically terminated. In spite of that they have been still in use on some older floating units.

Their short lifetime does not up to now prevent designers of car engines from their successful application. It mainly results from that car engine's lifetime is much lower than that of ship engine and is equal at the most to about 2000000 km (trucks, buses). As results from tractional tests of car combustion engines fitted with rubber torsional vibration dampers their operational effectiveness drops after about 180000 km of mileage.

The rubber torsional vibration damper consists of the boss and plunger connected to each other with the use of the rubber ring (Fig. 5). The rubber ring has an appropriate hardness, flexibility and internal damping.

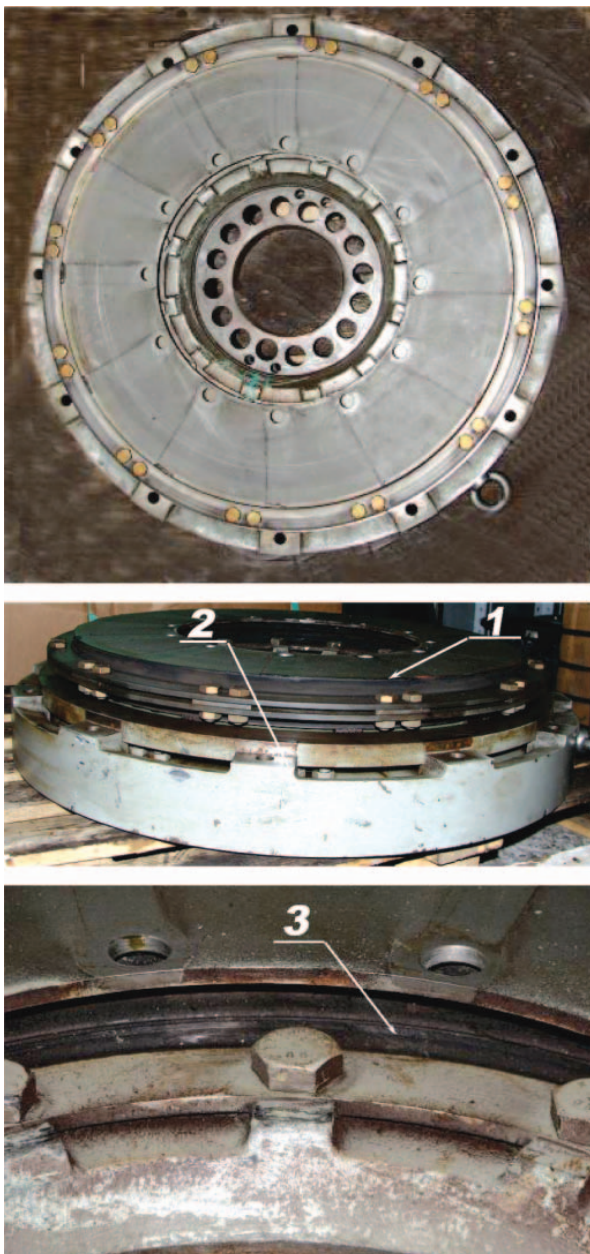


Fig. 5. A rubber torsional vibration damper undergoing overhaul in DAMPOL Co.: 1) inertia ring, 2) boss, 3) rubber damping element

Irrespective of damper's design solution and application (either to ship or car engines) their producers recommend to perform periodical survey mainly from the point of view of technical state of rubber. Producers of rubber dampers consider them to be disposable, i.e. those which should be replaced by new ones after a given period of service (ship engines) or mileage (car engines). As a rule their producers do not provide for any repair or regeneration of such dampers.

## DIAGNOSTICS AND REGENERATION OF VISCOUS TORSIONAL VIBRATION DAMPERS

In 1929 in U.S. shipbuilding industry viscous torsional vibration dampers were applied to damping torsional vibrations of governors of 3000 HP engines installed on submarines [12]. However no satisfactory results were obtained [13] though an innovative, as in those days, solution consisting in parallel connection of two dampers filled with different viscosity liquids, was used. The main reason of the failing was application, as damping medium, of silicone oil produced from organic compounds, whose viscosity was dramatically decreasing along with the increasing of operational temperature of the damper. The high operational temperature had also decisive impact on oil ageing rate, hence also on the damper's reliability and lifetime. The doubtless drawback of the viscous torsional vibration dampers resulted in that for many years they have been not applied at all.

They experienced their renaissance at the end of the 1950s when Dow Corning Corporation introduced engine oils on the market, whose physical properties ensured to obtain appropriate technical parameters of dampers in question. The improved effectiveness of the „new” damper made that it squeezed the friction and rubber dampers, out of the market, which have been applied so far, especially in shipbuilding industry.

The viscous torsional vibration dampers are composed of the tight casing filled with silicone oil, in which the inertia ring floats (Fig. 6) [5].

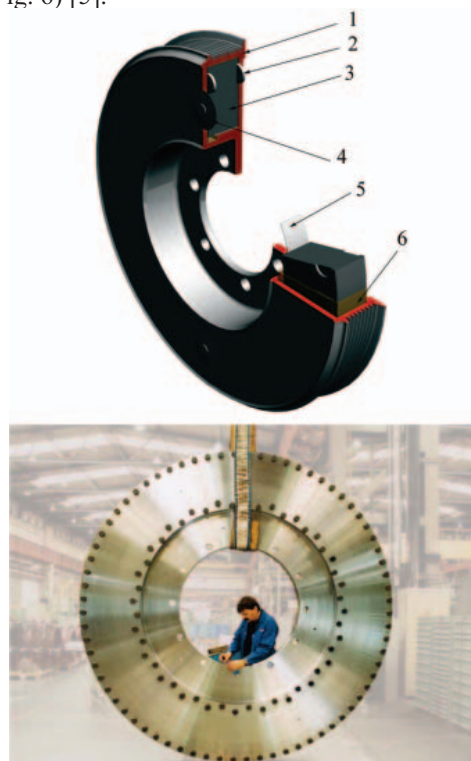


Fig. 6. Structural arrangement of a viscous torsional vibration damper and a view on a marine viscous torsional vibration damper [17]: 1) casing, 2) axial bearing, 3) inertia ring, 4) plug, 5) journal bearing, 6) oil

Diagnostics of such dampers depends on their design solutions. In present two design solutions are applied in industry: non-dismountable dampers (in car industry) and dismountable dampers (in shipbuilding industry).

Diagnostics of viscous torsional vibration dampers consists first of all in checking the vibration amplitude criterion and then measuring value of damping liquid viscosity [13].

Testing samples of the liquid (oil) should be taken from the damper being in neutral environment in order not to cause connection of oxygen and hydrogen atoms and tearing this way particle bonds and lowering real viscosity of the oil [14]. In the case of stating an inappropriate viscosity of the tested oil its replacement is recommended after very accurate cleansing all parts of the damper.

Statistical tests showed that the decreasing of oil viscosity during operation of dampers is a natural factor (Fig. 7). In many cases during diagnosing it turned out that it was not possible to take oil samples as its actual viscosity was several times or even a few dozen times greater than its initial viscosity (Fig. 8). The so significant increase of oil viscosity leads to the inertia ring immobilizing, hence to the situation in which the damper becomes a vibration exciter.

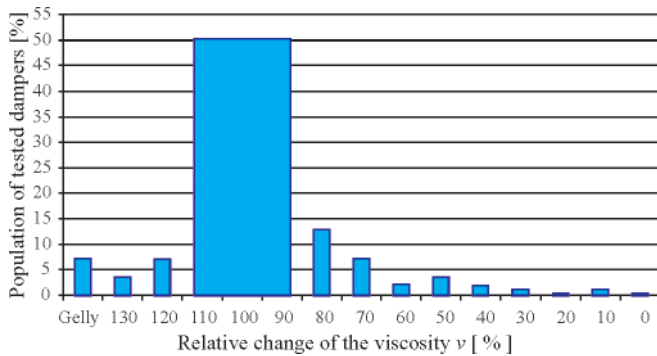


Fig. 7. Statistical results of testing the dampers fitted with bronze bearings,  $v [\%] = v_{real}/v_{initial} \cdot 100\%$

Kind of material used for inertia ring and its journal bearings and axial ones greatly influences changes of silicone oil viscosity and thereby damper's lifetime [14].



Fig. 8. Used silicone oil (solidified material) stuck to the casing of the viscous torsional vibration damper

Regeneration of viscous torsional vibration dampers consists in a.o. replacing their journal and axial bearings made of bronze with the bearings made of PTFE teflon.

Effectiveness of such operations is confirmed by results of statistical tests shown in the diagrams of Fig. 9, from which it results that in the case of replacing bronze bearings with teflon ones the above described phenomenon of the large increase of oil viscosity due to diffusion occurring at the place of contact between bearing and casing, was almost entirely eliminated, thereby mechanical failures of inner surfaces of the damper were prevented.

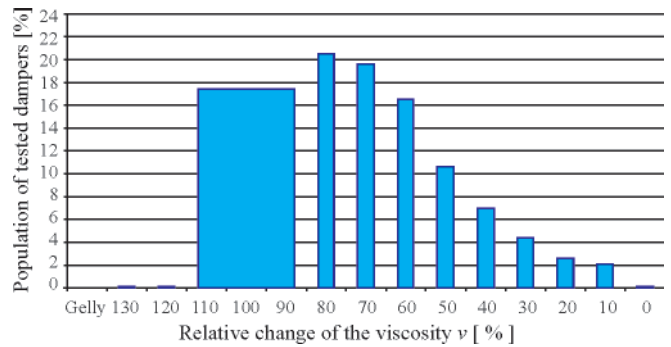


Fig. 9. Statistical results of testing the dampers fitted with teflon bearings,  $v [\%] = v_{real}/v_{initial} \cdot 100\%$



Fig. 10. Failures of inner surfaces of a viscous torsional vibration damper

In the case if mechanical failures on inner surfaces are disclosed during diagnosing the damper (Fig. 10) their regeneration is strongly recommended (turning the damaged surfaces and their repair by welding in justified cases). During

regeneration of inner surfaces of a damper, changes of their geometrical parameters occur thereby also changes take place of dynamic properties of the damper. In such cases the damper should be filled with a liquid of a greater viscosity than that initial in order to restore appropriate effectiveness of the damper.

Tightness of the damper constitutes a factor of great influence on its correct operation. During overhaul of the damper its sealing is replaced and after its closing and filling its tightness test is performed.

Also, non-dismountable viscous torsional vibration dampers, like the above described rubber dampers, are not subjected to repair and regeneration and considered by their producers to be disposable parts.

## DIAGNOSTICS AND REGENERATION OF SPRING TORSIONAL VIBRATION DAMPERS

Research on a spring torsional vibration damper was initiated in 1958 when it turned out that viscous vibration dampers did not effectively lower crankshaft torsional vibrations in power system engines. The first spring damper was manufactured by Geislinger firm and installed on the Danish ferry „Holger Danske” in 1962. The spring torsional vibration damper, like rubber one, is composed of a boss and inertia ring mutually connected with the use of flexible elements in the form of spiral springs, packets of flexible pads and bush springs.

Today such dampers can be commonly found in ship propulsion engines as well as large power plants.

Two types of spring dampers are presently produced for shipbuilding industry:

- Bush spring damper acc. Pielstick design (Fig. 11)
- Damper with packets of straight springs (radial springs) acc. Geislinger design (Fig. 12).

As compared with viscous torsional vibration dampers the spring dampers are characteristic of:

- smaller dimensions,
- small inertia moment of inertia ring relative to mass inertia moment of boss,
- greater resistance to mechanical failures,
- greater lifetime,
- higher allowable temperature of operation.

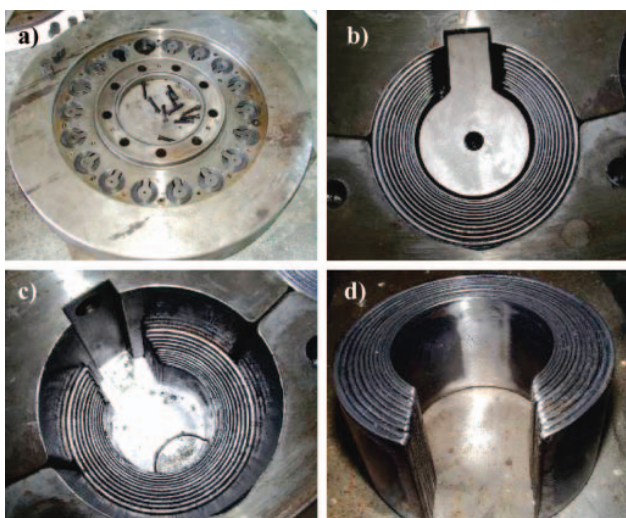


Fig. 11. Ship engine's spring torsional vibration damper with double packet of torsional springs, of Pielstick design: a) general view, b) socket with two packets of springs, c) socket with single packet of springs, d) packet of springs

Spring dampers should be serviced once a year at least and their overhaul should be performed after about 20000 h of operation. Apart from checking the basic effectiveness criterion (amplitude criterion) of such damper its overhaul consists mainly in:

- control of its tightness (after about 2000 h of operation),
- control of patency of lubricating channels through which oil is delivered between cooperating surfaces of boss and inertia ring,
- examination of technical state of flexible elements (springs, packets of springs) from the point of view of possible mechanical failures,
- control of technical state of bronze intermediate sliding pads.

In spring dampers, depending on design solutions, geometrical parameters of the sockets in which springs or packets of springs are placed, should be also controlled, especially in the case of the dampers with prestrained springs. In the case of the dampers with packets of radial spring plates (Fig. 12) the side clearance „z” between side surfaces of springs and sockets should be checked (Fig. 13).



Fig. 12. Spring torsional vibration damper with packet of radial springs, of Geislinger design

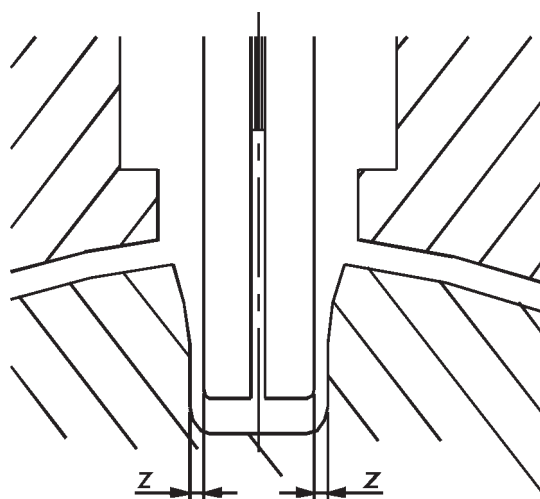


Fig. 13. Side clearance „z”

Values of the clearances depend on damper's size and reach a few dozen micrometers.

Statistical tests confirm that spring torsional vibration dampers are characterized by high reliability and their diagnostics consists mainly in adjustment of magnitude of clearances. (Fig. 14).

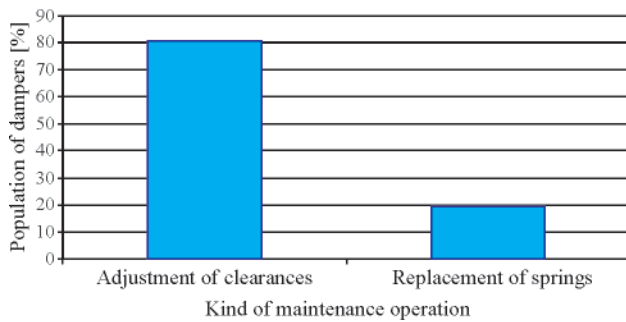


Fig. 14. Statistical results of testing the spring torsional vibration dampers

## CONCLUSIONS

- Repair or regeneration of all the above discussed dampers is associated with their disassembling off the crankshaft at which it is fixed, and their dismantling into parts. Before starting the damper's disassembling its position relative to the crankshaft should be marked and before its dismantling mutual position of all its parts should be also appropriately marked.
- Precise technical parameters dealing with diagnosing and servicing the torsional vibration dampers are kept confidential. They are only at disposal of producers of the dampers as well as firms which are engaged in their maintenance and regeneration under supervision of the worldwide ship classification institutions such as: Germanischer Lloyd, det Norske Veritas, Lloyd's Register, Bureau Veritas, Polish Register of Shipping, Russian Register of Shipping.
- The presented results of testing the torsional vibration dampers carried out in cooperation with their producer [15] prove that majority of users of combustion engines fitted with torsional vibration dampers do not appropriately monitor their technical state. It leads to the situation in which a vibration damper is converted into a generator of vibrations or undergoes damage (Fig. 15).

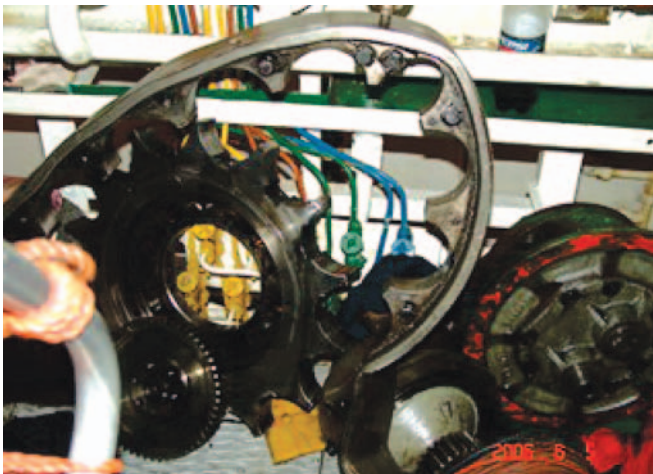


Fig. 15. A damaged spring torsional vibration damper of Pielstick [15]

Thorough capital repair of torsional vibration dampers are mainly performed during capital repair of entire ship propulsion systems.

## BIBLIOGRAPHY

1. Jędrzejowski J.: *Mechanics of crankshaft systems of car engines* (in Polish). WKiŁ, Warszawa 1986
2. Niewiarowski K.: *Piston combustion engines* (in Polish). Vol. I, II, WKiŁ Warszawa 1983
3. Homik W.: *Optimization of viscous torsional vibration damper* (in Polish), Doctor dissertation, Rzeszów 1997
4. Homik W.: *Designing viscous torsional vibration dampers* (in Polish). Przegląd Mechaniczny, October 2007
5. Homik W.: *Comparative analysis of torsional vibrations of engine crankshaft fitted with viscous damper and rubber one* (in Polish). 13th Scientific Conference on Vibro-acoustics and Vibro-engineering, Jachranka – Warszawa 2007; Przegląd Mechaniczny, November 2007
6. Homik W.: *Torsional vibrations of engine crankshaft fitted with rubber vibration damper* (in Polish). 18th International Conference SAKON: Computational and testing methods applied to development of car vehicles and self-propelled work machines, Rzeszów 2007
7. Homik W.: *Damping of torsional vibrations of crankshaft of multi-cylinder combustion engine* (in Polish). Transportna Akademia Ukraini, Praci Zachodnowo Naukowo Centrum 2009
8. Osinski Z.: *Damping of vibrations* (in Polish). PWN, Warszawa 1986
9. Giergiel J.: *Damping of mechanical vibrations* (in Polish). PWN, Warszawa 1990
10. Jaworski J.: *Rubber in mechanical vehicles* (in Polish). WKiŁ, Warszawa 1967
11. Pękala M., Radkowski S.: *Rubber flexible elements* (in Polish). PWN, Warszawa 1989
12. Wilson W. K.: *Practical solution of torsional vibration problems with examples from marine, electrical, aeronautical, and automobile engineering practice*. Chapman & Hall, London 1956
13. Homik W.: *Liquid viscosity changes during operation of a viscous vibration damper* (in Polish)., Przegląd Mechaniczny, March 2009
14. Homik W.: *Bronze or teflon bearing of inertia ring in viscous torsional vibration damper ?* (in Polish). Acta Mechanika Slovakia, 2008
15. DAMPOL: *Reports on maintenance and repair operations of torsional vibration dampers performed by DAMPOL firm* (in Polish).
16. [www.focus.pl/newsy/zobacz/publikacje/najwiekszy-wal-korbowy/](http://www.focus.pl/newsy/zobacz/publikacje/najwiekszy-wal-korbowy/)
17. [www.hassewrede.de](http://www.hassewrede.de)
18. [www.hcp.com.pl/hcp\\_oferta/ofe\\_silniki\\_02.html](http://www.hcp.com.pl/hcp_oferta/ofe_silniki_02.html)

## CONTACT WITH THE AUTHOR

Wojciech Homik, Ph. D.  
 Rzeszów University of Technology  
 The Faculty of Mechanical Engineering and Aeronautics  
 Al. Powstańców Warszawy 8,  
 35-959 Rzeszów, POLAND  
 tel.: 17 865 1100 w 1637, 17 865 1637  
 e-mail: whomik@prz.edu.pl  
 e-mail: whomik@interia.pl

# Correction of the combustion engine run irregularity in hybrid systems

Antoni Iskra, Prof.  
Poznan University of Technology

## ABSTRACT



*Possibilities of combustion engine – electric machine assembly run irregularity improvement have been presented in the following paper. Such system is the basic one in numerous hybrid car available on the market but the concept of using an electrical machine for reduction of rotational speed changeability amplitude in reciprocating machines could be utilized in any drive unit, especially in ship propulsion. This idea consists in generation of braking torque by the electric machine whenever the coupling shaft increases its rotational speed and vice versa, driving the system when the momentary speed is lower than the average speed within a complete shaft rotation.*

**Keywords:** hybrid drive, run irregularity

## INTRODUCTION

From the very beginning of its history an internal combustion engine which is one of the most important inventions initializing technical civilization created problems resulting from the changeability of torque transferred to the power receiver. Contrary to electric motors or turbines cyclicity of thermodynamic changes which cause the cyclicity of generated torque is the essence of reciprocating machine operation. However, there is no thermal machine as efficient as the piston engine in energy transformation from chemical to mechanical one. A question arises whether the basic disadvantage of reciprocating engine consisting in changeability of instantaneous speed within a single cycle could be eliminated. A flywheel, invention known from the very beginning of engine history serves as the device moderating the speed irregularity. Certainly, an increase in cylinder number contributes to the speed equalization as well. Unfortunately, both solutions used in almost every combustion engine bring about specific drawbacks. The flywheel increases weight of engine and vehicle as well. As a matter of fact a similar effect can be achieved by the increase in flywheel overall dimensions but hardly ever engine dimensions are defined by the flywheel. As the result dimensions and moment of inertia are the compromise of the possibly lowest speed irregularity and engine weight and dimensions. Without going into details one can assume that for a defined engine swept volume an increase in cylinder number leads to the deterioration of mechanical efficiency and to an increased specific fuel consumption as well. Other group of problems connecting with the subject of engine run irregularity are the torsional vibrations

within the range of unit natural frequencies. Following the development of combustion engines one can notice that the problems of resonance vibrations were the prime mover of the research on limitation of instantaneous speed change amplitude. Insufficient recognition of resonance vibration problem usually ends in a user dangerous failure consisting in the shaft breakup. The only solution that allow to avoid hazards is the use of torsional vibration dampers. Unfortunately, damping means energy dissipation and unavoidable increase in fuel specific consumption.

So what can be done to avoid the above mentioned disadvantages of solutions aimed at improvement of engine run irregularity?

The answer could be an application of hybrid drive to automobiles. There are forecasts that in a near future a considerable number of cars will be equipped with an arrangement facilitating the recovery of energy during braking and then using it to accelerate the car. However, the concept of application of electrical machine to the reduction in rotational velocity of reciprocating machines could be utilized in any drive unit including ship propulsion in particular. Such arrangement requires use of a set consisting of:

- generator that can operate as electrical motor,
- converter modifying the generated current to battery,
- suitable batteries.

In order to use the arrangement reasonably its power should correspond to the power of combustion engine, at least it should not be less than 10% of engine nominal power.

Tab. 1. Parameters of electrical energy accumulators where energy is freed as a result of reversible chemical reactions

Battery type	Energy concentration	Power concentration	Life span		Cost of energy concentration unit
			Number of charge cycles	Time of energy and power preservation k	
	kWh/kg	kW/kg	-	years	zł per kWh
Lead	0.03-0.04	0.2-0.3	300-400	2-3	400-600
Nickel-Cadmium	0.04-0.05	0.080-0.180	>2000 <sup>1)</sup>	3-10	2 500
Nickel-Metal Hydride (Ni-MH)	0.06-0.15	0.20-0.30	>1000	10	1200
Sodium-Nickel-Chloride (NaNiCl)	0.09-0.10	0.16	1000	5-10	1000
Lithium-Ion (Li-Ion)	0.09-0.14	0.30-0.60	500-750	4	1000-2000
Lithium-Polymer (Li-Po)	0.11-0.13	0.30	500	Data unavailable	1000
Zinc-Air	0.10-0.22	0.10	Data unavailable	Data unavailable	250
Capacitor	0.005	1-5	500 000	10	Very high
Target values	0.20	0.50	1000	10	100
Gasoline tank	8.5 or about 2 <sup>2)</sup>	1 limited by engine power	No limits	Practically no limits	2 or about 10 <sup>2)</sup>

<sup>1)</sup> on condition that user prevents so called memory effect caused by charging battery not fully discharged;

<sup>2)</sup> converted to the mechanical energy unit, which results from assumed efficiency of IC engine of about 25%

Amount of energy gathered cyclically in battery is not great. A simple calculation proves that amount of energy required for acceleration of a passenger car is far lower than that contained in start battery, i.e. about 1 kWh. As it turns out, so called energy concentration of known batteries is a crucial limitation. A classic lead battery of 100 Ah capacity and 12 V voltage can give back energy with satisfactory efficiency with power not exceeding 1 kW. So the use of batteries of higher capacity, e.g. 1000 Ah becomes a necessity in the hybrid arrangements. On that score a good solution is the use of high energy capacitors. High power concentration and low energy concentration are their properties. Table 1 presents basic properties of electrical energy accumulators, including high energy capacitors [1, 2].

The idea of hereby study is an evaluation of possibilities to make use of car hybrid drive in order to improve the engine run irregularity. In the case of ship propulsion the control of torque variability of the auxiliary electrical machine coupled to the piston engine of main propulsion in order to remove the rotational speed variable component is far easier thanks to the lower frequency of this component in comparison to the automobile drives.

### AN INSTANTANEOUS POWER OF IC ENGINE

A piston combustion engine generates momentary power far higher than the average one, i.e. power given by producer as nominal power. In principle, by the increase in cylinder number of an in-line engine one can achieve the mean power close to the instantaneous maximum power. Such direction of modifications leads to the improvement in the  $\delta$  engine run irregularity. Alas,

contrary situations also happen. Fig. 1 presents a course of torque momentary value generated by a 4-cylinder engine, while Fig. 2 presents the same for a 5-cylinder engine.

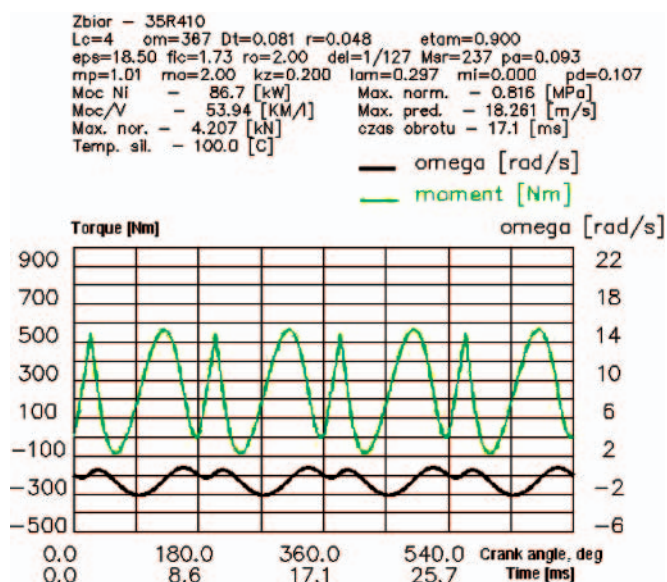


Fig. 1. Course of torque generated by an in-line 4-cylinder engine – green line and the course of speed produced by this torque

The run irregularity level  $\delta$  marked as “del” and the mean indicated torque marked as “Msr” can be found above charts in 3<sup>rd</sup> row. The relation of torque maximum value to its mean value is 2.4 for a 4-cylinder engine and 3.5 – for the 5-cylinder one.

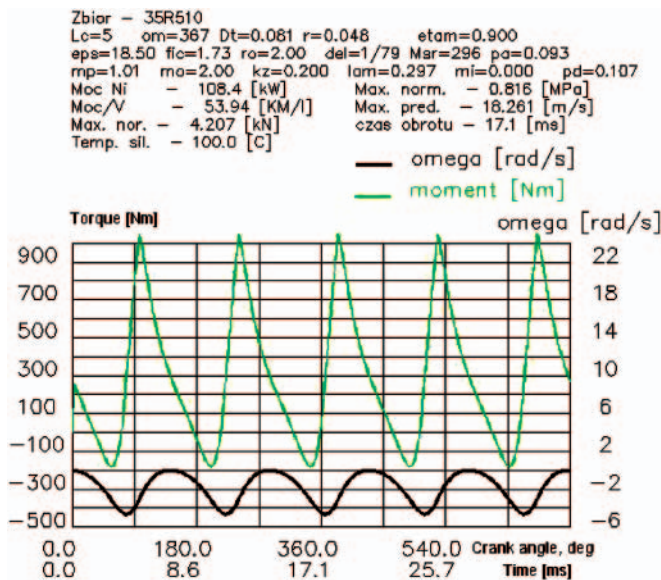


Fig. 2. Course of torque generated by an in-line 5-cylinder engine – green line and the course of speed produced by this torque

Presented examples show complexity of conditions affecting torque transmitted to the power receiver. Unfortunately, changeability of torque brings about negative results in form of vibrations which significantly increase the stress in power drive, i.e. in couplings, joints, gears and so on. These phenomena have been known for years. A counteraction consists in definition of vibration amplitude at resonance caused by a certain harmonics of torque and eventual check if admissible stress has not been exceeded in parts of drive train. Numerical methods used nowadays allow to predict parameters of vibrations generated simultaneously by all harmonics at any moment of engine run. Examples of such considerations will be presented in the next chapter.

## PARAMETERS OF ENGINE TO POWER RECEIVER COUPLING

Moment of force and instantaneous speed are the principal parameters of engine to power receiver coupling. On a real object these parameters vary independently of any rules. Hence, classic method of determination of natural frequencies produced by a specific harmonics does not allow to define the probability of exceeding permissible parameters with satisfying accuracy. The process of vibrations develops in time and only determination of real parameters of the phenomenon in sufficiently long time secures unfailling transmission of the torque to a power receiver. Therefore exists a need for definition of torque and instantaneous rotational speed in order to predict possible problems in the drive train. Definition of parameters of drive transmission using the numerical methods seems to be a simple task. Fig. 1 presents a schematic of drive train from IC engine to power receiver.

The mass moments of drive train elements inertia are marked as  $\Theta$ , the reduced length of elastic elements connecting inertial elements – L while the dumping between inertia elements – C. The key elements of drive train are:

- crankshaft of the  $\Theta_1$ ,  $L_{12}$  and  $C_{12}$ , i.e. reduced moment, reduced length and damping, respectively,
- flywheel of inertia moment  $\Theta_2$  – stiffly coupled to the crankshaft, reduced length  $L_{12}$  and dumping  $C_{12}$ , and transmitting the torque to an additional flywheel of the  $\Theta_3$  inertia moment, and so on.

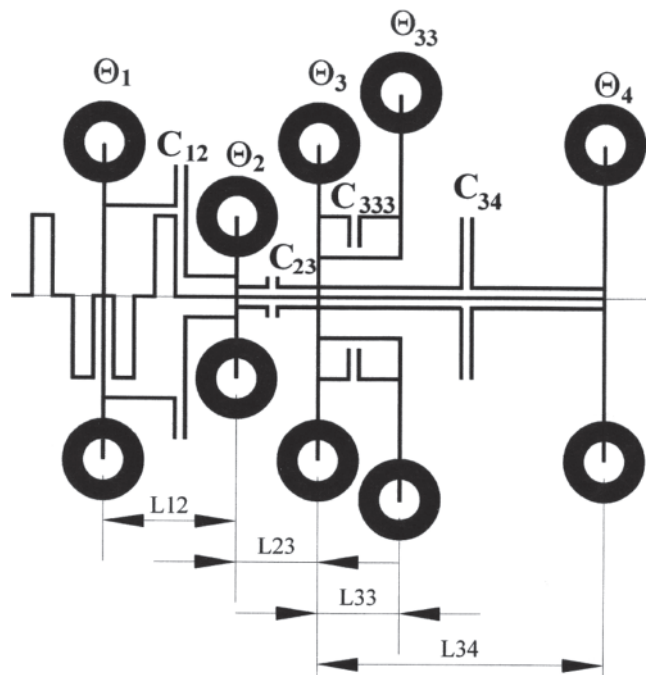


Fig. 3. Schematic of torque transmission from combustion engine to power receiver

The interrelations facilitating determination of coupling torque and momentary speed of drive train elements with an assumed time step  $\Delta t$  are presented in procedure 1 [3].

In procedure 1:

- variable  $b[j,i]$  is the coordinate of individual mass revolution angle,
- variable  $e[j]$  is the yield resulting from shaft length  $L_{j,j+1}$  – see Fig. 3,
- variable  $tet[j]$  is the mass moment of inertia  $\Theta_j$ ,
- $tlumj$  – dumping  $C_{j,j+1}$ ,
- whereas the sign of  $\Delta t m_o$  moment decides if moment is transmitted to the electrical motor which happens during stroke of expansion, or it is transmitted to the combustion engine, when auxiliary strokes are performed.

Other terms of the procedure are not important to understand the method of correction of the power transmission shaft instantaneous speed.

## CONCEPT OF VIBRATION LIMITATION USING THE HYBRID ARRANGEMENTS

Using the procedure 1 graphs of momentary angular speed of power train parts have been prepared which schematically are presented in Fig. 3. Corresponding results are presented in Fig. 4.

As it can be noticed, the quantity that varies most intensively is the shaft angular speed of the engine represented by the  $\Theta_1$  mass inertia moment in Fig. 3.

The concept of vibration limitation on hybrid arrangements consists in assumption that the rotor of electrical machine plays the role of a flywheel of the  $\Theta_2$  inertia moment. On such a system, presented schematically in Fig. 5, it is possible to extort a torque impulse from the electrical machine that could prevent the variability of its rotor angular speed.

Modern solutions of electric machine control allow to generate electric impulses affecting torque according to a given concept within a certain range. A number of ways have been investigated how to prevent the changes in rotational speed of electric machine rotor. Definitely the most effective way is to

```

for i:=0 to iii do
begin
  moms[1,i] :=(b[2,i]-b[1,i])/e[1];
  moms[2,i] :=(b[3,i]-b[2,i])/e[2];
  moms[3,i] :=(b[4,i] -b[3,i])/e[3];
  moms3[i] :=(b3[i] -b[3,i])/e3 ;

  om[1,i+1]:=om[1,i]+( + mom[i] +
                      +moms[1,i]-tlum*(om[1,i]-om[2,i])
                      )/tet[1]*delt;

  if i>20 then
  begin
    omegasrednie:=0;
    for nn:=1 to 20 do
      omegasrednie:=omegasrednie+om[1,i-21+nn]/20
    end
  else omegasrednie:=omeg;

  if om[1,i]>omegasrednie
  then deltmo:=-przeciw*momsr
  else deltmo:=+przeciw*momsr;
    moc :=deltmo*om[1,i];
    energia:=delt*moc;

  om[2,i+1]:=om[2,i]+(-moms[1,i]+moms[2,i] +deltmo
                    +tlum*(om[1,i]-om[2,i])
                    -tlum23*(om[2,i]-om[3,i]))/tet[2]*delt;

  om[3,i+1]:=om[3,i]+(
                    -moms[2,i] + moms[3,i] + moms3[i]
                    +tlum23*(om[2,i]-om[3,i])
                    -tlum34*(om[3,i]-om[4,i])
                    -tlum33*(om[3,i]-om3[i]))/tet[3]*delt;

  om3[i+1] :=om3[i] +(-moms3[i]
                    +tlum33*(om[3,i]-om3[i]))/tet3*delt;

  om[4,i+1]:=om[4,i]+(-moms[3,i] - momsr
                    +tlum34*(om[3,i]-om[4,i]))/tet[4]*delt;

  b[1,i+1]:=b[1,i]+om[1,i+1]*delt;
  b[2,i+1]:=b[2,i]+om[2,i+1]*delt;
  b[3,i+1]:=b[3,i]+om[3,i+1]*delt;
  b3[i+1] :=b3[i] +om3[i+1] *delt;
  b[4,i+1]:=b[4,i]+om[4,i+1]*delt;
end;

```

generate a torque proportional to rotor angular acceleration. So the problem is being reduced to the generation by the electric machine a torque counteractive to the engine torque. Alas, it is impossible by electric motor to generate a counteractive torque on the present stage of electric machine control. There are two reasons of such situation. Firstly, generation of torque maximal over engine operation cycle would require an electric motor of mass exceeding many times the mass of combustion engine. Secondly, it is impossible to react immediately to the changing engine speed.

Therefore it has been decided to affect the angular speed by the electric motor in a simple way consisting in:

- generation of negative torque equal to the engine average torque when rotor speed is higher than average speed,

- generation of positive torque of the same absolute value over the remaining period.

The effect of such operation can be evaluated when comparing graphs presented in Figs. 4 and 6.

Disregarding the technical possibilities of so precise reaction of electric motor to changing rotor speed, the correction of engine speed fluctuations using hybrid systems are explicitly limited. The carried out calculation of the real level of speed irregularity  $\delta$  proves that correction gives over double improvement of  $\delta$  factor. Above all such operation gives the reduction of engine generated noise. Obviously, the maximum values of coupling torque in individual parts of drive train reduce themselves as well. The values of

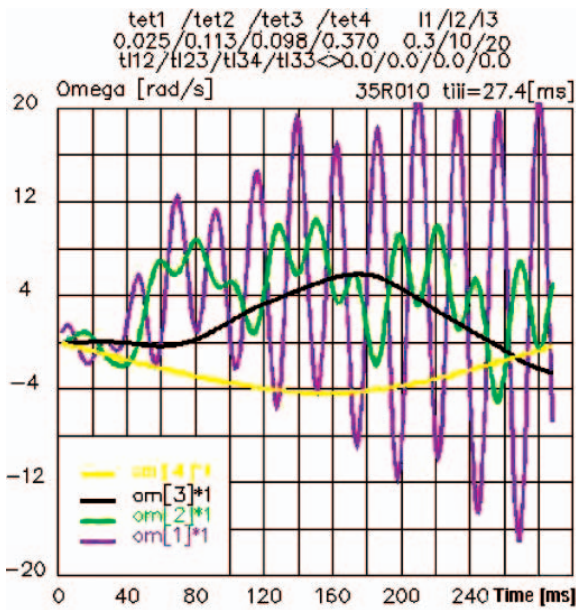


Fig. 4. Change in angular speed of drive train individual parts: description in text

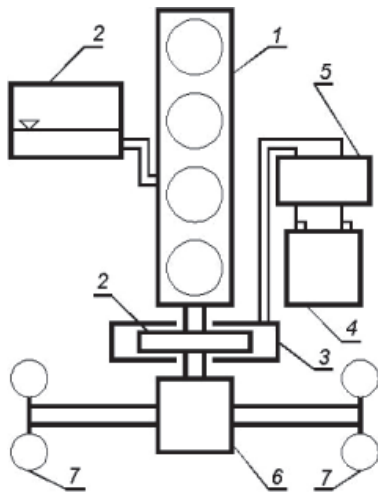


Fig. 5. Schematic of car hybrid drive: 1 – combustion engine, 2 – fuel tank, 3 – electric machine operating as motor or generator, 4 – accumulator of electric energy, 5 – electric machine and electric energy accumulator coupling control, 6 – differential, 7 – wheels

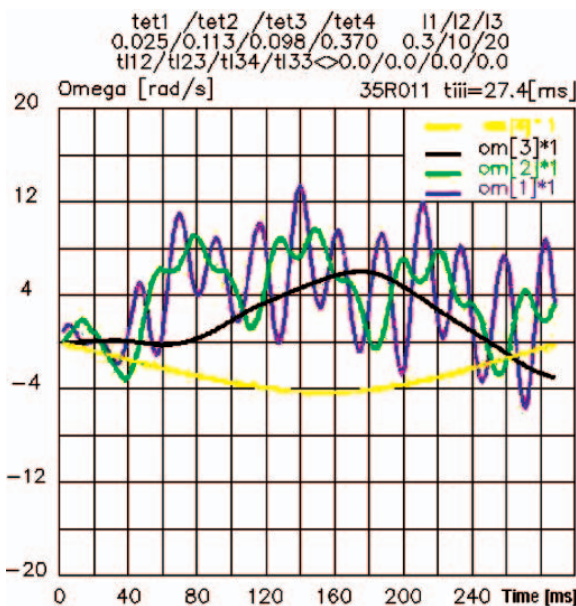


Fig. 6. Change in angular speed of drive train individual parts with speed correction performed by electric motor operating as a flywheel

coupling torque on individual sections of drive train have been presented in Fig. 7 without correction and in Fig. 8 – with correction.

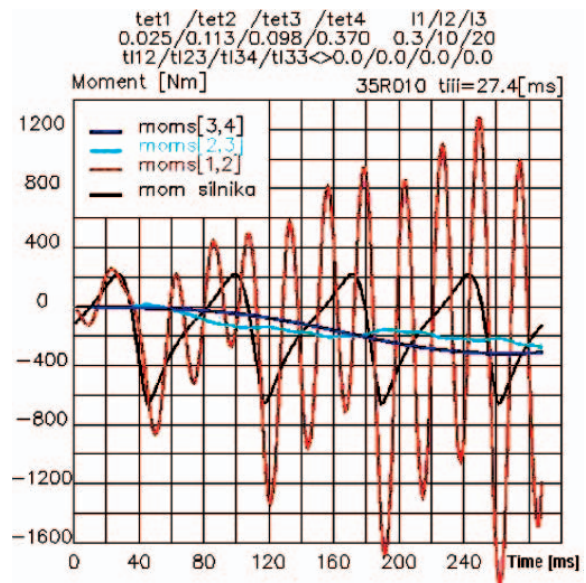


Fig. 7. Course of coupling torque between individual parts of drive train for example presented in Fig. 4

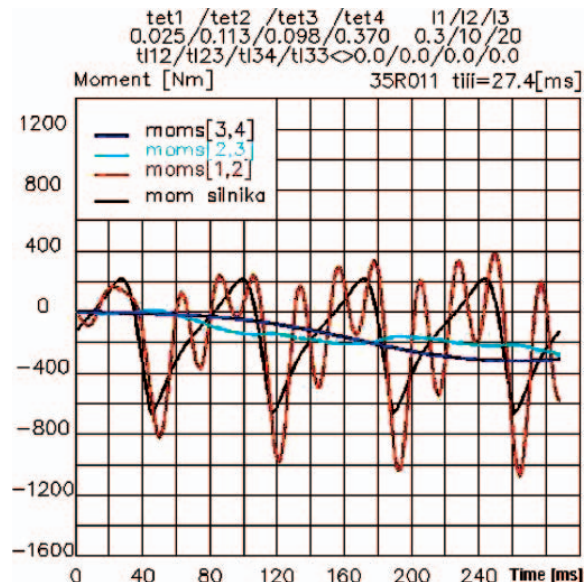


Fig. 8. Course of coupling torque between individual parts of drive train for example presented in Fig. 6

The presented considerations about the possibility of reduction the torsional vibrations in hybrid systems relate to the specific parameters of engine operation. As the additional analyses prove, the effect of vibration reduction not always is so spectacular as those presented in Figs. 4 and 6 to 8. The presented example relates to the case of resonance of the highest form (number 3 in this case) and 3 vibrations go to one cycle of engine operation. Lower form vibrations are dumped less. However, lower form of natural vibrations, especially the first form usually happens below the engine idle run speed, so it does not cause negative effects within the range of engine run.

## SUMMARY

The problem of torsional vibrations in drives incorporating reciprocating engines is still considered as difficult for satisfactory solution. In particularly on direct injection diesels

what is now a rule, double or even triple inertia flywheels are used in order to reduce torsional vibrations and accompanying noise. In extreme cases the use of viscous dampers becomes indispensable. All these solutions contribute to an increase in engine manufacturing costs, increase its weight while the use of viscous damper leads to energy dissipation which results in elevated fuel consumption. As it turns out by the efforts on application of hybrid drives to car drive trains a chance emerges to limit vibrations and noise by the use of hybrid drives primarily provided for ecologically justified coupled combustion and electric drive. The solution proposed in present study creates a chance to make use of instantaneous energy surplus in two aspects:

- energy of car braking is accumulated for its use during acceleration when further ride is possible
- energy relative to the increasing shaft momentary speed during expansion stroke of combustion engine is accumulated for stabilization of rotational speed during auxiliary strokes.

## BIBLIOGRAPHY

1. Braess HH, Seiffert U.: *Vieweg Handbuch Kraftfahrzeugtechnik*. Friedr. Vieweg & Sohn Verlag, Wiesbaden 2003
2. A. Iskra.: *Uwarunkowania techniczne stosowania paliw odnawialnych do napędu samochodów*. V Międzynarodowe Sympozjum „Polacy Razem” – Energia odnawialna w kontekście ochrony Środowiska”, Verein Polnischer Ingenieurinnen und Ingenieure in Österreich, Wien 16-18.11.2006
3. A. Iskra.: *Transformacja wyników pomiaru momentu sprzęgającego silnik z odbiornikiem mocy do momentu rzeczywistego. Transformation of the Engine-to-receiver Coupling Torque Measurement Results to the Actual Value of Torque*. *Pomiary Automatyka Kontrola*. 5/2006. Str. 41-45.

---

## CONTACT WITH THE AUTHOR

Antoni Iskra, Prof.  
Faculty of Mechanical Engineering and Management  
Poznan University of Technology  
Piotrowo 3  
60-965 Poznan, POLAND  
e-mail: antoni.iskra@put.poznan.pl

# Problems of welding in shipbuilding - an analytic-numerical assessment of the thermal cycle in haz with three dimensional heat source models in agreement with modelling rules

## Part I

### Theoretical basis of modelling and an analytical assessment of heat sources models

Eugeniusz Ranatowski, Prof  
University of Technology and Life Science, Bydgoszcz

#### ABSTRACT



*At the beginning of this paper a short characteristic of the methodology of classic Rosenthal-Rykalin solution of temperature distribution during welding is provided. In the further part, the requirements concerning process modelling were presented, particularly with thermal processes taken into consideration. Finally, the Cylindrical-Involution-Normal and Double-Ellipsoidal heat source models are presented.*

#### Keywords:

#### INTRODUCTION

Classic solutions of Fourier-Kirchhoff (F-K) partial differential equation, describing heat distribution and leading to analytic definition of temperature fields during welding process, were first started by works of Rykalin and Rosenthal. The temperature fields and other related parameters were found with assuming the following simplifications and presumptions:

- the analysis is limited to quasi-stationary state, stabilised temperature field
- heat sources are described by: point, line or plane models
- the material physical parameters are constant, temperature invariant
- welded parts structure is homogenous with isotropic physical properties
- there are no other inner heat sources during welding process
- three basic geometrical bodies are introduced in respect to the geometry:
  - the semi-infinitely extend solid
  - the infinitely extended plate
  - the infinitely extended rod.

The assumptions above were some necessary simplifications to get the solution but on the other hand affected the preciseness

of temperature field estimation. The necessary limitations are result of methods used for analytic calculation. The adopted methods mainly base on integral transform methods and Green's functions.

It should be said clearly that most of heat source analytical models as also solid material models are not adequate to presently used welding technologies, e.g. plasma stream, laser or an electron beam. In the aftermath of this, three-dimensional heat source model is introduced and also new relation Heat Source (HS) – Welded Material (WM) model is created.

Substantial imperfection of classic Rykalin's and Rosenthal's solution is a lack of taking into consideration the heat exchange at boundary surfaces. Another important problem is considering thermal process as linear, although in fact it's not linear.

#### BASIC REQUIREMENTS CONCERNING MODELLING RULES

Modelling is the process of fixing a computational model<sup>1</sup>. The bottom line of any correct modelling procedure is defining the parameters characterising the ideology and process dimensions.

An estimation of physic phenomenon during welding process, practically results in examining reciprocal relations between extensive and intensive parameters.

The transport process of extensive magnitudes requires estimation of intensive parameters during welding and is performed by using such procedures as transient Lagrangian or steady state Eulerian formulations of thermal cycle. We define an Eulerian (moving) frame with origin at the centre of the source and co-ordinates  $(x, y, z)$  – Fig. 1. For Cartesian co-ordinate system  $(x_0, y_0, z_0)$  which remains stationary for all time  $t$  and loading history, a Lagrangian co-ordinate reference is defined. Suppose a heat source is moving at a constant speed in the positive  $x_0$  direction.

The transformation from  $(x_0, y_0, z_0)$  to  $(x, y, z)$  is given by:  
 $x = x_0 - vt, y = y_0, z = z_0$ .

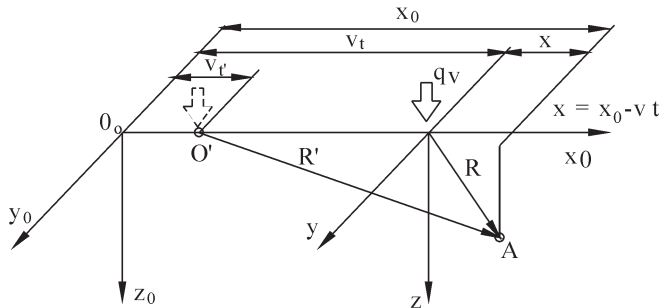


Fig. 1. Lagrangian and Eulerian co-ordinate reference

Specified phenomenon model is connected with presumption that the model represents the physic reality well enough. In addition, the characteristic feature of the model is ability to replace the actual object with the model, still committing transmitting the experimental results into actual research object.

Definition of theoretical structure of research object is performed with use of:

- physic model, describing the actual object
- mathematical model, being an equation or system of equations, describing processes together with boundary conditions, characteristic for given phenomenon.

Above mentioned statements are fundamentally in compliance with Fourier's observation – who stated in "Théorie analytique de la chaleur" that "...every phenomenon connected with heat depends on very little, general facts the way that every problem can be formulated using the language of mathematical analysis..." [2].

The basic physic laws are described mathematically, receiving first generation of mathematical models which are last modified (some of those modifications have empirical connections). In compliance with Riemann consolidations, real basic rules like heat flow, can occur for infinitely small magnitudes and must be defined as partial differential equations. Integration of such equations leads to settlements and rules for variables of space and time e.g. estimation of temperature distribution for a plate of optional thickness during welding. High conformity and quality of anticipating is obtained if definite phenomenon modelling rules are fulfilled.

Correct executing of research requires using the proper models and conditions with dependence on their likeness. Knowing the equations describing given process, for example heat flow according F-K equation the criterions and constants of similarity can be found.

If a given variable is marked  $x_i$  in actual object and  $\bar{x}_i$  in model object then the connection can be created:

$$\frac{X_1}{\bar{X}_1} = c_1, \dots, \frac{X_i}{\bar{X}_i} = c_i, \dots, \frac{X_n}{\bar{X}_n} = c_n \quad (1)$$

Modelling scale is a transforming factor. Therefore the following relation can be given:

$$\Phi(x_1, x_2, x_3, \dots, x_n) = \Phi(c_1 \bar{x}_1, c_2 \bar{x}_2, c_3 \bar{x}_3, \dots, c_n \bar{x}_n) \quad (2)$$

For similar phenomenon there is a relation given:

$$\Phi(x_1, x_2, x_3, \dots, x_n) = \Phi(\bar{x}_1, \bar{x}_2, \bar{x}_3, \dots, \bar{x}_n) \quad (3)$$

Equation (3) is fulfilled if  $c_n$  is in conformity with:

$$\Phi(c_1, c_2, c_3, \dots, c_n) = 1 \quad (4)$$

$$\Phi(c_1, c_2, c_3, \dots, c_n) =$$

$$= \frac{\Phi(c_1 \bar{x}_1, c_2 \bar{x}_2, c_3 \bar{x}_3, \dots, c_n \bar{x}_n)}{\Phi(x_1, x_2, x_3, \dots, x_n)} \quad (5)$$

In compliance with Federman's settlements it's known that if a number of variables used in experiment is equal to  $n$  and a few of them are independent  $k < n$ , then there are  $(n-k)$  equations expressed by modelling scale  $c$ . Therefore a few of dimensionless numbers may be proposed by an experimenter and be the constants of similarity. The remaining ones are described by dimensionless numbers and Federman's settlements and are called similarity criterions. The indispensable conditions for similarity existing between the models and actual objects is describing the happening physic processes by:

- the same differential equations with appropriate boundary conditions
- the similarity criterions verification.

Let's take into consideration F-K partial differential heat flow equation as a starting point – for stationary co-ordinates system  $x_0, y_0, z_0$ :

$$\text{div}(\lambda \cdot \text{grad } T) - c_p \cdot \rho \frac{\partial T}{\partial t} = -q_v(x_0, y_0, z_0, t) \quad (6)$$

The classic Rykalin's and Rosenthal's solutions assume that physic parameters describing the process model are constant whereas they are in fact non-linear for real welding system as a result of dependence on temperature.

According to that we have the following characteristic [following equations (1) – (4)]:

Process model	Actual welding system
$\lambda = \text{const}$	$\lambda(T) \neq \text{const}$
$c_p = \text{const}$	$c_p(T) \neq \text{const}$
$\rho = \text{const}$	$\rho(T) \neq \text{const}$

$$\frac{\lambda(T)}{\bar{\lambda}} = c_1; \frac{c_p(T)}{\bar{c}_p} = c_2; \frac{\rho(T)}{\bar{\rho}} = c_3 \quad (7)$$

$$c_1 \neq c_2 \neq c_3$$

$$\Phi(c_1, c_2, c_3) \neq 1 \quad (8)$$

Moreover,  $q_v$  doesn't fulfil geometric similarity condition for majority of contemporary welding methods like arc welding, GTA, GMA, plasma stream and others, assuming point, line or plain heat source model

Considering possibility of universal shape modelling and to fulfil conditions (4), (5), two main models are considered: Cylindrical-Involution-Normal (C-I-N) [3] and The Double Ellipsoidal Configuration of Source (D-E) [4]. Both models represent effective extended abilities of 3-dimensional heat distribution. The model that previously was used is the Gaussian surface flux distribution model:

$$q_v = \frac{Q \cdot k}{\pi \cdot s} \exp[-k(x^2 + y^2)] \cdot [1 - u(z-s)] \quad (9)$$

Unfortunately this one does not reflect heat power input change for “z” variable. For example Wei and Shian<sup>5</sup> constituted that under high-intensity laser beam welding the incident energy rate distribution is assumed to be Gaussian distribution and HS model is idealised by a paraboloid of revolution. This is one of main reasons why two more accurate models are implemented.

### THE CHARACTERISTIC OF HEAT SOURCE MODELS

The mathematical expression of the cylindrical-involution-normal C-I-N model is:

$$q_v = q_{vMAX} \cdot \exp[-k(x^2 + y^2) - K_z \cdot z] \cdot [1 - u(z-s)] \quad (10)$$

As it is seen “z” variable is not squared in contrast to other variables. This is an intentional purpose of this model to let it be easily integrated when using integral transformation method.

D-E model doesn't have this feature which makes it difficult to achieve precise solution while transforming.

Let's calculate  $q_{vMAX}$  factor for C-I-N. Provided that the following condition must be preserved:

$$Q = \int_0^\infty \int_{-\infty}^\infty \int_{-\infty}^\infty q_{vMAX} \cdot \exp[-k(x^2 + y^2) - K_z \cdot z] \cdot [1 - u(z-s)] dx dy dz \quad (11a)$$

and after integrate operation upon several variables we obtain:

$$Q = \int_0^\infty \int_{-\infty}^\infty \frac{\sqrt{\pi}}{\sqrt{k}} q_{vMAX} \cdot \exp(-ky^2 - K_z \cdot z) \cdot (1 - u(z-s)) dy dz \quad (11b)$$

$$Q = \int_0^\infty \frac{\pi}{k} q_{vMAX} \cdot \exp(-K_z \cdot z) \cdot [1 - u(z-s)] dz \quad (11c)$$

$$Q = -\frac{\pi}{k \cdot K_z} q_{vMAX} \cdot \exp(-K_z \cdot s) - \frac{-\pi}{k \cdot K_z} q_{vMAX} \quad (11d)$$

thus:

$$q_{vMAX} = \frac{Q}{\pi \cdot [1 - \exp(-K_z \cdot s)]} \cdot k \cdot K_z \quad (11e)$$

and finally:

$$q_v = \frac{Q}{\pi \cdot [1 - \exp(-K_z \cdot s)]} \cdot k \cdot K_z \cdot \exp[-k(x^2 + y^2) - K_z \cdot z] \cdot [1 - u(z-s)] \quad (12)$$

The  $[1 - u(z-s)]$  factor illustrates that  $q_v = 0$  if  $z > s$ , see Fig. 2.

By changing: s, k and  $K_z$  factors, C-I-N model can represent all presently used heat sources.

Let's use equation (12) to analyse the shape of the surface that limits the volume of effective C-I-N affect. Surfaces of constant values can be obtained by comparing:

$$q_v = q_{vMAX} \cdot \exp[-k((x^2 + y^2) - K_z \cdot z) \cdot (1 - u(z-s))] = \text{const} \quad (13)$$

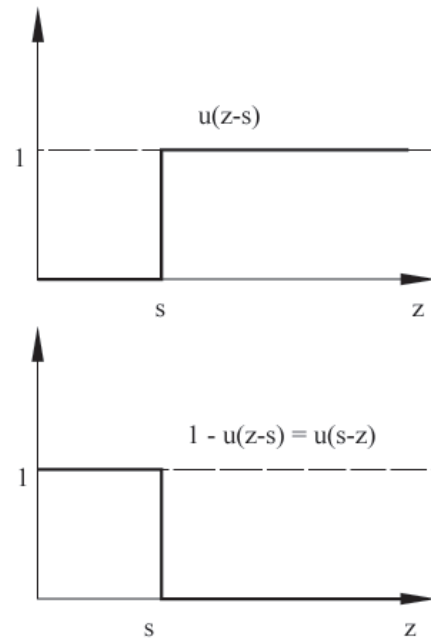


Fig. 2. Heaviside's functions

where:

$$q_{vMAX} = \frac{k \cdot K_z \cdot Q}{\pi \cdot [1 - \exp(-K_z \cdot s)]}$$

(according to (11e).

Presuming  $z < s$  we receive:

$$\exp[-k \cdot (x^2 + y^2) - K_z \cdot z] = \frac{\text{const}}{q_{vMAX}} = A$$

$$-k \cdot (x^2 + y^2) - K_z \cdot z = \ln(A) = -B$$

$$z = \frac{B - k \cdot (x^2 + y^2)}{K_z} \quad (14)$$

Solution (14) gives a family of paraboloids of revolution. Taking into consideration  $[1 - u(z-s)]$  factor, it is obvious that some of the paraboloids may be “cut”. A few examples of paraboloids are shown in Fig. 3. All of them have the same height  $h = s$ .

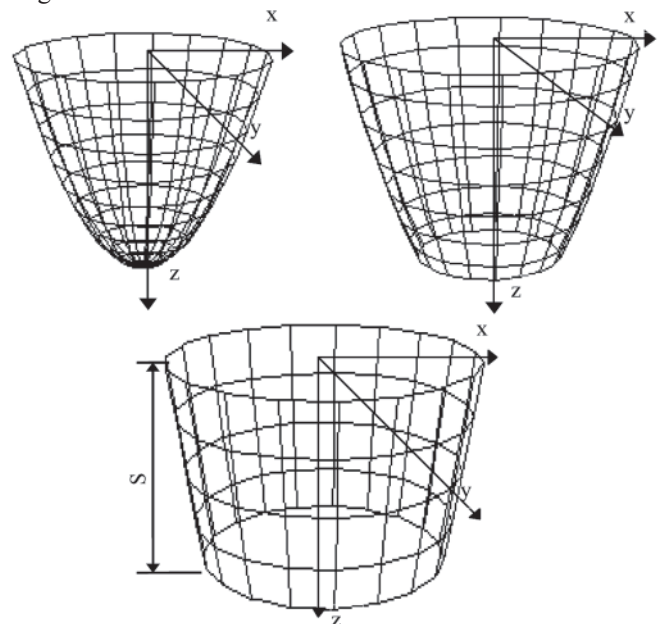


Fig. 3. Examples of the paraboloids of constant values of  $q_v$

The paraboloid that limits the volume of effective input affect can be obtained using Rykalin's suggestion that HS power loses its effectivity when:

$$q_{vMAX} \cdot \exp[-k \cdot (x^2 + y^2) - K_z \cdot z] = 0.05q_{vMAX}$$

$$-k \cdot (x^2 + y^2) - K_z \cdot z = 3$$

$$z = \frac{3}{K_z} - \frac{k}{K_z} \cdot (x^2 + y^2) \quad z \leq s \quad (15)$$

Equation (15) is an expression that describes effective input affect volume. In dependence on  $h = 3/K_z$  value, the mentioned paraboloids can be more or less slim – see Fig. 4. At extreme conditions one can obtain several, well known heat source models like:

- for  $K_z \rightarrow 0, k \neq 0$  – cylinder with height =  $s$  – disc heat source
- for  $K_z \rightarrow \infty, s \rightarrow 0, k \neq 0$  – surface heat source.

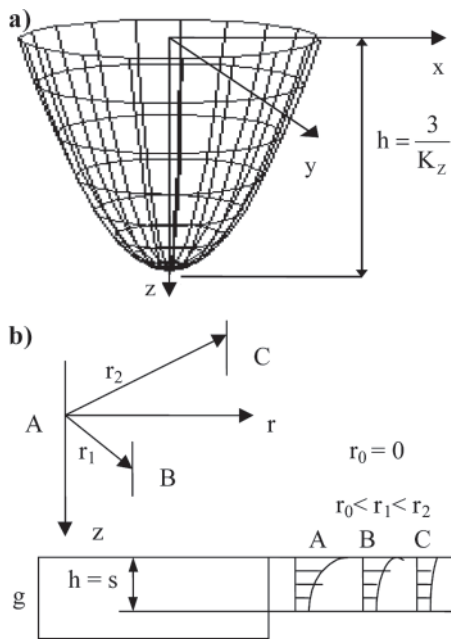


Fig. 4. The paraboloid limiting C-I-N effective input power volume (a) and power in dependence on distance from centre and depth

Possibility of changing  $K_z, k, s$  and Heaviside's function  $u(z-s)$  values makes C-I-N heat source a universal one.

The Double Ellipsoidal heat source model (D-E) (Fig. 5) established by J. Goldak [4] et al. has the following form:

$$q_{vf} = \frac{f_f \cdot 6 \cdot \sqrt{3} \cdot Q}{a \cdot b \cdot c \cdot \pi \cdot \sqrt{\pi}} \cdot \exp\left[-3 \left[ \left(\frac{x}{a_1}\right)^2 + \left(\frac{y}{b}\right)^2 + \left(\frac{z}{c}\right)^2 \right]\right]$$

$$q_{vr} = \frac{f_r \cdot 6 \cdot \sqrt{3} \cdot Q}{a \cdot b \cdot c \cdot \pi \cdot \sqrt{\pi}} \cdot \exp\left[-3 \left[ \left(\frac{x}{a_1}\right)^2 + \left(\frac{y}{b}\right)^2 + \left(\frac{z}{c}\right)^2 \right]\right]$$

$$f_r + f_f = 2 \quad (16)$$

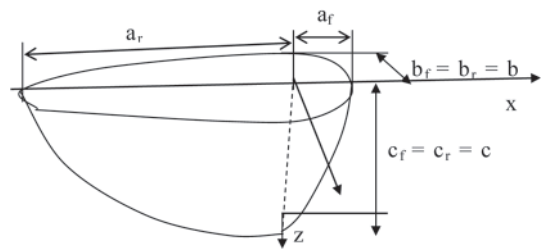


Fig. 5. The Double Ellipsoidal configuration of Heat Source model

D-E arrangement of volumetric heat sources is used for moving welding heat source of deep – penetrating surfacing or butt welds. The front half of the source is the quadrant of one ellipsoidal source, and the rear half is the quadrant of another ellipsoid. According to Godak [4] et al. some peculiar big pressure should be exerted on models, which are the combination of two or more usual heat source models, in order to effectively reflect the actual welding process. The structure of equation (16), which is an excellent one for numerical estimation of thermal cycles, has a few inconveniences when used for about finding analytic solution from methods described in this investigation. However, some estimation can be done as it is worthwhile to make some efforts, in order to obtain the necessary solution.

The adopted C-I-N model is favourable for simulation of welding process of high concentrated energy source used, like laser beam welding or electron beam welding. This one may also be used for the simulation of arc welding process.

## CONCLUSIONS

Base on the fact that substantial imperfection of Rosenthal's and Rykalin's solutions relies on:

- considering thermal process as linear
- lack of taking into study the heat exchange at boundary surface,

most of heat source analytical models and solid material models are not adequate to presently used welding methods, there are established the basic requirements which concern modelling rules of welding process.

It is constituted that the indispensable conditions for similarity existing between the actual object and model describe the happening physic process by:

- the same differential equations with appropriate boundary conditions,
- the similarity criterions verification.

In order to fulfill above conditions, at first two heat source models are considered: C-I-N and D-E which represent effective extended abilities of 3 - dimensional heat distribution.

## NOMENCLATURE

T	- temperature, [°C or K]
$\lambda$	- thermal conductivity, [W cm <sup>-1</sup> K <sup>-1</sup> ]
$c_p$	- specific heat, [J kg <sup>-1</sup> K <sup>-1</sup> ]
$\rho$	- mass density, [kg cm <sup>-3</sup> ]
t	- time, [sec]
$q_v$	- power input in volume, [W cm <sup>-3</sup> ]
Q	- net power received by the weldment, [W]
k	- a factor designating the HS concentration, [cm <sup>-2</sup> ]
s	- HS penetration depth, [cm]
$u(z-s)$	- Heaviside's function
$a_f, b_f, c_f, a_r, b_r, c_r$	- ellipsoids semiaxes, [cm]
$f_r, f_f$	- fraction of heat deposits in front and rear quadrants
$q_{vf}, q_{vr}$	- power density distribution inside the front and rear quadrants respectively, [W cm <sup>-3</sup> ]

$c_i$	- modelling scale
$K_z$	- involution factor of HS, [cm <sup>-1</sup> ]
HAZ	- Heat affected Zone
C-I-N	- Cylindrical-Involution-Normal heat source model
D-E	- Double-Ellipsoidal heat source model
HS	- Heat Source

#### BIBLIOGRAPHY

1. Lindgren L. E.: *Journal of Thermal Stresses*. Part 1. 2001. 24, pp. 141-192
2. Gårding L.: *Encounter with mathematics*. Springer-Verlag New York Inc. Copyright for Polish edition by PWN. Warsaw. 1993. pp. 278-279
3. Ranatowski E., Poćwiardowski A.: in' *Mathematical modelling of weld phenomena 4'* (ed. H. Cejrak). IoM Communications. London. 1998. pp. 379-395
4. Goldak J. et al.: *Metalurgical Transactions B*. 1984. Vol. 15B. pp. 299-305
5. Wei P. S., Shian M. D.: *Journal of Heat Transfer*. 1993. Vol. 115. pp. 848-856.

---

#### CONTACT WITH THE AUTHOR

Prof. Ranatowski Eugeniusz  
 Faculty of Mechanical Engineerig,  
 University of Technology and Life Science,  
 Prof. S. Kaliskiego 7  
 85-763 Bydgoszcz, POLAND  
 e-mail: ranatow@utp.edu.pl

# Dynamical control of dimensional quality of large steel structures in production enterprises of low - level technological support

Radosław Rutkowski, Ph. D.  
West Pomeranian University of Technology, Szczecin

## ABSTRACT



*In this paper problems of dimensional control in the building process of large steel structures are discussed. Results are presented of the research aimed at the improving of dimensional quality of prefabricated ship hull structures built in enterprises of medium – or low- level technological support. Problems of dimensional control in building process of large steel structures are highlighted. A solution is proposed of dynamical control of measurement operations as well as their optimization with taking into account current production process parameters. An example of calculations carried out in the frame of the presented solution is also attached.*

**Keywords:** shipbuilding metrology, technology, large steel structures, shipbuilding, dimensional quality, mathematical modelling.

## INTRODUCTION

As dimensional quality problems are not very much spread in shipbuilding circles, basic introductory information on the issue is presented below.

The main task of a shipyard is obviously to produce ships of the highest quality at the possibly lowest cost, i.e. arising from economical consumption of materials and the possible shortest production cycle. Moreover reaching the economic success depends on keeping the assumed contractual parameters such as a.o. ship's length, depth, breadth, minimum keel plate deformations, and finally- ship's speed, deadweight and fuel consumption etc. The reasons lead to very high quality requirements in the sense of design of technological processes and rationalization of processes of manufacturing and production quality control. Ship hull is assembled of many structural elements. Nowadays built ships are often consisted of more than a hundred sections. In Fig. 1 an example sectional division is presented. In order to make correct matching and joining the hull elements possible it is necessary to keep their dimensions, shapes and mutual position in compliance with design of the ship. In realizing the aim measurement control operations serve as main tools applied at every building phase beginning from lofting through cutting, bending, up to final assembling the ship hull after launching. They make it possible to check compliance of design of a given structure with its

realization during production cycle up to its end. The problems are covered by shipbuilding metrology.

Dimensional quality problems of small-size (up to 500 mm) and medium-size objects (up to 1150 mm), which concern both technological processes and means of production are fully mastered. For manufacturing such objects the GPS system (Geometry Product Specification) containing methods of dimensioning, dimensional tolerancing and fitting collaborating elements has been developed. Its description is given in [2]. In many cases the solutions proposed in the frame of the GPS system do not concern large-size objects which are produced mainly in shipbuilding industry. Scale of the dimensional quality problem is large in production enterprises of a technological level similar to that of Polish shipyards. As results from the author's experience in such shipyards the increase of labour consumption resulting from repair of dimensional quality errors reaches as much as  $30 \div 40\%$  of total labour consumption for building ship hull.

The problems in question are not widely discussed. Moreover the published solutions are mainly dedicated to shipyards of a high-level technological support. Such level has been reached by realization of complex restructuring projects for shipbuilding industry at the expense of very high initial outlays. To use the then-presented solutions in production enterprises of characteristics close to Polish shipyards is very difficult, if not impossible at all. Their features are discussed below.

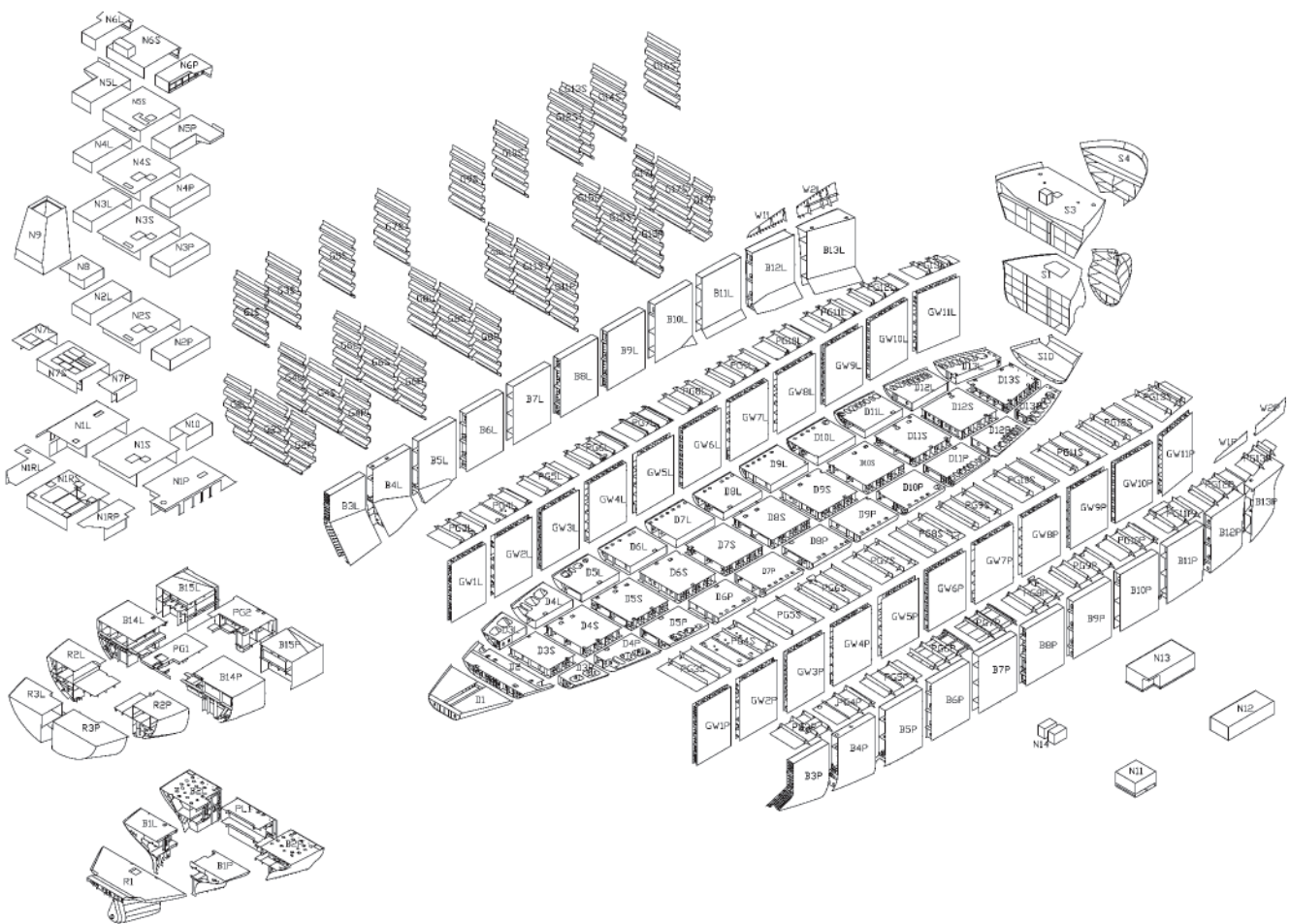


Fig. 1. Hull sectional division of a ship built by Szczecin Shipyard

## ASSUMPTIONS AND LIMITATIONS

As already mentioned the dimensional quality problems in production enterprises of characteristics similar to shipyards are very individual. It arises first of all from the following features:

- high production intensity
- large changeability of manufacturing process, that makes permanent control of dimensions during the process necessary
- separate dimensional quality requirements for particular units
- low investment possibilities
- a lack of roofing over hull assembly sites (which produces significant problems resulting from deformations due to insolation)
- a large degree of co-operation (many structural elements, e. g. hull sections and blocks, are produced by subcontractors in various manufacturing conditions).

The conditions make application of versatile measurement systems very difficult and even impossible in most cases. Moreover application of electronic measurement instrumentation which requires specialty measuring stands as well as significant financial outlays is rather troublesome.

The measuring methods most used in the above mentioned cases are those based on optical measuring instruments and, as far as conditions allow, electronic tachymeters with application of the pole measurement method. The crucial assumption (requirement) put for elaboration of solutions presented in this paper was to use the measurement methods which have been applied so far.

Moreover the necessity of application of optical measuring instruments results from the high degree of co-operation in the area of prefabrication of hull sections. In most cases the subcontractors do not have at their disposal production sites suitably prepared to carrying out dimensional quality control by using advanced measuring techniques.

## IDEA OF DYNAMICAL DIMENSIONAL CONTROL OF LARGE STEEL STRUCTURES IN PRODUCTION ENTERPRISES OF MEDIUM- AND LOW- LEVEL TECHNOLOGICAL SUPPORT

In structurebuilding process measuring processes intertwine with technological ones. We deal here with a complex technical system, to use system approach is therefore necessary for analysis of measurement control operations. Geometrical control system in the area of shipbuilding metrology is defined by this author as a set of elements of metrological operations, their manners and set of couplings between the elements and those of the technological process itself. The models in question make dynamical control of measuring processes possible on the basis of necessary accuracy standards as well as information gained from production process under way. The accuracy standards are determined by required dimensional accuracy of prefabricated and assembled hull structure elements. The problem is discussed in the further part concerning verification of the results obtained in modelling process.

The discussed models represent control and measurement systems mainly by using mathematical description as well as - to a much smaller extent - linguistic one. This is a simplified description of the process features considered important with

regard to application of the model. In the discussed case the task of the model is to indicate optimum parameters of control and measurement processes (i.e. their system).

The parameters are first of all the following:

- measurement accuracy
- measurement method to be used
- kind and model of measuring instrument
- co-ordinates of measuring instrument stand
- co-ordinates of base points.

Number of the parameters and their characteristics depend on a type of measuring task.

The overall schematic diagram of the discussed models is presented in Fig. 2.

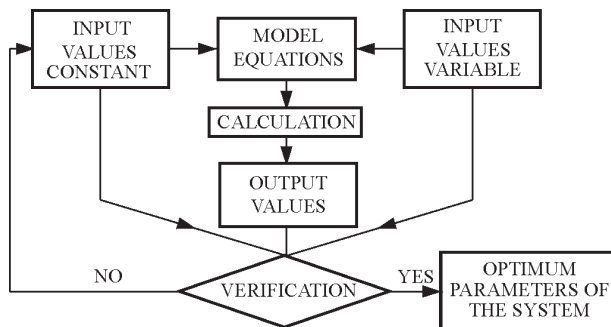


Fig. 2. Schematic diagram of modelling process

The modelling process begins from detail description of a measurement task for which control & measurement system has to be designed. Next, the following input quantities should be determined:

- constants characteristic for a given shipyard, available in the designing phase
- variables which characterize changes occurring in production process and affecting a modeled system.

The successive phases of modelling process are as follows:

- calculation processes performed on the basis of model's equations
- verification process.

„The heart” of the system is composed of the model's equations which determine input quantities on the basis of which are determined parameters subjected to verification in the successive step. The equations are elaborated on the basis of mathematical description of measurement methods. In order to present the described system it is necessary to highlight measurement methods used in shipbuilding industry, and their mathematical models.

## MEASUREMENT METHODS

As already mentioned the control & measurement operations during building process of ship hull are usually performed with the use of the pole method based on electronic tachymeters, as well as classical methods (the optical levelling method and reference line method) by using optical measuring instruments.

The pole method based on tachymeters is widely known and used during building process of large structures. Its application to shipbuilding metrology was described a. o. in [4]. And, as results from the author's experience, the shipbuilding metrology based on the classical optical instruments should be highlighted especially as regards its mathematical description on which further analyses are based.

The main characteristic feature of the discussed measurement methods is the necessity of carrying out measurements within inclined co-ordinate frames as well as in dynamically varying systems as ship hull assembling sites are usually inclined relative to levelling plane. Moreover a part of ship's outfitting operations is carried out on ships lying along berth (floating ships undergo oscillating motions). The conditions make direct application of typical measuring methods based on constant levelling plane determined by means of levels or self-levelling mechanisms, difficult and even impossible in many cases. The methods in question allow for making the reference frame independent of the levelling plane. Below is presented a short description of the mentioned methods as well as a procedure for elaborating their mathematical models.

## REFERENCE LINE METHOD

The reference line method finds broad application both to measurement of deformations and assembling control of objects. It is known in a few versions which differ to each other by measuring technique and kind of quantities to be determined. Measurements performed by using the method mostly relate to two mutually perpendicular planes: vertical one containing reference straight line, and horizontal one. During control & measurement operations carried out in ship building process the two -plane system must be replaced - for the above discussed reasons (to make the reference system independent of the levelling plane) - with the system of two mutually perpendicular planes  $\Pi_1$ ,  $\Pi_2$ , the first of which is parallel to ship's base plane (Fig. 3).

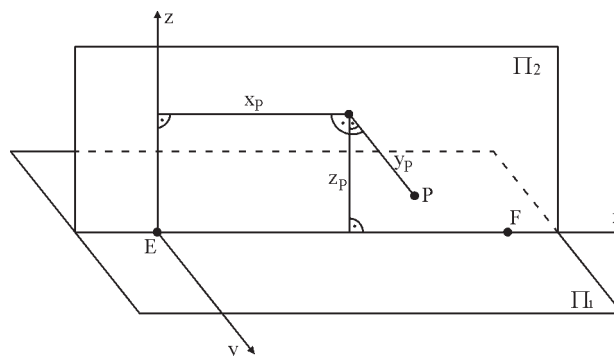


Fig. 3. Reference line method

The reference straight line is usually formed by sight line of theodolite or levelling instrument. The method in question is used to determine the coordinates  $y_p$ ,  $z_p$ ; the coordinate  $x_p$  plays an auxiliary role (as a calculation parameter). For every quantity other measuring technique is used. It results from that the quantity  $y_p$  is related to the plane  $\Pi_2$ , whereas  $z_p$  to  $\Pi_1$ . Hence separate mathematical descriptions were elaborated for determining the coordinates  $y_p$  and  $z_p$ . The coordinates  $z_p$  describe values of the sections perpendicular to the reference line and located on the plane  $\Pi_2$ . Fig. 4 was used to elaborate the mathematical model for determining the quantity  $z_p$ .

In the points E, F, and P measuring rods are placed perpendicularly to the  $\Pi_1$ . The sight line of measuring instrument determines readouts of  $h_E$ ,  $h_F$  and  $h_P$ . The searched-for value of  $z_p$  is determined by using the following relation:

$$z_p = \overline{P'P''} - h_p \quad (1)$$

On transformation the following is obtained:

$$z_p = h_E + \frac{(h_F - h_E)}{x_F} x_p - h_p \quad (2)$$

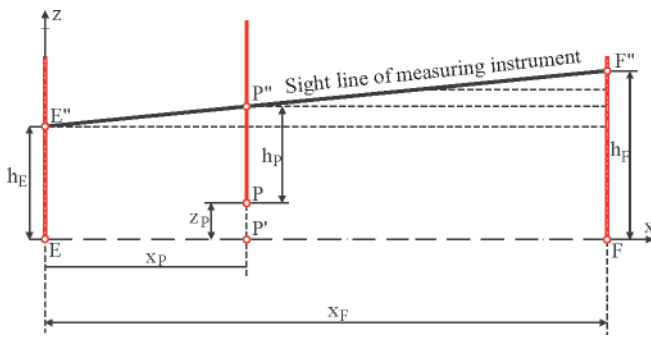


Fig. 4. Reference line method

The above given formula constitutes the mathematical model for determining the quantity  $z_p$  by means of the reference line method.

To carry out calculations by using Eq.(2) on the assembling stand is labour-consuming. To shorten them the measurement executor tries to reach the situation when  $h_E = h_P$ . In such case the determining of the quantity  $z_p$  is simplified to the following form:

$$z_p = h_E - h_p \quad (3)$$

that improves the measuring process considerably.

The coordinates  $y_p$  describe the sections perpendicular to the reference line and parallel to the plane  $\Pi_1$ . To determine the quantities, an instrument whose sight line is able to build the plane  $\Pi_2$  perpendicular to  $\Pi_1$  and directed along the reference line EF, is necessary. The searched- for value is equal to the distance of the point P from the plane  $\Pi_2$  (Fig. 5).

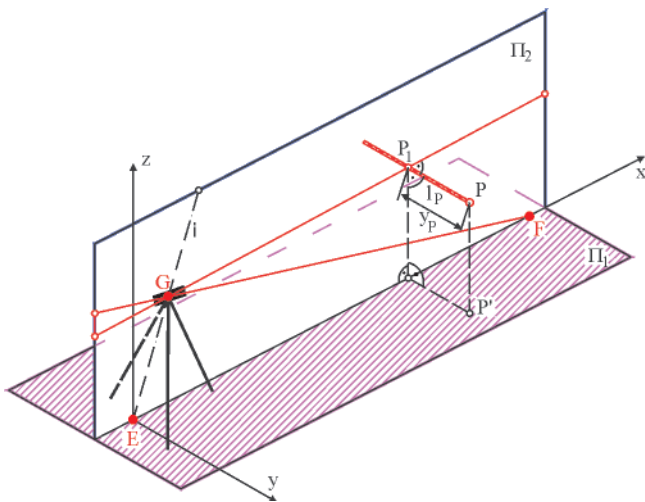


Fig. 5. Reference line method

Fig. 5 was used to elaborate the mathematical model for determining the quantity  $y_p$ . The model in question was formed on the basis of the expression describing the distance of the point  $P(x_p, l_p, z_p)$  from the plane  $\Pi_2$  which contains the points  $E(x_E, y_E, z_E)$ ,  $F(x_F, y_F, z_F)$ ,  $G(x_G, y_G, z_G)$ :

$$y_p = \frac{Rl_p + Sx_p + Tz_p + U}{\sqrt{R^2 + S^2 + T^2}} \quad (4)$$

where:

$$\begin{aligned} R &= (x_E \cdot z_F - x_E \cdot z_G - x_F \cdot z_E + x_F \cdot z_G + x_G \cdot z_E - x_G \cdot z_F) \\ S &= (-y_E \cdot z_F - y_F \cdot z_G - y_G \cdot z_E + y_E \cdot z_G + y_F \cdot z_E - y_G \cdot z_F) \\ T &= (y_F \cdot x_G - y_F \cdot x_E + y_G \cdot x_E + y_E \cdot x_F - x_F \cdot y_G - y_E \cdot x_G) \\ U &= (-y_G \cdot x_E \cdot z_F - y_E \cdot x_F \cdot z_G + y_G \cdot x_F \cdot z_E + y_E \cdot x_G \cdot z_F + \\ &\quad - y_F \cdot x_E \cdot z_G - y_F \cdot x_G \cdot z_E) \\ Rl_p + Sx_p + Tz_p + U &> 0 \end{aligned}$$

On the assumption that the auxiliary coordinate system Oxy associated with the planes  $\Pi_1$  and  $\Pi_2$  satisfies the following conditions:

- $x$  - axis of the system forms edge of intersection of the planes  $\Pi_1$  and  $\Pi_2$
- $y$  - axis lays on the plane  $\Pi_1$
- $z$  - axis lays on the plane  $\Pi_2$

the following can be assumed:

$$\left. \begin{aligned} & \bullet y_E = y_F = y_G = 0 \\ & \bullet z_E = z_F = 0 \\ & \bullet x_E = 0 \end{aligned} \right\} \quad (5)$$

On insertion of Eq. (5) to Eq. (4) the following was obtained:

$$y_p = l_p \quad (6)$$

As results from Eq. (6), in the assumed system the measuring of the quantity  $y_p$  is equivalent to the reading-out of value of the quantity  $l_p$  on the measuring rod put against the object in the point P and placed perpendicularly to the plane  $\Pi_2$ . The complexity degree of Eq. (4) makes calculating  $y_p$ - values greatly difficult. In practice one tries to reach the situation where the conditions (5) are satisfied that makes using Eq. (6) for the calculations possible.

## OPTICAL LEVELLING METHOD

As already mentioned in shipbuilding metrology it is necessary to relate measurements to planes or near-planar surfaces inclined relative to levelling plane by the small angle  $\Theta$ . In such cases appropriate measurements are performed with the use of the optical levelling method in which the reference level is not used, but the auxiliary plane  $\Pi_c$  is applied (Fig. 6) relative to which measurements are carried out. The method may be applied both to carrying out measurements on land-based assembling stands and on floating ships (floating dock, ship after launching). It is schematically presented in Fig. 6.

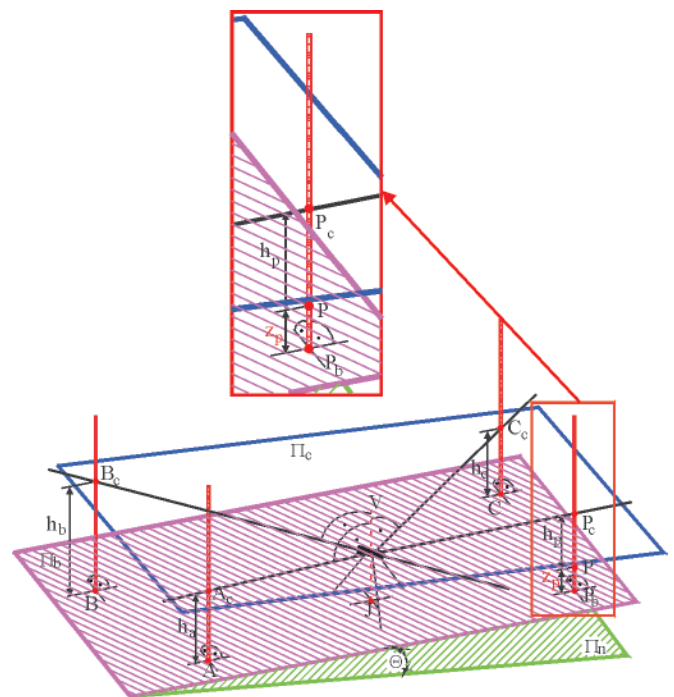


Fig. 6. Optical levelling method

The crucial task in conducting the measurements by means of the optical levelling method is to determine the coordinates

$z_p$  of the points  $P_i$  in an orto-cartesian coordinate system  $Oxyz$ . In the case when the plane  $\Pi_b$  constitutes the reference surface, the axes  $x, y$  of the system are assumed to lay just on the plane, giving them this way orientation appropriate to given purposes. The plane  $\Pi_b$  is determined by three suitably chosen points  $A, B, C$  which usually lay on a measured structure. The points are called the base.

Value of  $z_p$  is calculated in accordance with the following relation:

$$z_p = z_{P_C} - h_p \quad (7)$$

where:

$z_{P_C}$  - „ $z$ ” - coordinate of the point  $P_C$ .

Value of  $z_{P_C}$  can be determined by using the relation which expresses the equation of the plane  $\Pi_c$  which contains the points  $A(x_A, y_A, h_A), B(x_B, y_B, h_B), C(x_C, y_C, h_C)$ :

$$\begin{vmatrix} x_P & y_P & z_{P_C} & 1 \\ x_A & y_A & h_A & 1 \\ x_B & y_B & h_B & 1 \\ x_C & y_C & h_C & 1 \end{vmatrix} = 0 \quad (8)$$

On transformation, Eq. (7) can be presented as follows:

$$z_{P_C} = \frac{(\Delta x_{AB} y_P + \Delta x_{BP} y_A - \Delta x_{AP} y_B) h_C + (\Delta x_{AP} y_C - \Delta x_{AC} y_P - \Delta x_{CP} y_A) h_B + (\Delta x_{BC} y_P - \Delta x_{BP} y_C + \Delta x_{CP} y_B) h_A}{\Delta x_{AB} y_C + \Delta x_{BC} y_A - \Delta x_{AC} y_B} \quad (9)$$

where:

$$\begin{aligned} \Delta x_{AB} &= x_B - x_A \\ \Delta x_{BP} &= x_P - x_B \\ \Delta x_{AP} &= x_P - x_A \\ \Delta x_{AC} &= x_C - x_A \\ \Delta x_{CP} &= x_P - x_C \\ \Delta x_{BC} &= x_C - x_B \end{aligned}$$

On insertion of the right-hand side of Eq. (9) to Eq. (7) the following was obtained:

$$z_p = \left( \frac{(\Delta x_{AB} y_P + \Delta x_{BP} y_A - \Delta x_{AP} y_B) h_C + (\Delta x_{AP} y_C - \Delta x_{AC} y_P - \Delta x_{CP} y_A) h_B + (\Delta x_{BC} y_P - \Delta x_{BP} y_C + \Delta x_{CP} y_B) h_A}{\Delta x_{AB} y_C + \Delta x_{BC} y_A - \Delta x_{AC} y_B} \right) - h_p \quad (10)$$

This is the mathematical model of the optical levelling method.

The carrying out of calculations on the basis of the above given expression makes the control & measurement process much longer. The calculations in question become simpler when  $h_A = h_B = h_C$ . In such situation Eq. (10) takes the following form:

$$z_p = h_A - h_p \quad (11)$$

In practice one should aim at the situation when to apply Eq. (11) is possible as it greatly simplifies calculation process.

By analysing the above presented mathematical descriptions of the measurement methods it is easy to come to the conclusion that accuracy of determining measured values is first of all affected by errors of readouts taken from measuring rods. The quantities are described in the subject-matter literature, e.g. [3], by means of some approximate formulas which are decisively too-low exact for purposes of shipbuilding metrology. Therefore the quantities were determined experimentally. To this end a special testing device was elaborated by using which tests were performed for selected measuring instruments. In consequence of the tests regression equations which describe values of the errors in question, were obtained depending on aimed length values. The equations were elaborated individually both for particular instruments and measuring stands. The obtained results confirmed the above given thesis on too-low exactness of the approximate formulas describing the errors in question.

A way of making use of the obtained equations has been presented with the use of a calculation example given below.

## MODEL EQUATIONS

During modelling process calculations are carried out on the basis of model equations elaborated by using mathematical description. The models were used for elaborating accuracy description of measurements performed by using particular methods. The description was prepared with the use of the principle of proliferation of mean errors. As a result of the operation the following was obtained:

For optical levelling:

$$\begin{aligned} m_{z_{P_i}}^2 &= \left( \frac{\partial z_{P_i}}{\partial h_A} \right)^2 m_{h_A}^2 + \left( \frac{\partial z_{P_i}}{\partial h_B} \right)^2 m_{h_B}^2 + \left( \frac{\partial z_{P_i}}{\partial h_C} \right)^2 m_{h_C}^2 + \\ &+ \left( \frac{\partial z_{P_i}}{\partial h_{P_i}} \right)^2 m_{h_{P_i}}^2 + \left( \frac{\partial z_{P_i}}{\partial x_A} \right)^2 m_{x_A}^2 + \left( \frac{\partial z_{P_i}}{\partial y_A} \right)^2 m_{y_A}^2 + \\ &+ \left( \frac{\partial z_{P_i}}{\partial x_B} \right)^2 m_{x_B}^2 + \left( \frac{\partial z_{P_i}}{\partial y_B} \right)^2 m_{y_B}^2 + \left( \frac{\partial z_{P_i}}{\partial x_C} \right)^2 m_{x_C}^2 + \\ &+ \left( \frac{\partial z_{P_i}}{\partial y_C} \right)^2 m_{y_C}^2 + \left( \frac{\partial z_{P_i}}{\partial x_{P_i}} \right)^2 m_{x_{P_i}}^2 + \left( \frac{\partial z_{P_i}}{\partial y_{P_i}} \right)^2 m_{y_{P_i}}^2 \end{aligned} \quad (12)$$

$i = 1, 2, \dots, n$

where:

- $n$  – number of points P,  
 $m_{h_A}, m_{h_B}, m_{h_C}, m_{h_{P_i}}$  – standard deviations of respective readouts from measuring rods  
 $m_{x_A}, m_{y_A}, m_{x_B}, m_{y_B}, m_{x_C}, m_{y_C}, m_{x_{P_i}}, m_{y_{P_i}}$  – standard deviations of determination of coordinates of the points A, B, C and  $P_i$ .

To the variable  $z_p$  the parameter „i” was introduced, ( $z_p$ ), which describes a number of the points P whose coordinates „z” are to be determined in one measuring process.

For the reference line method the following was achieved:

For  $z_p$ :

$$m_{z_p}^2 = \left( \frac{\partial z_p}{\partial h_E} \right)^2 m_{h_E}^2 + \left( \frac{\partial z_p}{\partial h_B} \right)^2 m_{h_B}^2 + \left( \frac{\partial z_p}{\partial h_p} \right)^2 m_{h_p}^2 + \left( \frac{\partial z_p}{\partial x_F} \right)^2 m_{x_F}^2 + \left( \frac{\partial z_p}{\partial x_P} \right)^2 m_{x_P}^2 \quad (13)$$

where:

- $x_E, x_P$  – coordinates of the points E and P  
 $h_E, h_p, h_P$  – readouts from measuring rods placed in the points E, F, and P  
 $m_{x_E}, m_{x_P}$  – standard deviations of determination of coordinates of the points E, P  
 $m_{h_E}, m_{h_F}, m_{h_P}$  – standard deviations of appropriate readouts from measuring rods.

For  $y_p$ :

$$m_{y_p}^2 = \left( \frac{\partial y_p}{\partial x_E} \right)^2 m_{x_E}^2 + \left( \frac{\partial y_p}{\partial y_E} \right)^2 m_{y_E}^2 + \left( \frac{\partial y_p}{\partial z_E} \right)^2 m_{z_E}^2 + \left( \frac{\partial y_p}{\partial x_F} \right)^2 m_{x_F}^2 + \left( \frac{\partial y_p}{\partial y_F} \right)^2 m_{y_F}^2 + \left( \frac{\partial y_p}{\partial z_F} \right)^2 m_{z_F}^2 + \left( \frac{\partial y_p}{\partial x_G} \right)^2 m_{x_G}^2 + \left( \frac{\partial y_p}{\partial y_G} \right)^2 m_{y_G}^2 + \left( \frac{\partial y_p}{\partial z_G} \right)^2 m_{z_G}^2 + \left( \frac{\partial y_p}{\partial x_P} \right)^2 m_{x_P}^2 + \left( \frac{\partial y_p}{\partial l_P} \right)^2 m_{l_P}^2 + \left( \frac{\partial y_p}{\partial z_P} \right)^2 m_{z_P}^2 \quad (14)$$

where:

- $m_{x_E}, m_{y_E}, m_{z_E}, m_{x_F}, m_{y_F}, m_{z_F}, m_{x_G}, m_{y_G}, m_{z_G}, m_{x_P}, m_{y_P}, m_{z_P}, m_{l_P}$  – standard deviations of determination of appropriate quantities.

Mathematical model of the pole method as well as description of accuracy of measurements carried out by using the method, was presented in [4].

## CALCULATIONS AND THEIR VERIFICATION

Description of procedure of using particular equations would require a very extensive elaboration. Therefore the author considered it reasonable to present only a selected calculation process based on the equations of the optical levelling method. Calculation procedures for the remaining equations are carried out by using similar principles.

The calculations consist in finding optimum parameters (decision variables) for assumed input data. To this end, appropriate optimization methods were selected to take into account complexity of particular models. In the case in question searching for optimum parameters consists in finding an extremum of the function (15) which describes standard deviation of a given measuring process. In the case of measurements carried out by means of the optical levelling method the function takes the following form:

$$F = \sum_{i=1}^n r_{z_{P_i}} \rightarrow \min \quad (15)$$

$i = 1, 2, \dots, n$

where:

- $n$  – number of the points P (measured ones),  
 $r_{z_{P_i}}$  – quantity which expresses determination accuracy of the coordinate „z” for a given point  $P_i$ .

The task is realized by finding a value of the vector  $u$ , Eq.(16), which minimizes the above given function.

$$u = [x_A, y_A, x_B, y_B, x_C, y_C, x_P, y_P] \quad (16)$$

where:

- $x_A, y_A, x_B, y_B, x_C, y_C$  – coordinates of the base points,  
 $x_P, y_P$  – coordinates of the measuring stand.

The quantity  $r_{z_{P_i}}$  was defined on the basis of Eq. (12). Its form is given by the following expression:

$$r_{z_{P_i}} = \left( \frac{\partial z_{P_i}}{\partial h_A} \right)^2 \cdot t_A^2 + \left( \frac{\partial z_{P_i}}{\partial h_B} \right)^2 \cdot t_B^2 + \left( \frac{\partial z_{P_i}}{\partial h_C} \right)^2 \cdot t_C^2 + \left( \frac{\partial z_{P_i}}{\partial h_{P_i}} \right)^2 \cdot t_{P_i}^2 + \left( \frac{\partial z_{P_i}}{\partial x_A} \right)^2 + \left( \frac{\partial z_{P_i}}{\partial y_A} \right)^2 + \left( \frac{\partial z_{P_i}}{\partial x_B} \right)^2 + \left( \frac{\partial z_{P_i}}{\partial y_B} \right)^2 + \left( \frac{\partial z_{P_i}}{\partial x_C} \right)^2 + \left( \frac{\partial z_{P_i}}{\partial y_C} \right)^2 + \left( \frac{\partial z_{P_i}}{\partial x_{P_i}} \right)^2 + \left( \frac{\partial z_{P_i}}{\partial y_{P_i}} \right)^2 \quad (17)$$

$i = 1, 2, \dots, n$

where:

- $n$  – number of the points P  
 $t_A, t_B, t_C, t_{P_i}$  – equations which describe standard deviation of readouts taken from measuring rod.

In the above given equation, values of standard deviations of determination of coordinates of particular points (see Eq. 12) were not taken into account as they can be considered constant and mutually identical. The performed calculation tests which consisted in inserting the constants to the optimization equation, showed that they did not affect the obtained results.

On the basis of the analysis of values of readout errors the following general form of the equations „t” which describe standard deviation of readouts taken from measuring rod, was assumed:

$$t_i = a g_i^2 + b g_i + c \quad (18)$$

where:

- $l = A, B, C, P_i$  – location points of measuring rods,  
 $a, b, c$  – coefficients of the equation which describes aiming error,

$g_1 = \sqrt{(x_1 - x_j)^2 + (y_1 - y_j)^2}$  – sight line length for readouts taken from measuring rods located in the points A, B, C, P<sub>i</sub>  
 $x_1, x_j, y_1, y_j$  – coordinates of the points A, B, C, P<sub>i</sub> as well as the measuring stand location point J, respectively.

Values of the coefficients a, b, c of the equations „t” result from a regression analysis performed for the obtained test results. Example results obtained for measurements carried out on slipway are presented in Fig. 7.

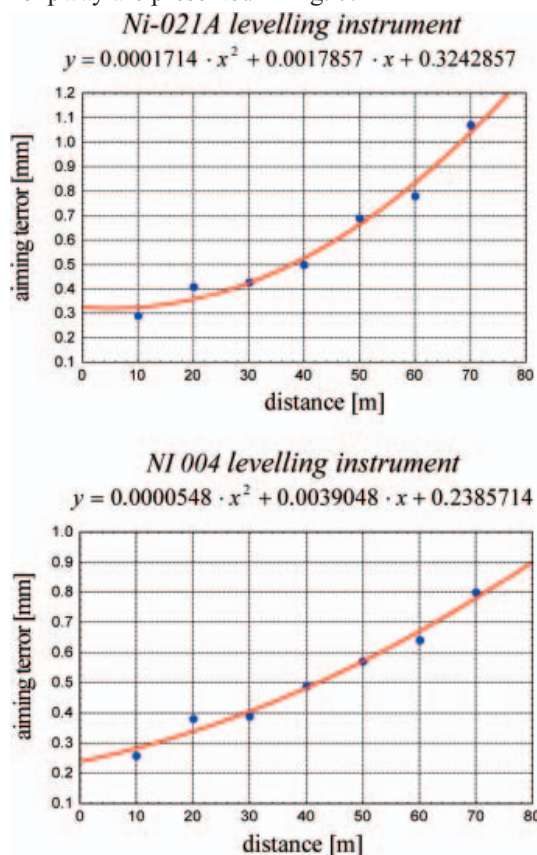


Fig. 7. Aiming error and reading-out error of values taken from measuring rod

Values of the searched-for vector **u**, Eq. (16), are to satisfy a given set of equations or inequalities – constraints. In the discussed optimization process the constraints result from an allowable location of measuring stand and base points. The location can be determined as an area of set of coordinates. If this is an area, the inequality constraints  $a \leq c \leq b$  are used, where c stands for the coordinate x or y of the points A, B, C, J, and a, b constitute its lower and upper constraint. And, if the set of coordinates is selected, the equality constraints:  $c = (d_1, \dots, d_n)$ , where  $d_n$  stand for values of the above mentioned coordinates, possible to be selected, are applied. In practice, location of base points is usually described by pairs of coordinates, but location of measuring instrument is indicated as an area.

In shipyard practice the coordinates „z” are determined even for a dozen or so points P. It generates a dozen or so objective function components described by Eq. (17). Finally for the case in question a very complex formula has been obtained. To make applying the proposed solutions to shipbuilding metrology possible it is necessary to use a software by which it would be possible to fast elaborate and minimize the discussed functions.

Choice of such software and optimization method is rather subjective, depending on which computer and software is at

hand. This author selected the Mathcad software. The choice was supported by multiple test calculations. The software offers two optimization methods:

- quasi-Newtonian one
- method of coupled gradients.

Calculations were performed by using both the methods. Differences in their results were found small. Better results (the objective function reached smaller values) were achieved by using the quasi-Newtonian method. Moreover superiority of the method was supported by that some problems with satisfying constraints arose when the method of coupled gradients was used. Summing up, the Mathcad software satisfies the following basic requirements for solving the calculation tasks of the kind:

- repeatability of results
- fulfilment of constraints
- short time of calculations (if suitable calculation modules are prepared in advance the time of realization of a complex optimization task by using the optical levelling method will not exceed one hour).

The detail description of the software as well as its optimization methods can be found a.o. in [1].

In order to better highlight the described process in the further part of the paper a simple example of the modelling process which covers also the optimization process based on the optical levelling method, is given. Of course there is possible to present more complex calculation processes. However it would require to make a separate elaboration.

The next step of the modelling of a given system is the process of verification aimed at selection of parameters of the system, which make it possible to reach such accuracy of measuring process that satisfies technical and economical requirements. The technical requirements are associated with manufacturing tolerances on the basis of which minimum accuracy of measurements is determined. However the economical requirements are connected with cost of performance of measurements as well as accompanying operations (e.g. stopping production process, reorganization of a production stand on which measurements have to be carried out etc). The latter criterion is deemed secondary for the process in question as that orientated towards fulfilment of technical requirements is of priority importance.

In order to determine minimum accuracy to apply the commonly used „golden principle of measuring technique” of Berndt, consisting in that standard deviation of a measurement should not exceed 10 % of manufacturing tolerance, was proposed. And, in the case of obtaining a measurement result placed within uncertainty area (see Fig. 8) a technological analysis of production process under way should be performed. In the situation when the procedure indicates necessity of increasing measurement accuracy the modelling should be repeated for a modified technical criterion and to perform again measuring process.

In the case when obtained results do not satisfy verification criteria, input constant data should be changed by applying another:

- measuring instrument
- measuring method.

As already mentioned, the calculation and verification processes make it possible to determine the optimum parameters of modelled measurement process, such as:

- measurement accuracy
- measurement method to be used
- type and model of measuring instrument
- coordinates of measuring instrument stand
- coordinates of base points.

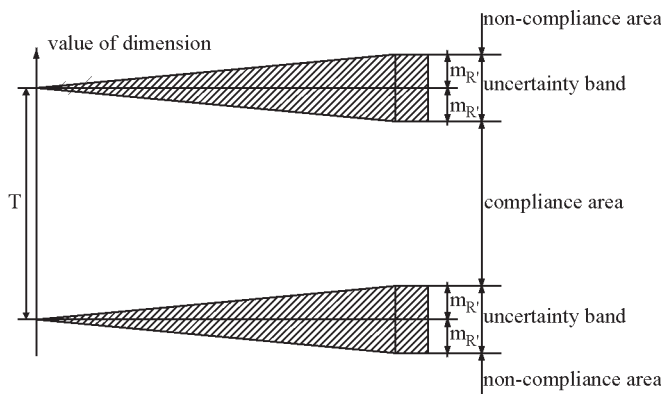


**Fig. 8.** Influence of measurement uncertainty on assessment of obtained results, where:  $m_R$  – standard deviation of determination of R – dimension; T – manufacturing tolerance, **compliance area** – tolerance area lessened by standard deviation of determination of R – dimension; **non-compliance area** – areas outside the tolerance area increased by standard deviation of measurement; **uncertainty band** – the interval within which neither compliance nor non-compliance can be stated

## EXAMPLE MODELLING PROCESS

To better highlight the described processes and their possible applications an example of modelling process based on a real measurement task is presented below.

In the given example the modelling equation was subjected also to maximization process that showed a scale of possible profits available due to optimizing process.

The four phases can be distinguished in the modelling process in question:

- 1<sup>st</sup> phase: Determination of input parameters (measurement method, measuring instrument, available coordinates of base points, admissible location of measuring instrument, manufacturing tolerance of an object to be measured);
- 2<sup>nd</sup> phase: Determination of optimum location of measuring instrument and base points [acc.Eqs (15) (17) (18)];
- 3<sup>rd</sup> phase: Calculation of standard deviation of „z” – coordinates of measurement points [acc. Eq.(12)];
- 4<sup>th</sup> phase: Verification.

The designed control & measurement system is aimed at checking waviness of inner bottom of a bottom section of ship hull during its assembling on slipway. The schematic situation diagram of the object to be measured is presented in Fig. 9.

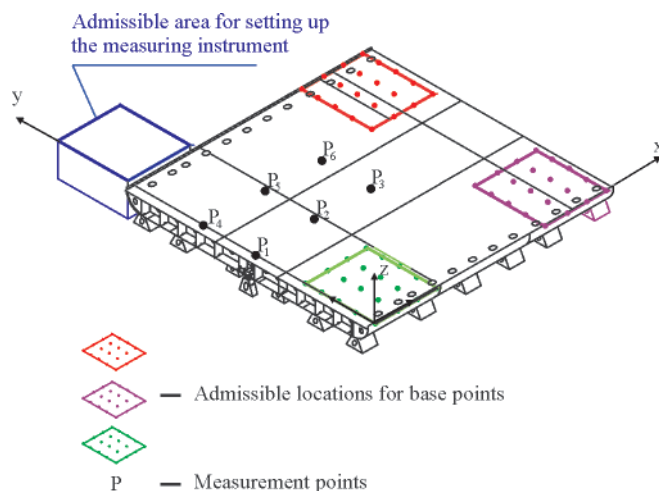


**Fig. 9.** Schematic situation diagram of the discussed measurement task

As assumed, the measurements were performed with the use of Ni-021A levelling instrument (a relevant value of readout error taken from measuring rod is given in Fig. 7). Tolerances

for measured quantities, established by ship design office were equal to  $\pm 7$  mm.

In order to keep this presentation as clear as possible only final results of particular calculations are attached.

In the case in question the objective function is composed of six components  $r_{z_{P_i}}$ :

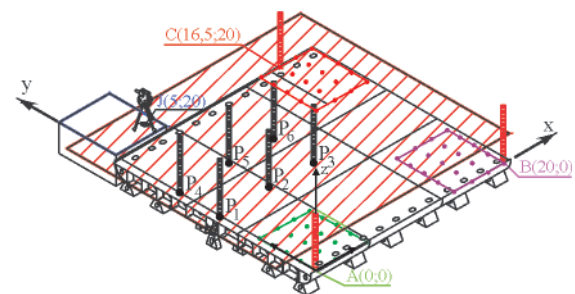
$$F = r_{z_{P_1}} + r_{z_{P_2}} + r_{z_{P_3}} + r_{z_{P_4}} + r_{z_{P_5}} + r_{z_{P_6}} \quad (19)$$

Particular elements of the objective function are described by using Eq. (17). The component t described by means of Eq. (18) took the following form for the investigation results shown in Fig. 7:

$$t_1 = 0.0001714[(x_1 - x_j)^2 + (y_1 - y_j)^2] + 0.0017857\sqrt{(x_1 - x_j)^2 + (y_1 - y_j)^2} + 0.3242857 \quad (20)$$

The obtained optimization results, i.e. the coordinates of the base points as well as measuring stand, are presented in Fig. 10. Values of the coordinates are given in meters. In Fig. 10 the most unfavourable variant is also given.

a) VARIANT 1 (optimal)



b) VARIANT 2 (most unfavourable)

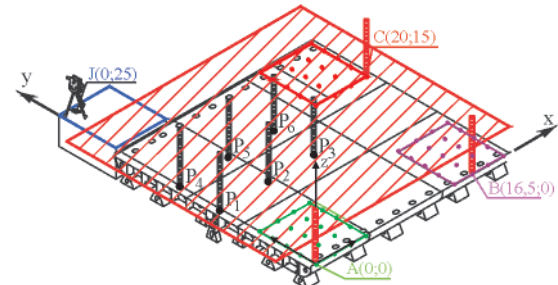


**Fig. 10.** The optimum variant of the measurements, (a), and the most unfavourable one, (b)

For the parameters presented in the figure was determined standard deviation of „z” – coordinate of the points  $P_1, P_2, P_3, P_4, P_5, P_6$ . For the calculations Eqs. (12) were used. The value of the standard deviation of determination of location coordinates of measuring rods was assumed to be 5 mm. The obtained results are graphically presented in Fig. 11.

Taking into account the value of manufacturing tolerances of the measured object, equal to  $\pm 7$  mm, one can state that the obtained results of measurement uncertainty satisfy the basic requirements according to the Berndt principle. When after completing the measurements the obtained results are placed within the uncertainty area (see Fig. 8) the measurements should be repeated with changed input parameters. In the case in question the most suitable operation would be to use a measuring instrument of a smaller error of readouts taken from measuring rod.

On the basis of the obtained results it can be stated that this is choice of location of base points and measuring instrument stand which is crucial for accuracy of measurements performed

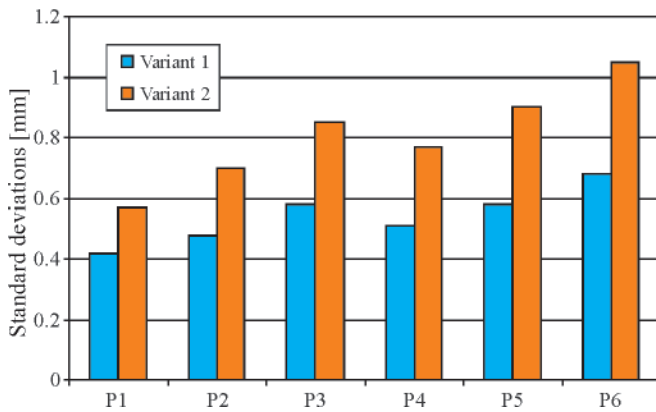


Fig. 11. Values of standard deviation of determination of  $z''$  – coordinates of the points  $P_i$

with the use of the optical levelling method. The results obtained from the above presented calculation process for the most unfavourable variant as well as the optimum one reveal positive consequences of application of optimization methods. The presented case is rather not complex, for more complex measuring processes profits due to application of the discussed methods are greater.

As the presented example confirms, due to the application of modelling process effective control of manufacturing tolerances can be ensured by using optical measuring instruments.

## CONCLUSIONS

- The solutions presented in this paper result from investigations in the area of shipbuilding metrology, carried out for the sake of production enterprises of medium- or low- level technological support. The fact has determined the guidelines as well as limitations which appeared during realization of the task in question. The proposed solutions are mainly addressed to enterprises of the above mentioned kind. In such enterprises permanent dimensional control is

essential, that makes role of measurement processes more meaningful and in consequence the discussed problems more important.

- The solutions proposed in this paper are tested by GEOMETR company which carries out measurement operations in the enterprises producing large-size steel structures.

## BIBLIOGRAPHY

- Fausett, Laurene V.: *Numerical methods using MathCAD*, Upper Saddle River, Prentice Hall, 2002
- Humienny Z.; Bialas S.; Osanna P.H.; Tamre M.; Weckenmann A., Blunt L. (et al.): *Geometrical Product Specifications (GPS) – course for Technical Universities*. Warsaw University of Technology Printing House, Warsaw, 2001
- Jagielski A.: *Geodesy I*. Stabill Publishing House, Cracow 2002.
- Niebylski J.: *Optimization of the collection of geometrical data in shipbuilding*. The International Conference on Marine Technology ODRA 99, Computational Mechanics Publications, Southampton – Boston, 2000
- Okumoto Y.: *Dimensional Error of Assembled Blocks*. Journal of Ship Production, Vol. 17, No. 1, 2001
- Okumoto Y.: *Optimization of Block Erection Using a Genetic Algorithm*. Journal of Ship Production, Vol. 18, No. 2, 2002.
- Rutkowski R.: *Geometrical control systems modeling of three-dimensional steel structures referring to the required accuracy standards*. Doctoral thesis, Szczecin University of Technology, Maritime Technology Faculty, Szczecin, 2005.

## CONTACT WITH THE AUTHOR

Radosław Rutkowski, Ph. D.  
 West Pomeranian University of Technology, Szczecin  
 Faculty of Marine Technology  
 Al. Piastów 41  
 71-065 Szczecin, POLAND  
 e-mail: rutex@zut.edu.pl